Springer Theses
Recognizing Outstanding Ph.D. Research

Kirsten Schnorr

XUV Pump-Probe Experiments on Diatomic Molecules

Tracing the Dynamics of Electron Rearrangement and Interatomic Coulombic Decay

Springer

Springer Theses

Recognizing Outstanding Ph.D. Research

Aims and Scope

The series "Springer Theses" brings together a selection of the very best Ph.D. theses from around the world and across the physical sciences. Nominated and endorsed by two recognized specialists, each published volume has been selected for its scientific excellence and the high impact of its contents for the pertinent field of research. For greater accessibility to non-specialists, the published versions include an extended introduction, as well as a foreword by the student's supervisor explaining the special relevance of the work for the field. As a whole, the series will provide a valuable resource both for newcomers to the research fields described, and for other scientists seeking detailed background information on special questions. Finally, it provides an accredited documentation of the valuable contributions made by today's younger generation of scientists.

Theses are accepted into the series by invited nomination only and must fulfill all of the following criteria

- They must be written in good English.
- The topic should fall within the confines of Chemistry, Physics, Earth Sciences, Engineering and related interdisciplinary fields such as Materials, Nanoscience, Chemical Engineering, Complex Systems and Biophysics.
- The work reported in the thesis must represent a significant scientific advance.
- If the thesis includes previously published material, permission to reproduce this must be gained from the respective copyright holder.
- They must have been examined and passed during the 12 months prior to nomination.
- Each thesis should include a foreword by the supervisor outlining the significance of its content.
- The theses should have a clearly defined structure including an introduction accessible to scientists not expert in that particular field.

More information about this series at http://www.springer.com/series/8790

Kirsten Schnorr

XUV Pump-Probe Experiments on Diatomic Molecules

Tracing the Dynamics of Electron Rearrangement and Interatomic Coulombic Decay

Doctoral Thesis accepted by
the University of Heidelberg, Germany

Springer

Author
Dr. Kirsten Schnorr
Department of Quantum Dynamics and Control
Max Planck Institute for Nuclear Physics
Heidelberg
Germany

Supervisor
Priv.-Doz. Dr. Robert Moshammer
Department of Quantum Dynamics and Control
Max Planck Institute for Nuclear Physics
Heidelberg
Germany

ISSN 2190-5053 ISSN 2190-5061 (electronic)
Springer Theses
ISBN 978-3-319-12138-3 ISBN 978-3-319-12139-0 (eBook)
DOI 10.1007/978-3-319-12139-0

Library of Congress Control Number: 2014956713

Springer Cham Heidelberg New York Dordrecht London

Printed on acid-free paper

Springer International Publishing AG Switzerland is part of Springer Science+Business Media (www.springer.com)

Supervisor's Foreword

The advent of free-electron lasers (FELs) has opened up entirely new research opportunities by combining the key features of optical lasers, such as short and intense pulses, with those of synchrotron sources, which routinely deliver extreme-ultraviolet (XUV) and X-ray radiation. In this thesis, the first FEL that reached into the XUV, the free-electron laser in Hamburg (FLASH), has been employed to investigate fundamental relaxation mechanisms of excited molecules in the time domain.

The short pulse-durations in combination with high intensities allow XUV-pump–XUV-probe experiments to be performed: The first laser pulse ionizes a molecule, thereby initiating a certain reaction and a delayed copy of the first pulse probes the transient state by further ionizing the molecular ion. The pump–probe technique was combined with multi-particle coincidence spectroscopy by using a so-called reaction microscope to investigate electron transfer in dissociating multiply charged iodine molecules and to determine the lifetime of interatomic Coulombic decay (ICD) in neon dimers.

Electron transfer is a ubiquitous relaxation process in plasma physics, chemical reactions, and ion collisions, in particular for slowly moving nuclei. This energy regime is challenging for theory and experimentally difficult to access. However, this thesis presents an elegant way to study and control electron transfer between two dissociating iodine ions by combining the pump–probe technique with Coulomb explosion imaging. The obtained results are in excellent agreement with the intuitive over the barrier model, which is commonly used in slow ion-atom collisions.

Due to the high FEL intensities, charge states up to I_2^{17+} were reached upon impact of a single 87 eV pulse. Understanding the fragmentation dynamics of multiply ionized molecules, in particular those with heavy constituents serving as photoabsorption centers, is of crucial importance for the realization of single particle imaging at FELs. This technique is only possible if the molecule is imaged before it is damaged. Therefore, the present prototype study gives precious input on

how efficiently and over which distances electrons are transferred in multiply charged molecules.

In ICD, a highly excited atom or ion transfers its excess energy radiationless over quite large distances to one of its neighbors, which is consequently ionized. This process occurs in weakly bound systems, like van der Waals and hydrogen bonded clusters, and happens on timescales that are typically two to three orders of magnitude shorter than competing relaxation mechanisms. The ejection of slow electrons together with the aforementioned key features make ICD an important contributor to radiation-induced DNA damage in tissue, with far reaching consequences for cancer therapy. Since the prediction of ICD in 1997, it has triggered a large amount of theoretical and experimental effort; however, no direct time-resolved measurement of the quintessential lifetime had been performed until now. Within this thesis an XUV pump-probe scheme was applied to determine the ICD lifetime in neon dimers, resulting in a value of 150 ± 50 fs, which agrees well with calculations, provided nuclear motion is explicitly taken into account.

Heidelberg, August 2014 Priv.-Doz. Dr. Robert Moshammer

Abstract

Within this thesis the dynamics of diatomic molecules, initiated and probed by intense extreme-ultraviolet (XUV) radiation delivered by the free-electron laser in Hamburg (FLASH), is investigated by means of three-dimensional recoil-ion momentum spectroscopy.

In a study on iodine molecules I_2, ultrafast charge rearrangement between the two ions of a dissociating molecule is triggered by the localized absorption of short 87 eV XUV pulses at either of the ions and studied as a function of their internuclear distance. This yields the critical distance and the corresponding time up to which charge transfer along the internuclear axis can take place dependent on the charge state of the photon-absorbing ion. Additionally, the response to intense XUV radiation of molecules and of isolated atoms is compared, yielding that higher charge states are reached for the latter.

The lifetime of interatomic Coulombic decay (ICD), an efficient relaxation mechanism in weakly bound systems, is determined for the $(2s^{-1})$ inner-valence vacancy of the neon dimer Ne_2. Applying an XUV pump-probe scheme at a photon energy of 58 eV, the dynamics of ICD is for the first time traced directly. The measured lifetime of 150 ± 50 fs only agrees well with predictions that explicitly take nuclear dynamics prior to the decay into account, demonstrating the key role of the motion for ICD in light systems.

Contents

1 Introduction 1
References 6

2 Photoionization and Interatomic Coulombic Decay 9
2.1 Photon-Atom Interaction 10
2.1.1 Single- and Multi-photon Absorption 10
2.1.2 Atoms in Strong Laser Fields 14
2.2 Many-Electron Systems 16
2.2.1 Hartree–Fock Method 17
2.2.2 Electron Correlation 19
2.2.3 Diatomic Molecules 20
2.3 Photoionization for High Photon Energies 24
2.3.1 4*d* Shape Resonance 25
2.4 Relaxation Processes in Atoms and Molecules 26
2.5 Interatomic Coulombic Decay 27
2.5.1 Theoretical Treatment 29
2.6 Classical Treatment of the Pump-Probe Technique 36
2.7 Charge Transfer and Classical Over-the-Barrier Model 38
References 41

3 Free-Electron Lasers 45
3.1 Undulator Radiation 45
3.2 Microbunching and SASE 48
3.3 Pulse Characterization 49
3.4 FLASH 52
References 54

4 Experimental Setup 57
4.1 Reaction Microscope (REMI) 57
4.1.1 Supersonic Gas Jet 58
4.1.2 Spectrometer 61

4.1.3 Detectors . . . 62
4.1.4 Data Acquisition . . . 66
4.1.5 Vacuum Requirements . . . 67
4.2 Setup for the Iodine Experiments . . . 68
4.2.1 Iodine Target . . . 69
4.2.2 Autocorrelator . . . 72
4.2.3 IR Laser . . . 73
4.3 Setup for the Neon Experiments . . . 74
4.3.1 Neon Target . . . 74
4.3.2 Beamline . . . 76
4.3.3 Mirror Chamber . . . 77
4.4 The Trouble with the Electrons . . . 79
References . . . 80

5 Data Analysis . . . 83
5.1 Acquire Step . . . 83
5.2 Unpack Step . . . 85
5.3 Calculate Step . . . 88
5.3.1 Calculation of Momenta . . . 89
5.3.2 Assignment of Coincidences . . . 90
5.3.3 Kinetic Energy Release . . . 92
5.4 Momentum Resolution . . . 93
5.5 Acceptance . . . 95
References . . . 97

6 Ionization Dynamics of I_2 in XUV and IR Laser Pulses . . . 99
6.1 Single XUV Pulse Measurements . . . 100
6.1.1 Cross Section in the Region of the Shape Resonance . . . 100
6.1.2 Single-Photon Absorption in I_2 . . . 101
6.1.3 Multi-photon Absorption in Xe . . . 102
6.1.4 Single-Photon Absorption in Iodine . . . 103
6.1.5 Coulomb-Explosion Imaging in I_2^{n+} . . . 109
6.2 XUV Pump-Probe Measurements . . . 115
6.2.1 Interpretation of Pump-Probe Spectra . . . 115
6.2.2 Relevant Charge States and Dissociation Channels . . . 118
6.2.3 Comparison with Simulated Pump-Probe Spectra . . . 120
6.2.4 Simulation with Finite Pulse Length . . . 121
6.2.5 Break-Up into Asymmetrically Charged Fragments . . . 123
6.2.6 Determination of the Critical Distance for Charge Transfer . . . 126
6.2.7 Collision Physics from a Different Perspective . . . 131
6.2.8 Reaching the High Charge States . . . 132

6.3 IR/XUV Pump-Probe Measurements . . . 133
6.3.1 Ionization of I_2 in Strong IR Laser Fields . . . 133
6.3.2 Combining IR and XUV Radiation . . . 138
6.3.3 What Can Be Charged Up Higher, Two Atoms or a Molecule? . . . 143
References . . . 145

7 ICD Lifetime in Ne_2 . . . 149
7.1 Single-Pulse Measurements on Ne and Ne_2 . . . 150
7.1.1 Photoionization of Ne . . . 150
7.1.2 Photoionization of Ne_2 by a Single Photon . . . 152
7.1.3 Interatomic Coulombic Decay . . . 155
7.1.4 Shake-Up Processes . . . 158
7.2 Pump-Probe Measurements on Ne_2 . . . 159
7.2.1 Delay-Dependence of Coincident Ne^+-Ne^+ Ions . . . 159
7.2.2 Pump-Probe Scheme for the ICD Lifetime Determination . . . 161
7.2.3 Fragmentation Channel Ne^+-Ne^{2+} as a Function of the Pump-Probe Time Delay . . . 162
7.2.4 Classical Simulation . . . 164
7.2.5 Lifetime Determination . . . 167
7.2.6 Alternative Pathways to Ne^+-Ne^{2+} Ion Pairs . . . 168
7.2.7 Simulation of Competing Processes . . . 172
7.2.8 Discussion of the Lifetime and Comparison with Theory . . . 174
References . . . 177

8 Conclusions and Outlook . . . 181
8.1 Results from the I_2 Experiments . . . 181
8.2 Results from the Ne_2 Experiments . . . 184
8.3 Outlook . . . 186
References . . . 187

Appendix: Units . . . 189

Chapter 1
Introduction

Molecules undergoing a chemical reaction, such as dissociation or ionization, are essentially few-particle quantum systems that dynamically evolve as a function of time. They progress from an initial to a final state, passing through—quite often very short lived—intermediate states. While the study of the initial and the final state can provide some aspects, such as lifetimes and state populations, a deeper insight into the dynamical properties calls for the investigation of the intermediate states. This is the subject of femtochemistry, which aims to study the formation and breaking of chemical bonds on their natural time and length scales [71]: the femtosecond (10^{-15}s) and the Ångström (10^{-10}m). It requires dedicated time-dependent methods, capable of isolating each intermediate state temporally and determining their essential features.

The most prominent experimental technique for tracing the real-time evolution of photo-induced processes is pump-probe spectroscopy [72]. A first light pulse initiates a reaction in the system of interest, which is then followed in time by probing the system's state with a second light pulse at variable time delay. The resolvable time scales are on the order of the pulse duration, limiting the range and nature of dynamical processes that can be explored. Thus, in order to trace vibrational and dissociative motion in molecules, which occur within tens to hundreds of femtoseconds, pulses of corresponding duration are required. The production of such pulses became possible with advances in laser technology, in particular by the development of the mode-locking technique [23]. This method has quickly developed due to the use of Titanium:Sapphire lasers that deliver pulses with a duration in the femtosecond regime at near infrared (IR) wavelengths ($\sim$800 nm) [66]. Thus, they allow the resolution of even the fastest vibrations in small molecules [18, 22].

Nuclear motion in molecules is usually quantum mechanically treated within the Born–Oppenheimer approximation [8], which neglects coupling between electronic and nuclear motion as the former is typically a factor of thousand faster than the latter. In this estimate the potential energy of the molecule is represented by potential energy surfaces, which for diatomic molecules simplify to potential energy curves and are thus only dependent on the internuclear distance of the two nuclei. The nuclear dynamics within a molecule is described by nuclear wave packets evolving

K. Schnorr, *XUV Pump-Probe Experiments on Diatomic Molecules*,
Springer Theses, DOI 10.1007/978-3-319-12139-0_1

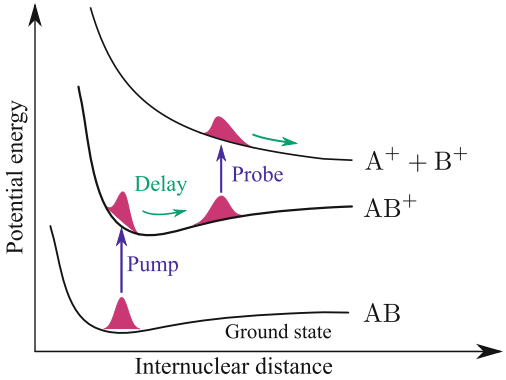

Fig. 1.1 Illustration of the pump-probe technique in a diatomic dummy molecule AB. The molecule is ionized by the pump pulse leading to the formation of a nuclear wave-packet that evolves in time in a bound electronic state of AB^+. After an adjustable time delay the probe pulse further ionizes the molecular ion leading to the population of a repulsive state resulting in a Coulomb explosion into the fragments A^+ and B^+

in time, as illustrated in Fig. 1.1: The ionization of a molecule by the pump pulse may initiate wave-packet dynamics in an intermediate electronic state due to the coherent superposition of vibrational levels. This leads to a modulated nuclear wave packet propagating along the internuclear coordinates. Probing the time evolution of the wave packet is thus equivalent to tracing the motion of the nuclei. If the probe pulse further ionizes the molecule onto a repulsive Coulomb curve, Coulomb-explosion imaging (CEI) [65] allows to access the molecular geometry by exploiting the repulsion of the quickly ionized heavy constituents. A more detailed discussion on how the interaction of light with atoms and molecules can be treated theoretically, is given in Chap. 2.

Ionization with IR lasers typically requires the simultaneous absorption of a large number of photons and thus the application of intense pulses. However, the thereby induced strong electromagnetic fields disturb the studied systems and the ongoing dynamics [15]. In order to return to the perturbative regime of single or few photon absorption, while still being able to ionize a molecule, one has to apply higher photon energies, such as that of extreme ultraviolet (XUV) radiation. Developments in recent years have yielded two different types of XUV sources capable of producing the necessary short pulses:

- High harmonic generation (HHG) sources [38, 48],
- Free-electron lasers (FELs) [7].

Each of them has its advantages and drawbacks, depending on the goal of the specific pump-probe experiment.

As HHG allows the generation of XUV and soft X-ray pulses with durations below 100 as and a fixed phase relation to the fundamental pulses [73], it enables experiments with unprecedented temporal resolution. Applying XUV-IR streaking techniques [33], delays in photoemission of tens of attoseconds [61] as well as Auger

lifetimes of a few femtoseconds [16] could be determined. Recent improvement of HHG sources has led to intensities higher than $10^{13}\,\frac{\mathrm{W}}{\mathrm{cm}^2}$ [41], which are sufficient to perform XUV pump-probe experiments. However, these intensities are not yet routinely available and they are still not high enough for inducing non-linear processes. Therefore, XUV pump-probe experiments are predominantly performed at FELs [31, 32], which deliver intensities up to $10^{18}\,\frac{\mathrm{W}}{\mathrm{cm}^2}$ [10].

FELs are able to produce coherent radiation ranging from the XUV to the hard X-ray regime with pulse durations in the order of ten femtoseconds and peak brilliances up to 8 orders of magnitude larger than that of the most powerful synchrotrons [50]. The pulses consist of stochastic spikes [1] of a few femtoseconds width that corresponds to the temporal coherence length [42]. FELs have opened up a whole new research area, as they combine the key features of lasers, such as short and intense pulses, with those of synchrotron sources delivering XUV and X-ray radiation. Before the advances in FEL technology, dynamical and non-linear studies could only be carried out with ultra-short pulses in the optical and IR regime, while inner-valence and core ionization investigations were limited to the single-photon regime by using picosecond synchrotron pulses. The first FEL that reached into the XUV regime, the free-electron laser in Hamburg (FLASH) [21], became operational in 2005, and the first hard X-ray FEL, the linac coherent light source (LCLS) in Stanford followed in 2009 [17]. At the moment, two further XUV FELs, one in Italy (FERMI) [2] and one in Japan (SCSS) [63], are available. Another hard X-ray FEL (SACLA) [29] became recently operational in Japan. Still some more are to come in the next few years, such as the European XFEL [25] in Hamburg and the SwissFEL [47] in Villigen. A basic introduction in the underlying operation principles of an FEL is given in Chap. 3.

One of the most far reaching visions for the application of FEL radiation is the imaging of single biomolecules with intense femtosecond X-ray pulses [40, 62]. By using X-ray diffraction the electron density and thus the structure of molecules can be reconstructed, which is crucial for the understanding of the functionality of biomolecules. Such studies have been performed for many years at synchrotrons and yielded hundred thousands of molecular structures so far [11]. However, the method requires large crystallized samples that for most molecules are often very difficult or even impossible to produce [13]. The intense coherent radiation of FELs with pulse durations in the femtosecond regime enables imaging of much smaller crystals (nano-crystals) [6]. Recently, the first so far unknown molecular structure, namely the *Trypanosoma brucei* enzyme, could be extracted from an experiment at LCLS [34].

Molecular imaging relies on the so-called *diffract before destroy* concept [43], where a snapshot of a structure is taken before it had time to change. Once a sample is irradiated with intense X-ray radiation, its electron density distribution and consequently the structure is modified, i.e., the molecule suffers damage. Therefore, the central question arises how fast the structural rearrangement takes place and thus whether the damage hinders the imaging of single biomolecules. Recent experiments on nano-crystalized lysozyme have shown signatures of radiation damage from X-ray pulses as short as 70 fs [39]. Photon absorption within molecules is strongly

localized at constituents with high atomic number, often having more than an order-of-magnitude larger cross sections than H or C atoms [69]. Therefore, it is crucial to understand the underlying ultrafast dynamics in order to develop improved damage models that take the spatio-temporal spread of the induced damage into account.

Localized photoabsorption efficiently triggers nuclear motion and electronic rearrangement across the entire molecule, mainly leading to its fragmentation. The induced rearrangement for few femtosecond pulses has been investigated in a recent study on methyl- and ethylselenol, both containing a heavy selenium atom as photoabsorption center [19, 20]. It could be concluded that even inside pulses as short as 5 fs ultrafast charge rearrangement took place and that it was accompanied by considerable displacement of the constituents. However, the essential questions about the time and length scales of the rearrangement remained open. This question is addressed in this thesis in the form of a pump-probe experiment on a diatomic model system, the iodine molecule I_2, with the goal to gain time resolution for the aforementioned charge rearrangement and the accompanied nuclear motion [59, 60]. In particular, the internuclear separation at which charge transfer is not possible anymore is investigated. I_2 is a well-suited target system, as it features a large cross section for the removal of inner-valence electrons around a photon energy of 90 eV [14]. Earlier studies have already explored the dissociation dynamics of molecular iodine ions [35, 36], however only for charge states up to I_2^{5+}. We reach considerably higher charge states and in addition investigate whether the highest charge states are reached for the molecule or separated iodine atoms. The production of these highly charged ions requires the absorption of multiple photons: It takes place via sequences of single-photon absorption and from some point on several photons must be absorbed simultaneously to remove further electrons [26, 51]. Investigating the pathways of multiple ionization is important to gain insight into the fundamental processes occurring when intense FEL radiation interacts with matter. The first studies of that kind were carried out in the XUV wavelength regime on Xe clusters and atoms [49, 68] and were later extended into the X-ray regime [28, 52, 70].

A completely different situation arises, when weakly bound complexes are studied. The aforementioned electron transfer, induced by the localized absorption of high energetic photons, occurs only up to a certain internuclear distance. Hydrogen bonds, which are ubiquitously contained in large biomolecules, are often so weak that the distance between the constituents are too large for electron transfer, even at equilibrium internuclear distances. If this is the case, excited species within the molecule relax by transferring their excess energy solely through the Coulomb force. An example for such a process is the Förster resonant energy transfer (FRET) between molecules, which enables for instance the light harvesting in photosynthesis [24]. Another process of this type is interatomic or intermolecular Coulombic decay (ICD) [12] taking place in weakly bound van-der-Waals and hydrogen bound clusters. Here, an excited monomer ion relaxes by transferring its excess energy to a neighboring atom or molecule, which consequently emits an electron. ICD is an extremely efficient relaxation process and ubiquitous in different chemical environments like clusters [55], He droplets [37], fullerenes [5] and aqueous solutions [45]. The ejected ICD electrons usually have low energies and therefore destroy efficiently

chemical bonds in close-by molecules [9]. Therefore ICD is expected to affect the DNA damage in radiation tumor therapy [27].

ICD occurs on time-scales of a few femtoseconds up to nanoseconds [74], depending on the system and the type of decay mechanism. From a quantum dynamical point of view, ICD and its related phenomena allow to study processes in the interesting regime where electronic transitions couple strongly to nuclear degrees of freedom. For large internuclear distances R the ICD rate is proportional to $\sim R^{-6}$ [56]. For smaller distances other decay pathways may open up, resulting in shorter lifetimes [4]. Thus, if the decaying system is given time to change its internuclear distance, the decay rate will change significantly [54, 57]. For a decay occurring within a few femtoseconds, the accompanying nuclear motion is negligible [5, 30, 44]. In contrast, it plays a crucial role for relaxation times larger than that [54]. Therefore the ICD lifetime is a crucial parameter for understanding the complex interplay between electronic and nuclear motion.

The first ICD lifetime determination in large neon clusters yielded 6 fs for $Ne^+(2s^{-1})$ ions from the bulk [44]. It neglected nuclear motion prior to the decay, which is justified because of the fast decay and the slow nuclear dynamics in the cluster. In contrast for dimers like Ne_2, lifetimes of 64–92 fs (for fixed $R = 3.2$ Å) are theoretically predicted [3, 53, 67], which are long enough to allow significant nuclear movement prior to the decay. Therefore, different experimental techniques capable of including intramolecular dynamics are required. Moreover, the calculation of distance dependent ICD decay rates is a demanding task and a recent study on NeAr showed that theory had clearly overestimated the decay width [46]. Therefore, experimentally determined lifetimes are urgently needed to benchmark theory. In the scope of this thesis the first direct time-resolved measurement of an ICD lifetime was performed by means of an XUV pump-probe scheme applied to the $(2s^{-1})$ vacancy in Ne_2 [58].

Both experiments presented in this thesis are performed applying recoil-ion momentum spectroscopy by means of a reaction microscope (REMI) [64], which was especially designed for experiments at FELs. It enables the determination of the ion momentum vectors and thus, by momentum conservation, an unambiguous identification of the fragment pairs that emerged from the same molecule. A detailed description of the operation principle of a REMI including all relevant components of the setup are given in Chap. 4.

This thesis is organized as follows: Chap. 2 begins with a theoretical description of single-electron atoms in an electromagnetic field. This is followed by a discussion of many-electron atoms and molecules. Then, the relevant relaxation processes initiated by XUV radiation are introduced with special emphasis on ICD. The basic operation principle of an FEL and the resulting characteristic radiation are introduced in Chap. 3. The experimental setup with its core, the REMI, is presented in Chap. 4, including the actual setups of the I_2 and the Ne_2 experiments. In Chap. 5 the analysis of the recorded data is discussed and the relevant observables for the interpretation of the data are introduced. The results for the I_2 experiment are presented in Chap. 6 and the ICD lifetime determination in Chap. 7. In the final Chap. 8 we conclude with a summary of the obtained results.

References

1. W. Ackermann et al., Operation of a free-electron laser from the extreme ultraviolet to the water window. Nat. Photonics **1**(6), 336–342 (2007)
2. E. Allaria et al., Highly coherent and stable pulses from the FERMI seeded free-electron laser in the extreme ultraviolet. Nat. Photonics **6**(10), 699–704 (2012)
3. V. Averbukh, L.S. Cederbaum, Calculation of interatomic decay widths of vacancy states delocalized due to inversion symmetry. J. Chem. Phys. **125**, 094107 (2006)
4. V. Averbukh, I.B. Müller, Mechanism of interatomic Coulombic decay in clusters. Phys. Rev. Lett. **93**, 263002 (2004)
5. V. Averbukh, L.S. Cederbaum, Interatomic electronic decay in endohedral fullerenes. Phys. Rev. Lett. **96**, 053401 (2006)
6. A. Barty et al., Self-terminating diffraction gates femtosecond X-ray nanocrystallography measurements. Nat. Photonics **6**(1), 35–40 (2012)
7. R. Bonifacio, C. Pellegrini, L. Narducci, Collective instabilities and high-gain regime in a free electron laser. Opt. Commun. **50**(6), 373–378 (1984)
8. M. Born, R. Oppenheimer, Zur Quantentheorie der Molekeln. Ann. Phys. **389**(20), 457–484 (1927)
9. B. Boudaïffa et al., Resonant formation of DNA strand breaks by low-energy (3 to 20 eV) electrons. Science **287**(5458), 1658–1660 (2000)
10. J.D. Bozek, AMO instrumentation for the LCLS X-ray FEL. Eur. Phys. J. Spec. Top. **169**(1), 129–132 (2009)
11. Cambridge Crystallographic Data Centre (2013), http://www.ccdc.cam.ac.uk/. Accessed Dec 2013
12. L.S. Cederbaum, J. Zobeley, F. Tarantelli, Giant intermolecular decay and fragmentation of clusters. Phys. Rev. Lett. **79**, 4778 (1997)
13. H.N. Chapman et al., Femtosecond X-ray protein nanocrystallography. Nature **470**(7332), 73–77 (2011)
14. F.J. Comes, U. Nielsen, W.H.E. Schwarz, Inner electron excitation of iodine in the gaseous and solid phase. J. Chem. Phys. **58**(6), 2230–2237 (1973)
15. N.B. Delone, V.P. Krainov, AC Stark shift of atomic energy levels. Phys. Usp. **42**(7), 669 (1999)
16. M. Drescher et al., Time-resolved atomic inner-shell spectroscopy. Nature **419**(6909), 803–807 (2002)
17. P. Emma et al., First lasing and operation of an angstrom-wavelength free-electron laser. Nat. Photonics **4**(9), 641–647 (2010)
18. T. Ergler et al., Quantum-phase resolved mapping of ground-state vibrational D2 wave packets via selective depletion in intense laser pulses. Phys. Rev. Lett. **97**, 103004 (2006)
19. B. Erk et al., Inner-shell multiple ionization of polyatomic molecules with an intense x-ray free-electron laser studied by coincident ion momentum imaging. J. Phys. B: At. Mol. Opt. Phys. **46**(16), 164031 (2013)
20. B. Erk et al., Ultrafast charge rearrangement and nuclear dynamics upon inner-shell multiple ionization of small polyatomic molecules. Phys. Rev. Lett. **110**, 053003 (2013)
21. J. Feldhaus, FLASH-the first soft x-ray free electron laser (FEL) user facility. J. Phys. B: At. Mol. Opt. Phys. **43**(19), 194002 (2010)
22. B. Fischer et al., Steering the electron in H_2^+ by nuclear wave packet dynamics. Phys. Rev. Lett. **105**, 223001 (2010)
23. R.L. Fork, B.I. Greene, C.V. Shank, Generation of optical pulses shorter than 0.1 psec by colliding pulse mode locking. Appl. Phys. Lett. **38**, 671–672 (1981)
24. T. Förster, Ein Beitrag zur Theorie der Photosynthese. Z. Naturforsch. **2b**, 174–182 (1947)
25. G. Gelon et al., Coherence properties of the European XFEL. New J. Phys. **12**(3), 035021 (2010)
26. M. Göppert-Mayer, über Elementarakte mit zwei Quantensprüngen. Ann. Phys. **401**(3), 273–294 (1931)

27. P. Harbach et al., Intermolecular coulombic decay in biology: the initial electron detachment from FADH- in DNA photolyases. J. Phys. Chem. Lett. **4**, 943 (2013)
28. M. Hoener et al., Ultraintense X-Ray induced ionization, dissociation, and frustrated absorption in molecular nitrogen. Phys. Rev. Lett. **104**, 253002 (2010)
29. Z. Huang, I. Lindau, Free-electron lasers: SACLA hard-X-ray compact FEL. Nat. Photonics **6**(8), 505–506 (2012)
30. T. Jahnke et al., Ultrafast energy transfer between water molecules. Nat. Phys. **6**, 139 (2010)
31. Y.H. Jiang et al., Investigating two-photon double ionization of D_2 by XUVpump- XUV-probe experiments. Phys. Rev. A **81**, 051402 (2010)
32. Y. Jiang et al., Ultrafast extreme ultraviolet induced isomerization of acetylene cations. Phys. Rev. Lett. **105**, 263002 (2010)
33. R. Kienberger et al., Atomic transient recorder. Nature **427**(6977), 817–821 (2004)
34. R. Koopmann et al., In vivo protein crystallization opens new routes in structural biology. Nat. Methods **9**(3), 259–262 (2012)
35. M. Krikunova et al., Strong-field ionization of molecular iodine traced with XUV pulses from a free-electron laser. Phys. Rev. A **86**, 043430 (2012)
36. M. Krikunova et al., Ultrafast photofragmentation dynamics of molecular iodine driven with timed XUV and near-infrared light pulses. J. Chem. Phys. **134**(2), 024313 (2011)
37. N.V. Kryzhevoi, V. Averbukh, L.S. Cederbaum, High activity of helium droplets following ionization of systems inside those droplets. Phys. Rev. B **76**, 094513 (2007)
38. M. Lewenstein et al., Theory of high-harmonic generation by low-frequency laser fields. Phys. Rev. A **49**, 2117–2132 (1994)
39. L. Lomb et al., Radiation damage in protein serial femtosecond crystallography using an x-ray free-electron laser. Phys. Rev. B **84**, 214111 (2011)
40. A.V. Martin et al., Single particle imaging with soft x-rays at the Linac coherent light source. Proc. SPIE **8078**, 807809-9 (2011)
41. H. Mashiko, A. Suda, K. Midorikawa, Focusing multiple high-order harmonics in the extreme-ultraviolet and soft-x-ray regions by a platinum-coated ellipsoidal mirror. Appl. Opt. **45**(3), 573–577 (2006)
42. R. Moshammer et al., Second-order autocorrelation of XUV FEL pulses via time resolved two-photon single ionization of He. Opt. Express **19**(22), 21698–21706 (2011)
43. R. Neutze et al., Potential for biomolecular imaging with femtosecond X-ray pulses. Nature **406**(6797), 752–757 (2000)
44. G. Öhrwall et al., Femtosecond interatomic Coulombic decay in free neon clusters: large lifetime differences between surface and bulk. Phys. Rev. Lett. **93**, 173401 (2004)
45. G. Öhrwall et al., Charge dependence of solvent-mediated intermolecular Coster- Kronig decay dynamics of aqueous ions. J. Phys. Chem. B **114**(51), 17057–17061 (2010)
46. T. Ouchi et al., Interatomic Coulombic decay following Ne 1s Auger decay in NeA. Phys. Rev. A **83**, 053415 (2011)
47. B.D. Patterson et al., Coherent science at the SwissFEL x-ray lase. New J. Phys. **12**(3), 035012 (2010)
48. P.M. Paul et al., Observation of a train of attosecond pulses from high harmonic generation. Science **292**(5522), 1689–1692 (2001)
49. M. Richter et al., Extreme ultraviolet laser excites atomic giant resonance. Phys. Rev. Lett. **102**, 163002 (2009)
50. I. Robinson, G. Gruebel, S. Mochrie, Focus on X-ray beams with high coherence. New J. Phys. **12**(3), 035002 (2010)
51. N. Rohringer, R. Santra, X-ray nonlinear optical processes using a selfamplified spontaneous emission free-electron laser. Phys. Rev. A **76**, 033416 (2007)
52. B. Rudek et al., Resonance-enhanced multiple ionization of krypton at an x-ray free-electron laser. Phys. Rev. A **87**, 023413 (2013)
53. R. Santra, An efficient combination of computational techniques for investigating electronic resonance states in molecules. J. Chem. Phys. **115**, 6853 (2001)

54. R. Santra et al., Interatomic Coulombic decay in van der Waals clusters and impact of nuclear motion. Phys. Rev. Lett. **85**, 4490 (2000)
55. R. Santra et al., Intermolecular coulombic decay of clusters. J. Electron Spectrosc. Relat. Phenom. **114–116** (2001). In: *Proceeding of the Eight International Conference on Electronic Spectroscopy and Structure*, pp. 41–47
56. R. Santra, L.S. Cederbaum, Non-Hermitian electronic theory and applications to clusters. Phys. Rep. **368**(1), 1–117 (2002)
57. S. Scheit et al., On the interatomic Coulombic decay in the Ne dimer. J. Chem. Phys. **121**, 8393 (2004)
58. K. Schnorr et al., Time-Resolved measurement of interatomic Coulombic decay in Ne_2. Phys. Rev. Lett. **111**, 093402 (2013)
59. K. Schnorr et al., Electron rearrangement dynamics in dissociating I_2^{n+} molecules accessed by extreme ultraviolet pump-probe experiments. Phys. Rev. Lett. **113**, 073001 (2014)
60. K. Schnorr et al., Multiple ionization and fragmentation dynamics of molecular iodine studied in IR-XUV pump-probe experiments. Faraday Discuss. **171** (2014)
61. M. Schultze et al., Delay in photoemission. Science **328**(5986), 1658–1662 (2010)
62. M.M. Seibert et al., Single mimivirus particles intercepted and imaged with an x-ray laser. Nature **470**(7332), 78–81 (2011)
63. T. Shintake et al., A compact free-electron laser for generating coherent radiation in the extreme ultraviolet region. Nat. Photonics **2**(9), 555–559 (2008)
64. J. Ullrich et al., Recoil-ion and electron momentum spectroscopy: reactionmicroscopes. Rep. Prog. Phys. **66**(9), 1463 (2003)
65. Z. Vager, R. Naaman, E.P. Kanter, Coulomb explosion imaging of small molecules. Science **244**(4903), 426–431 (1989)
66. J.A. Valdmanis, R.L. Fork, J.P. Gordon, Generation of optical pulses as short as 27 femtoseconds directly from a laser balancing self-phase modulation, group-velocity dispersion, saturable absorption, and saturable gain. Opt. Lett. **10**(3), 131–133 (1985)
67. N. Vaval, L.S. Cederbaum, Ab initio lifetimes in the interatomic Coulombic decay of neon clusters computed with propagators. J. Chem. Phys. **126**, 164110 (2007)
68. H. Wabnitz et al., Multiple ionization of atom clusters by intense soft x-rays from a free-electron laser. Nature **420**(6915), 482–485 (2002)
69. J. Yeh, I. Lindau, Atomic subshell photoionization cross sections and asymmetry parameters: $1 \leq Z \leq 103$. At. Data Nucl. Data Tables **32**(1), 1–155 (1985)
70. L. Young et al., Femtosecond electronic response of atoms to ultra-intense x-rays. Nature **466**(7302), 56–61 (2010)
71. A.H. Zewail, Laser femtochemistry. Science **242**(4886), 1645–1653 (1988)
72. A.H. Zewail, Femtochemistry: atomic-scale dynamics of the chemical bond using ultrafast lasers (Nobel Lecture). Angew. Chem. Int. Ed. **39**(15), 2586–2631 (2000)
73. K. Zhao et al., Tailoring a 67 attosecond pulse through advantageous phase-mismatch. Opt. Lett. **37**(18), 3891–3893 (2012)
74. J. Zobeley, R. Santra, L.S. Cederbaum, Electronic decay in weakly bound heteroclusters: energy transfer versus electron transfer. J. Chem. Phys. **115**(11), 5076–5088 (2001)

Chapter 2
Photoionization and Interatomic Coulombic Decay

The type of process that may be induced in an atom by the interaction with a single photon is strongly dependent on the photon energy. An overview of the energy regimes in the electromagnetic spectrum is given in Fig. 2.1. For wavelengths in the infrared (IR) and optical regime, electron-photon interaction is dominated by elastic Rayleigh scattering. For ultraviolet (UV) radiation and X-rays up to a few keV, inelastic photoabsorption is the most relevant process. For even higher photon energies, Compton scattering becomes dominant and is eventually taken over by pair creation when the energy increases further. Throughout this thesis we will mostly address the interaction of extreme ultraviolet radiation (XUV), corresponding to the energy regime of $10\,\mathrm{eV} < h\nu < 124\,\mathrm{eV}$, with atoms and molecules, which usually leads to photoionization.

The absorption of a single and of multiple photons in a one-electron system is introduced in Sect. 2.1. For the description of a system consisting of more than just a core and an electron, the electron-electron interaction must be taken into account. Common techniques and approximations used to describe the Coulomb repulsion between the electrons and the electron correlation for atoms and molecules are presented in Sect. 2.2. The cross sections for the absorption of single XUV photons are discussed in Sect. 2.3. As high energetic photons efficiently remove inner-shell and core electrons, highly excited ions are often created. The most relevant relaxation mechanisms are explained in Sect. 2.4. One particular relaxation mechanism, interatomic Coulombic decay (ICD), which relies on the Coulomb interaction of a highly excited monomer with its environment, is presented in Sect. 2.5. A classical simulation for pump-probe schemes, which is applied to extract time-information for such molecular processes, is presented in Sect. 2.6. The chapter concludes with a model for charge transfer in dissociating molecules in Sect. 2.7.

K. Schnorr, *XUV Pump-Probe Experiments on Diatomic Molecules*,
Springer Theses, DOI 10.1007/978-3-319-12139-0_2

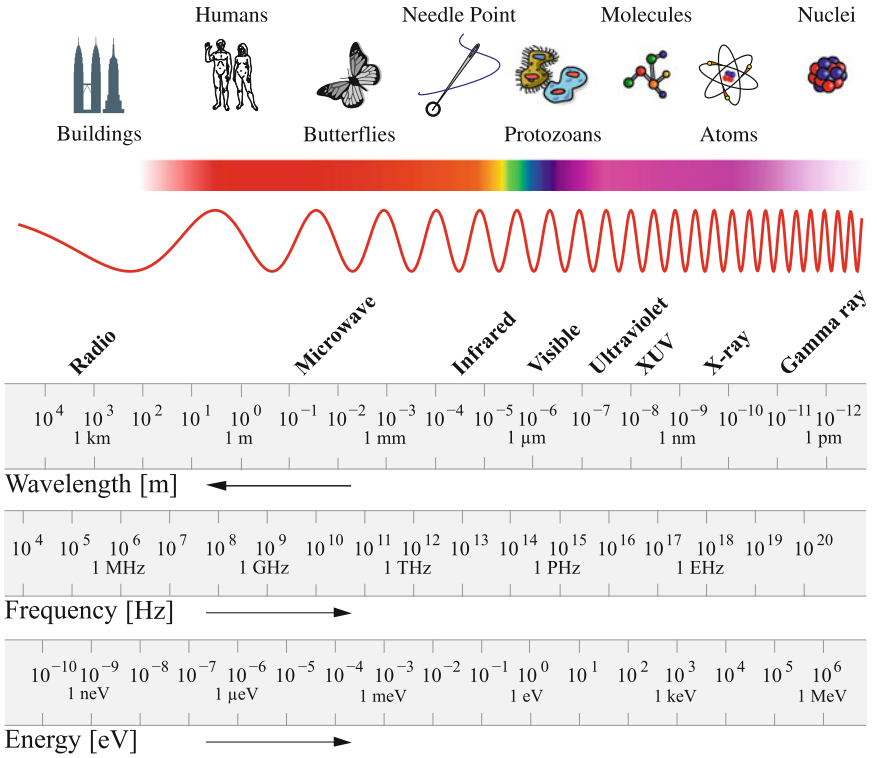

Fig. 2.1 Electromagnetic spectrum. Adapted from [79, 80]

2.1 Photon-Atom Interaction

The response of atoms to electromagnetic radiation depends on the wavelength and the field strength. While weak fields may be treated perturbatively, strong fields require a different approach. These two regimes will be discussed in the following section, starting with the weak field in Sect. 2.1.1. Following this, the transition from weak to strong fields is discussed in Sect. 2.1.2.

2.1.1 Single- and Multi-photon Absorption

We start by giving a short introduction to the quantum mechanical treatment of a hydrogen-like atom interacting with an electromagnetic wave. The following considerations are compiled from [29, 38, 44]. Please note, that the equations are given in atomic units. For further details on the applied unit system see Appendix.

The interaction of an atom with a classical field is described by introducing the minimal coupling $\boldsymbol{p} \rightarrow \boldsymbol{p} - \boldsymbol{A}/c$ into the non-relativistic Hamiltonian:

$$\hat{H} = \frac{1}{2}\left(\boldsymbol{p} - \frac{\boldsymbol{A}}{c}\right)^2 + V(r). \tag{2.1}$$

Here, $\boldsymbol{p}$ is the momentum operator, $\boldsymbol{A}$ is the vector potential of the electromagnetic field in Coulomb gauge $\nabla \boldsymbol{A} = 0$, and $V(r) = -Z/r$ is the Coulomb potential for an electron in the field of a nucleus with charge Z. The $\boldsymbol{A}^2$ term is neglected as we assume the electromagnetic field to be weak. The full Hamiltonian from Eq. (2.1) is separated into the Hamiltonian of a free atom $\hat{H}_0 = \boldsymbol{p}^2/2 - Z/r$ and the interaction term $H_{\text{int}} = -\boldsymbol{p}\boldsymbol{A}/c$, describing the coupling to the external field. Here, we made use of $\boldsymbol{p}\boldsymbol{A} = \boldsymbol{A}\boldsymbol{p}$. The time evolution of the system is governed by the time-dependent Schrödinger equation

$$\mathrm{i}\frac{\partial}{\partial t}\Psi(\boldsymbol{r}, t) = \hat{H}\Psi(\boldsymbol{r}, t) = \left(\hat{H}_0 + \hat{H}_{\text{int}}\right)\Psi(\boldsymbol{r}, t). \tag{2.2}$$

If the interaction term is weak, Eq. (2.2) can be solved using time-dependent perturbation theory. In order to do so we introduce the parameter λ, which will denote the order of perturbation theory:

$$\mathrm{i}\frac{\partial}{\partial t}\Psi(\boldsymbol{r}, t) = \left(\hat{H}_0 + \lambda\hat{H}_{\text{int}}\right)\Psi(\boldsymbol{r}, t). \tag{2.3}$$

The unperturbed Hamiltonian $\hat{H}_0$ is not anymore the exact Hamiltonian of the system. Its known eigenfunctions $\psi_k(\boldsymbol{r})$ form a complete basis set. Therefore, the full solution of the Schrödinger equation may be expanded in this basis with the time-dependent expansion coefficients $c_k(t)$:

$$\Psi(\boldsymbol{r}, t) = \sum_k c_k(t)\psi_k(\boldsymbol{r})\mathrm{e}^{-\mathrm{i}E_k t}. \tag{2.4}$$

Upon insertion of this expansion into Eq. (2.3), a system of coupled differential equations enumerated by b, is obtained:

$$\frac{\partial c_b(t)}{\partial t} = \frac{1}{\mathrm{i}}\sum_k \lambda c_k(t)\langle\psi_b|\hat{H}_{\text{int}}|\psi_k\rangle\mathrm{e}^{\mathrm{i}(E_b - E_k)t}. \tag{2.5}$$

This system may be solved by using a perturbative approach, if $\lambda\hat{H}_{\text{int}}$ is small. The coefficients c_k are expanded in powers of the parameter λ:

$$c_k(t) = c_k^{(0)}(t) + \lambda c_k^{(1)}(t) + \lambda^2 c_k^{(2)}(t) + \cdots \tag{2.6}$$

The expansion from Eq. (2.6) is then inserted into Eq. (2.5) and the solutions of the individual orders are found iteratively by integration in time. At time $t = 0$ the system is prepared in its initial state ψ_a, which has to be ensured by the zeroth order of the expansion series, thus $c_k^{(0)} = \delta_{ka}$. In order to calculate the next higher order term the resulting coefficient from the previous order is inserted into Eq. (2.5) and integrated in time. Exemplary, the first- and second-order terms in λ are given in the following. They describe a single or a double interaction with the electromagnetic field, leading to the transition of the system from the initial state ψ_a to a final state ψ_b.

$$\lambda^0: \quad c_b^{(0)}(t) = \delta_{ba} \tag{2.7}$$

$$\lambda^1: \quad c_b^{(1)}(t) = \frac{1}{\mathrm{i}} \int_0^t dt' \langle \psi_b | \hat{H}_{\mathrm{int}}(t') | \psi_a \rangle \mathrm{e}^{\mathrm{i}(E_b - E_a)t'} \tag{2.8}$$

$$\lambda^2: \quad c_b^{(2)}(t) = \frac{1}{\mathrm{i}^2} \sum_k \int_0^t dt' \int_0^{t'} dt'' \langle \psi_b | \hat{H}_{\mathrm{int}}(t') | \psi_k \rangle \langle \psi_k | \hat{H}_{\mathrm{int}}(t'') | \psi_a \rangle \times \mathrm{e}^{\mathrm{i}(E_b - E_k)t'} \mathrm{e}^{\mathrm{i}(E_k - E_a)t''} \tag{2.9}$$

The contribution of the electromagnetic field is expressed by the interaction Hamiltonian $\hat{H}_{\mathrm{int}} = -\boldsymbol{p}\boldsymbol{A}/c$. The vector potential is assumed to be a plane wave

$$\boldsymbol{A}(\boldsymbol{r}, t) = \boldsymbol{A}_0 \boldsymbol{e}_{\mathrm{pol}} \left(\mathrm{e}^{\mathrm{i}(\boldsymbol{k}\boldsymbol{r} - \omega t)} + \mathrm{e}^{-\mathrm{i}(\boldsymbol{k}\boldsymbol{r} - \omega t)} \right), \tag{2.10}$$

where $\boldsymbol{e}_{\mathrm{pol}}$ is a unit vector in polarization direction and $\boldsymbol{k}$ is the wave vector with $|\boldsymbol{k}| = 2\pi/\lambda$. If the wavelength of the electromagnetic wave λ is large compared to the dimensions of an atom, $\boldsymbol{k}\boldsymbol{r} \ll 1$, the dipole approximation $\mathrm{e}^{i\boldsymbol{k}\boldsymbol{r}} \approx 1$ is applicable. This assumption is justified up to photon energies of a few kiloelectronvolt and is thus also valid for the XUV regime.

Then, the interaction Hamiltonian can be rewritten as $\hat{H}_{\mathrm{int}} = -\boldsymbol{d}\boldsymbol{\epsilon}$ using the electric field $\boldsymbol{\epsilon} = -\frac{1}{c}\frac{\partial \boldsymbol{A}}{\partial t}$ and the dipole operator $\boldsymbol{d} = q\boldsymbol{r}$. According to our applied unit system, we set the charge $q = e = 1$. An instructive derivation of this transformation may be found in [23], using the kinetic momentum $\boldsymbol{p} = \frac{\partial \boldsymbol{r}}{\partial t}$:

$$\hat{H}_{\mathrm{int}} = -\frac{1}{c}\boldsymbol{p}\boldsymbol{A} = -\frac{1}{c}\frac{\partial \boldsymbol{r}}{\partial t}\boldsymbol{A} = \boldsymbol{r}\underbrace{\frac{1}{c}\frac{\partial \boldsymbol{A}}{\partial t}}_{-\epsilon} - \frac{1}{c}\underbrace{\frac{\partial}{\partial t}(\boldsymbol{r}\boldsymbol{A})}_{0}, \tag{2.11}$$

where the latter term vanishes due to the Coulomb gauge. For an exact derivation, which is also valid beyond the dipole approximation, the so-called Power–Zienau–Woolley transformation must be performed [59, 82].

For a electromagnetic field polarized in x-direction and the absorption[1] of photons this leads to

$$\hat{H}_{\text{int}} = x\epsilon_0 \mathrm{e}^{-\mathrm{i}\omega t}. \tag{2.12}$$

Inserting this $\hat{H}_{\text{int}}$ into Eqs. (2.8) and (2.9) yields the first and second order expansion coefficients, respectively. Particularly, the integrations in time may be performed using a representation of Dirac's δ-function:

$$\delta(x) = \frac{1}{2\pi} \int_0^\infty dt\ \mathrm{e}^{\mathrm{i}xt}. \tag{2.13}$$

The probability for finding the system in the eigenstate ψ_b, due to n-photon absorption, after a certain time t is given by

$$w_{a\to b}^{(n)}(t) = \left| c_b^{(n)}(t) \right|^2. \tag{2.14}$$

Assuming that the transition is induced by a laser with intensity $I_0 \propto \epsilon_0^2$, which is turned on for a duration τ, the transition rate is given by

$$R_{a\to b}^{(n)} = \frac{w_{a\to b}^{(n)}(\tau)}{\tau}. \tag{2.15}$$

Note that, the squared δ-function in $w_{a\to b}^{(n)}$ leads to a factor containing the duration τ [8], which cancels with the $1/\tau$ in $R_{a\to b}^{(n)}$. Thus, the rate for the first and second order process reads:

$$R_{a\to b}^{(1)} \propto I_0 |\langle \psi_b | x | \psi_a \rangle|^2 \delta(E_b - E_a - \omega), \tag{2.16}$$

$$R_{a\to b}^{(2)} \propto I_0^2 \sum_k \langle \psi_b | x | \psi_k \rangle \langle \psi_k | x | \psi_a \rangle \delta(E_b - E_a - 2\omega). \tag{2.17}$$

The intuitive picture for the two-photon absorption process is that an electron is excited from the initial state ψ_a to an intermediate state ψ_k by the first photon and from the intermediate state to the final state ψ_b by the second photon [33]. Note that the intermediate state is virtual, i.e., not necessarily an eigenstate of the atom.

So far, we found that the transition rate for the single-photon absorption grows linearly in the laser intensity, while the two-photon case grows squared. Continuing our consideration to the absorption of n photons, by taking the respective orders in the perturbative expansion from Eq. (2.6), shows

[1] Had we chosen the negative exponent of Eq. (2.10), $\mathrm{e}^{-\mathrm{i}(\boldsymbol{kr}-\omega t)}$, stimulated emission instead of photon absorption would be described.

$$R_{a\to b}^{(n)} \propto I_0^n. \tag{2.18}$$

Although the previous derivations were only made for a transition between two bound states, the same behavior is found for a final state in the continuum. Thus, the result is also applicable for photoionization [29].

It is important to stress that we observe two different mechanisms of multi-photon absorption in the experiment, sequential and direct photon absorption. The I_0^n-scaling found in this section is valid for the direct case. There, the intermediate states are virtual and their—usually short—lifetime is determined by Heisenberg's uncertainty relation. Thus, the photon absorption must occur directly within the limited lifetime of the state, i.e., quasi simultaneously.

In the sequential case, the first photon ionizes the system, another photon ionizes the created ion and so forth. This process can be described as a sequence of single-photon absorptions, which may occur at any time during the pulse. Thus, all populated intermediate states are stationary and the probability to absorb another photon is linearly dependent on the intensity and the number of available ions.

2.1.2 Atoms in Strong Laser Fields

The motion of an atom in a laser field $\epsilon = \epsilon_0 \cos \omega t$ can be simplified by assuming that a single electron oscillates in an electromagnetic field, while the much heavier core remains fixed. Classically, the electron's oscillation is described via Newton's *lex secunda*, as described in [38]:

$$m_e \frac{dv}{dt} = e\epsilon \quad \rightarrow \quad v = \frac{e\epsilon_0}{m_e \omega} \sin \omega t \tag{2.19}$$

with a kinetic energy of

$$\frac{1}{2} m_e v^2 = \frac{e^2 \epsilon_0^2}{2 m_e \omega^2} \sin^2 \omega t. \tag{2.20}$$

The average of Eq. (2.20) over one laser period is the so-called ponderomotive potential U_p, which is interpreted as the energy of an electron that performs a quiver motion in the oscillating electric field of the laser. It is given by

$$U_p = \frac{1}{2} m_e \left\langle v^2 \right\rangle = \frac{e^2 \epsilon_0^2}{4 m_e \omega^2} = \frac{e^2}{8\pi^2 \varepsilon_0 c^3 m_e} I_0 \lambda^2. \tag{2.21}$$

A comparison of U_p for ionization with an IR and an equally intense XUV pulse is given in Table 2.1. While the ponderomotive potential of an electron in the XUV field is completely negligible, it is already two times larger than the electron's binding energy in I_2 for the IR pulse. Therefore, the influence of the XUV pulse may be

Table 2.1 Ionization of I_2 with an ionization potential $E_I = 10\,\text{eV}$ via an IR pulse of $3.4 \times 10^{14}\,\frac{\text{W}}{\text{cm}^2}$ and an XUV pulse with the same intensity. The Keldysh parameter γ and the ponderomotive potential U_p are given

	λ (nm)	γ	U_p (eV)
IR	800	0.5	20
XUV	14	84	<0.001

treated as a weak perturbation. In contrast, the IR field is strong enough to deform the potential.

The ionization of atoms in strong laser fields is described within two different pictures, which one applies is characterized by the so-called Keldysh parameter [42]

$$\gamma = \sqrt{\frac{E_I}{2U_p}}, \tag{2.22}$$

with E_I being the ionization energy of the atom. For $\gamma > 1$ the electron's binding energy is larger than the maximal kinetic energy gained in the laser field. This is the regime of multi-photon ionization, where the rate of n-photon absorption is proportional to I_0^n. In contrast, for $\gamma < 1$ the laser field bends the potential barrier of the atom or molecule so far, that the electron may tunnel through the barrier or even until the electron is quasi free, as illustrated in Fig. 2.2. This is the strong field regime, in which the maximum energy gained in the laser field is larger than the electron's binding energy. It should be noted, that there is no strict transition between the regimes and experiments around $\gamma \approx 1$ exhibit typical features of both mechanisms [10, 52].

According to the Keldysh parameters, listed in Table 2.1, the XUV experiments are clearly situated in the multi-photon regime, while the experiments carried out with the IR laser are better described and understood in the tunneling regime.

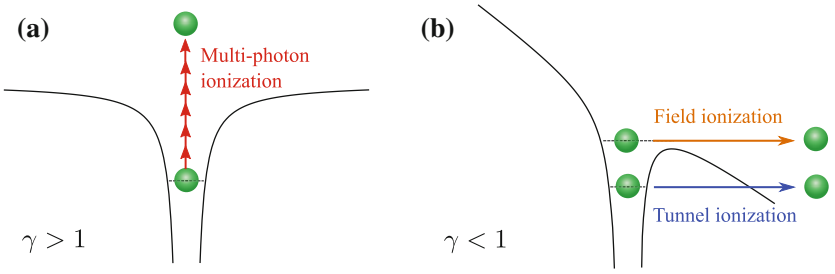

Fig. 2.2 Mechanisms of **a** multi-photon ionization ($\gamma > 1$) and **b** tunnel and field ionization ($\gamma > 1$)

2.2 Many-Electron Systems

In order to describe an atom consisting of N electrons and a nucleus of charge Z, the kinetic energy of all particles and the interaction between them must be taken into account. In a non-relativistic fashion this is done by including all attractive terms from the nucleus-electron interaction and all Coulomb-repulsion terms from the electron-electron interaction into the Hamiltonian[2]

$$\hat{H} = \sum_{j=1}^{N} \left(-\frac{1}{2}\Delta_j - \frac{Z}{r_j} + \frac{1}{2}\sum_{k\neq j}^{N} \frac{1}{r_{jk}} \right) \tag{2.23}$$

with the Laplace operator $\Delta_j = \nabla_j^2$, the distance $r_{jk} = \left|\boldsymbol{r}_j - \boldsymbol{r}_k\right|$ between the electrons j and k, and the distance $r_j = \left|\boldsymbol{r}_j - \boldsymbol{r}_n\right|$ between the electrons and the nucleus. The central task is to solve the Schrödinger equation

$$\hat{H}\Psi(q_1, q_2, \ldots) = E\Psi(q_1, q_2, \ldots), \tag{2.24}$$

in order to get the multi-electron wave function $\Psi(q_1, q_2, \ldots)$ with the coordinates $q_i = (\boldsymbol{r}_i, s_i)$, where $\boldsymbol{r}_i$ denotes the spatial and s_i the spin coordinates. In the following we will only consider the spatial coordinate. In the mean-field approximation [56] the potential V_j seen by the electron j is approximated by an averaged central potential of all other electrons and the nucleus

$$V_j(r_j) = -\frac{Z}{r_j} + \left\langle \sum_{k\neq j}^{N} \frac{1}{r_{jk}} \right\rangle. \tag{2.25}$$

Therefore each electron moves in a field of the point-like nucleus and the mean field created by the other $N-1$ electrons. The motion of a single electron is independent of the motion of the other electrons. This allows a separation ansatz for the multi-electron wave function consisting of single-electron wave functions $\phi_i(\boldsymbol{r}_i)$:

$$\psi(\boldsymbol{r}_1, \boldsymbol{r}_2, \ldots) = \phi_1(\boldsymbol{r}_1)\phi_2(\boldsymbol{r}_2)\ldots\phi_N(\boldsymbol{r}_N). \tag{2.26}$$

The single-electron wave functions, also called orbitals, are obtained by solving the single-particle Schrödinger equations with the averaged potentials $V_j(r_j)$. These potentials can only be determined precisely by integrating over the density of all other orbitals, which are generally not known. Therefore, the Schrödinger equation may be iteratively solved via the variational Hartree-method [35]. One starts with a set of single-particle wave functions, which are expanded in an appropriate basis set and assumes some initial averaged potential for each electron. In every iteration

[2] If not indicated otherwise, the presentation given here follows that of [38].

step the Schrödinger equation is solved and the computed orbitals are compared to those of the previous step. If the agreement is not good enough, a modified potential is calculated and the next iteration is started by calculating new orbitals. Only if self-consistency [61] is reached, meaning the previous and present orbitals agree (up to a predefined accuracy), the iteration stops. In the end, one obtains a set of N orbitals $|\phi_i(r_i)\rangle$, called an electron configuration, which allows the determination of the total energy of the electron configuration

$$E = \langle \phi_1(\boldsymbol{r}_1)\phi_2(\boldsymbol{r}_2)\dots\phi_N(\boldsymbol{r}_N)|\hat{H}|\phi_1(\boldsymbol{r}_1)\phi_2(\boldsymbol{r}_2)\dots\phi_N(\boldsymbol{r}_N)\rangle. \tag{2.27}$$

2.2.1 Hartree–Fock Method

So far, the fact that electrons are indistinguishable particles and fermions, and consequently that their total wave function has to be antisymmetric, has not been taken into account. This is taken care of in the Hartree–Fock formalism by using the Slater determinant

$$\Psi(q_1, q_2, \dots, q_N) = \frac{1}{\sqrt{N!}} \begin{vmatrix} \phi_\alpha(q_1) & \phi_\beta(q_1) & \dots & \phi_\nu(q_1) \\ \phi_\alpha(q_2) & \phi_\beta(q_2) & \dots & \phi_\nu(q_2) \\ \vdots & \vdots & \ddots & \vdots \\ \phi_\alpha(q_N) & \phi_\beta(q_N) & \dots & \phi_\nu(q_N) \end{vmatrix}, \tag{2.28}$$

which guarantees the required symmetry properties. The $\phi_\lambda(q_i)$ are single electron wave functions, where λ denotes a set of quantum number $(n_l\, m_l\, m_s)$ and $q_i = (\boldsymbol{r}_i, s_i)$. In the following we will only consider the spatial coordinates.

The Hartree–Fock Hamiltonian $\hat{F}$ is expressed in terms of single-electron Hamiltonians $\hat{f}_i$ consisting of $\hat{h}_i = -\frac{1}{2}\Delta_i - \frac{Z}{r_i}$ and the electron-electron interaction $\hat{v}_i = \hat{j}_i - \hat{k}_i$:

$$\hat{F} = \sum_i \hat{f}_i \quad \text{with} \quad \hat{f}_i = \hat{h}_i + \hat{v}_i, \tag{2.29}$$

with the Coulomb operators $\hat{j}_i$ and the exchange operators $\hat{k}_i$ defined via their action on a single electron wave function ϕ_λ [86]:

$$\hat{j}_i(r_n)\phi_\lambda(r_n) = \left[\int \phi_i^\dagger(r_m)\frac{1}{|r_{nm}|}\phi_i(r_m)\, d^3r_m\right]\phi_\lambda(r_n), \tag{2.30}$$

$$\hat{k}_i(r_n)\phi_\lambda(r_n) = \left[\int \phi_i^\dagger(r_m)\frac{1}{|r_{nm}|}\phi_\lambda(r_m)\, d^3r_m\right]\phi_i(r_n). \tag{2.31}$$

The N-electron wave function is found by solving the Hartree–Fock equation

$$\hat{F}|\Psi\rangle = E_{\mathrm{HF}}|\Psi\rangle. \tag{2.32}$$

When deriving the total energy $E_{\mathrm{HF}} = \langle \Psi(q_1, q_2, \ldots, q_N)|\hat{F}|\Psi(q_1, q_2, \ldots, q_N)\rangle$ of a certain electron configuration, using the Slater determinant from Eq. (2.28) and the Hamiltonian from Eq. (2.29), one arrives at

$$E_{\mathrm{HF}} = \sum_{\nu} \epsilon_{\nu}, \tag{2.33}$$

with the energy of an individual orbital ν being

$$\epsilon_{\nu} = E_{\nu\nu} + \sum_{\lambda \neq \nu} V_{\nu\lambda[\nu\lambda]}. \tag{2.34}$$

Here, $E_{\nu\nu} = \langle \phi_{\nu}|\hat{h}_{\nu}|\phi_{\nu}\rangle$ is the single-electron energy in the field of the nucleus and $V_{\nu\lambda[\nu\lambda]} := V_{\nu\lambda\nu\lambda} - V_{\nu\lambda\lambda\nu}$ is the electron-electron Coulomb matrix element consisting of two terms [86]:

$$\text{Direct term:} \quad V_{\nu\lambda\nu\lambda} = \iint \phi_{\nu}^{\dagger}(r_i)\phi_{\lambda}^{\dagger}(r_k)\frac{1}{|r_{ik}|}\phi_{\nu}(r_i)\phi_{\lambda}(r_k)\, d^3r_i d^3r_k, \tag{2.35}$$

$$\text{Exchange term:} \quad V_{\nu\lambda\lambda\nu} = \iint \phi_{\nu}^{\dagger}(r_i)\phi_{\lambda}^{\dagger}(r_k)\frac{1}{|r_{ik}|}\phi_{\lambda}(r_i)\phi_{\nu}(r_k)\, d^3r_i d^3r_k. \tag{2.36}$$

The direct term corresponds to the energy of an electron in the averaged field of another electron. The exchange term arises from the fact that the electrons are indistinguishable and describes their exchange.

The Hartree–Fock equation in Eq. (2.32) consists of a set of N coupled single-particle differential equations $\hat{f}_i\phi_i(r_m) = \epsilon_i\phi_i(r_m)$ that cannot be solved analytically. Thus, in practice, the solution is found via a self-consistent iterative method as introduced in the previous section: A set of basis functions is chosen in which each single-electron wave function ϕ_i is expanded. The variation consists of modifying the expansion coefficients in each iteration step and thereby finding the best suited orbitals (single-particle wave functions). In order to do so a large amount of integrals of the type of Eqs. (2.35) and (2.36) must be calculated. It should be emphasized that the quality of the single-particle wave functions strongly depends on the chosen basis set [19]. However if the complexity of the basis functions increases, which is needed to correctly describe many-electron configurations correctly, the computational effort increases strongly. A compromise between accuracy and calculation time is usually made by choosing a standard basis set, such as Slater functions or Gauß functions. In particular the latter type of basis function allows fast calculations due to the advantageous integration properties of Gauß functions. More details can for instance be found in [46].

2.2.2 Electron Correlation

The Hartree–Fock method allows to account for the nucleus-electron interaction precisely and treats electron-electron interaction by an approximated overall potential seen by each electron. However, this picture of independently behaving electrons is not completely accurate as effects like autoionization (cf. Sect. 2.4), which rely on the correlation between the electrons in the atom, are impossible to describe in the Hartree–Fock picture.

One method to account for electron correlation[3] is the so-called Configuration Interaction (CI) method [70] where the multi-electron wave function is a linear combination of Slater determinants (electron configurations). Thus, the total wave function Ω is a superposition of different electron configurations Ψ_k, which can each be obtained by the Hartree–Fock method:

$$\Omega = \sum_k c_k \Psi_k. \tag{2.37}$$

The central task consists of finding the optimal coefficients c_k, which can again be done iteratively, as introduced before.

Usually the expansion contains a leading term, the Hartree–Fock ground-state configuration, and further excited configurations, created by substituting filled orbitals with empty ones. Depending on how many substitutions are performed one speaks about single excitation for one and double excitation for two substitutions. In the literature, e.g., [66], the different configurations are referred to as n-hole and m-particle (nhmp) configurations with n being the number of considered excitations with respect to the ground state and m being the number of excited electrons. Thus, a 1h1p-state is singly excited compared to the reference ground state. If the ground state is already composed of more than one Slater determinant, one speaks of a multi-reference CI calculation (MRCI) [78]. If all excited states are taken into account, a full-CI calculation is performed, however this is only feasible for very small systems [6].

Another method, that can be used to construct the wave function in a basis of correlated electron states is the so-called Algebraic Diagrammatic Construction (ADC) method [69]. It is based on the Green's function formalism that is applicable to describe transitions in many-electron systems including correlation effects [17]. In order to describe a transition from an initial to a final state the wave functions of the participating states were so-far derived separately. The Green's function method allows to calculate energy differences and transition amplitudes directly. However, the Green's function cannot be calculated exactly due to the high complexity of many electron systems, thus one chooses a perturbative approach in which the total Hamiltonian is split into a non-perturbed and an interaction part. One way to determine the Green's function in the framework of perturbation theory is the ADC method. Thus,

[3] The presentation in this chapter follows [19, 86].

if all orders of the expansion were taken into account the resulting wave functions would be exact. The expansion is truncated at a given order n, which is then denoted as an ADC(n) scheme. The ADC(2) scheme, for instance, describes singly ionized systems (one hole) with a wave function including all 1h0p and 2h1p contributions.

2.2.3 Diatomic Molecules

Diatomic molecules, consisting of two atoms, A and B, are described by considering the kinetic energies of all constituents and the interaction between them.[4] The kinetic energies of the nuclei and the electrons is given by

$$\hat{T}_N = -\frac{1}{2\mu}\Delta_R \quad \text{and} \quad \hat{T}_e = -\frac{1}{2}\sum_i^N \Delta_{r_i}, \tag{2.38}$$

with the reduced nuclear mass $\mu = {}^{M_A M_B}/_{(M_A+M_B)}$, the internuclear distance vector $\boldsymbol{R} = \boldsymbol{R}_B - \boldsymbol{R}_A$, and $\boldsymbol{r}_i$ the electrons' distance vectors from the center of mass. Thus, the Hamilton operator reads

$$\hat{H} = \hat{T}_N(\boldsymbol{R}) + \hat{T}_e(\boldsymbol{r}) + V(\boldsymbol{R}, \boldsymbol{r}), \tag{2.39}$$

with the potential

$$V(\boldsymbol{R}, \boldsymbol{r}) = V_{Ae} + V_{Be} + V_{ee} + V_{AB} \tag{2.40}$$

$$= -\sum_{i=1}^{N} \frac{Z_A}{|\boldsymbol{r}_i - \boldsymbol{R}_A|} - \sum_{i=1}^{N} \frac{Z_B}{|\boldsymbol{r}_i - \boldsymbol{R}_B|} + \sum_{i<k}^{N} \frac{1}{|\boldsymbol{r}_i - \boldsymbol{r}_k|} + \frac{Z_A Z_B}{R}. \tag{2.41}$$

In order to describe the system, the stationary Schrödinger equation $\hat{H}\Psi(\boldsymbol{r}, \boldsymbol{R}) = W\Psi(\boldsymbol{r}, \boldsymbol{R})$ must be solved, where W is the total energy of the system. No analytical solution exists, even for the smallest molecule H_2^+, calling for a numerical solution. However, by introducing reasonable approximations, the Schrödinger equation may be significantly simplified. The most important complexity reduction is achieved by applying the so-called Born–Oppenheimer approximation [13]. It allows the separation of the Schrödinger equation into one equation for the electrons and one for the nuclei. Neglecting the coupling between electronic and nuclear motion is possible, because the electronic motion is roughly a factor of 1,000 faster than that of the nuclei. Therefore, electrons adapt virtually immediately to the movement of the nuclei and the electronic wave function is solved for stationary interatomic distances R. The product ansatz $\Psi(\boldsymbol{r}, \boldsymbol{R}) = \phi(\boldsymbol{r})\chi(\boldsymbol{R})$ leads to the decoupling of the Schrödinger equation into an electronic and a nuclear part:

[4] The presentation given in this section is compiled from [19, 34, 39].

$$\text{Electronic:} \qquad \left(\hat{T}_e + V(\boldsymbol{r}, \boldsymbol{R})\right) \phi(\boldsymbol{r}) = W_\gamma(\boldsymbol{R})\, \phi(\boldsymbol{r}), \tag{2.42}$$

$$\text{Nuclear:} \qquad \left(\hat{T}_N + W_\gamma(\boldsymbol{R})\right) \chi(\boldsymbol{R}) = W_{\gamma,\nu}\, \chi(\boldsymbol{R}). \tag{2.43}$$

$W_\gamma(R)$, depending on a set of electronic quantum numbers γ, denotes the R-dependent eigenvalues of the electronic Schrödinger equation, which serve as the potential of the nuclear Schrödinger equation. The R-dependent behavior of $W_\gamma(R)$ is known as a molecular potential energy curve, which will be denoted as $V(R)$ for the rest of this work. All potential energy curves show a steep rise for small R due to the repulsion of the nuclei and converge to the asymptotic behavior of separated atoms or ions for large R. Bound molecular states exhibit a potential minimum at an intermediate R, which is the equilibrium internuclear distance R_{eq}. The eigenvalues of the nuclear equation $W_{\gamma,\nu}$ correspond to the total energy of a molecular state with a set of electronic quantum numbers γ and a set of nuclear quantum numbers ν. The total energy of a molecule is composed of three different contributions:

$$W_{\gamma,\nu} = W_\gamma(\boldsymbol{R}) + W_{\text{vibration}}(\boldsymbol{R}) + W_{\text{rotation}}(\boldsymbol{R}) = \text{const.} \tag{2.44}$$

Each term has its characteristic energy and time scale. The binding energies of electronic states are usually in the order of several electronvolt and the motion of electrons takes place within tens to hundreds of attoseconds. Vibrational states exhibit typical energies in the order of 0.1 eV and the time scales range from a few to hundred femtoseconds. The binding energies of rotational states are even lower and rotation periods are in the order of picoseconds.

Within this work typical time scales of vibrational motion will be investigated, while rotations will not be considered. If the vibration of a molecule is a small displacement around R_{eq}, a Taylor expansion around that distance leads to

$$V_\gamma(R) = V_\gamma(R_{\text{eq}}) + (R - R_{\text{eq}}) \left.\frac{dV_\gamma}{dR}\right|_{R=R_{\text{eq}}} + \frac{1}{2}(R - R_{\text{eq}})^2 \left.\frac{d^2V_\gamma}{dR^2}\right|_{R=R_{\text{eq}}} + \cdots \tag{2.45}$$

As $\left.\frac{dV_\gamma}{dR}\right|_{R=R_{\text{eq}}}$ vanishes at the potential minimum, we arrive at the potential of an harmonic oscillator

$$V_\gamma(R) = V_\gamma(R_{\text{eq}}) + \frac{1}{2}k(R - R_{\text{eq}})^2, \tag{2.46}$$

with the coupling constant $k = \left.\frac{d^2V_\gamma}{dR^2}\right|_{R=R_{\text{eq}}}$.

Classically, this potential leads to vibrations with the frequency $\omega = \sqrt{\frac{k}{\mu}}$. The solution of the corresponding Schrödinger equation yields the Hermitian polynomials [19]. A harmonic potential is the most basic assumption for a molecular potential. A better estimate is usually gained with the Morse potential [53], while weakly bound systems, such as Ne_2, are well characterized by a Lennard-Jones potential [41].

We will now consider transitions between vibrational levels of different electronic states m and k. The vibrational and rotational quantum numbers will be denoted as ν and J respectively. The transition matrix element with the nuclear wave functions χ_i is given by

$$\boldsymbol{D}_{mk} = \int \chi_m^* \boldsymbol{D}_{mk}^{el} \chi_k d^3R', \tag{2.47}$$

with $\boldsymbol{D}_{mk}^{el}$ being the electronic matrix element, which depends on the electronic dipole moment. The nuclear wave function separates into a vibrational part $S_{\mathrm{vib}}(R)$, which is only dependent on R, and a rotational part $Y_J^M(\theta, \phi)$, which depends on the polar angle θ and the azimuthal angle ϕ. Thus, $\boldsymbol{D}_{mk}$ reads

$$\boldsymbol{D}_{mk} = \int S_{\mathrm{vib}}(\nu'') \boldsymbol{D}_{mk}^{el} S_{\mathrm{vib}}(\nu') R^2 dR \iint Y_{J''}^{M''} Y_{J'}^{M'} d\cos\theta d\phi. \tag{2.48}$$

If the dipole operator is independent of R, it is moved out of the integral and the absolute square of the first integral can be written as:

$$q_{\nu',\nu''} = \left| \int S_{\mathrm{vib}}(\nu'') S_{\mathrm{vib}}(\nu') R^2 dR \right|^2, \tag{2.49}$$

which is known as the Franck–Condon factor. Thus, the probability for a transition from one vibrational level to another is determined by the spatial overlap of the vibrational wave functions, as illustrated in Fig. 2.3. The second integral in Eq. (2.48)

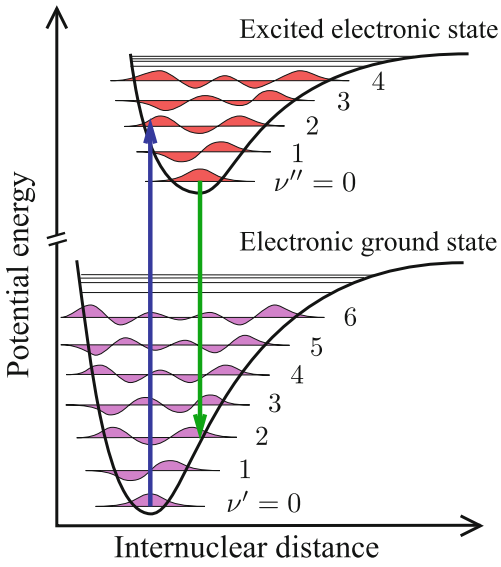

Fig. 2.3 Illustration of the Franck–Condon principle. The *blue arrow* (pointing upwards) indicates a (*vertical*) Franck–Condon transition from the vibrational and electronic ground state of the molecule into an excited electronic state. Mostly the second excited vibrational state ($\nu'' = 2$) is populated due to the large overlap with the nuclear wave function of the ground state. The *green arrow* (pointing downwards) shows a relaxation of the molecule. Figure adapted from [81]

is the so-called Hönl–London factor, which depends on the rotational quantum numbers. The transition between two vibrational levels via the absorption of a photon is occurring so fast, that the internuclear distance and kinetic energies of the nuclei are considered as fixed. Therefore, these transitions occur on vertical lines at a fixed distance R, which is known as the Franck–Condon principle (cf. Fig. 2.3). Nuclear dynamics within a molecule is often described by a nuclear wave packet propagating in time. The coherent superposition of several vibrational states, that may be populated by photoionization, leads to the modulation of the nuclear wave packet propagating along the internuclear distance.

Solving the multi-electron Schrödinger equation of molecules relies on the methods presented in Sects. 2.2.1 and 2.2.2 for multi-electron atoms. The ansatz for the total wave function is again the product of single-electron wave functions. However, the single electron wave functions are so-called molecular orbitals, which are expressed as linear combinations of atomic orbitals.

The molecular orbitals have more complex symmetry properties when the system is not central symmetric anymore. Due to the symmetry breaking, the characterization of electronic states is more complicated. Here, we will only introduce the nomenclature of electronic states in diatomic homonuclear molecules, as those are relevant for our experimental investigation:

$$^{2S+1}\Lambda^{(+,-)}_{(g,u)}, \tag{2.50}$$

where Λ is the angular momentum and $\boldsymbol{S}$ is the total spin, resulting in the multiplicity $2S + 1$ of each state. The angular momentum is commonly denoted similarly to atoms with Σ, Π, Δ for $\Lambda = 0, 1, 2$. The superscript $(+, -)$ and the subscripts (g, u) indicate symmetry properties of the wave function Ψ. For diatomic molecules, reflection on a plane through the axis of the nuclei, denoted by the operator σ, is a symmetry operation. As applying this reflection operator twice leads to the original wave function,

$$\sigma(\sigma\Psi) = \sigma^2\Psi = \Psi, \tag{2.51}$$

one finds that $(+, -)$ are the eigenvalue of σ:

$$\sigma\Psi = \pm\Psi. \tag{2.52}$$

For diatomic homonuclear molecules another symmetry operation can be defined, inversion I on the center of mass:

$$I^2\Psi = \Psi \quad \text{with} \quad I\Psi_g = +\Psi_g \quad \text{and} \quad I\Psi_u = -\Psi_g. \tag{2.53}$$

Thus, g-states have "gerade" and u-states have "ungerade" symmetry. As an example, the ground state X in H_2 is denoted by $X^1\,\Sigma_g^+$.

Atoms with closed atomic shells, i.e., the rare gases, are not able to form covalent bonds due to the lack of unpaired valence electrons. Nevertheless, they are able to

assemble in weakly bound structures because of the attractive van-der-Waals forces. Neutral atoms do neither have a net charge nor a dipole moment, when averaged over time. The situation changes if an atom A approaches atom B and the momentary induced dipole moment creates an electric field at B and vice versa. This results in an attractive potential energy of [19]

$$E_{\text{pot}} \propto \frac{\alpha_A \, \alpha_B}{R^6}, \tag{2.54}$$

where α_A and α_B are the polarisabilities of the respective atoms. Van-der-Waals bonds are weaker than hydrogen bonds and roughly a factor of 100–1,000 weaker than typical chemical bonds. This results in very shallow potential energy curves with only few vibrational states. Therefore, rare gas dimers are usually only stable at low temperatures. The most remarkable example is the He dimer, which has a mean internuclear distance of 52 Å and a binding energy of 95 neV $\widehat{=}$ 1.1 mK [32].

2.3 Photoionization for High Photon Energies

In photoionization, the energy of a photon, $\hbar\omega$, is transferred to a bound electron that is consequently ejected into the continuum. For an atom A with the initial state $|a\rangle = |nl\rangle$ and the continuum state $|b\rangle = |\epsilon l'\rangle$, the reaction reads

$$A + \hbar\omega \rightarrow A^+ + e^-. \tag{2.55}$$

The kinetic energy ϵ of the ejected electron equals the photon energy minus the binding energy of the electron: $\epsilon = \hbar\omega - W_I$. The probability for the absorption of a photon is proportional to the transition matrix amplitude $\hat{T}_{ab} = \langle b|\hat{T}|a\rangle$, which is derived via first-order perturbation theory, as presented in Sect. 2.1. The cross section for the process is given by

$$\sigma_{ab}(\hbar\omega) = 4\pi^2 \alpha \hbar\omega \left|\hat{T}_{ab}\right|^2. \tag{2.56}$$

For large photon energies, where $W_I \ll \hbar\omega \ll mc^2$, and for one-electron systems, the wave function of the outgoing electron can be approximated by a plane wave. Further assuming hydrogen-like radial wave functions, the total cross section for photoionization reads [38]:

$$\sigma_{ab} \propto \frac{Z^5}{n^3 (2\hbar\omega)^{7/2}}. \tag{2.57}$$

This formula illustrates some of the characteristic features in photoionization cross sections, such as the strong decrease with the photon energy and the increase for heavier nuclei. In addition the removal of electrons from outer orbitals is preferred.

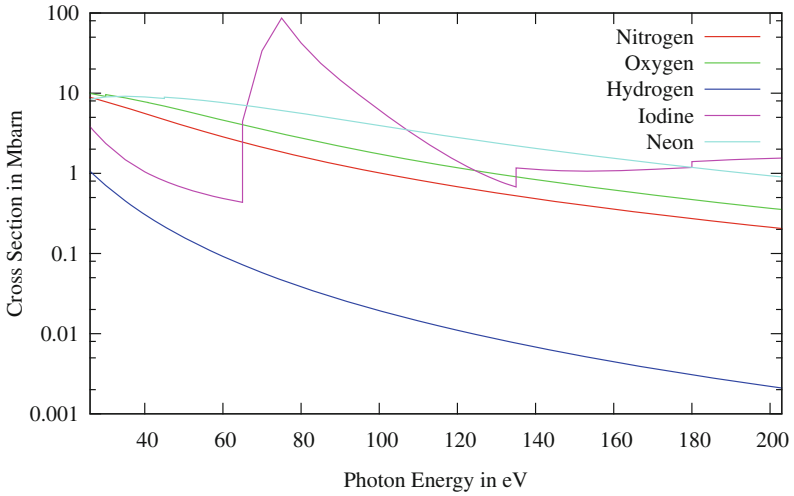

Fig. 2.4 Photoionization cross sections of background species nitrogen, oxygen and hydrogen, and the target species iodine and neon [83]

Figure 2.4 shows the cross sections for relevant background species and the investigated targets as a function of the photon energy. The aforementioned features are clearly present in these spectra. However, iodine shows an exceptional behavior with a distinct maximum above 80 eV and further steps at photon energies of 140 and 180 eV. These characteristic steps can usually be attributed to the break-up of an additional shell, e.g., the photon energy overcomes the ionization potential of the electrons sitting in the next tighter bound shell. At these so-called absorption edges the cross section is usually maximal and drops off afterwards. In iodine the step at 140 eV corresponds to the break-up of the $4p$ shell, while the 180 eV step corresponds to that of the $4s$ shell. The broad maximum in the cross section above 80 eV is assigned to a so-called shape resonance, which will be discussed in the following.

2.3.1 4d Shape Resonance

The observed increase in the photoionization cross section of I in a broad region above 80 eV is assigned to the excitation of a $4d$ shape resonance [73]. Here, we will give an intuitive explanation for this effect [15, 18]. The effective potential of atoms other than hydrogen is given by a Coulomb potential modified by a repulsive centrifugal term:

$$V_{\text{eff}}(r) = -\frac{Z}{r} + \frac{l(l+1)}{2r^2}, \tag{2.58}$$

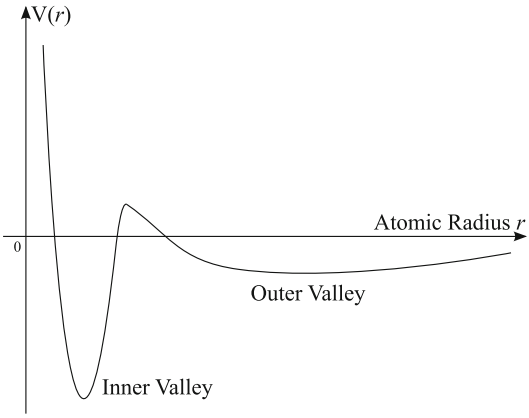

Fig. 2.5 Double valley potential, that may lead to the formation of a shape resonance: The $4f$ wave function collapses from the *outer* well into the *inner* well, where the $4d$ wave function is localized

with l being the angular momentum quantum number of the respective electronic state. For certain combinations of Z and l, particularly for the $4f$ shell in iodine, a potential with the eponymous *shape*, a so-called *double valley* (cf. Fig. 2.5), may arise. In this situation the $4f$ wave function may *collapse* from the outer well (where all nf states would be expected) into the inner well, leading to an increased spatial overlap with the $4d$ wave function, which is localized in the inner well. Due to the enhanced overlap, exciting a $4d$ electron by photoabsorption will most likely induce a transition to $4f$, while a transition to the spatially separated nf for $n > 4$ is very unlikely. The resulting $4f$ state lies above the ionization potential and will thus autoionize, as discussed in Sect. 2.4. In conclusion, we note that if the initial and the final state overlap perfectly, due to the collapse of the latter, a strong increase in the cross section for this transition occurs, a so-called *giant* resonance. In fact, this is the case for the $4d$ and the $4f$ wave functions in Xe and I.

2.4 Relaxation Processes in Atoms and Molecules

The removal of electrons from outer-valence shells usually leaves the created ions in their ground state and therefore does not trigger further relaxation dynamics in atoms and molecules. If instead excited ions are produced, due to vacancies in an inner-valence or core shell or due to excited outer-valence electrons, the system may relax via different pathways.

Figure 2.6 shows different relaxation mechanisms for ionized and simultaneously excited atoms. The presented processes can equally well take place in molecules and are not limited to atoms. Due to electron correlation, one photon may also excite two electrons into the continuum at the same time, as shown in Fig. 2.6a. If one of the electrons relaxes, it transfers its energy to the other excited electron, which is consequently ejected. This process is called autoionization and has typical decay

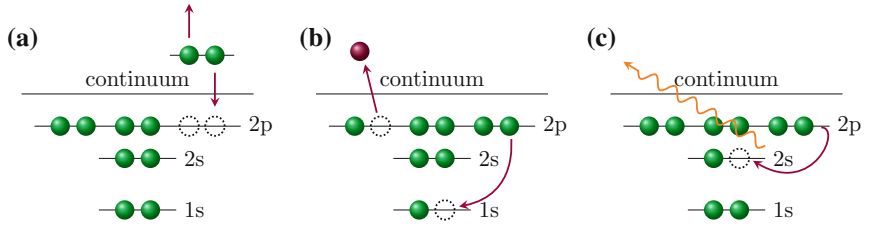

Fig. 2.6 Illustration of the relaxation mechanisms that may occur in excited atoms and molecules. **a** Autoionization **b** Auger decay **c** Radiative decay

times of a few femtoseconds. As autoionization is usually indistinguishable from direct photoionization of the valence shell, these two pathways may interfere and give rise to the famous Fano-resonance line shapes [25].

Depending on the atomic number Z and the binding energy of the electrons, inner-valence and core vacancies relax via two different mechanisms. For intermediate Z (or inner-valence vacancies in high-Z atoms), the dominating effect is Auger decay [51], as illustrated in Fig. 2.6b: An outer-valence electron fills the core hole and the energy released upon the relaxation is transferred to another valence electron, which is then ejected. In larger atoms the entire relaxation process may involve several electrons, resulting in Auger cascades. The ion is still excited after the first Auger decay and relaxes via further Auger decays. For instance the $4d$ vacancy in I_2^+ mostly relaxes via a single or a cascade of two Auger decays [12]. The typical time scales of Auger decay are a few femtoseconds. Note that autoionization and Auger decay are possible due to the Coulomb interaction between the electrons involved in the processes.

For core holes in heavy elements, radiative decay, as shown in . 2.6c, is usually the dominating relaxation pathway, with typical lifetimes in the order of a few femtoseconds [4]. For light elements, Auger decay is often energetically forbidden and the only remaining relaxation pathway is radiative decay. There, excited states often have lifetimes in the pico- to nanosecond regime. Notably, the lifetime of a $Ne^+(2s^{-1})$ ion is 0.2 ns [31].

2.5 Interatomic Coulombic Decay

The lifetimes of core vacancies in strongly bound molecules and solids can be affected by the environment, which is known as chemical shift [48]. However the effect is weak and van-der-Waals and hydrogen bonds have hardly any influence on the dynamics of core- and inner-valence vacancies. Despite these findings, a new relaxation mechanism for inner-valence ionized atoms and molecules embedded into a weakly interacting environment was proposed in 1997: interatomic or intermolecular Coulombic decay (ICD) [16]. The vacancy is filled by an outer-valence electron and the released energy is transferred to a neighboring particle, which then emits an electron.

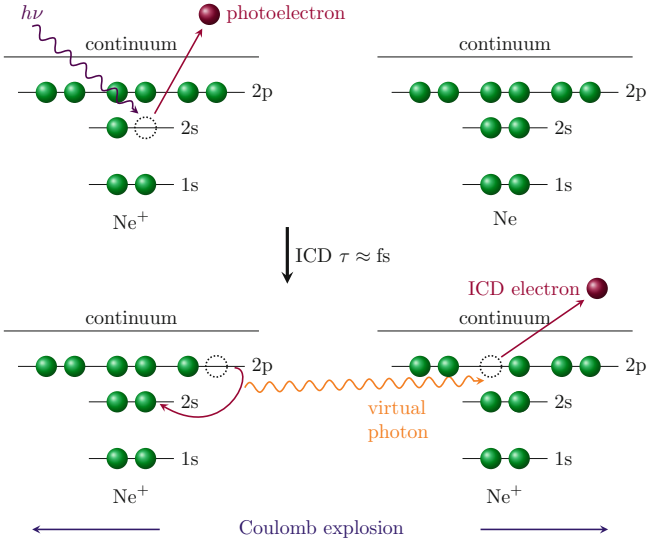

Fig. 2.7 Illustration of the ICD process in Ne_2 dimers. A $2s$ electron in either of the two Ne atoms is removed. The relaxation energy of 27.2 eV (insufficient for the removal of a $2p$ electron in the same ion) is transferred to the neutral Ne atom via virtual photon exchange. Since a $2p$ electron in the neutral Ne is bound with only 21.6 eV, the excess energy is large enough to ionize the formerly neutral side of the dimer. The final state consists of two singly charged Ne^+ ions, which Coulomb explode

In 2003, ICD was first experimentally confirmed in large neon clusters [49] via a low-energetic feature in the electron spectra, which was not present for monomers. A further proof of ICD was given in 2004 by a kinematically complete experiment on Ne_2 [40]. The process is depicted in Fig. 2.7: An isolated $2s$ inner-valence ionized Ne^+ ion can only relax radiatively, which occurs within 0.2 ns, because Auger decay is energetically forbidden. If another Ne atom is placed nearby, the hole is filled by a $2p$ electron and the excess energy is transferred to the neighboring atom, which is consequently ionized. The relaxation energy of 27 eV is not sufficient to remove a second electron from the ion, which requires more than 40 eV. However it is sufficient to remove a $2p$ electron from a neutral Ne atom, which is bound with 21 eV. Finally, two singly charged Ne^+ ions are produced, which repel each other with the Coulomb force. The process is possible because the double ionization threshold in clusters is considerably lowered compared to monomers as the charges can be distributed among the constituents.

By now, a whole plethora of ICD phenomena in different systems was predicted and many of them have been experimentally verified. In the following, we discuss the processes relevant for Ne_2. An overview of the experimental status of ICD research can be found in [37], a review on ICD theory is given in [3].

2.5.1 Theoretical Treatment

The goal of our experiment on Ne_2 is the determination of the lifetime τ of the excited $Ne_2^+(2s^{-1})$ state. The probability p for finding the system in the excited state at a certain time t is given by

$$p = p_0 e^{\frac{-\Gamma \cdot t}{\hbar}} \quad \text{with} \quad p_0 = p(t = 0). \tag{2.59}$$

While the obvious choice of observable from the experiment is the lifetime, theory prefers the decay width $\Gamma = \hbar/\tau$. Besides Γ, electron and ion spectra for comparison with the experiment may be calculated.

The theoretical treatment of ICD is a challenging task as it requires the full quantum mechanical description of a many electron system for which electron correlation must be taken into account. Moreover, nuclear motion occurring while the decay takes place, must be included. In order to gain further insight into the ICD mechanism, we begin in Sect. 2.5.1.1 by giving an expression for Γ derived within the framework of time-dependent perturbation theory via the Wigner–Weißkopf method, following the presentation in [66]. Since this method is not routinely applied for the determination of decay widths, a brief discussion of other methods will be given in Sect. 2.5.1.2. An overview of the existing calculations for the $2s^{-1}$ vacancy in Ne_2^+, is presented in Sect. 2.5.1.3. In order to obtain a complete theoretical treatment for ICD, nuclear motion must be included, which will be introduced in Sect. 2.5.1.4.

2.5.1.1 Wigner–Weißkopf Method

An expression for the decay width Γ_{iv} of an inner-valence ionized system, such as $Ne_2^+(2s^{-1})$, may be derived by applying the Wigner–Weißkopf method [66, 77]:

$$\Gamma_{\mathrm{iv}} = 2\pi \sum_k \sum_{\mathrm{ov}_1} \sum_{\mathrm{ov}_2 > \mathrm{ov}_1} \underbrace{\left| V_{\mathrm{ov}_1,\mathrm{ov}_2[\mathrm{iv},k]} \right|^2}_{\text{(a)}} \tag{2.60}$$
$$\times\ \delta(\epsilon_{\mathrm{iv}} \underbrace{-\epsilon_{\mathrm{ov}_1} - \epsilon_{\mathrm{ov}_2} + V_{\mathrm{ov}_1,\mathrm{ov}_2[\mathrm{ov}_1,\mathrm{ov}_2]}}_{\text{(b)}} + \underbrace{\epsilon_k - V_{k,\mathrm{ov}_1[k,\mathrm{ov}_1]} - V_{k,\mathrm{ov}_2[k,\mathrm{ov}_2]}}_{\text{(c)}}),$$

with the summation indices k for the continuum, iv for the inner-valence hole, ov_1 and ov_2 for the first and the second outer-valence hole, respectively. Energies are denoted by ϵ. The notation $V_{pq[rs]} = V_{pqrs} - V_{pqsr}$ for the direct and the exchange terms respectively has been introduced in Sect. 2.2.

We will first discuss the argument of the delta function, which ensures energy conservation and thus specifies the possible decay channels of the inner-valence vacancy. The binding energy ϵ_{iv} of the ejected inner-valence electron, i.e., the total energy available, is distributed among the terms (b) and (c). Term (b) corresponds

to the energy of a doubly outer-valence-ionized state consisting of the ionization potentials of the outer-valence electrons $\epsilon_{\mathrm{ov}_{1,2}}$ and the Coulomb interaction between the holes. This term illustrates why ICD is possible: The double ionization threshold of clusters is lower than that of monomers. Therefore the decay becomes energetically allowed as the outer-valence holes can be placed at two "distant" monomers, which lowers the Coulomb repulsion of the holes. If both electrons were removed from the same monomer, the required energy would be higher than the available $-\epsilon_{\mathrm{iv}}$ and consequently the argument of the delta function never vanishes. Term (c) corresponds to the energy of an emitted electron ϵ_k corrected by the interaction with the two holes.

We conclude that the two outer-valence holes must be located at different monomers in order to get a non-vanishing Γ_{iv} and proceed by discussing the overlap matrix elements $V_{\mathrm{ov}_1,\mathrm{ov}_2,[\mathrm{iv},k]}$, appearing in (a) from Eq. (2.60), which consists of two contributions:

Direct term:

$$V_{\mathrm{ov}_1,\mathrm{ov}_2,\mathrm{iv},k} = \iint \phi^{\dagger}_{\mathrm{ov}_1}(\boldsymbol{x}_1)\phi_{\mathrm{iv}}(\boldsymbol{x}_1)\frac{1}{|\boldsymbol{x}_1-\boldsymbol{x}_2|}\phi^{\dagger}_{\mathrm{ov}_2}(\boldsymbol{x}_2)\phi_k(\boldsymbol{x}_2)\,d^3x_1 d^3x_2. \quad (2.61)$$

Exchange term:

$$V_{\mathrm{ov}_1,\mathrm{ov}_2,k,\mathrm{iv}} = \iint \phi^{\dagger}_{\mathrm{ov}_1}(\boldsymbol{x}_1)\phi_k(\boldsymbol{x}_1)\frac{1}{|\boldsymbol{x}_1-\boldsymbol{x}_2|}\phi^{\dagger}_{\mathrm{ov}_2}(\boldsymbol{x}_2)\phi_{\mathrm{iv}}(\boldsymbol{x}_2)\,d^3x_1 d^3x_2. \quad (2.62)$$

Each matrix element describes one of the physical processes illustrated in Fig. 2.8 for the $Ne^+(2s^{-1})$ dimer ion. The direct term in Eq. (2.61) corresponds to the situation in which the inner-valence vacancy ϕ_{iv} is filled by an outer-valence electron from the same monomer ϕ_{ov_1} and an outer-valence electron ϕ_{ov_2} from the other monomer is ejected into the continuum ϕ_k. The exchange term in Eq. (2.62) describes a process in which an electron from the neighboring atom ϕ_{ov_2} fills the inner-valence vacancy ϕ_{iv} and an outer-valence electron from the inner-valence side ϕ_{ov_1} is ejected into the continuum ϕ_k. However, for rare gas clusters the exchange term is very weak at equilibrium internuclear distance because the overlap of ϕ_{ov_2} and ϕ_{iv} is more or less negligible. Therefore the direct ICD process dominates by far. It should be noted though that exchange ICD might also occur under certain circumstances, as will be shown in Sect. 7.2.7.

Now we will discuss the general distance dependence of ICD. The orbital overlap of two neighboring atoms—even at large distance R as occurring in van-der-Waals clusters—is usually non-negligible. However, for inner-valence orbitals the assumption of vanishing overlap is reasonable and a power series expansion may be performed:

$$\frac{1}{|\boldsymbol{x}_1-\boldsymbol{x}_2|} = \frac{1}{R} - \frac{(\boldsymbol{r}_1-\boldsymbol{r}_2)\cdot\boldsymbol{u}_R}{R^2} + \frac{3\left[(\boldsymbol{r}_1-\boldsymbol{r}_2)\cdot\boldsymbol{u}_R\right]^2-(\boldsymbol{r}_1-\boldsymbol{r}_2)^2}{2R^3} + O\left(\frac{1}{R^4}\right), \quad (2.63)$$

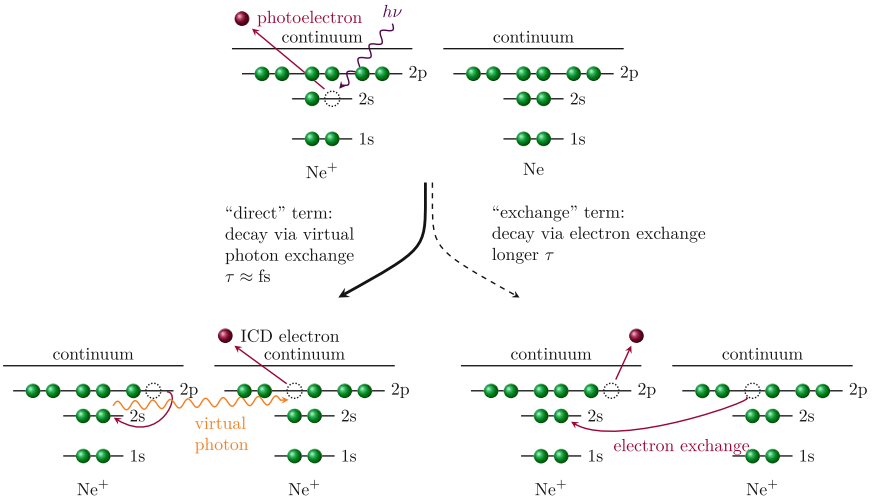

Fig. 2.8 Illustration of the two competing ICD processes: direct ICD and exchange ICD. In the direct process the $2s$ vacancy at the left neon ion is filled by a $2p$ electron from the same ion and the excess energy is transferred to a neighboring $2p$ electron, which is then ejected. In the exchange process the $2s$ vacancy is filled by a neighboring $2p$ electron and the released energy is given to a $2p$ electron at the *left* side, which is then emitted

with $\boldsymbol{R} = \boldsymbol{R}_1 - \boldsymbol{R}_2$, the unit vector $\boldsymbol{u}_R$ along the internuclear axis and the position $\boldsymbol{r}_i$ of the electrons relative to the monomers' centers of mass $\boldsymbol{R}_i$. If we insert this expansion into Eq. (2.61), the first two terms cancel and the first non-vanishing term is

$$V_{\mathrm{ov}_1,\mathrm{ov}_2,\mathrm{iv},k} \propto \frac{1}{R^3}. \tag{2.64}$$

Here, one has to assume that $\langle \phi_{\mathrm{ov}_1} | \phi_{\mathrm{iv}} \rangle = \langle \phi_{\mathrm{ov}_2} | \phi_k \rangle = 0$. Therefore, for large R we obtain

$$\Gamma_{\mathrm{iv}} \propto \frac{1}{R^6}. \tag{2.65}$$

The characteristic $1/R^6$ behavior is also known from other intermolecular processes, such as Förster resonances [28] and Penning ionization [58, 72]. In the *Förster Resonant Energy Transfer* (FRET) the excitation energy of one molecule is non-radiatively transferred to a close-by molecule that absorbs the energy and subsequently emits it via fluorescence. The occurrences and applications of FRET are manifold. Notable examples are light harvesting in photosynthesis [27] and the structural and functional studies of proteins [30]. All involved electronic states in FRET are bound, therefore discrete and thus the energy emitted from one molecule must be resonant with the excitation of the other molecule. Achieving the resonance condition often requires nuclear motion, which determines the duration of the process [64]. For (direct) ICD a resonant energy transfer is not required as the electron, which absorbs the relaxation

energy, is ejected into the continuum. Therefore it takes place much faster. Penning ionization is a process occurring in slow ion-atom collisions: An excited atom collides with a neutral one, thereby forming a quasimolecular state for a short time. The excitation energy is transferred to the neutral particle, which is consequently ionized [72].

2.5.1.2 Decay Widths

In practice, ICD widths are usually calculated within two different theoretical frameworks, which are briefly introduced here.[5] In atomic physics, resonances are, for instance, found in electron scattering with atoms or molecules or in photoionization, resulting in an enhanced cross section for a certain process. Related are autoionization, Auger decay and ICD. Resonances are characterized by their complex Siegert energy [71], consisting of their position on the energy scale E_R and their decay width Γ:

$$E_{\text{res}} = E_R - \mathrm{i}\frac{\Gamma}{2}. \tag{2.66}$$

A major difficulty that arises in calculating the lifetime of resonances is the wave function of the outgoing electron. As it is not square integrable, standard electronic structure theory is not applicable [65]. One method is to make the electron wave function square integrable by introducing a Complex Absorbing Potential (CAP), which creates an absorbing boundary condition around the considered molecular system. It is important to note, that the boundary condition must be chosen in such a way that the wave function in the vicinity of the molecule is not disturbed [63]. The absorption of the electron is achieved by adding a complex term to the original Hamiltonian $\hat{H}$ of the system:

$$\hat{H}(\eta) = \hat{H} - \mathrm{i}\eta\hat{W}. \tag{2.67}$$

The parameter η is a real positive number and referred to as the CAP strength and $\hat{W}$ is a local semi-definite one-particle operator. The new Hamiltonian still fulfills the Schrödinger equation, but is non-Hermitian. Thus, its eigenvalues are no longer real numbers. Even though the CAP disturbs the Hamiltonian, the exact eigenvalues of the resonance are obtained in the limit of vanishing η [60]. If a complete basis set is given, each resonance has an eigenvalue $E(\eta)$ with

$$\lim_{\eta\to 0} E(\eta) = E_R - \mathrm{i}\frac{\Gamma}{2} \tag{2.68}$$

corresponding to the Siegert energy. Thus, the complex part of the eigenvalue $E(\eta)$ yields the decay width.

[5] If not indicated otherwise, the presentation given here is compiled from [3, 63, 75].

In order to perform the actual calculation, many-electron wave functions of the initial and final state of the system are needed. The wave functions and, thus, the energy eigenvalues can be determined using different *ab initio* techniques: Two commonly used methods for ICD calculations are the configuration interaction (CI) and the algebraic diagrammatic construction (ADC) [69] method, which have been introduced in Sect. 2.2.2. For a detailed treatment of the CAP-CI method see [66]. The application of CAP-ADC to the $Ne^+(2s^{-1})$ decay rate is presented in [75].

Another method[6] used to calculate ICD decay widths is based on the Fano theory of resonances [25]. The wave function Ψ_E at the energy E, which is beyond the ionization energy, is expressed as a superposition of a bound-like state Φ and a continuum-like state χ:

$$\Psi_E = a(E)\Phi + \sum_{\beta=1}^{N_c} \int C_\beta(E,\epsilon)\chi_{\beta,\epsilon} d\epsilon. \tag{2.69}$$

The initial state of the decay Φ corresponds to the $Ne^+(2s^{-1})$ state of our system. $\chi_{\beta,\epsilon}$ is the final state with the continuum energy ϵ and enumerated by β, which counts the decay channels up to N_c. Here, this is the doubly ionized $Ne^+ - Ne^+$ state. The decay width Γ is expressed in the Fano theory as:

$$\Gamma = \sum_{\beta=1}^{N_c} \Gamma_\beta = 2\pi \sum_{\beta=1}^{N_c} \left| \left\langle \Phi \left| \hat{H} - E_r \right| \chi_{\beta,\epsilon_\beta} \right\rangle \right|^2. \tag{2.70}$$

E_r is the energy of the decaying state: $E_r \approx E_\Phi = \left\langle \Phi \left| \hat{H} \right| \Phi \right\rangle$ and ϵ_β is the asymptotic kinetic energy of the ICD electron emerging from the decay channel β.

In order to calculate Γ via Eq. (2.70), the wave functions of the initial and the final states are needed. These correlated many-electron states can for instance be constructed via the ADC method [69].

2.5.1.3 Decay Widths for the Neon Dimer

The ICD lifetime of the $2s^{-1}$ vacancy in Ne_2^+ was subject to many theoretical studies, which will be reviewed here. In a study on the dependence of the lifetime on the cluster size, it was shown that the lifetime of the $2s$ hole decreases from $\tau = 85$ fs for Ne_2 down to $\tau = 3$ fs for Ne_{13} [64]. The decay width for the $^2\Sigma_u$ state was calculated using the Stieltches–Chebyshev moment theory [66]. As the initial and final states were determined via Hartree–Fock calculations, no correlation effects were included and the geometry of the clusters was kept at a fixed solid-neon-like internuclear distance of 3.13 Å [64].

[6] This discussion is adapted from [3].

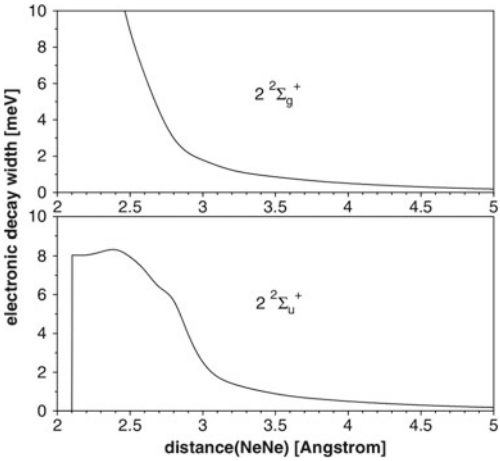

Fig. 2.9 Decay width Γ as a function of the internuclear distance for both intermediate states $^2\Sigma_u$ and $^2\Sigma_g$ calculated via CAP-CI. Figure taken from [65]

Another study [65] found a strong dependence of the decay width on the internuclear distance R in $Ne^+(2s^{-1})$ for both intermediate inner-valence states $^2\Sigma_u$ and $^2\Sigma_g$, as shown in Fig. 2.9. There, a lifetime of approximately $\tau = 530$ fs at $R = 3.2$ Å for both states was calculated. The result shown in Fig. 2.9 was obtained using the CAP-CI method with a CI expansion for the $Ne_2^+(2s^{-1})$ state including all one-hole states and their single and double excitations [66]. A more precise CAP calculation with a multi-reference CI (MRCI) expansion yielded a value of $\tau = 64$ fs for the $^2\Sigma_g$ state at $R = 3.2$ Å [63]. However the latter calculation was only performed at a single internuclear distance due to the high computational complexity.

A further study was carried out in the CAP framework to calculate Γ as a function of the cluster size with optimized cluster geometry, and to investigate its dependence on the used basis set for the calculation [75]. With the most accurate basis, the application of the CAP-ADC method yielded a value of $\tau = 92$ fs at $R = 3.2$ Å for the $^2\Sigma_g$ state while the basis set used in [63, 65] gives a slightly smaller lifetime of $\tau = 74$ fs.

Using the Fano-ADC method to determine the ICD decay widths of the $^2\Sigma_g$ state yields a lifetime of $\tau = 82$ fs at $R = 3.2$ Å [2]. These calculations were performed at several internuclear distances, as shown in Fig. 7.19.

Concluding we note that the most accurate results for the τ of $^2\Sigma_g$ at $R = 3.2$ Å are to be expected from the CAP-MRCI (64 fs) [63], the CAP-ADC (92 fs) [75] and the Fano-ADC (82 fs) method [2].

2.5.1.4 Nuclear Dynamics

The previously presented calculations, performed for a fixed internuclear distance, predicted ICD lifetimes in the order of 100 fs, which gives the nuclei enough time to move prior to the decay. Therefore, it is crucial to include nuclear dynamics into

calculations as the decay width is strongly dependent on the internuclear distance (cf. Figs. 2.9 and 7.19). Only if nuclear motion is included, the calculated electron and ion spectra are comparable to experimental data [65, 67]. Since the behavior of $\Gamma(R)$ is non-linear, a non-trivial impact on the lifetime is expected [68].

The theoretical description of ICD is usually performed in the Born–Oppenheimer approximation where the electronic and the nuclear dynamics are decoupled. Thus, the nuclear motion is added on top of the calculated potential energy curves by describing the whole ICD process as transitions of wave packets between different electronic states. In the following, we give an overview of the method of time-dependent propagation of nuclear wave packets, following the description in [3, 67].

The ground state wave packet is instantaneously projected onto the intermediate inner-valence potential energy curve, where it starts to propagate. As the equilibrium internuclear distances of the intermediate inner-valence states are usually located at smaller R, due to the tighter bound of the singly ionized system, the wave packet usually starts to propagate towards smaller R. Simultaneously the decay process sets in and the final state is populated at the same rate as the density drops in the intermediate state. The final wave packets, associated to the different energies of the ICD electron, are generated and start propagating along the repulsive curve of the final state. The wave packet dynamics is described by a set of coupled differential equations (time-dependent Schrödinger equations) with i denoting the initial, d the intermediate and f the final electronic state with the corresponding nuclear wave functions Ψ_i, Ψ_d and Ψ_{mf}, where m counts the different final electronic states:

$$\begin{aligned}
\mathrm{i}\frac{\partial}{\partial t}|\Psi_i(R,t)\rangle &= \hat{H}_i(R)|\Psi_i(R,t)\rangle, \\
\mathrm{i}\frac{\partial}{\partial t}|\Psi_d(R,t)\rangle &= \hat{F}_i(R)|\Psi_i(R,t)\rangle + \hat{H}_d(R)|\Psi_d(R,t)\rangle, \\
\mathrm{i}\frac{\partial}{\partial t}\left|\Psi_{m,f}(R,t,\epsilon)\right\rangle &= \hat{W}_m(R,\epsilon)|\Psi_d(R,t)\rangle + \left(\hat{H}_{m,f}(R)+\epsilon\right)\left|\Psi_{m,f}(R,t,\epsilon)\right\rangle
\end{aligned} \tag{2.71}$$

The initial Hamiltonian $\hat{H}_i = \hat{T}_N + \hat{V}_i$ consists of the nuclear kinetic energy $\hat{T}_N$ and the potential energy $\hat{V}_i$ according to the populated potential energy curve. In order to describe the dynamics of the intermediate state, the decay process must be taken into account by introducing a complex part with the decay width Γ: $\hat{H}_d(R) = \hat{T}_N(R) + \hat{V}_d(R) - \mathrm{i}\Gamma(R)/2$. The coupling between the initial and final state is taken care of by $\hat{F}$, which is only a delta function $\delta(t = 0)$ for instantaneous ionization. The coupling strength W_m between the intermediate and the final state is related to the partial decay widths Γ_m via $\Gamma_m(R) = 2\pi\left|\hat{W}_m(R)\right|$ with $\Gamma = \sum_m \Gamma_m$. The final state Hamiltonian reads $\hat{H}_{m,f} = \hat{T}_N(R) + \hat{V}_{m,f}(R)$ and ϵ is the energy of the outgoing electron. In the system of coupled Schrödinger equations, Eq. (2.71), the norm of the intermediate wave packet decreases with increasing time at a rate given by $\Gamma(R)$. This is caused by the non-hermiticity of $\hat{H}_d$. The norm of the final wave packet increases accordingly with the same rate. Thus, the norm of the total wave function

for the whole system is constant in time. When the entire wave packet has decayed from the intermediate to the final state, all the information required to compute the ICD electron spectrum and the kinetic energy release for the fragments formed after Coulomb explosion is contained in the final wave packet [67, 68]. Results from calculations including nuclear dynamics, are discussed in Sect. 7.2.8.

2.6 Classical Treatment of the Pump-Probe Technique

No detector is able to resolve processes in the femtosecond time domain, in particular the motion of nuclei in molecules. Therefore dedicated experimental techniques have to be developed, such as the pump-probe method for which Ahmed Zewail was awarded the Nobel Prize in chemistry in 1999 [84]. A preceding pump pulse initiates a certain reaction by populating intermediate states and a probe pulse samples the evolution of the system by further ionizing it at an adjustable time delay. As the achievable temporal resolution lies in the order of the pulse duration, femtosecond pulses are needed to observe nuclear motion in real time. Typical Ti:Sa lasers, operating at 800 nm, deliver pulse durations of 25 fs, which can be further shortened to $\approx$6 fs by spectral broadening [26]. Therefore, even fast molecular processes are accessible via pump-probe spectroscopy in the IR regime [24].

Only in recent years the creation of ultra-short pulses in the XUV to X-ray regime became feasible due to the development of HHG sources [47, 57] and FELs [11]. In order to produce high harmonic radiation an intense femtosecond IR pulse is focused into a gas cell. A target electron absorbs several photons, recollides with its atom and thereby emits one high energetic photon. Using HHG sources, pulses in the XUV regime with durations as short as 68 as [85] can be produced. They provide excellent conditions for IR/XUV experiments: The IR pulse for the HHG is also used as probe pulse and is therefore intrinsically synchronized with the XUV pump pulse. The peak intensities achievable by HHG ($>10^{13}\,\frac{\mathrm{W}}{\mathrm{cm}^2}$ [50]) are starting to become sufficient for XUV pump-probe experiments [45]. However the generation of these high intensities is still difficult and not yet sufficient for all systems. FELs instead routinely deliver much higher intensities up to $10^{18}\,\frac{\mathrm{W}}{\mathrm{cm}^2}$ [14] in the XUV and X-ray regime. Therefore most of the XUV pump-probe experiments are performed at FELs.

In this work XUV pump-probe experiments on two different systems, the iodine molecule I_2 and the neon dimer Ne_2, are discussed. Our studies rely on Coulomb-explosion imaging (CEI) [74], which allows to access the molecules' geometry by exploiting the large Coulomb repulsion of the quickly ionized constituents. One XUV photon is usually sufficient to ionize an atom or molecule. At the present intensities the most likely scenario is single-photon absorption within the pump and single-photon absorption within the probe. Under these conditions mostly repulsive molecular curves are accessed at a well-defined time. These requirements justify the application of the classical model, that will be presented in the following.

The most intuitive way to simulate the measurements is by modeling molecular motion in a diatomic molecule as a classical point-like particle moving on the involved

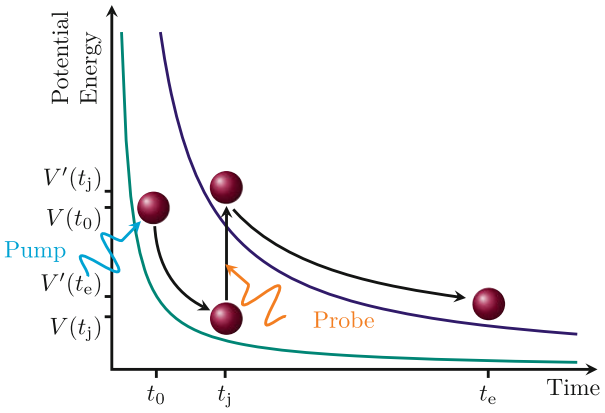

Fig. 2.10 Illustration of the classical simulation used for the present pump-probe studies. At t_0 the pump pulse prepares the classical point-like particle on the potential energy curve $V(R)$ thereby initiating dynamics in the molecule. The evolution of the system is sampled via the probe pulse at t_j by populating a different potential energy curve $V'(R)$

potential energy curves. A similar method was already successfully applied in earlier XUV pump-probe experiments [9].

According to the Franck–Condon approximation, the pump process is implemented by placing the particle on an intermediate potential curve at equilibrium internuclear distance $R(t_0) = R_{\mathrm{eq}}$ of the neutral molecule at time t_0, as shown in Fig. 2.10. The particle is given the reduced mass $\mu = \frac{m_1 m_2}{m_1+m_2}$ and a vanishing initial velocity: $\frac{dR}{dt}\big|_{t_0=0} = 0$. In order to describe the motion of the particle, moving on the molecular potential curve $V(R)$, Newton's classical equation of motion is solved for all internuclear distances R. The simulation is performed on an equidistant grid $(R_1, R_2, \ldots, R_i, \ldots, R_n)$ starting from R_{eq} with a constant step size of $\Delta R = R_i - R_{i-1}$. We start by calculating the acceleration a for each step R_i:

$$a(R_i) = -\frac{1}{\mu}\frac{V(R_i) - V(R_{i-1})}{\Delta R}. \tag{2.72}$$

The time $\Delta t(R_i - R_{i-1})$ needed to overcome ΔR with the velocity $v(R_{i-1})$ is given by

$$\Delta t(R_i - R_{i-1}) = \frac{-v(R_{i-1}) + \sqrt{v^2(R_{i-1}) + 2a(R_i)\Delta R}}{\Delta R}, \tag{2.73}$$

while the total time t_m for passing m intervals ΔR is composed of all infinitesimal intervals $t_m = \sum_{i=1}^{m} \Delta t(R_i - R_{i-1})$. At the end of each step the present kinetic energy of the particle is evaluated via

$$E_{\mathrm{kin}}(R_i) = V(R_i) - V(R_{\mathrm{eq}}), \tag{2.74}$$

in order to provide the velocity input $v(R_i)$ for the next step:

$$v(R_i) = \sqrt{\frac{2E_{\text{kin}}(R_i)}{\mu}}. \tag{2.75}$$

The particle pursues its motion on $V(R)$ until the probe pulse promotes it onto a different potential curve $V'(R)$ at t_j. Thus, after each step the passed time t_m must be compared with a predetermined time delay $t_D = t_j - t_0$ before starting the calculation of the trajectories. If t_m exceeds t_D the calculational procedure continues on the new potential curve $V'(R)$ with the previously gained velocity as initial condition. The transition onto a different potential energy curve is not always induced by the probe, alternatively it may occur via ICD or other decay mechanisms, as will be shown in Sect. 7.2.4.

Once the particle has reached its final potential curve, the propagation is carried on until the change in its velocity is negligible. This way the "infinite" distance $R_\infty = n\Delta R$ passed by the particle on its way to the detector is approximated. At R_∞ the total energy of the particle, gained on all populated potential curves, is evaluated. The obtained value is directly comparable to the experimentally observed kinetic energy release of the fragments (cf. Sect. 5.3.3). The used potential energy curves are either taken from literature or if not existent—which is typically the case for multiply charged molecular ions—assumed to be Coulombic.

2.7 Charge Transfer and Classical Over-the-Barrier Model

Charge transfer describes a reaction, in which electrons are transferred from one system to another. It occurs efficiently in slow ion-atom collisions, where single or multiple electrons from a typically neutral target are transferred to a highly charged projectile ion while it flies by [54]. These conditions are present in astrophysical plasmas, where charge transfer occurs between ions from solar winds and neutral clouds from comets and planetary atmospheres, leading to highly excited ions that relax via radiative decay [7]. The same effects are important for the analysis of earth-bound plasmas, as those in tokamaks [36]. Furthermore, understanding the interaction of low-energetic ions with matter plays a crucial role for heavy ion therapy [1, 43], as the deposited energy is maximal for the low projectile energies where charge transfer plays an essential role. Therefore collision experiments have explicitly addressed this question by bombarding biomolecules with low-energetic ions in order to identify the relevant break-up channels leading to DNA damage [20, 21, 76].

Here, we consider charge transfer of t electrons between the dissociating fragments B^{p+} and A^{q+} of a molecule AB:

$$A^{q+} + B^{p+} \quad \rightarrow \quad A^{(q-t)+} + B^{(p+t)+}, \quad q > p. \tag{2.76}$$

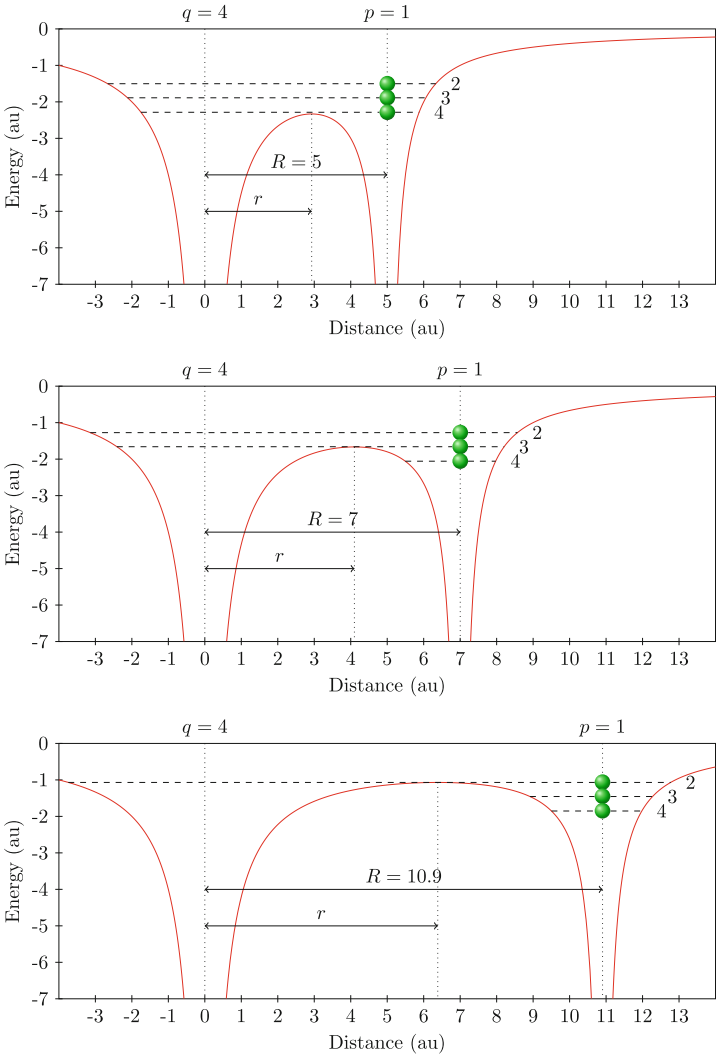

Fig. 2.11 Illustration of the over-the-barrier model for a I^{1+} and a I^{4+} ion moving apart from each other. The internuclear distance R increases from the *top* to the *bottom*. At the equilibrium internuclear distance of I_2 at 5 au the three least bound electrons may transfer to I^{4+}. Beyond 10.9 au charge transfer is not possible anymore. The required ionization potentials were taken from Table 6.2

The electrons of B^{p+} are affected by the Coulomb field of A^{q+} resulting in a lowering of the potential barrier between the two. Thus, a loosely bound electron migrates from B^{p+} to A^{q+} as soon as the potential barrier is lower than the electron's binding energy, as shown in Fig. 2.11. This process is described in the classical over-the-barrier (COB) model, first formulated in [62] and extended to state selective capture

of multiple electrons in [55]. This illustrative model and its extensions are in good agreement with experimental data and thus very popular for the description of charge transfer at low energies, like for the examples mentioned above.

The goal of the following considerations is to find an analytical expression for the critical internuclear distance R_{crit} at which charge exchange between A^{q+} and B^{p+} is not possible anymore. The binding energy $E_i'(R)$ of electron i of B^{p+} is increased in the external field of A^{q+} according to

$$E_i'(R) = -E_i - \frac{q}{R}, \tag{2.77}$$

where E_i is the binding energy experienced by the electron in the unperturbed case and R the internuclear distance. The potential $V_i(r, R)$ seen by the electron i at distance r is a superposition of the potential of its own nucleus with effective charge p_i^* and the potential of the other ion (cf. Fig. 2.11):

$$V_i(r, R) = -\left(\frac{p_i^*}{R - r} + \frac{q}{r}\right) \quad \text{for} \quad 0 < r < R. \tag{2.78}$$

In order to determine the distance $r_{i,\max}$ at which the maximum of the barrier occurs, the derivative of Eq. (2.78) is used:

$$\frac{\partial V_i(r, R)}{\partial r} = \frac{q}{r^2} - \frac{p_i^*}{(R - r)^2} \stackrel{!}{=} 0. \tag{2.79}$$

The local maximum is found by solving Eq. (2.79) for r:

$$r_{i,\max} = \frac{R\sqrt{q}}{\sqrt{q} + \sqrt{p_i^*}}. \tag{2.80}$$

Upon insertion of $r_{i,\max}$ into Eq. (2.78) an expression for the height of the potential barrier as a function of the internuclear distance R is found:

$$V_{i,\max}(R) = -\frac{q + 2\sqrt{q} + p_i^*}{R}. \tag{2.81}$$

Since the electron i is able to overcome the potential barrier as soon as its binding energy $E_i'(R)$ is above $V_{i,\max}(R)$ (cf. Fig. 2.11), Eq. (2.81) must be compared to Eq. (2.77):

$$-\frac{q}{R} + \frac{2\sqrt{q\, p_i^*} + p_i^*}{R} = -E_i - \frac{q}{R}, \tag{2.82}$$

This leads to

$$R_{i,\mathrm{crit}} = \frac{2\sqrt{q\, p_i^*} + p_i^*}{E_i}. \tag{2.83}$$

With the help of the critical distance, the geometrical cross section for electron capture is defined as:

$$\sigma = C\pi R_{i,\mathrm{crit}}^2 = \frac{\pi}{2}\left(\frac{2\sqrt{q\ p_i^*} + p_i^*}{E_i}\right)^2 . \tag{2.84}$$

In order to account for the oscillatory behavior of the electron bouncing back and forth between the two ions as long as charge transfer is possible, the additional weighting factor C is introduced. Assuming that beyond $R_{i,\mathrm{crit}}$ the electron localizes at either of the ions with equal probability, C is set[7] to $1/2$ in Eq. (2.84).

For the purpose of this thesis extensions of the COB model [55] are not necessary since only half-collisions are considered, i.e., only the outgoing ionic fragments are observed (cf. Sect. 6.2.7).

In Fig. 2.11 the COB model is illustrated for a I^{1+} and a I^{4+} ion moving apart for various R. The effective charge p_i^* seen by electron i is assumed such that each tighter bound electron screens the nuclear charge by one. Thus, the least bound electron $i = 2$ in I^{1+} is attracted by the nucleus via the potential $-2/r$. The ionization potential of I^{1+} is taken from Table 6.2.

References

1. U. Amaldi, G. Kraft, Radiotherapy with beams of carbon ions. Rep. Prog. Phys. **68**(8), 1861 (2005)
2. V. Averbukh, L.S. Cederbaum, Calculation of interatomic decay widths of vacancy states delocalized due to inversion symmetry. J. Chem. Phys. **125**, 094107 (2006)
3. V. Averbukh et al., Interatomic electronic decay processes in singly and multiply ionized clusters. J. Electron Spectrosc. Relat. Phenom. **183**, 36 (2011)
4. L.V. Azároff (ed.), *X-ray Spectroscopy*, International Series in Pure and Applied Physics (MacGraw-Hill, New York, 1974), p. 560
5. A.P.M. Baede, *Charge Transfer between Neutrals at Hyperthermal Energies*, Advances in Chemical Physics (Wiley, Chichester, 2007), pp. 463–535
6. C.W. Bauschlicher, P.R. Taylor, Full CI benchmark calculations for molecular properties. Theoret. Chim. Acta **71**(4), 263–276 (1987)
7. P. Beiersdorfer et al., Laboratory simulation of charge exchange-produced X-ray emission from comets. Science **300**(5625), 1558–1559 (2003)
8. J.D. Bjorken, S.D. Drell, *Relativistic Quantum Mechanics*, in Sect. 7.1 (McGraw-Hill, New York, 1964)
9. I.A. Bocharova et al., Time-resolved Coulomb-explosion imaging of nuclear wavepacket dynamics induced in diatomic molecules by intense few-cycle laser pulses. Phys. Rev. A **83**, 013417 (2011)
10. R. Boge et al., Probing nonadiabatic effects in strong-field tunnel ionization. Phys. Rev. Lett. **111**, 103003 (2013)
11. R. Bonifacio, C. Pellegrini, L. Narducci, Collective instabilities and high-gain regime in a free electron laser. Opt. Commun. **50**(6), 373–378 (1984)

[7] Comparison of measured (0.46 ± 0.05) [22] and calculated 0.452 [5] values of C shows that the assumption of $1/2$ is reasonable.

12. B.H. Boo, N. Saito, Dissociative multiple photoionization of Br_2, IBr, and I_2 in the VUV and X-ray regions: a comparative study of the inner-shell processes involving Br(3d,3p,3s) and I(4d,4p,4s,3d,3p). J. Electron Spectrosc. Relat. Phenom. **127**(3), 139–152 (2002)
13. M. Born, R. Oppenheimer, Zur Quantentheorie der Molekeln. Ann. Phys. **389**(20), 457–484 (1927)
14. J.D. Bozek, AMO instrumentation for the LCLS X-ray FEL. Eur. Phys. J. Spec. Top. **169**(1), 129–132 (2009)
15. C. Brechignac, J.P. Connerade, Giant resonances in free atoms and in clusters. J. Phys. B: At. Mol. Opt. Phys. **27**(17), 3795 (1994)
16. L.S. Cederbaum, J. Zobeley, F. Tarantelli, Giant intermolecular decay and fragmentation of clusters. Phys. Rev. Lett. **79**, 4778 (1997)
17. L.S. Cederbaum, *Green's Functions and Propagators for Chemistry*, Encyclopedia of Computational Chemistry (Wiley, Chichester, 2002)
18. J.P. Connerade, The non-Rydberg spectroscopy of atoms. Contemp. Phys. **19**(5), 415–447 (1978)
19. W. Demtröder, *Molekülphysik, theoretische Grundlagen und experimentelle Methoden*, 2 überarb. und erw. Aufl. (Oldenbourg, München, 2013), p. 487
20. Z. Deng et al., Beyond the bragg peak: hyperthermal heavy ion damage to DNA components. Phys. Rev. Lett. **95**, 153201 (2005)
21. Z. Deng et al., Reactive scattering damage to DNA components by hyperthermal secondary ions. Phys. Rev. Lett. **96**, 243203 (2006)
22. D. Dijkkamp et al., Subshell-selective electron capture in collisions of C^{4+}, N^{5+}, O^{6+} with H, H_2 and He. J. Phys. B: At. Mol. Phys. **18**(24), 4763 (1985)
23. F. Ehlotzky, *Quantenmechanik und Ihre Anwendungen* (Springer London, Limited, Heidelberg, 2005)
24. T. Ergler et al., Quantum-phase resolved mapping of ground-state vibrational D_2 wave packets via selective depletion in intense laser pulses. Phys. Rev. Lett. **97**, 103004 (2006)
25. U. Fano, Effects of configuration interaction on intensities and phase shifts. Phys. Rev. **124**, 1866–1878 (1961)
26. B. Fischer et al., Steering the electron in H_2^+ by nuclear wave packet dynamics. Phys. Rev. Lett. **105**, 223001 (2010)
27. T. Förster, Ein Beitrag zur Theorie der Photosynthese. Z. Naturforsch. **2b**, 174–182 (1947)
28. T. Förster, Zwischenmolekulare Energiewanderung und Fluoreszenz. Ann. Phys. **437**(1–2), 55–75 (1948)
29. H. Friedrich, *Theoretical Atomic Physics*, 2nd Rev. and Enl. edn. (Springer, Berlin, 1998), p. 416
30. B.N.G. Giepmans et al., The fluorescent toolbox for assessing protein location and function. Science **312**(5771), 217–224 (2006)
31. D.C. Griffin, D.M. Mitnik, N.R. Badnell, Electron-impact excitation of Ne^+. J. Phys. B: At. Mol. Opt. Phys. **34**(22), 4401 (2001)
32. R.E. Grisenti et al., Determination of the bond length and binding energy of the helium dimer by diffraction from a transmission grating. Phys. Rev. Lett. **85**, 2284–2287 (2000)
33. M. Göppert-Mayer, Über Elementarakte mit zwei Quantensprüngen. Ann. Phys. **401**(3), 273–294 (1931)
34. H. Haken, H.C. Wolf, *Molecular Physics and Elements of Quantum Chemistry. Introduction to Experiments and Theory*, 2nd Engl. edn. (Springer, Berlin, 2004), p. 592
35. D.R. Hartree, The calculation of atomic structures. Rep. Prog. Phys. **11**(1), 113 (1947)
36. M. von Hellermann et al., Investigation of thermal and slowing-down alpha particles on JET using charge-exchange spectroscopy. Plasma Phys. Control. Fusion **33**(14), 1805 (1991)
37. U. Hergenhahn, Interatomic and intermolecular Coulombic decay: the early years. J. Electron Spectrosc. Relat. Phenom. **184**, 78 (2011)
38. I.V. Hertel, C.-P. Schulz, *Atome, Moleküle und optische Physik 1. Atomphysik und Grundlagen der Spektroskopie* (Springer, Berlin, 2008)

39. I.V. Hertel, C.-P. Schulz, *Atome, Moleküle und optische Physik 2. Moleküle und Photonen - Spektroskopie und Streuphysik* (Springer, Berlin, 2010), p. 639
40. T. Jahnke et al., Experimental observation of interatomic Coulombic decay in neon dimers. Phys. Rev. Lett. **93**, 163401 (2004)
41. J.E. Jones, On the determination of molecular fields. II. From the equation of state of a gas. Proc. R. Soc. Lond. Ser. A **106**(738), 463–477 (1924)
42. L. Keldysh, Ionization in the field of a strong electromagnetic wave. Sov. Phys. JETP **20**(5), 1307–1314 (1965)
43. G. Kraft, M. Scholz, U. Bechthold, Tumor therapy and track structure. Radiat. Environ. Biophys. **38**(4), 229–237 (1999)
44. M. Kurka, Zwei-Photonen-Doppelionisation von Helium und D_2-Molekülen am Freie-Elektronen-Laser in Hamburg. Ph.D. thesis, Heidelberg, 2011
45. D.E. Laban et al., Extreme ultraviolet interferometer using high-order harmonic generation from successive sources. Phys. Rev. Lett. **109**, 263902 (2012)
46. I.N. Levine, *Quantum Chemistry*, 7th edn. Pearson Advanced Chemistry Series, Internat. edn. (Pearson, Boston, 2014), p. 700 (erschienen 2013)
47. M. Lewenstein et al., Theory of high-harmonic generation by low-frequency laser fields. Phys. Rev. A **49**, 2117–2132 (1994)
48. H.H. Madden, Chemical information from Auger electron spectroscopy. J. Vac. Sci. Technol. **18**(3), 677–689 (1981)
49. S. Marburger et al., Experimental evidence for interatomic Coulombic decay in Ne clusters. Phys. Rev. Lett. **90**, 203401 (2003)
50. H. Mashiko, A. Suda, K. Midorikawa, Focusing multiple high-order harmonics in the extreme-ultraviolet and soft-X-ray regions by a platinum-coated ellipsoidal mirror. Appl. Opt. **45**(3), 573–577 (2006)
51. L. Meitner, Über die Beta-Strahl-Spektra und ihren Zusammenhang mit der Gamma-Strahlung. Z. Phys. **11**(1), 35–54 (1922)
52. E. Mevel et al., Atoms in strong optical fields: evolution from multiphoton to tunnel ionization. Phys. Rev. Lett. **70**, 406–409 (1993)
53. P.M. Morse, Diatomic molecules according to the wave mechanics. II. Vibrational levels. Phys. Rev. **34**, 57–64 (1929)
54. A. Müller, E. Salzborn, Scaling of cross sections for multiple electron transfer to highly charged ions colliding with atoms and molecules. Phys. Lett. A **62**(6), 391–394 (1977)
55. A. Niehaus, A classical model for multiple-electron capture in slow collisions of highly charged ions with atoms. J. Phys. B: At. Mol. Phys. **19**(18), 2925 (1986)
56. G. Parisi, *Statistical Field Theory*. Frontiers in Physics, vol. 66 (Addison-Wesley, Redwood City, 1988), p. 352
57. P.M. Paul et al., Observation of a train of attosecond pulses from high harmonic generation. Science **292**(5522), 1689–1692 (2001)
58. F. Penning, Über Ionisation durch metastabile Atome. Naturwissenschaften **15**(40), 818–818 (1927)
59. E.A. Power, S. Zienau, Coulomb gauge in non-relativistic quantum electro-dynamics and the shape of spectral lines. Philos. Trans. R. Soc. Lond. A Math. Phys. Sci. **251**(999), 427–454 (1959)
60. U.V. Riss, H.D. Meyer, Calculation of resonance energies and widths using the complex absorbing potential method. J. Phys. B: At. Mol. Opt. Phys. **26**(23), 4503 (1993)
61. B.O. Roos, *The Complete Active Space Self-Consistent Field Method and Its Applications in Electronic Structure Calculations*, Advances in Chemical Physics (Wiley, Chichester, 2007), pp. 399–445
62. H. Ryufuku, K. Sasaki, T. Watanabe, Oscillatory behavior of charge transfer cross sections as a function of the charge of projectiles in low-energy collisions. Phys. Rev. A **21**, 745–750 (1980)
63. R. Santra, L.S. Cederbaum, An efficient combination of computational techniques for investigating electronic resonance states in molecules. J. Chem. Phys. **115**, 6853 (2001)

64. R. Santra, J. Zobeley, L.S. Cederbaum, Electronic decay of valence holes in clusters and condensed matter. Phys. Rev. B **64**, 245104 (2001)
65. R. Santra et al., Interatomic Coulombic decay in van der Waals clusters and impact of nuclear motion. Phys. Rev. Lett. **85**, 4490 (2000)
66. R. Santra, L.S. Cederbaum, Non-Hermitian electronic theory and applications to clusters. Phys. Rep. **368**(1), 1–117 (2002)
67. S. Scheit, L.S. Cederbaum, H.-D. Meyer, Time-dependent interplay between electron emission and fragmentation in the interatomic Coulombic decay. J. Chem. Phys. **118**, 2092 (2003)
68. S. Scheit et al., On the interatomic Coulombic decay in the Ne dimer. J. Chem. Phys. **121**, 8393 (2004)
69. J. Schirmer, L.S. Cederbaum, O. Walter, New approach to the one-particle Green's function for finite Fermi systems. Phys. Rev. A **28**, 1237–1259 (1983)
70. C.D. Sherrill, H.F. Schaefer III, in *The Configuration Interaction Method: Advances in Highly Correlated Approaches*, ed. by M.C.Z. Per-Olov Löwdin, J.R. Sabin, E. Brändas. Advances in Quantum Chemistry, vol. 34 (Academic Press, New York, 1999), pp. 143–269
71. A.J.F. Siegert, On the derivation of the dispersion formula for nuclear reactions. Phys. Rev. **56**, 750–752 (1939)
72. B.M. Smirnov, Ionization in low-energy atomic collisions. Phys. Usp. **24**(4), 251–275 (1981)
73. J. Tremblay et al., Photoelectron spectroscopy of atomic iodine produced by laser photodissociation. Phys. Rev. A **38**, 3804–3807 (1988)
74. Z. Vager, R. Naaman, E.P. Kanter, Coulomb explosion imaging of small molecules. Science **244**(4903), 426–431 (1989)
75. N. Vaval, L.S. Cederbaum, Ab initio lifetimes in the interatomic Coulombic decay of neon clusters computed with propagators. J. Chem. Phys. **126**, 164110 (2007)
76. J. de Vries et al., Charge driven fragmentation of nucleobases. Phys. Rev. Lett. **91**, 053401 (2003)
77. V. Weisskopf, E. Wigner, Berechnung der natürlichen Linienbreite auf Grund der Diracschen Lichttheorie. Z. Phys. **63**(1–2), 54–73 (1930)
78. H. Werner, P.J. Knowles, An efficient internally contracted multiconfiguration-reference configuration interaction method. J. Chem. Phys. **89**(9), 5803–5814 (1988)
79. Wikimedia Commons [GFDL or CC-BY-SA-3.0-2.5-2.0-1.0], Electromagnetic Spectrum (2011)
80. Wikimedia Commons [GFDL or CC-BY-SA-3.0-migrated], EM Spectrum Properties (2007)
81. Wikimedia Commons [Public Domain], Franck-Condon-Prinzip (2007)
82. R.G. Woolley, Molecular quantum electrodynamics. Proc. R. Soc. Lond. A Math. Phys. Sci. **321**(1547), 557–572 (1971)
83. J. Yeh, I. Lindau, Atomic subshell photoionization cross sections and asymmetry parameters: $1 \leq Z \leq 103$. At. Data Nucl. Data Tables **32**(1), 1–155 (1985)
84. A.H. Zewail, Femtochemistry: atomic-scale dynamics of the chemical bond using ultrafast lasers (Nobel lecture). Angew. Chem. Int. Ed. **39**(15), 2586–2631 (2000)
85. K. Zhao et al., Tailoring a 67 attosecond pulse through advantageous phasemismatch. Opt. Lett. **37**(18), 3891–3893 (2012)
86. J. Zobeley, Elektronische Relaxationsprozesse Inner-Valenz-ionisierter Moleküle und Cluster. Ph.D. thesis, Heidelberg, 2005

Chapter 3
Free-Electron Lasers

Free-electron lasers (FELs) are accelerator-based light sources that produce light with laser-like properties. The conventional definition of a laser as *light amplification by stimulated emission of radiation* does not apply to FELs. However, the usual criteria are well met in the light they produce: low divergence, high photon density, spatial and (partially) temporal coherence. While the first FEL in the infrared (IR) regime was already proposed in 1971 [1] and became operational shortly after [2], it took until 2004 to realize its first counterpart in the XUV regime: the free-electron laser in Hamburg (FLASH) [3]. With the start of operation of the Linear Coherent Light Source (LCLS) in 2009 the wavelength regime accessible by FELs has been extended into the hard X-ray region [4].

The question arises why it took so long to realize the first FEL producing XUV or X-ray radiation. As conventional optics do not work beyond UV wavelengths, only FELs from the optical to the THz regime can be operated with classical optical resonators and a different concept had to be developed to access high photon energies. For XUV and X-ray FELs laser saturation must be reached within a single passage through an undulator, which is achievable via the mechanism of microbunching.

This chapter will cover the basics of the operation principle of an FEL, mostly compiled from [5], starting with the radiation produced by an undulator in Sect. 3.1. This is followed by an overview of microbunching and Self-Amplified Spontaneous Emission (SASE) in Sect. 3.2. SASE has direct implications on the light properties such as pulse shape and coherence, which will be discussed in Sect. 3.3. A summary on the available beam parameters at FLASH and an overview of the facility will be given in Sect. 3.4.

3.1 Undulator Radiation

Electrons passing through a structure of magnets with alternating polarity, a so-called undulator, are forced on an oscillatory trajectory due to the Lorentz force. The deflection causes the electrons to emit synchrotron radiation which is characterized

K. Schnorr, *XUV Pump-Probe Experiments on Diatomic Molecules*,
Springer Theses, DOI 10.1007/978-3-319-12139-0_3

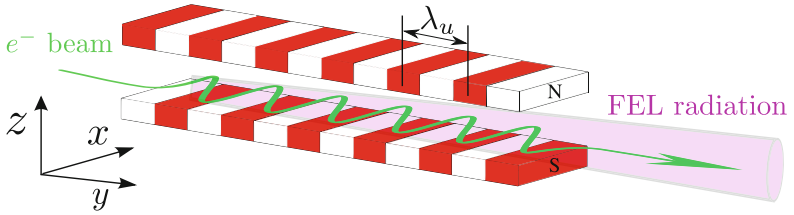

Fig. 3.1 Principle of undulator radiation: a relativistic electron beam is deflected by an alternating magnet structure, the so-called undulator. Thereby the electrons emit radiation of a small spectral range within a narrow cone

by the properties of a relativistic electron beam and the undulator geometry (cf. Fig. 3.1). The period of the magnet arrangement λ_u is reduced to $\lambda_u^* = \lambda_u/\gamma$ in the coordinate system of the moving electron due to the relativistic length contraction, by the Lorentz factor $\gamma = 1/\sqrt{1-\frac{v^2}{c^2}}$. In the moving frame the electrons oscillate with the frequency $\nu^* = c/\lambda_u^* = c\,\gamma/\lambda_u$. For an observer in the laboratory frame looking against the beam the emitted frequency is Doppler shifted to $\nu = \gamma(1+\beta)\nu^*$ with $\beta = v/c$ and thus the measured rest frame wavelength λ is

$$\lambda = \frac{\lambda_u}{\gamma^2}\frac{1}{(1+\beta)} \approx \frac{\lambda_u}{2\gamma^2} \quad \text{with} \quad \beta \approx 1. \tag{3.1}$$

Wavelengths down to the Ångström regime are accessible by accelerating electrons to highly relativistic velocities at typically cm-sized undulator periods. In a more accurate treatment including the oscillatory trajectory of the electrons, Eq. (3.1) is generalized to [5]

$$\lambda = \frac{\lambda_u}{2\gamma^2}\left(1+\frac{K^2}{2}\right) \quad \text{with} \quad K = \frac{eB_0\lambda_u}{2\pi m_e c}. \tag{3.2}$$

The so-called undulator parameter K is determined by the magnetic field in the undulator plane B_0 and the undulator period λ_u. As the latter is usually a fixed parameter, the FEL wavelength is tuned by varying the electron energy or B_0.

Due to the relativistic electron velocities the radiation is emitted in forward direction within a narrow cone around the tangent at the particles' trajectories. The opening angle of the cone is given by $\theta_{\max} \approx K/\gamma$. Only if the directional spread of the emitted photons is smaller than $1/\gamma$, corresponding to $K \leq 1$, contributions from various sections of the trajectory overlap and interfere, and consequently a monochromatic beam is obtained [5, 6].

Now we will discuss under which conditions energy is transferred from the electrons to the light field [5]. The light field, which is in practice a short pulse, is approximated as a plane wave. In the coordinate system used throughout this work, as introduced in Fig. 3.1, the propagation direction of the wave is denoted as y,

the polarization direction as x and the magnetic field of the undulator equals the z-direction. The electron beam co-propagates with the electric field of the wave

$$E_x(y,t) = E_0 \cos(k_l y - \omega_l t + \psi_0) \quad \text{with} \quad k_l = \frac{\omega_l}{c} = \frac{2\pi}{\lambda_l}. \tag{3.3}$$

The time derivative of the electron energy W with transversal velocity v_x is given by

$$\frac{dW}{dt} = v_x(t) F_x(t) = -e v_x(t) E_x(t). \tag{3.4}$$

Only if $^{dW}/_{dt} < 0$ energy is transferred from the electrons to the light field implying that v_x and E_x must be oriented in the same direction, as indicated in Fig. 3.2. This condition will be automatically fulfilled at several points throughout the undulator. However the condition must be maintained during the whole passage through the undulator, because if v_x and E_x would point in opposite directions the light wave would lose the previously gained energy. The electron beam and the light wave move with different velocities due to the detour of the oscillating electrons and the fundamental velocity limitation of a massive particle. The averaged electron velocity in the direction of propagation is given by [5]

$$\bar{v}_y = \left(1 - \frac{1}{2\gamma}\left(1 + \frac{K^2}{2}\right)\right). \tag{3.5}$$

The gain condition is fulfilled by choosing the phase and the wavelength λ_l of the light wave such that it is always half a wavelength ahead of the electron trajectory, as indicated in Fig. 3.2. The difference Δt between the time that the electrons (t_e) and the light wave (t_l) need to overcome half an undulator period is given by

$$\Delta t = t_e - t_l = \left(\frac{1}{v_y} - \frac{1}{c}\right)\frac{\lambda_u}{2} \overset{!}{=} \frac{\lambda_l}{2c}. \tag{3.6}$$

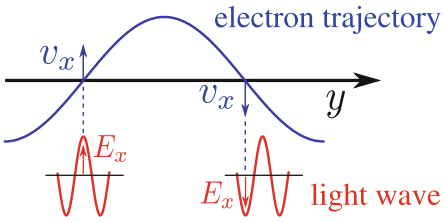

Fig. 3.2 Only if the electric field vector $\boldsymbol{E} = (E_x, 0, 0)$ of the wave points into the same direction as the transversal component of the electron trajectory v_x at all times, continuous energy transfer from the electrons into the light field is guaranteed (Figure adapted from [5])

Inserting the expression for the electron velocity from Eq. (3.5) yields the wavelength that will lead to an amplified light wave:

$$\lambda_l = \frac{\lambda_u}{2\gamma^2}\left(1 + \frac{K^2}{2}\right). \tag{3.7}$$

The obtained expression is equal to that for the undulator radiation in Eq. (3.2). Therefore the light amplification process can start from spontaneously emitted undulator radiation, which builds the foundation of the SASE principle.

3.2 Microbunching and SASE

FELs that operate in the XUV or X-ray regime are so-called high gain FELs because intensity saturation is reached within a single passage through the undulator [7]. This is in contrast to IR and THz FELs, also called low gain FELs, where an optical resonator is combined with an electron storage ring allowing the electron beam to pass through the undulator repeatedly until saturation is reached. As conventional optics are unavailable in the XUV and X-ray regime and optical resonators cannot be realized, the high gain FEL requires a different working principle.

This problem is solved using the formation of so-called microbunches, as illustrated in Fig. 3.3: The electron bunch is split into microbunches with a spacing in the order of one photon wavelength while it passes the undulator [8]. Assuming that Eq. (3.6) is fulfilled, electrons gaining energy from the light wave travel on a sinusoidal trajectory of smaller amplitude than electrons losing energy to the light wave. Therefore the longitudinal velocity is modified such that the electrons are concentrated around the maxima of the energy transfer into (micro)bunches shorter than the optical wavelength. Within one microbunch the electrons oscillate collectively, acting as a single point-like particle of charge Ne. This leads to correlated emission of radiation, which is fully coherent within one microbunch. As the photon intensity grows, the microbunching effect is even enhanced. Only because of this effect the intensity of the high gain FEL scales with the squared number of electrons in each microbunch $I \sim N^2$. This is in contrast to all other undulator based radiation sources, such as synchrotrons, where the electrons emit their radiation independently from each other resulting in an intensity that is proportional to N.

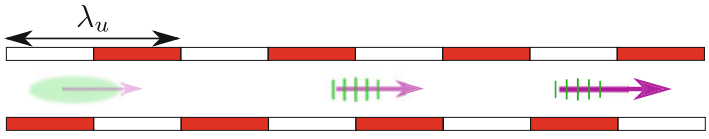

Fig. 3.3 Build-up of electron microbunches. During its passage through the undulator the electron bunch is split up into narrow electron microbunches that radiate coherently (adapted from [8])

High gain FELs owe their name to the exponential amplification of the radiation while the electrons pass through the undulator [4]:

$$I = I_0 \mathrm{e}^{\frac{x}{L_g}}, \tag{3.8}$$

with x being the transversal undulator coordinate and L_g the gain length. However, the amplification stops once the saturation length is reached, then the microbunches start to collapse and the intensity decreases. Thus it is crucial to choose the correct undulator length of a high gain FEL.

The microbunching process can be initiated in different ways: If the process is triggered by an external laser one speaks of seeding, if it starts from spontaneous emission of undulator radiation it is called *self-amplified spontaneous emission* (SASE) [7]. SASE has the great advantage that it allows the operation of an FEL over a wide range of wavelengths without requiring an external source. Although SASE was already suggested theoretically in the 1980s [7, 9], it took roughly 20 years to realize it experimentally for the first time in the IR regime [10]. The SASE process is interpreted in different ways: In an intuitive picture spontaneously emitted undulator radiation is amplified in the first section of the undulator and then provides the seeding beam for the microbunching process in the rest of the undulator. The second interpretation is a start from a periodic charge density modulation in the electron beam, which is imprinted in the beam because only one component of the electrons' white shot noise is amplified [5].

Both start-up interpretations show the stochastic nature of the process, which leads to spectrally broad and noisy pulses with poor temporal coherence [11]. This is avoided by using a seeding laser with well defined spectral properties. Seeding in the XUV regime was already demonstrated with a high harmonic source at FLASH [12] and frequency doubled optical lasers at FERMI@Elettra [13]. Recently self-seeding in the X-ray regime was accomplished at LCLS [14].

Here, only a short quantitative description of the FEL theory was given, for further reading on an introductory level see [5, 15], while a thorough mathematical treatment is given in [16]. A recent review about high gain FELs and the status of available facilities can be found in [17].

3.3 Pulse Characterization

As SASE is a stochastic process, strongly fluctuating pulses with broad and noisy spectra are produced [11]. Each individual pulse consists of spikes on top of a noisy background, as illustrated in Fig. 3.4. However, the knowledge of the pulse length is crucial for pump-probe measurements in order to determine the limits of temporal resolution. Furthermore the pulse shape influences the experimental results, in particular those for non-linear processes, such as multi-photon absorption [18]. Therefore it is important to characterize the FEL pulse properties in order to arrive at a correct interpretation of the experimental data.

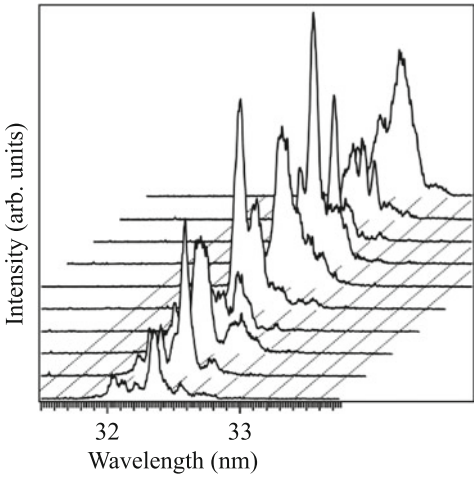

Fig. 3.4 Ten exemplary FEL pulses with wavelengths centered around 32.2 nm with an averaged width of 0.4 nm. Figure adapted from [20]

Determining the relevant pulse parameters is a demanding task in the XUV regime at femtosecond time resolution. Suitable tools are under development, but not yet routinely available at FELs. Therefore we apply intensity autocorrelation, a well known technique for optical wavelengths, in order to determine the pulse length and thereby get additional insight into the internal pulse structure [19]. The general idea is to split the beam into two identical parts that are delayed with respect to each other and send them onto a target generating a non-linear signal, which is then monitored as a function of the delay.

We implement this scheme by splitting the FEL beam geometrically into two halves with the split mirror described in Sect. 4.3.3, which at the same time introduces a delay between the pulses and focuses them into a dilute gas target, discussed in Sect. 4.1.1. The ionization yield of the atoms or molecules in the gas target depends on the intensity like $N \sim I_0^n$ (cf. Sect. 2.1) and thus serves as the nth order non-linear signal. The expected autocorrelation signal $A^{(n)}$ for pulses exhibiting a time delay of τ reads

$$A^{(n)}(\tau) = \int_{-\infty}^{\infty} dt \left| (E(t) + E(t-\tau))^n \right|^2 . \tag{3.9}$$

The time-dependent electric fields of the delayed and the non-delayed pulse are denoted by $E(t-\tau)$ and $E(t)$ respectively. For short wavelengths the uncertainty in τ is mostly larger than the optical period permitting to resolve the oscillations of the electric field. Therefore we average $A^{(n)}$ over one optical cycle to obtain an nth order intensity autocorrelation signal [21]

$$\bar{A}^{(n)}(\tau) = \sum_{i=1}^{n-1} \binom{n}{i} \int_{-\infty}^{\infty} dt\, I(t)^i\, I(t-\tau)^{n-i}. \tag{3.10}$$

The measured spectra can also be simulated via the so-called partial coherence model (PCM), in which statistically fluctuating, partially coherent single FEL pulses are generated and the autocorrelation function is evaluated [22]. By comparing the recorded data with the outcome of the simulation we conclude on the pulse parameters.

Figure 3.5 shows the Ar^{3+} ion yield recorded at a photon energy of 28 eV for two different accelerator settings. The goal of both settings was to generate as short pulses as possible. The data are overlayed with a second order autocorrelation function generated by the PCM (green dashed line) as the ionization step $Ar^{2+} \rightarrow Ar^{3+}$ requires direct two-photon absorption. In addition, Ar^{3+} might be produced via three-photon absorption from the neutral atom, thus the third order PCM autocorrelation function is also shown in Fig. 3.5 (blue dotted line). The PCM simulations use an average pulse length of 28.2 fs (FWHM) for the first FLASH setting and 42.5 fs (FWHM) for the second, utilizing a spectral width of 0.33 eV (FWHM), which matches the width of a photon spectrum obtained by averaging many FLASH pulses directly before recording the autocorrelation traces. Both spectra in Fig. 3.5 show two clear features: A sharp spike sitting on a broader pedestal. The broad structure is related to the averaged pulse duration. It is a factor $\sqrt{2}$ broader than the pulse duration for the second and a factor $\sqrt{1.5}$ broader for the third order autocorrelation trace. The sharp peak stems from interference of the spikes within the FEL pulse and corresponds to the temporal coherence length of the FEL pulse [22]. This length

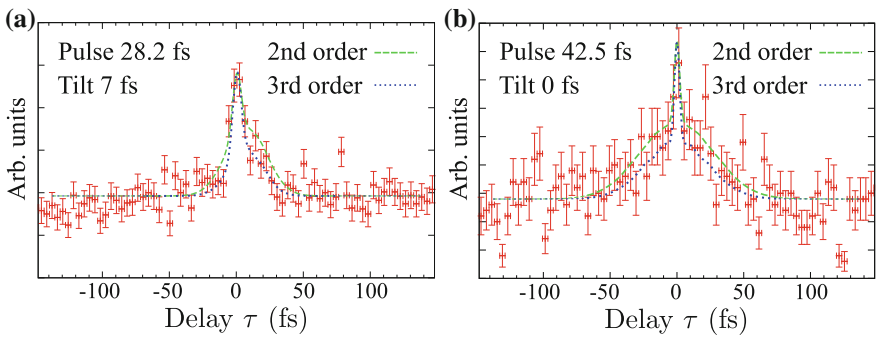

Fig. 3.5 Yield of Ar^{3+} ions recorded as a function of the time delay τ for a wavelength of 28 eV and two different FLASH settings. The experimental data are shown in *red* with error bars. The *dashed green lines* indicate the second order autocorrelation function while *blue dotted lines* stand for the third order autocorrelation function. Both are generated with the PCM with a pulse duration for (**a**) of 28.2 fs (FWHM) and (**b**) of 42.5 fs (FWHM) with a spectral width of 0.33 eV (FWHM) [23]. The asymmetry in (**a**) with respect to the *sharp coherence peak*, is due to a wave front tilt resulting in an additional time delay of 7 fs

was already determined in earlier experiments to be around 7 fs [24, 25] which is in good agreement with the results of the method presented here [26]. The open question remains why the broad feature in Fig. 3.5a shows an asymmetry with respect to the coherence spike. This is explained by a tilted wave front of the FEL pulse which causes an additional time delay, here 7 fs, of the pulses and results in an asymmetry [19].

It is well known that the pump-probe time resolution is limited by the pulse duration. However due to the intrinsic spiky structure of the FEL pulses the resolution is no more limited to the overall pulse duration but to the spikes' widths. Therefore processes occurring on shorter time scales than the overall pulse length may still be resolvable [27, 28].

3.4 FLASH

Originally, FLASH's accelerator section was planned as a test facility to demonstrate the feasibility of superconducting cavities for a compact linear electron-positron collider for particle physics. Only three years after proposing the TESLA (Teraelectronvolt Energy Superconducting Linear Accelerator) Test Facility (TTF), in 1994, first plans of extending it to a light source were put forward. Today, the free-electron laser in Hamburg (FLASH) is a user facility delivering pulses of tens of fs in the XUV range at intensities up to $10^{16}\ \frac{\mathrm{W}}{\mathrm{cm}^2}$ [29].

In this section the essential components needed to realize an FEL will be explained: an electron gun, a linear accelerator and an undulator. All components and their requirements will be introduced by the example of the FLASH facility and the possible operation parameters will be presented. Information, given here, are mainly compiled from [29, 30].

An overview of the FLASH facility, which has a total length of 315 m, is given in Fig. 3.6. The requirements on the electron beam quality to produce radiation through SASE are very demanding: Short, high-density electron bunches with a low energy spread and a narrow beam diameter are needed. So far, this is only possible with linear

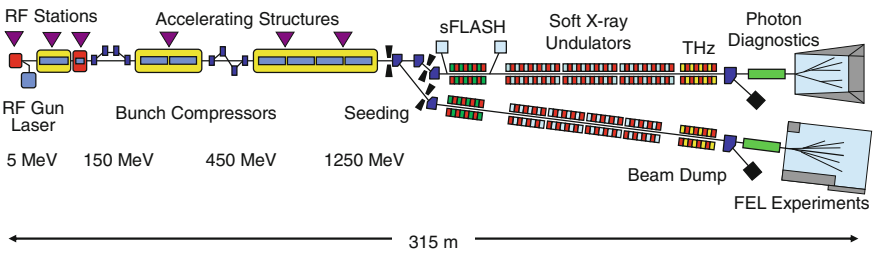

Fig. 3.6 Layout of the FLASH facility with the extension FLASH II (*lower branch*) which is under construction at the moment (taken from [30])

Table 3.1 FLASH parameters (taken from [30])

Parameter	Value
Wavelength range	4.2–45 nm
Average single pulse energy	10–500 μJ
Pulse duration (FWHM)	<50–200 fs
Spectral width (FWHM)	0.7–2 %
Photons per pulse	10^{11}–10^{13}

accelerators. Since FLASH has superconducting accelerator cavities, thousands of electron bunches can be accelerated within a second. The duty cycle is organized in such a way that the main repetition rate is 10 Hz with a train of 1–400 minibunches[1] arriving each 10 Hz. The length of each minibunch train is limited to a maximum of 800 μs which imposes the maximum time difference between two minibunches. A list of FLASH parameters can be found in Table 3.1.

The electron source needs to emit short pulses with large currents of 20 pC to 1 nC at a high repetition rate. The electron bunches are produced by bombarding a Cs_2Te photocathode with 262 nm laser pulses of 4.6 ± 0.1 ps (corresponding to 2 mm long electron bunches) and accelerating them with a high gradient radio frequency (normal conducting) cavity [31]. Afterwards the electron beam is further accelerated and compressed in the seven TESLA modules, each containing eight superconducting niobium cavities and cooled to 2 K. Further compression of the bunches is achieved by sending the beam through magnetic chicanes. The total length of the linear accelerator section, which delivers the beam to the undulator, is 120 m.

As intensity saturation must be achieved within a single passage for a high gain FEL, rather long undulators are needed. At FLASH six undulator modules, each with a length of 4.5 m, are installed. At a fixed undulator gap of 12 mm a peak magnetic field of 0.48 T is reached using permanent NdFeB magnets. With an undulator period $\lambda_u = 27.3$ mm, an undulator parameter $K = 1.23$ and the available electron beam energies between 0.37 and 1.25 GeV, wavelengths ranging from 120 mm to 4 nm can be produced. The electron beam is dumped after it has passed the undulator. The FEL radiation is transported through a photon diagnostic section into the experimental hall where it is distributed to one of five different experimental stations [32]. In the photon diagnostic section the FEL beam properties, such as intensity, shape and position are characterized. The absolute position of the beam is monitored at various places on Ce:YAG crystals by means of cameras while the photon number is determined via two gas monitor detectors [32]. The beam size is adjustable with the help of apertures behind the undulator and the beam position is steered by motorized mirrors. More information about FLASH can be found in [29, 30, 32].

[1] Please note that minibunches are not related to microbunches.

References

1. J.M.J. Madey, Stimulated emission of bremsstrahlung in a periodic magnetic field. J. Appl. Phys. **42**(5), 1906–1913 (1971)
2. D.A.G. Deacon et al., First operation of a free-electron laser. Phys. Rev. Lett. **38**, 892–894 (1977)
3. V. Ayvazyan et al., First operation of a free-electron laser. Eur. Phys. J. D At. Mol. Opt. Plasma Phys. **37**(2), 297–303 (2006)
4. P. Emma et al., First lasing and operation of an angstrom-wavelength free-electron laser. Nat. Photonics **4**(9), 641–647 (2010)
5. P. Schmüser, M. Dohlus, J. Rossbach, *Ultraviolet and Soft X-ray Free-electron Lasers. Introduction to Physical Principles, Experimental Results, Technological Challenges*, Springer Tracts in Modern Physics (Springer, Berlin, 2008)
6. J.D. Jackson, *Classical Electrodynamics*, 3rd edn. (Wiley, New York, 1999)
7. R. Bonifacio, C. Pellegrini, L. Narducci, Collective instabilities and high-gain regime in a free electron laser. Opt. Commun. **50**(6), 373–378 (1984)
8. G. Margaritondo, P. Rebernik Ribic, A simplified description of X-ray freeelectron lasers. J. Synchrotron Radiat. **18**(2), 101–108 (2011)
9. K.-J. Kim, Three-dimensional analysis of coherent amplification and self-amplified spontaneous emission in free-electron lasers. Phys. Rev. Lett. **57**, 1871–1874 (1986)
10. M.J. Hogan et al., Measurements of gain larger than 10^5 at $12\,\mu$m in a self-amplified spontaneous-emission free-electron laser. Phys. Rev. Lett. **81**, 4867–4870 (1998)
11. W. Ackermann et al., Operation of a free-electron laser from the extreme ultraviolet to the water window. Nat. Photonics **1**(6), 336–342 (2007)
12. sFLASH, First results of direct seeding at Flash (2010)
13. E. Allaria et al., Highly coherent and stable pulses from the FERMI seeded free-electron laser in the extreme ultraviolet. Nat. Photonics **6**(10), 699–704 (2012)
14. J. Amann et al., Demonstration of self-seeding in a hard-X-ray free-electron laser. Nat. Photonics **6**(10), 693–698 (2012)
15. C.A. Brau, *Free-Electron Lasers*. Advances in Electronics and Electron Physics: Supplement 22 (Academic Press, Boston, 1990), p. 420
16. E.L. Saldin, E.A. Schneidmiller, M.V. Jurkov, *The Physics of Free Electron Lasers*, Advanced Texts in Physics (Springer, Berlin, 2000)
17. B.W.J. McNeil, N.R. Thompson, X-ray free-electron lasers. Nat. Photonics **4**(12), 814–821 (2010)
18. N. Rohringer, R. Santra, X-ray nonlinear optical processes using a selfamplified spontaneous emission free-electron laser. Phys. Rev. A **76**, 033416 (2007)
19. R. Moshammer et al., Second-order autocorrelation of XUV FEL pulses via time resolved two-photon single ionization of He. Opt. Express **19**(22), 21698–21706 (2011)
20. S. Düsterer et al., Spectroscopic characterization of vacuum ultraviolet free electron laser pulses. Opt. Lett. **31**(11), 1750–1752 (2006)
21. A. Senftleben et al., Characterization of extreme ultra-violet free-electron laser pulses by autocorrelation, in *Multiphoton Processes and Attosecond Physics*, ed. by K. Yamanouchi, K. Midorikawa (Springer, Heidelberg, 2012), p. 61
22. T. Pfeifer et al., Partial-coherence method to model experimental free-electron laser pulse statistics. Opt. Lett. **35**(20), 3441–3443 (2010)
23. A. Senftleben, Private Communication
24. R. Mitzner et al., Direct autocorrelation of soft-x-ray free-electron-laser pulses by time-resolved two-photon double ionization of He. Phys. Rev. A **80**, 025402 (2009)
25. F. Sorgenfrei et al., The extreme ultraviolet split and femtosecond delay unit at the plane grating monochromator beamline PG2 at FLASH. Rev. Sci. Instrum. **81**(4), 043107 (2010)
26. Y.H. Jiang et al., Temporal coherence effects in multiple ionization of N_2 via XUV pump-probe autocorrelation. Phys. Rev. A **82**, 041403 (2010)

27. Y.H. Jiang et al., Investigating two-photon double ionization of D_2 by XUV pump-XUV-probe experiments. Phys. Rev. A **81**, 051402 (2010)
28. K. Meyer et al., Noisy optical pulses enhance the temporal resolution of pump-probe spectroscopy. Phys. Rev. Lett. **108**, 098302 (2012)
29. J. Feldhaus, FLASH-the first soft x-ray free electron laser (FEL) user facility. J. Phys. B At. Mol. Opt. Phys. **43**(19), 194002 (2010)
30. DESY: FLASH. http://flash.desy.de/. Accessed Sept 2013
31. F. Stephan et al., Detailed characterization of electron sources yielding first demonstration of European X-ray free-electron laser beam quality. Phys. Rev. ST Accel. Beams **13**, 020704 (2010)
32. K. Tiedtke et al., The soft X-ray free-electron laser FLASH at DESY: beamlines, diagnostics and end-stations. New J. Phys. **11**(2), 023029 (2009)

Chapter 4
Experimental Setup

The purpose of this thesis is to gain insight into the dynamics of small molecules upon impact of intense femtosecond XUV pulses. In order to do so recoil ion momentum spectroscopy is applied. It relies on the coincident detection of all ions and thus enables the reconstruction of the interaction process by calculating the particles' initial momenta. Therefore, the detection setup must be capable of preparing a well defined initial target state and detecting the final state of the molecule after the interaction. These requirements are fulfilled by a reaction microscope (REMI) equipped with a supersonic gas jet. In order to gain temporal resolution of molecular processes we apply pump-probe spectroscopy, experimentally realized by a delay stage. The REMI for FLASH is not permanently installed in Hamburg and is thus modified in order to meet the optimal conditions for each experiment.

The key components of the REMI will be discussed in Sect. 4.1 and specialties for the I_2 and the Ne_2 experiments will be presented in Sects. 4.2 and 4.3, respectively.

4.1 Reaction Microscope (REMI)

Originally designed for ion-atom collisions [26], the reaction microscope (REMI) has become a versatile tool for kinematically complete studies of atomic and molecular processes [34]. It relies on the coincident detection of all produced charged particles. The target, in our case a supersonic gas jet, is bombarded with a projectile, such as ions, electrons or photons, and the charged fragments created upon the collision are guided onto time- and position-sensitive detectors by an electric field, as illustrated in Fig. 4.1. For the light electrons an additional magnetic field is needed to ensure 4π solid angle acceptance. From the impact time and position on the detectors the three-dimensional momentum vectors of all charged particles are calculated. By momentum- and energy-conservation each interaction process is reconstructed. Since electron spectra have not been recorded in the experiments discussed here, the following considerations will focus on the coincident detection of ions. A brief discussion of the difficulties of electron detection is given in Sect. 4.4.

K. Schnorr, *XUV Pump-Probe Experiments on Diatomic Molecules*,
Springer Theses, DOI 10.1007/978-3-319-12139-0_4

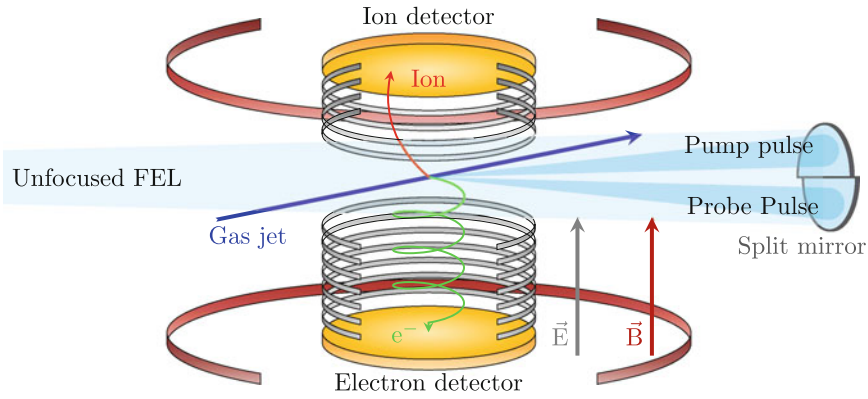

Fig. 4.1 REMI setup used for the FLASH experiments in combination with our split-and-delay mirror described in Sect. 4.3.3

4.1.1 Supersonic Gas Jet

The momenta transferred to atoms and molecules via photoionization vary over several orders of magnitude from below 1 au up to hundreds of au. In order to resolve even small transfers, the uncertainty of the initial target momentum must be well below the momentum gain in the ionization process. At room temperature, the momentum spread of the target, caused by thermal motion, is already larger than 10 au for heavier target species. For neon dimers another important aspect comes into play: The binding energy of a neon dimer in its vibrational ground state is only 3 MeV. For comparison, the internal energy $E_{\text{therm}} = \frac{3}{2} k_B T_0$ of a single atom at room temperature $T_0 = 300\,\text{K}$ is already 39 MeV. Thus, in order to create neon dimers, a jet temperature below their binding energy is crucial, which requires an internally cool gas target ($<$24 K). A broad overview about atomic and molecular beam sources can be found in [30], where the content of this chapter is mostly compiled from.

4.1.1.1 Theoretical Description

The aforementioned requirements are fulfilled by a supersonic gas jet, where a gas is expanded through a narrow nozzle from a reservoir with high pressure P_0 into a region of lower pressure P_f. The underlying working principle is conversion of undirected thermal energy of a gas into a directional kinetic energy in form of a jet. Heat dissipation during the expansion can be neglected for short nozzles, thus the process is considered adiabatically. Under the assumption that the whole enthalpy, which consists of the internal energy E_{therm} and the compression energy $k_B T_0$, is converted into directed motion, the jet velocity v_{jet} is estimated via [24]:

$$\frac{1}{2}mv_{\text{jet}}^2 = \frac{f}{2}k_B T_0 + k_B T_0 \quad \rightarrow \quad v_{\text{jet}} = \sqrt{\frac{2k_B T_0}{m}\left(1 + \frac{f}{2}\right)}, \tag{4.1}$$

with f being the degrees of freedom. In this idealized case the temperature of the jet after expansion is 0 K, which is in practice not possible. Typical gas jet temperatures range from tens of millikelvin to a few kelvin. Even colder targets are producible by laser cooling in magneto-optical traps [17] and dipole traps [11, 16].

In order to characterize a jet the speed ratio S_∞ is introduced: It is defined as the ratio of the longitudinal jet velocity and the thermal velocity of the molecules v_{therm} in the rest frame of the jet:

$$S_\infty = \frac{v_{\text{jet}}}{v_{\text{therm}}}. \tag{4.2}$$

In terms of experimentally accessible parameters the speed ratio is expressed as [24]

$$S_\infty = A\left[\sqrt{2}\frac{P_0 d}{k_B T_0}\left(\frac{53C_6}{k_B T_0}\right)^{1/3}\right]^B, \tag{4.3}$$

where A, B and C_6 are empirical constants, d is the nozzle diameter, P_0 the initial pressure and T_0 the initial temperature. The crucial experimental parameter is the final[1] temperature T_∞ of the jet, which is related to S_∞ and T_0 by

$$T_\infty = T_0 \frac{\gamma}{\gamma - 1}\frac{1}{S_\infty^2}. \tag{4.4}$$

The parameter $\gamma = \frac{C_P}{C_V} = 1 + \frac{2}{f}$ is the heat capacity ratio built from the heat capacity at constant pressure C_P and the heat capacity at constant volume C_V. For an ideal gas of diatomic molecules with $f = 5$ (3 translational and 2 rotational degrees of freedom, vibrational motion is negligible for gas jet temperatures) the heat capacity ratio yields $\gamma = 1.4$.

The temperatures of the jet in longitudinal direction T_∞ and transversal direction T_{rad} are different, but T_∞ imposes an upper limit on the temperature, as it is always larger than T_{rad}.

4.1.1.2 Principle of Operation

The velocity of the molecules is characterized by the Mach number $M_a = v/a$, with v being the particle velocity and a being the speed of sound in the present medium. The pressure difference between P_0 and P_f causes acceleration of the gas towards the low pressure region. Due to the acceleration, the Mach number grows from $M_a \ll 1$ to $M_a > 1$. Upon leaving the nozzle v exceeds the speed of sound explaining the name supersonic gas jet.

[1] The subscript ∞ indicates far away from the expansion region.

In an ideal supersonic expansion, the particles move without interacting with neighboring particles in the region behind the nozzle, the so-called zone of silence. However, this is only true for perfect vacuum conditions, which is not fulfilled in the experiment. The experimentally achievable zone of silence is restricted to a small region behind the nozzle and breaks down beyond. Therefore the beam forming the target must be cut out of the zone of silence before the break down.

In our setup, the nozzle is realized by a thin platinum plate with a 30 µm diameter hole, which is mounted on a steel pipe. It is adjustable in the three spatial dimensions via an x-y-z-manipulator. An overview of the setup is given in Fig. 4.2. The high pressure side of the nozzle is usually connected to a gas bottle, with a pressure typically ranging from 1 to 25 bar. The first jet stage behind the nozzle has the highest gas load in the entire vacuum system. It is evacuated via a 350 $\frac{\mathrm{L}}{\mathrm{s}}$ pump and typical pressures of 10^{-3}–10^{-4}mbar are reached, depending on the injection pressure and the target species. A part of the expansion cone that builds up behind the nozzle is cut out by a conical skimmer producing a molecular beam. Varying the distance between the nozzle and the skimmer allows to adjust the density of the gas target, as the particle density decreases quickly with increasing distance. A second skimmer is mounted behind the first one, to cut out those particles with larger transversal momentum in order to reduce the transverseal temperature of the gas jet. After the second skimmer the beam passes four additional differential pumping stages, each of them separated by a 2 mm diameter aperture.

The skimmers and apertures reduce the expansion pressure of several bars by 14 orders of magnitude. This way, the base pressure in the interaction chamber of roughly 10^{-11}mbar is achieved. Due to the large number of differential pumping stages a comparably small target density of 10^{9}–10^{10}particles/cm^3 is reached. If all apertures and skimmers are centered perfectly with respect to the nozzle, the gas jet diameter in the interaction region is roughly 1.2 mm. Optionally, the dimensions of the beam can be cut by three pairs of slits, mounted in the jet stages 4, 5, and 6. Two

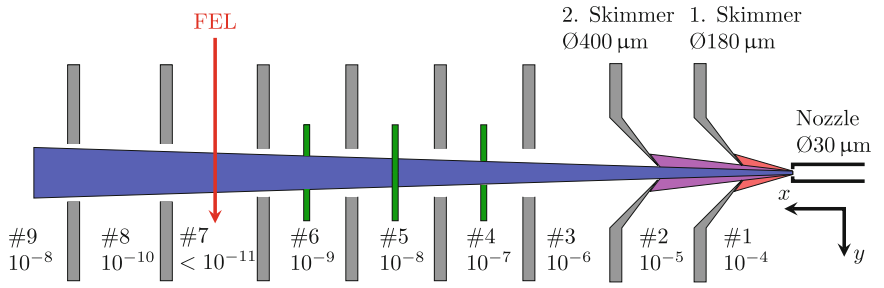

Fig. 4.2 Setup of the supersonic gas jet. Gas expansion from a high to a low pressure region through a 30 µm diameter nozzle. The first skimmer peels a beam out of the expansion cone and the second skimmer cuts off atoms with large transversal momentum to reduce the temperature in that direction. Three pairs of slits (*green*) are mounted perpendicular to the jet propagation direction in order to adjust the dimensions of the jet. The number of the jet stage and the respective pressure in mbar is given in the *lower part* of the figure

of them allow cuts in the propagation direction of the FEL beam, while the third pair allows cuts perpendicular to that. After passing the interaction point the molecular beam is dumped into a turbomolecular pump via two further differential pumping stages. The latter are needed to avoid backscattering of gas particles into the main chamber.

4.1.2 Spectrometer

Figure 4.3 shows the spectrometer used in our REMI. The homogeneous electric field of the spectrometer accelerates the ions and electrons towards opposite directions onto the corresponding detectors. This is realized by an array of 22 ring-like steel plates with equidistant spacing. As voltage is only applied on the upper most and lowest spectrometer ring, two neighboring rings are connected via 100 kΩ resistors creating a constant voltage gradient along the whole spectrometer. An exception

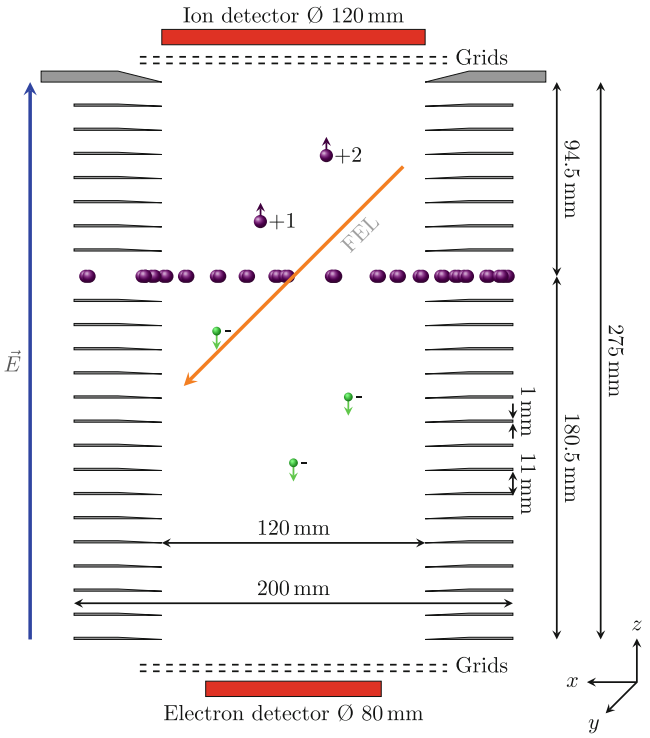

Fig. 4.3 Setup of the spectrometer. Ions, created in the interaction point of the FEL and the gas target, are accelerated onto a 120 mm time- and position-sensitive detector on the *top* and electrons to the *bottom*

are the innermost plates above and below the reaction point, which are separated by the doubled spacing and two resistors. This allows the unfocussed FEL beam to pass through without scattering. In addition the plates are sloped towards the center in order to create well defined equipotential planes resulting in a higher degree of electric field homogeneity.

The electric field is oriented such that ions are guided to the top, while electrons are accelerated to the bottom detector. The spectrometer has a total length of 275 mm, with the electron arm being roughly a factor of two longer than that for the ions. A long electron arm is favorable in order to stretch the time interval at which the fast electrons arrive at the detector. In contrast, for the presented experiments a short ion arm is necessary, because fragments with large transversal momentum are created in Coulomb explosions due to the produced high charge states. Thus, in order to prevent ions from flying off the detector, a moderate acceleration distance in combination with relatively high acceleration voltages is used. It is crucial for a coincidence experiment that full 4π acceptance for the ions is guaranteed. Typical electric fields for the presented measurements lie between 35 and 70 $\frac{\mathrm{V}}{\mathrm{m}}$.

The spectrometer is closed by high transmission gratings on the top and the bottom. This extends the homogeneous electric field until the very end of the spectrometer. Additionally, the gratings avoid field distortion originating from the high voltages applied to the detectors. On both sides, additional gratings are mounted and put to high voltage, in order to post-accelerate the ions and electrons towards the detector, as will be discussed in Sect. 4.1.3.1.

In a traditional REMI spectrometer setup an additional field free drift region with length d_d is added after the acceleration distance d_a. For a ratio of $d_a/d_d = 2$, the so-called time-focusing condition [34] is fulfilled, which compensates an uncertainty in the ions' time-of-flight caused by the finite dimension of the interaction region and the projectile beam. Our spectrometer is designed without a drift region, as the FEL is focused down to a diameter of approximately 20 µm. This is in the order of the detector resolution limit and thus the compensating effect of the drift region is not needed.

At this point a short remark on the coordinate system used throughout this work should be made. As shown in Fig. 4.3, the spectrometer axis, which defines the direction of ion acceleration, will be denoted as z-axis. The FEL beam and the gas jet are oriented perpendicular to the spectrometer axis and perpendicular to each other. The propagation direction of the gas jet defines the x-axis and the FEL beam propagates along the y-axis with its polarization in x-direction.

4.1.3 Detectors

Coincidence measurements, such as the ones performed with a REMI, rely crucially on the detection of all particles. Therefore, the main requirements on the detectors are high efficiency, multi-hit capability, i.e., short dead times, and good temporal and spatial resolution. In our setup, this is achieved by a stacked detector consisting of

a time-sensitive microchannel plate, which is presented in Sect. 4.1.3.1, mounted in front of a position-sensitive delayline anode, as described in Sect. 4.1.3.2.

4.1.3.1 Microchannel Plate

The detection of a single particle is difficult as it induces only a small signal, which then must be amplified. This is done with a microchannel plate (MCP), which provides the additional information at which time the charged particle has impacted on the detector, the so-called time-of-flight (TOF). In principle an MCP is a large array of micrometer-sized individually-working electron multipliers, embedded in a 1 mm thick plate [14]. The upper and lower surface of the MCP are metal-coated, while the plate itself is made of an insulator such as glass. This allows to create a strong electric field between the top and the bottom by applying a voltage of typically 1 kV. The surface inside of the capillaries is coated with a semiconductor, e.g., gallium phosphide (GaP) or gallium arsenide phosphide (GaAsP), that has a low electron work function upon bombardment with charged particles and photons (beyond the UV range). Thus, when a charged particle impinges on the surface inside a capillary, electrons are released and get accelerated through the channel. Thereby they gain enough energy to eject secondary electrons by hitting the wall repeatedly. This way an electron avalanche is formed along the channel, which amplifies the original signal by roughly a factor of 10^4, as shown in Fig. 4.4. By tilting all channels—which are aligned in parallel—by typically 8° towards the surface normal, hitting the a wall surface is almost unavoidable.

The signal is further amplified by stacking a second MCP on top of the first one. This enhances the gain to 10^5–10^6. For a stack of three plates a gain of more

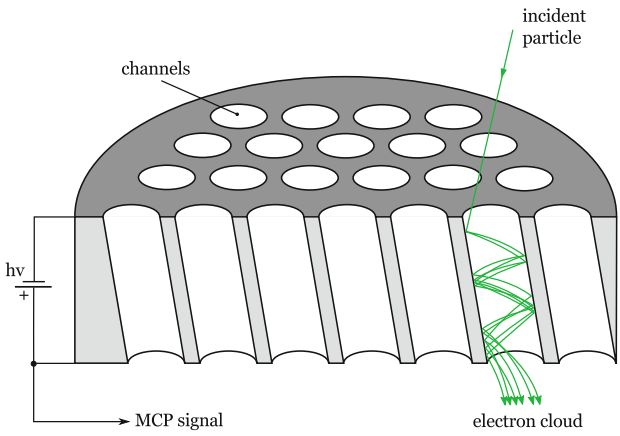

Fig. 4.4 Operation principle of a microchannel plate (MCP). Particles impinging on the surface inside the channels release secondary electrons. The resulting avalanche leaves the channel as an electron cloud. Figure taken from [27]

than 10^7 is reachable. The orientation of the plates is chosen such, that the channels form a V-shape (or N-shape for three plates), known as the *chevron* geometry. This arrangement increases the gain, since no electron can fly through the channels without hitting a wall. At the same time it reduces the feedback from background ions created by electron impact ionization inside the channels. If these ions would escape the channel, they would be accelerated away from the detector towards the spectrometer and cause background counts in the ion detector. By orienting the MCPs in chevron geometry they will be mostly dumped on a channel wall, instead.

The probability that an ion gets detected is dependent on how likely it ends up in a channel and how efficient it creates electrons therein. The former factor is determined by the geometry of the plate, meaning how much area consists of holes (active area). We use MCPs with a diameter of 120 mm, a channel diameter of 25 µm and a center-to-center spacing of 32 µm. This results in a typical active area of 60 % [2]. The probability to create electrons upon ion impact is highly dependent on the energy and the type of impinging particle: The detection of ions works best for high particle energies, e.g., in the keV range. These energies are by far not reached during the interaction of the FEL with the molecules, thus the created ions are post-acceleration behind the spectrometer before hitting the detector. This is done by the second grating, mounted just in front of the MCP, which is supplied with a voltage of 1 kV (cf. Fig. 4.3). In principle the efficiency is different for each charge state and for every ion species [14]. To give an example, the detection efficiency for a He^+ ion accelerated to ≈1 kV is roughly 50 % for our MCPs [2]. If we nevertheless assume this detection efficiency for all ions and take the two gratings with a transmission of 78 % into account, the probability for detecting a single ion is about 30 %. However, the presented measurements rely on two ion coincidences which further reduces the detection probability of a coincident ion pair to 9 %.

The timing information t_{MCP} on the impact of the particle is obtained from the signal that arises from the build-up of the electron avalanche. It results in a short drop of the MCP voltage that is recorded during the measurement. The TOF of a charged particle created in the interaction point is determined from the impact time on the detector with respect to an external trigger signal (here provided by FLASH, indicating the arrival time of the photons):

$$\mathrm{TOF} = t_{\mathrm{MCP}} - t_{\mathrm{trigger}}. \tag{4.5}$$

In principal the MCP also provides spatial resolution since the charge cloud is localized in the individual channel where the particle originally hit the detector. The electron cloud could for instance be imaged onto a phosphor screen making the impact position visible. This technique is routinely used in velocity map imaging (VMI) [29]. However, our experiments require single particle resolution and read out, which is not possible with a phosphor screen. Instead, we image the electron cloud onto a delayline anode (cf. Sect. 4.1.3.2).

4.1.3.2 Delayline Anode

The delayline anode is used to determine the impact position of charged particles on the detector [18]. This detector type is chosen since it requires only a few read-out chains and, despite its large sensitive detector area, has fast read-out times. Additionally, it is to some extend multi-hit capable. We use a quad-anode with a quadratic shape featuring two sets of parallel wires oriented perpendicular to each other.

The wires are biased with a positive voltage, typically 200 V, with respect to the exit side of the MCP. They thus attract the electron cloud leaving the MCP. When the electron cloud arrives at the delayline plane a signal is induced and propagates along the wires towards both ends (cf. Fig. 4.5). From the arrival time difference $(t_1 - t_2)$ at the wire ends, counted from the impact time on the MCP, the impact position x is deduced:

$$x \sim (t_{x1} - t_{\mathrm{MCP}}) - (t_{x2} - t_{\mathrm{MCP}}) = (t_{x1} - t_{x2}). \tag{4.6}$$

The conversion factor from a time difference to a space coordinate is a constant factor that is extracted from the detector size. In order to receive 2D information on the impact position additional perpendicular wires are needed from which the y-position is deduced. In the actual delayline setup not only one, but two parallel wires, insulated from each other, are used for every direction. This is done for two reasons: One of the two parallel wires, the reference wire, is set to a voltage that is typically 50 V lower than that of the other wire, the signal wire. Therefore the electron charge is predominantly picked up by the signal wire. Noise, instead, is detected equally strong by both wires. Thus subtraction of the signal and the reference allows to discriminate noise and thus clean up of the signal. An additional reason for using a pair of wires is the reduction of dispersion, known from Lecher lines [4], as compared to a single wire.

With this detector two arriving signals are separable as long as the difference of their arrival times is larger than the propagation time on the wires. Even if another

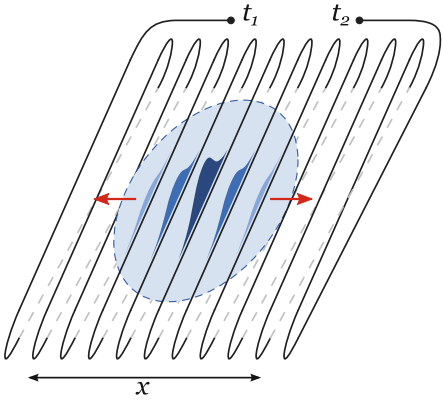

Fig. 4.5 Operation principle of a delayline anode. The electron cloud leaving the MCP is accelerated onto the delayline wires. From the arrival time difference of the signals at both ends of the wire the impact position of the cloud is reconstructed. Figure taken from [27]

signal arrives within the propagation time and thereby introduces the wrong arriving order at the end of the wires, the associated particles are reconstructed via the time-sum condition shown in Eqs. (5.1) and (5.2). In the presented setup, signals arriving as close as 8 ns are separable. The multi-hit ability could be further improved by introducing redundancy in the data by adding a third layer of wires [31].

4.1.4 Data Acquisition

In order to determine the initial momenta of the charged particles the TOF for each particle and the corresponding impact coordinates (x_i, y_i) on the detector are needed. Thus the collected signals from the MCP and the delayline wires must be translated into timing information, which are later converted to positions for the delayline. The first step to do so is to assign a time to each detector signal. Each signal has a different height, width and overall shape, as shown in Fig. 5.1. Therefore a reliable way must be found to make this assignment independently of the individual signal features. This is usually done with a CFD (Constant Fraction Discriminator), which electronically identifies the peak and sends a success-signal to a TDC (Time-to-Digital-Converter), which then assigns a timing information to the peak position [31]. Typically only the timing information from the detector is stored.

In contrast to this scheme, we acquire our data with so-called digitizer cards which record the complete signal trace by sampling the voltage with a certain repetition rate. The analysis is then done afterwards in a software-based peak finding procedure by evaluating the shape of the recorded trace. This type of data acquisition provides several advantages needed for FEL experiments. The high ionization rate caused by the intense radiation requires multi-hit ability. Using digitizer cards the dead time of delayline anodes can be reduced down to 2 ns [3]. Working on recorded data allows to adjust the peak-finding algorithm to the features of the trace, as will be discussed in Sect. 5.1. Particularly, the ability to resolve two partially overlapping peaks is optimized. An additional advantage of the digitizer cards is that no TDC dead time, which is usually in the order of 10–20 ns, occurs. The signal storage procedure is organized in a way that only those signals are written to disk which overcome an adjustable noise threshold for a certain time. The acquisition time before and after the signal is also adjustable. This way only non-zero traces are recorded to save storage space. More details on the Acqiris system and the AGAT software, used to store the recorded data, may be found in [10].

In total four DC282 digitizer cards from Agilent were used, each with one trigger and four acquisition channels. The highest possible voltage signal sampling rate is 2 GHz (equal to 0.5 ns between two samples) with a maximal voltage range of ± 5 V. As the read-out time for the cards is 5 ms but the distance between two minibunches is usually less than 10 µs the digitizer cards are read out after each pulse train. The read-out process is triggered by the FLASH master trigger that indicates the arrival of time each minibunch train. Therefore the memory of the digitizer cards must be sufficiently large to save the data amount of an entire pulse train. A classical TDC

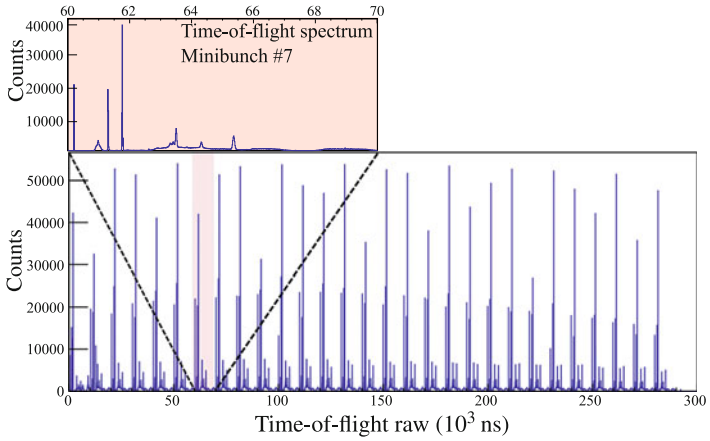

Fig. 4.6 Recorded MCP raw data spectrum that shows one read-out cycle with 30 minibunches per pulse train. The *inset* shows a time-of-flight spectrum from a single minibunch

could not handle this large amount of data. As the digitizer cards are read out with 10 Hz repetition rate, after each pulse train of n minibunches the recorded raw data contain n single shot spectra per read out, as illustrated in Fig. 4.6. In the analysis the n individual spectra are convoluted into one. The data processing will be described in Chap. 5

4.1.5 Vacuum Requirements

The interaction of atoms and molecules with XUV radiation mostly leads to the ejection of valence and inner-shell electrons. The photoabsorption cross sections usually are largest in the XUV range, which leads to efficient ionization of the target as well as the remaining residual gases. An overview of the absolute cross sections for the dominating residual gases and the chosen targets is given in Fig. 2.4. The comparison shows that great care must be taken to reduce the base pressure in the vacuum chamber as much as possible. Otherwise the assignment of coincidences, which requires the detection of all fragments, becomes impossible, because the detectors will be saturated by background events. In order to assure ultra-high-vacuum (UHV) conditions ($P < 10^{-9}$ mbar) only special materials with low outgassing rate are used. Additionally, the whole chamber must either be heated or cooled down to cryogenic temperatures to remove or freeze material that adsorbs on all surfaces.

In our interaction chamber a typical base pressure of 10^{-11} mbar is reached. Assuming the FEL settings for the I_2 experiments (cf. Table 6.1), the cross sections from Fig. 2.4 and a beam diameter of 10 mm the number of ions from the residual gas amounts to 16 per pulse. For comparison, the FLASH beamline system is kept at

a pressure of roughly 10^{-8} mbar. If we operated the REMI at that pressure we would receive 16,000 background events per pulse, which would render our experiment impossible. Therefore differential pumping stages have to be mounted between the FLASH beamline and our REMI to ensure the required low base pressure.

The key points for achieving these extreme vacuum conditions will be explained in the following. The vacuum chamber, fabricated from annealed antimagnetic steel, has a very low outgassing rate and is evacuated by turbo-molecular pumps with additional pre-vacuum pumps mounted upstream. Even at highest pumping powers a certain base pressure cannot be overcome—at least not on short time scales—because of the adsorbed atoms and molecules that continuously come off all surfaces. By heating the whole vacuum vessel (in a process called *baking*) this emission process is accelerated and the ejected atoms and molecules are removed by the pumping system. The most important background component removed by baking is water, which sticks well to all surfaces due to its polarity. In order to achieve even better vacuum conditions, the inner surface of our interaction chamber is coated with a non-evaporable getter (NEG) material. Once the NEG material is heated above roughly 180° for at least 24 h and then cooled down again it is activated. Afterwards it is able to react chemically with the residual gas in the chamber, thereby binding it. Thus the entire surface of the vacuum chamber acts as an additional vacuum pump.

4.2 Setup for the Iodine Experiments

With the setup depicted in Fig. 4.7, we have performed different types of experiments on the iodine molecule I_2:

- Single pulse XUV
- Single pulse IR
- XUV pump-probe
- XUV/IR pump-probe

This section gives an overview of the geometry of the experiment and the applied delay stages.

The XUV and the IR beam are delivered to the experiment in parallel beamlines. While the XUV beam is directly focused into the gas jet, the IR laser is guided through a viewport perpendicular to the XUV beam onto an in-vacuum mirror oriented under 45° towards the IR. This mirror reflects the previously focused IR beam into the gas target. The mirror has a hole of 5 mm diameter drilled through the center under an angle of 45°. This allows the FEL to pass through the back of the mirror towards the target. As the FEL beam is already tightly focused by the time it passes the mirror, no beam loss occurs. An IR focusing lens is placed just before the vacuum viewport, thus the beam is still spread over a sufficiently large area to lose only a small fraction in the non-reflecting hole.

In order to perform XUV pump-probe experiments the FEL beam is split and delayed by an autocorrelator (AC), which is presented in Sect. 4.2.2. For IR/XUV

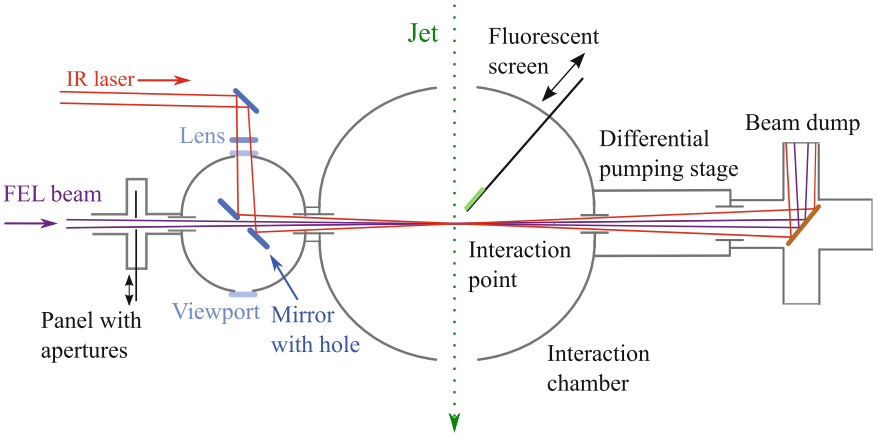

Fig. 4.7 Experimental setup for IR/XUV pump-probe experiments on I_2. The IR beam is guided into the vacuum chamber onto a mirror, which reflects the beam into the gas target. The focusing on the gas target is achieved by a lens placed directly in front of the vacuum viewport. The FEL passes the IR incoupling mirror from behind through a hole of 5 mm diameter. The XUV beam is focused into the gas target without further detours and both lasers are dumped onto a tilted copper blade, which avoids stray light and secondary electrons to scatter back in the interaction chamber. Differential pumping stages before and behind the interaction chamber ensure the UHV conditions needed to operate the REMI at FLASH

pump-probe experiments, the arrival time of the IR laser is varied, as presented in Sect. 4.2.3. For both types of experiments the spatial and temporal overlap of pump and probe pulse is crucial. The spatial overlap is adjusted by simultaneously monitoring the beams on a screen, that is moved into the interaction point. In order to visualize the XUV beam the screen is coated with a fluorescing powder (ZnS). The temporal overlap of the IR and the XUV beam is found by scanning the delay stage and monitoring the emission characteristic of the ions, which is different for a preceding or a delayed IR laser. Exemplary spectra will be shown in Sect. 6.3.2, for instance Fig. 6.30. As the delay axis of the AC is already calibrated, the beams are delivered with a known delay. During all pump-probe experiments, the delay is continuously scanned over a range of 4 ps for XUX pump-probe and over 10 ps for IR/XUV pump-probe.

4.2.1 Iodine Target

At room temperature iodine is a solid that starts to sublimate. In order to achieve a gaseous iodine target with reasonable concentration, solid iodine is heated. Consequently the vapor pressure rises and the gas is expanded into the vacuum chamber. Experimentally this is realized by placing iodine flakes (∼1 g) in an evacuated steel

cylinder, the so-called "bubbler". The lid of this reservoir is equipped with two pipes: One serves as inlet for a seeding gas flowing through the vapor and the other as outlet for the gas mixture. The seeding gas, here He, is used to increase the backing pressure and cools the iodine molecules that have a large momentum spread due to the heating. In order to avoid clogging of the nozzle by resublimated iodine, the whole setup is heated with a temperature gradient rising from the bottom of the bubbler (373 K) to the nozzle (423 K). Once clogged the nozzle must be replaced, which requires dismounting of several components and new alignment afterwards. This is obviously very undesirable during a running experiment. The heating of the in-vacuum nozzle is provided by a heating wire (thermocoax) surrounding the mount and connected via a vacuum feed-through. The temperature is controlled with the current flowing through this wire. In order to monitor the temperature two thermal elements (PT1000) are used, one mounted just behind the nozzle and another behind the vacuum feed-through.

The behavior of a mixed gas jet, here I_2 mixed with He, is difficult to predict, but the properties will lie somewhere between a pure jet of the one or the other component. One assumes that the constituents of the mixed jet thermalize before the expansion and that both gases will have the same asymptotic velocity after the expansion, v_{jet}, determined by the mixing ratio of the gases [23]. With these assumptions an average jet velocity $\bar{v}_{\text{jet}} = 1433\,\frac{\text{m}}{\text{s}}$ is calculated via Eq. (4.1) using an averaged mass composed of the two gas components according to their mixing ratio[2] of $\bar{m} = 98\,\% \, m_{\text{He}} + 2\,\% \, m_{\text{I}_2} = 9.04\,\text{amu}$. This is in relatively good agreement with the velocity that is extracted from the momentum calibration in Sect. 5.3.1, yielding a value of $\bar{v}_{\text{jet}} = 1{,}595\,\frac{\text{m}}{\text{s}}$. From Eq. (4.1) it becomes immediately clear that the reduced mass leads to a higher jet velocity and consequently a larger speed ratio and finally a lower jet temperature T_∞, the latter two given in Eqs. (4.2) and (4.4), respectively.

However, Eq. (4.3), which is used to calculate the speed ratio from experimental parameters, is only applicable to the two constituents separately. The lighter gas thus determines the lower temperature limit, while the heavier constituent gives the upper limit. In addition, for heated sources, Eq. (4.3) has to be modified: The cross section $\sqrt[3]{\frac{53C_6}{k_B T_0}}$ must be replaced by the hard-sphere cross section $\pi\sigma^2$ [24]. Using this modified speed ratio the temperature limits are calculated to be 11 and 28 K for He and I_2, respectively, as summarized in Table 4.1.

The target temperature can also be estimated from experimental parameters, particularly from the width of the ions' momentum distribution in jet propagation direction: The width $\sigma_v = \sqrt{\frac{k_B T_\infty}{m}}$ of the Maxwell–Boltzmann distribution of the particles' thermal velocities is translated into the momentum width

[2] The mixing ratio is only a rough estimate counting the number of ions emerging from I_2 and from He and accounting for the different photoionization cross sections at 87 eV: $\sigma(\text{I}_2) \sim 2 \times \sigma(\text{I}) \approx 40\,\text{Mb}$, $\sigma(\text{He}) = 0.47\,\text{Mb}$.

Table 4.1 Theoretical jet temperatures T_∞^{calc} calculated using Eqs. (4.3) and (4.4), with the required parameters for He, I_2 and Ne

	He	I_2	Ne
A	0.778	0.783	0.778
B	0.495	0.353	0.495
σ (Å)	2.66	4.98	–
C_6/k_b (10^{-44}cm^6 K)	–	–	7.58
T_0 (K)	423	423	300
P_0 (bar)	1	1	21
γ	1.67	1.40	1.67
S_∞^{calc}	9.64	7.34	53.29
T_∞^{calc} (K)	11.38	27.50	0.26

The empirical constants are taken from [24]

$$\sigma_p = \sigma_v \cdot m = \sqrt{k_B T_\infty m} \quad \rightarrow \quad T_\infty = \frac{\sigma_p^2}{k_B m}. \tag{4.7}$$

However, this is only true if the target temperature is the dominating effect broadening this distribution. In the following the validity of this assumption is tested. Due to momentum conservation the photoelectron transfers a recoil momentum to the nucleus that is equal to the electron's momentum. For instance, a He 1s electron, which is bound with 24 eV, transfers roughly 2 au to its nucleus when photoionized by 87 eV photons. These photoelectrons are emitted in a dipole shape along the polarization axis of the FEL, which corresponds to the jet propagation direction. Thus, we conclude that the He^+ momentum distribution along the x-axis should exhibit two dipole lobes, separated by 4 au. The measured momentum distributions along all three spatial axes are given in Table 4.2. In contradiction to the theoretical expectation, the experimental momentum in x-direction exhibits only one peak with $\sigma_x = 1.33$ au. From this we conclude that the detected width does not originate from the recoil, instead it is most likely caused by detector saturation effects. Consequently, the determination of the target temperature is not possible from the He^+ data.

Table 4.2 Momentum distributions of detected molecular ions along x-, y- and z-direction

	He^+	I_2^{2+}	Ne^{2+}
σ_x (au)	1.330 ± 0.001	5.10 ± 0.06	1.364 ± 0.001
σ_y (au)	0.770 ± 0.001	1.67 ± 0.02	3.236 ± 0.002
σ_z (au)	0.600 ± 0.001	0.668 ± 0.001	0.760 ± 0.001
m (amu = 1,836 au)	4	254	20
T_∞^{exp} (K)	–	17.07	–

An estimate of the temperature is given for I_2^{2+}

The momentum distribution of I_2^{2+} instead is not severely affected by saturation effects. The experimental width $\sigma_x = 5.10$ au, corresponding to $\Delta p_x = 12$ au, translates into a temperature of 17 K. The typical recoil momentum of a photoelectron emerging from I_2 at 87 eV photon energy is roughly 1 au and the second electron contributes another 1 au. Therefore the width is dominated by the temperature. However, the given value should be understood as an upper limit as the experimental distribution contains the broadening by the electron recoil.

4.2.2 Autocorrelator

The autocorrelator (AC) at FLASH [25] is installed permanently at beamline 2 and allows to perform jitter-free XUV–pump-probe experiments. The incoming beam is geometrically split and deflected by mirror 1 (M1), as shown in Fig. 4.8. One part of the beam is guided into the fixed arm of the AC onto M3 and M4, where it passes a chicane of constant length. The other part of the beam is deflected onto the mirrors M5 and M6, which are moved together with respect to M2 and M7. Thereby an adjustable path difference between the split beams is introduced. The mirrors M7 and M8 deflect the beams back into the direction of the incoming beam. Both beams are afterwards focused by a grazing incidence mirror to a diameter of 35 µm. The spatial overlap between the beams is adjusted by changing the angles of M7 and M8, and simultaneously monitoring the beam on a fluorescing screen mounted in the focal plane. In addition a Ce:YAG screen is mounted behind the interaction point to survey the beams. It allows to distribute the FEL intensity equally among the pump and the probe pulse.

The possible delays lie between −5 and +20 ps with a minimal step-size of 40 as. The eight mirrors are housed in a chamber with a length of 1.8 m in the direction of beam travel and a diameter of 0.5 m. In order to guarantee a high transmission of at least 50 % between 20 and 200 eV photon energy, grazing incidence mirrors were chosen, mounted under 3° for the fixed arm and 6° for the delay arm [36].

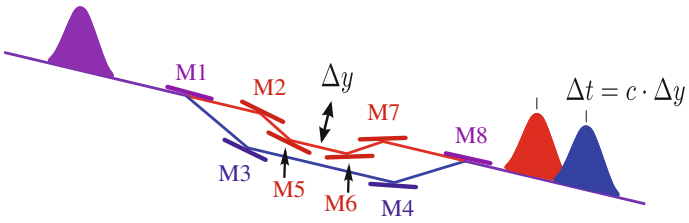

Fig. 4.8 Working principle of the autocorrelator (adapted from [36]). The incoming pulse (*purple*) is split by mirror *M1* into a fixed (*blue*) and an adjustable arm (*red*). The delay Δy is varied by moving *M5* and *M6* perpendicular to the beam propagation direction

4.2.3 IR Laser

Two infrared (IR) laser systems with a central wavelength of 800 nm are installed at FLASH and available for IR/XUV pump-probe experiments [28]. One of the systems operates in a burst mode, thereby mimicking the minibunch repetition rate of FLASH. It provides an output energy of maximal 60 μJ per pulse train at a pulse length of 120 fs. The second laser system shoots at 10 Hz repetition rate with a pulse energy of up to 20 mJ and a pulse duration larger than 50 fs. Details of both laser systems may be found in [28]. The IR lasers are installed in a separated lab within the experimental hall. From there the beam is guided into beamlines that run in parallel to the XUV beamlines to the endstations.

In the experiments presented here (cf. Sect. 6.3), the second laser system was used, as the burst-mode laser did not provide enough energy to ionize I_2. The pulse energy was measured to be roughly 2 mJ before coupling the beam into the vacuum chamber. A recent experiment with similar settings has characterized the pulse length to be 120 fs (FWHM) [22]. For a 50 μm (FWHM) diameter focus, the intensity on target was approximately $3.4 \times 10^{14} \frac{\mathrm{W}}{\mathrm{cm}^2}$. The estimate of the intensity includes beam losses due to the hole in the incoupling mirror, as discussed in Sect. 4.2.

In contrast to the AC (described in Sect. 4.2.2), where pump and probe pulse are inherently synchronized, the synchronization of the IR laser and the FEL is non-trivial. Here, the two pulses originate from different sources. Thus, special care must be taken to determine the timing between the IR- and the XUV-pulse, as it cannot be actively stabilized. The tools that were used for the precise determination of the delay are described in the following. It should be noted that all of them measure the timing between the IR pulse and the electron bunches in the undulator, not the XUV pulse.

Timing drifts on the order of a few hundred femtoseconds up to picoseconds may occur within a day due to temperature differences and other external influences. For online monitoring of the long-term drift between the electron bunches and the IR laser a streak camera [28, 33] is used. The timing reference for the electron bunch originates from optical synchrotron radiation that is produced when the electron beam is deflected by a dipole magnet into the dump. For the IR beam a part is split off and guided onto the streak camera.

However, since the goal of this work is the study of molecular dissociation dynamics that take place on time scales of 100 fs, the correction of the long-term drift is not sufficient. Additionally, a shot-to-shot fluctuation of the arrival times of the both pulses, the jitter, has to be accounted for. For a more precise shot-to-shot analysis, another tool is used based on the electro-optical effect, the so-called TEO (Timing by electro-optical sampling) [9, 33] method. Part of the IR laser is sent trough a glass fiber into the accelerator section. There, the beam impinges on and passes through an electro-optically active crystal. The crystal is only a few millimeters away from the electron beam. Thus, when the electron bunch flies by, its electric field causes a change of the birefringence in the crystal, slightly changing the polarization of the

laser light. By monitoring the polarization, the timing jitter is reconstructed. With this technique a resolution of about 100 fs is reached.

In order to record the presented pump-probe spectra, such as Fig. 6.32, the arrival time between IR and XUV pulse is continuously scanned by sending the IR beam through a delay stage. The delay stage position and the jitter monitored by the streak camera are read out online via the DESY data distribution system DOOCS [5]. The TEO data are recorded on demand only and stored separately. All presented pump-probe spectra have a calibrated delay axis corrected by the information provided by the timing tools. As only a small fraction of data was recorded together with the TEO tool, the presented spectra will only include the streak-camera correction.

4.3 Setup for the Neon Experiments

For the XUV pump-probe experiment on Ne_2 we use our own delay stage, which requires the unfocused FEL beam to cross the main chamber before it hits the mirror, which then focuses the beam into the gas target (cf. Fig. 4.1). In order to avoid stray light from the unfocused beam an additional piece of beamline is mounted between the end of the FLASH beamline and the REMI. The production of a Ne_2 cluster beam will be discussed in Sect. 4.3.1, followed by a description of the beamline in Sect. 4.3.2 and the split-and-delay mirror setup in Sect. 4.3.3.

4.3.1 Neon Target

Neon dimers do not occur at room temperature and special measures have to be taken to produce them. Stable clusters are only produced if the internal kinetic energy of the gas particles is smaller than the cluster's binding energy. The formation of a dimer is based on the collision of three particles, in which two of them form a van-der-Waals bond, their relative kinetic energy is transferred to a third particle. This process does usually take place in two steps [1, 20]:

$$A + A \rightleftharpoons A_2^*, \tag{4.8}$$

$$A_2^* + A \rightarrow A_2 + A. \tag{4.9}$$

Larger clusters are then formed by combining small ones.

The essential collisions are favored in areas where the gas density is high. This is the case close to the nozzle area of the supersonic gas jet, making it a well-suited tool for the production of clusters. The number of collisions at the nozzle is proportional to $\frac{P_0 d}{T_0}$ [12], with the injection pressure P_0, the nozzle diameter d and the nozzle temperature T_0. Thus by varying these parameters all cluster sizes can be produced, however not size-selectively but with a distribution centered around a most likely

Table 4.3 Relative abundances of Ne isotopes [35]

Isotope Ne	Abundance in %
20	90.48
21	0.27
22	9.25

Table 4.4 Relative abundances of Ne_2 isotope mixtures

Isotope combination Ne–Ne	Abundance in %
20–20	81.866
20–21	0.489
20–22	16.739
21–21	0.001
21–22	0.050
22–22	0.856

cluster size N_c. This means shifting the expansion conditions towards larger clusters comes along with less smaller clusters and vice versa.

There is no way to precisely predict the cluster size distribution. However, the empirical scaling parameter Γ^*, known as the Hagena parameter [13], allows an estimate. This parameter takes into account target specific properties as well as setup specific parameters.

$$\Gamma^* = k \frac{P_0 d^{0.85}}{T_0^{2.29}}, \tag{4.10}$$

with d in µm, P_0 in mbar, T_0 in K and the element specific parameter k, which is related to the bond forming [32]. The scaling of N_c with the Hagena parameter depends on the studied range of cluster sizes. In general, clustering starts for $\Gamma^* >$ 100–300 with the formation of dimers.

For our parameters,[3] we calculate $\Gamma^* = 148$ predicting the formation of only small clusters, which is in agreement with the experimental observation of Ne_2 as largest cluster. Besides these general considerations studies on the maximal yield of neon dimers have been carried out predicting a maximum yield of 2 % dimers [7].

In principle, an estimate of the dimer-to-monomer ratio present in the experiment is gained by comparing the relative abundances of ionized monomers and dimers. Apart from ^{20}Ne, neon has two further stable isotopes that occur in nature, ^{22}Ne and ^{21}Ne, with their relative abundances given in Table 4.3. Therefore six different dimer compounds are formed, which are listed in Table 4.4 with their relative abundances. As the time-of-flight of the ionized dimers is proportional to the square root of their mass, they impinge at different times on the detector, as shown in Fig. 4.9. However, due to saturation effects, ionized monomers $^{20,21,22}Ne^+$ are not counted correctly by the detector (cf. Fig. 7.1). Thus, we are not able to determine the dimer-to-monomer ratio present in the experiment.

[3] Parameters: k(Ne) = 185 [32], $P_0 = 21$ bar, $d = 30\,\mu$m, $T_0 = 300$ K.

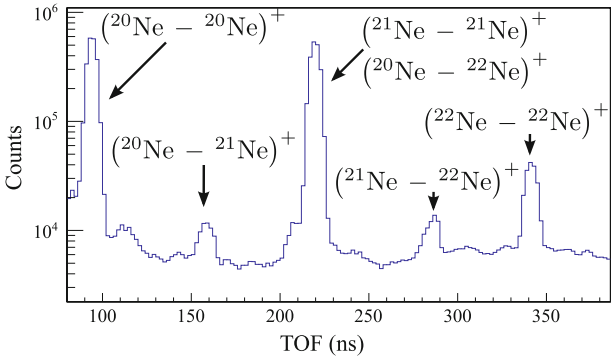

Fig. 4.9 Time-of-flight spectrum of singly charged dimer ions. The isotope compounds arrive at the detector at different times and are indicated by *arrows*

The jet temperature is determined via the speed ratio, given in Eq. (4.3), in the same way as for I_2 in Sect. 4.2.1. The relevant parameters are summarized in Table 4.1 leading to a theoretical temperature of $T_\infty^{\text{calc}} = 26\,\text{mK}$. An experimental determination of the temperature from the width of the momentum distribution along the jet propagation direction is not possible due to the recoil of the electrons (cf. Sect. 4.2.1). Ne^{2+} is produced via two-photon absorption and thus receives a recoil of 1.3 au from the first and 0.6 au from the second electron, which is in the order of the measured width. A precise determination of the target temperature is not possible, but it should be well below the thermal energy needed to populate the first excited level in the dimer ground state, when compared with similar settings of previous experiments [19, 21].

4.3.2 Beamline

We have used an additional beamline between the FLASH beamline and the REMI. It is needed for three reasons: It serves as a differential pumping stage between FLASH and the UHV in the REMI, it enables manipulation of the XUV beam via apertures and foils, and it blocks stray light produced by the unfocused beam passing the main chamber.

The base pressure in the FLASH beamline of roughly 10^{-8} mbar would directly spoil the pressure in the interaction chamber, which is roughly three orders of magnitude lower. Therefore the beamline consists of three differential pumping stages to "secure" the low pressure in the interaction chamber.

In order to manipulate the FEL, the beamline is equipped with apertures, slits, wires and foils. The aperture panels are mounted on x-y-z-manipulators, allowing a precise alignment of each hole. During the setup phase, the apertures are centered with respect to an alignment laser and then provide reference points for aligning the

FEL beam with the gas jet. The apertures are also used to confine the beam size, which is important for the prevention of stray light.

While on its way to the split-and-delay mirror, the unfocussed FEL beam crosses the gas jet creating background events. This is prevented by wires in the beamline, which cut out a jet-sized slice such that no photons may interact with the target on the way in.

4.3.3 Mirror Chamber

The purpose of the mirror chamber is to simultaneously split, delay and focus the FEL beam. XUV radiation is efficiently absorbed in almost all materials making it difficult to steer and focus it. Thus special mirrors, such as grazing incidence and multi-layer mirrors, are used. The first class of mirrors is applicable from hard X-rays down to the EUV range. They offer a relatively constant reflection behavior over a wide wavelength range, depending on the specific absorption edges of the coating material. In addition, the reflectivity depends on the—preferentially very small—angle of incidence of the beam onto the mirror. For instance, the FLASH mirrors for switching the FEL between the different beamlines are 0.5 m long plane mirrors that reflect the beam at grazing incidence of 2° and 3° [6]. The drawback of these mirrors are the large dimensions due to the small incidence angle, which complicates mounting and housing. In addition they are hard to produce and quite costly.

In contrast, multi-layer mirrors work at normal incidence and therefore have the same dimensions as optics in the visible regime. The drawback of these mirrors is, that they are manufactured for a specific wavelength. Multilayer mirrors consist of glass substrates that are coated with hundreds of alternating layers of typically two materials with different refractive indices. In our case these are molybdenum (Mo) and silicon (Si). One material is a high-mass metal (here Mo) and the other is a spacer material of lower mass (here Si). According to Bragg's law, the thickness of the layers must be designed in such a way that the summed thickness of one Si and one Mo layer corresponds to half the incoming wavelength that should be reflected. In this case, constructive interference between the waves reflected off each layer may occur. Depending on the wavelength, a reflectivity up to 70 % (at 90 eV) is feasible [8]. For the neon experiment a mirror with a reflectivity of roughly 40 % with a centroid energy of 58 eV and a bandwidth of 3 eV (FWHM) was used. It focuses the beam down to a diameter of 10–15 μm at a 50 cm focal length.

The design of an XUV pump-probe setup to be used at FLASH has some special requirements that need to be fulfilled. Just like the rest of the setup it must be transportable, but at the same time stable enough to guarantee a fixed position of the mirror. Particularly, it must be insensitive to vibrations from pumps and other external sources. For multi-photon ionization a high photon density is needed, which requires a tight focus and a short focal length. This typically conflicts with the demanding vacuum requirements, since the used optics can only be baked at comparatively low temperatures <100°C. In addition, all applied optomechanical components for the

mirror adjustment must be suitable for UHV conditions. Even if taking great care when choosing components, the required base pressure of the interaction chamber is not reached in the mirror chamber. Thus, it is mounted in a separate vacuum chamber connected to the interaction chamber via a 12 cm long differential pumping stage with a diameter of 17 mm.

One block of beamtime is usually used for experiments at various wavelengths, which all require a different XUV mirror. Therefore, changing the mirror must be accomplished in a few hours to avoid beamtime loss. The precise alignment of the mirrors is done prior to the start of the experiment with the help of alignment lasers.

The whole mirror setup is mounted on a massive pipe connected to a x-y-z-manipulator. This is used to center the focused beam with respect to the incoming beam and the gas target. The fine-adjustment of the mirrors is achieved with the help of several optomechanical elements mounted inside the mirror chamber. Two goniometers (Micos WT-85) are mounted perpendicularly to each other. They allow the horizontal and vertical rotation of both mirrors around the focal point with a maximum deflection angle of $\pm 5°$ with respect to the incoming beam. In order to overlap the two foci, the upper half is mounted on a piezo tip/tilt stage (S-325 from Physik Instrumente). The maximum travel range of the tip/tilt unit is on a radius of 4 mm in the focal plane. The lower mirror half is mounted on a piezo driven translation stage (P-628 from Physik Instrumente) that allows to shift the mirrors with respect to each other in the plane of the beam and thereby introduces a time delay between the split beams. In order to overcome the total travel range of 800 µm (resolution 0.5 nm) the light needs 2.67 ps. As the light travels back and forth, a maximum delay of 5.33 ps is achievable, which is sufficient for the time scales of vibrational and dissociative motion of small molecules. The temporal overlap is usually placed in the middle of the delay stage, which enables autocorrelation measurements for pulse analysis, as presented in Sect. 3.3. The intensity was distributed equally among the pump and the probe beam in all presented spectra (Fig. 4.10).

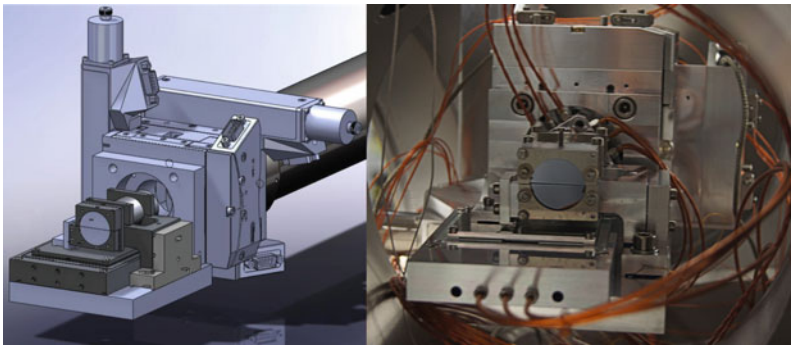

Fig. 4.10 Split-and-delay mirror setup. The *left panel* shows a CAD drawing of the optomechanical components (taken from [15]) and the *right panel* shows a photograph of the implementation

The pre-alignment of the mirrors is achieved by overlapping the foci of the split beam with an optical laser that is monitored on a screen in the interaction point. More challenging is the temporal overlap of the split beams, which is determined using a special diode laser with a broad spectrum and consequently a short coherence length. This results in an interference pattern of the two overlapping beams that is only present for roughly $\pm 20\,\mu m$ around the perfect temporal overlap. Using this method the temporal overlap of the two beams is determined up to a precision of typically $5\,\mu m$ (150 fs).

4.4 The Trouble with the Electrons

As introduced in the first section of this chapter, the REMI is capable of detecting ions and electrons in coincidence. However in this work only ion spectra are recorded and discussed. The reasons for this are technical difficulties that arise when operating a REMI at FLASH. Due to the large photoionization cross sections for basically all elements at XUV wavelengths, low base pressure in the interaction chamber is essential. Even for the reached 10^{-11} mbar, roughly 16 background ions per pulse are produced with the I_2 beam parameters. Rest gas ionization is also clearly visible in the detector image in Fig. 5.3. Since each photon-atom interaction creates at least one electron-ion pair, the residual gas may cause false coincidences.

Even without background the coincident detection of electrons is difficult for high FEL intensities. The used detectors are multi-hit capable up to a certain degree: For the delayline, particles impinging within a few nanoseconds are indistinguishable. During the I_2 measurement, we detected on average ten ions per FEL pulse, including two background events. Since every $4d$-ionized iodine molecule ejects at least two electrons when hit by a 87 eV photon, typically more than twenty electrons have to be detected per shot. Due to the high energetic Coulomb-explosion fragments, strong electric field gradients are applied to the spectrometer in order to guarantee full 4π resolution for the ions. Therefore, the estimated twenty electrons impact in a short time interval on the electron detector and thus become indistinguishable. Thus, for experiments at high intensities, such as the one for iodine, the coincident recording of electron spectra is a demanding task. The situation could be improved by a longer electron spectrometer arm, which is at the moment limited by the dimensions of the vacuum chamber.

A further difficulty emerges from scattered photons close to the interaction chamber. They typically have enough energy to eject electrons from surfaces or trigger the detectors directly. Considering an ionization potential of 4.34 eV for steel, which is omnipresent in our interaction chamber, a single photon creates a reasonable amount of secondary electrons without even hitting the target. Therefore, several measures are taken to hinder scattered photons and secondary electrons to reach the spectrometer region, such as the additional beamline discussed in Sect. 4.3.2. An unavoidable stray light source is the back-reflecting multi-layer mirror that scatters many photons in random directions. A new mirror setup might be able to overcome these difficulties.

References

1. D.L. Bunker, Mechanics of atomic recombination reactions. J. Chem. Phys. **32**(4), 1001–1005 (1960)
2. Burle Industries, MCP Data Sheet, Germany, 2005
3. G.D. Costa et al., Design of a delay-line position-sensitive detector with improved performance. Rev. Sci. Instrum. **76**(1), 013304 (2005)
4. W. Demtröder, *Experimentalphysik 2. Elektrizität und Optik*, 6 überarb. u. akt. Aufl. (Springer, Heidelberg, 2013), p. 482
5. DESY. DOOCS. http://tesla.desy.de/doocs/ (2013)
6. DESY. FLASH. http://flash.desy.de/ (2013)
7. A. van Deursen, J. Reuss, Molecular beam intensities and collision crosssections of small Ne, H_2, N_2, NO, O_2 and clusters. Int. J. Mass Spectrom. Ion Phys. **23**(2), 109–122 (1977)
8. T. Feigl et al., Heat resistance of EUV multilayer mirrors for long-time applications. Microelectron. Eng. **57–58**, 3–8 (2001). Micro- and Nano-Engineering (2000)
9. J. Feldhaus, FLASH-the first soft X-ray free electron laser (FEL) user facility. J. Phys. B: At. Mol. Opt. Phys. **43**(19), 194002 (2010)
10. L. Foucar, Auslese von Delaylinedetektoren mit Hilfe von Transientenrekordern. Ph.D. thesis, Frankfurt, 2008, p. 190
11. R. Grimm, M. Weidemüller, Y.B. Ovchinnikov, Optical dipole traps for neutral atoms. Adv. At. Mol. Opt. Phys. **42**, 95–170 (2000)
12. O.F. Hagena, W. Obert, Cluster formation in expanding supersonic jets: effect of pressure, temperature, nozzle size, and test gas. J. Chem. Phys. **56**(5), 1793–1802 (1972)
13. O.F. Hagena, Cluster ion sources (invited). Rev. Sci. Instrum. **63**(4), 2374–2379 (1992)
14. Hamamatsu Photonics K.K. MCP & MCP Assembly Selection Guide TMCP 0001 E10. http://www.hamamatsu.com/resources/pdf/etd/MCPassy_5FTMCP0001E10.pdf. Japan, 2013
15. O. Herrwerth, Atomic and molecular ionization dynamics in strong IR and XUV fields probed by time-resolved coincidence spectroscopy. Ph.D. thesis, LMU Müchen, 2011
16. R. Hubele, Implementation of an optical dipole trap for lithium. Diplomarbeit, Ruprecht-Karls-Universität, Heidelberg, 2009
17. R. Hubele, Kinematisch vollständige und zustands-selektive Untersuchung der stoßinduzierten Einfachionisation von Lithium. Ph.D. thesis, Heidelberg, 2013, p. 199
18. O. Jagutzki et al., Position sensitive anodes for MCP read-out using induced charge measurement. Nucl. Instrum. Methods Phys. Res. Sect. A: Accel. Spectrom. Detect. Assoc. Equip. **477**(1–3) (2002). In: *5th International Conference on Position-Sensitive Detectors*, pp. 256–261
19. T. Jahnke, Interatomic Coulombic Decay - Experimentelle Untersuchung eines neuartigen, interatomaren Abregungsmechanismus. Ph.D. thesis, Frankfurt, 2005, p. 201
20. E.L. Knuth, Dimer-formation rate coefficients from measurements of terminal dimer concentrations in free-jet expansions. J. Chem. Phys. **66**(8), 3515–3525 (1977)
21. K. Kreidi, Untersuchung der Zerfallsmechanismen und der Lokalisierung von Vakanzen in Ne_2. Ph.D. thesis, Frankfurt, 2005, p. 201
22. M. Krikunova et al., Strong-field ionization of molecular iodine traced with XUV pulses from a free-electron laser. Phys. Rev. A **86**, 043430 (2012)
23. C. Langbrandtner, Experimente zur Ionisation von atomarem Wasserstoff im Ionenstoß. Diploma thesis, Heidelberg, 2007, p. 93
24. D.R. Miller, in *Free Jet Sources*, ed. by G. Scoles. Atomic and Molecular Beam Methods, vol. 1 (Oxford University Press, Oxford, 1988)
25. R. Mitzner et al., An x-ray autocorrelator and delay line for the VUV-FEL at TTF/DESY. Proc. SPIE **5920**, 59200D-1–59200D-10 (2005)
26. R. Moshammer et al., A 4π recoil-ion electron momentum analyzer: a highresolution "microscope" for the investigation of the dynamics of atomic, molecular and nuclear reactions. Nucl. Instrum. Methods Phys. Res. Sect. B: Beam Interact. Mater. At. **108**(4), 425–445 (1996)

27. T. Pflüger, Electron impact ionization studies of small rare gas clusters. Ph.D. thesis, Heidelberg, 2012
28. H. Redlin et al., The FLASH pump-probe laser system: setup, characterization and optical beamlines. Nucl. Instrum. Methods Phys. Res. Sect. A: Accel. Spectrom. Detect. Assoc. Equip. **635**(1, Supplement), S88–S93 (2011)
29. D. Rolles et al., A velocity map imaging spectrometer for electron-ion and ion-ion coincidence experiments with synchrotron radiation. Nucl. Instrum. Methods Phys. Res. Sect. B: Beam Interact. Mater. At. **261**(1–2) (2007). In: *Proceedings of the Nineteenth International Conference on The Application of Accelerators in Research and Industry*, pp. 170–174
30. G. Scoles, *Atomic and Molecular Beam Methods: 1. Atomic and Molecular Beam Methods* (Oxford University Press, Incorporated, 1988)
31. A. Senftleben, Kinematically complete study on electron impact ionisation of aligned hydrogen molecules. Ph.D. thesis, Heidelberg, 2009
32. R.A. Smith, T. Ditmire, J.W.G. Tisch, Characterization of a cryogenically cooled high-pressure gas jet for laser/cluster interaction experiments. Rev. Sci. Instrum. **69**(11), 3798–3804 (1998)
33. K. Tiedtke et al., The soft X-ray free-electron laser FLASH at DESY: beamlines, diagnostics and end-stations. New J. Phys. **11**(2), 023029 (2009)
34. J. Ullrich et al., Recoil-ion and electron momentum spectroscopy: reactionmicroscopes. Rep. Prog. Phys. **66**(9), 1463 (2003)
35. R.C. Weast (ed.), *Handbook of Chemistry and Physics. A Ready-Reference Book of Chemical and Physical Data*, 64th edn., 2nd pr. (CRC Press, Boca Raton, 1984)
36. M. Wöstmann et al., The XUV split-and-delay unit at beamline BL2 at FLASH. J. Phys. B: At. Mol. Opt. Phys. **46**(16), 164005 (2013)

Chapter 5
Data Analysis

The data analysis process is divided into three steps. In the first step, the *Acquire step*, all recorded voltage traces are translated into timing signals by peak finding procedures, as described in Sect. 5.1. In the following *Unpack step* the assignment of signals to time-of-flights and positions is performed, which is presented in Sect. 5.2. In the *Calculate step* the particle momenta are calculated and coincident particles are assigned to each other, as shown in Sect. 5.3. The advantage of splitting up the analysis process into different steps is that the outcome of each step is saved and used as input for the next one. Thus, if changes are made in later steps, the results of the previous ones are already available and don't have to be generated again. This way, the data analysis process is sped up as the particularly time-consuming Acquire step must not be repeated over and over. The analysis code GENERiC (General Analysis Code for Reaction Microscopes) [14] is embedded in the Go4 (GSI Object Oriented On-line Off-line system) analysis environment [6] based on CERN's ROOT [1]. Go4 already provides the organization structure into different steps, which are accessible via a graphical user interface. The chapter is also covering the momentum resolution in Sect. 5.4 and the acceptance in Sect. 5.5.

5.1 Acquire Step

In this step the stored voltage traces, as described in Sect. 4.1.4, are read-in and analyzed. This is done via peak-finding procedures that assign peak positions to each voltage trace. The applied algorithms must be robust with respect to the pulse shape and capable of finding peaks occurring at close temporal distances. Exemplary voltage traces are depicted in Fig. 5.1, showing some of the possible peak shapes.

The acquire step is not needed for hardware based data acquisition systems with CFDs and TDCs as voltage traces from the detector are already converted into times before they are recorded. This way the traces are not accessible after the experiment anymore, making an optimization of CFD settings for a given dataset impossible. Instead, if the traces are recorded via digitizer cards the settings can be adjusted and

K. Schnorr, *XUV Pump-Probe Experiments on Diatomic Molecules*,
Springer Theses, DOI 10.1007/978-3-319-12139-0_5

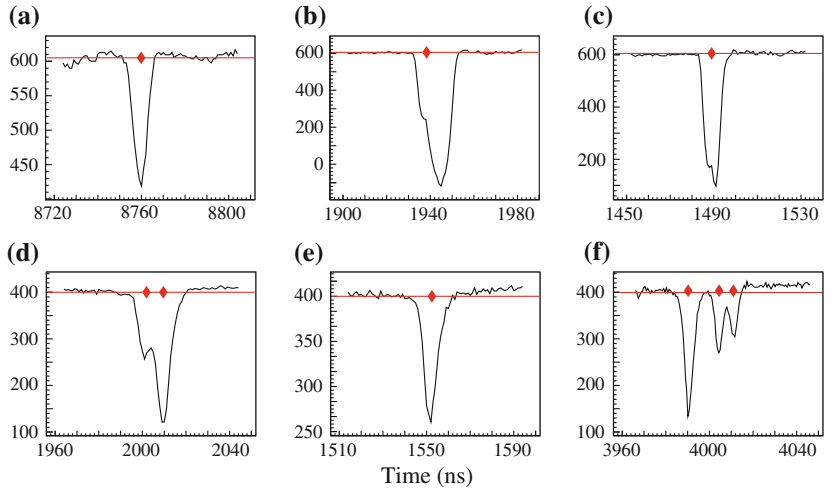

Fig. 5.1 Examples for recorded voltage traces, the *upper row* (**a**–**c**) shows MCP traces while the *lower row* (**d**–**f**) shows delayline signals. The *red line* indicates the baseline, while the *red diamonds* indicate found peaks by the CFD algorithm

compared until the optimum is found. This increases the quantity of usable data, as well as the quality of the results.

Three different peak finding algorithms are implemented in the Acquire step, which can be assigned to each recorded channel individually:

- SearchHighRes (SHR) [12]
- Constanst Fraction Discriminator (CFD) [11]
- Center of Mass (COM) [10]

Here, only a brief overview of the different methods is given. For more details on the different algorithms and their performance see [3, 10].

The SHR algorithm is routinely applied for peak identification in gamma-ray spectra. It is implemented in ROOT [2] and is applicable to the recorded voltage traces without further modifications. It performs best for double peaks and for noisy spectra with bad signal-to-noise ratio. At the same time it has the highest computational complexity and is therefore the slowest algorithm. In addition it requires well defined boundary conditions to enable successful peak finding, which is a disadvantage as the conditions might change during the measurement. Despite these disadvantages, the SHR algorithm was used for the MCP signal in the neon experiment as there the amount of double peaks was particularly high.

The CFD algorithm works also well for double peaks but is roughly a factor of five faster than the SHR algorithm. However, it performs worse when searching peaks in noisy spectra. The latter drawback is compensated by smoothing the voltage traces before applying the peak finding, however this deteriorates the resolution. The working principle of the algorithm is based on that of a hardware CFD [5]. The

strength of the CFD algorithm becomes obvious, when comparing it to the alternative *rising edge* peak finding: If peaks are identified by their rising edge a significant deviation in the peak position for small and large signals may occur, because large signals pass the trigger level earlier than small ones with the same peak position. The CFD algorithm is able to overcome this difficulty and identifies peaks independently of their height [11]. We apply the CFD algorithm for the delayline signals as it is relatively fast and performs reasonable well for double peaks.

The COM algorithm assumes that the recorded traces are symmetric and that the full rise and fall time of the trace is recorded. The latter point is important as the algorithm works by comparing the height of neighboring points in the signal. If a certain number of points rises above background level and returns to it again, a peak is identified. Therefore the COM is neither suited for double peaks nor for asymmetric pulses.

For every minibunch a set of found peaks is passed on to the unpack step, for each recorded channel separately.

5.2 Unpack Step

In the Unpack step the found peak positions of each channel are assigned to the corresponding physical observable, such as time-of-flight or detector position. In principle, each particle impinging on the detector creates one MCP signal and four delayline signals. In order to identify the five signals corresponding to one particle all signals in each channel must be tested. This is done via so-called time-sum conditions: The sum of the arrival times t_1 and t_2 on the delayline ends is always equal to the time the signal needs to travel along the whole wire in x- and y-direction, respectively. The MCP arrival time t_{MCP} is taken as reference for the start of the propagation:

$$t_{x,\mathrm{sum}} = (t_{x,1} - t_{\mathrm{MCP}}) + (t_{x,2} - t_{\mathrm{MCP}}) = \mathrm{const.} \tag{5.1}$$

$$t_{y,\mathrm{sum}} = (t_{y,1} - t_{\mathrm{MCP}}) + (t_{y,2} - t_{\mathrm{MCP}}) = \mathrm{const.} \tag{5.2}$$

where $t_{x,\mathrm{sum}} \approx t_{y,\mathrm{sum}}$.

All possible combinations of signals occurring within a certain time interval are checked for the time-sum condition. In case of a match they are assigned to each other. Thus one complete hit is characterized by a set of five coordinates $(t_{x,1}, t_{x,2}, t_{y,1}, t_{y,2}, t_{\mathrm{MCP}})$. During the assignment procedure all signals are used only once. After the signals are matched to each other using the time-sum condition, some will still remain unassigned because they were either caused by noise or one of the five required coordinates forming one hit was not detected. The latter may occur if two signals arrive so close to each other that they are identified as one signal or if the amplitude of a signal was below the threshold of the applied peak-finding algorithm. However there are means to reconstruct an event even if one of the five signals is missing. If a delayline signal is missing one of the time-sum conditions Eqs. (5.1) or

(5.2) is fulfilled and used to determine the missing time. If the MCP signal is missing, which is the prevalent case, combinations of x- and y-pairs are tested to result in the same t_{MCP}.

The timing information has to be translated to a position on the detector and an absolute TOF. In order to do so, the detector size must be calibrated, i.e. the proportionality factor of Eq. (4.6) must be found. For the TOF calibration the precise time when the FEL hits the target must be determined. This is roughly determined by the FLASH trigger that starts the data acquisition system, however not at the level of precision needed for the absolute TOF determination of each particle. The precise starting time with respect to the trigger is determined as a constant offset in the raw TOF-spectra:

The TOF t of a particle with charge Q and mass m without initial momentum is only dependent of the spectrometer length d_a and the applied voltage U.

$$d_a = \frac{1}{2}at^2 \quad \rightarrow \quad t = \sqrt{\frac{2d_a}{a}}, \tag{5.3}$$

where the acceleration a is gained from

$$F = m \cdot a = \frac{Q\,U}{d_a}. \tag{5.4}$$

Inserting a into Eq. (5.3) results in an expression for the TOF

$$t = d_a\sqrt{\frac{2m}{QU}} \sim \sqrt{\frac{m}{Q}}. \tag{5.5}$$

The raw TOF of all identified ion species deviates from Eq. (5.5) by the aforementioned constant, allowing to extract this offset from the y-intercept of a linear fit. The resulting offset is then subtracted from the raw spectrum.

An exemplary I_2 TOF spectrum recorded at $U = 350\,\mathrm{V}$ with an acceleration length of $d_a = 10.1\,\mathrm{cm}$ is shown in Fig. 5.2. The ion species are ordered according to their mass-to-charge ratio. The particle with the highest ratio, here the singly charged molecular ion I_2^+, will have the largest TOF. With $m(I_2) = 254\,\mathrm{amu}$ and $Q(I_2^+) = 1$, a TOF of $12.47\,\mu\mathrm{s}$ is expected from Eq. (5.5). As this time is larger than the time difference between two minibunches ($10\,\mu\mathrm{s}$), the fragment will impact on the detector within the following minibunch. As all minibunches of one pulse train are folded on top of each other, the I_2^+ molecular ion should appear in the spectrum at $12.47\,\mu\mathrm{s} - 10\,\mu\mathrm{s} = 2.47\,\mu\mathrm{s}$, which is confirmed in Fig. 5.2. Applying this method we calibrate the absolute TOF of all particles, which is needed to calculate the correct momenta of the ions.

The corresponding detector image for I_2 is shown in Fig. 5.3. The FEL passes the interaction chamber along the y-direction and thereby ionizes the rest gas, which results in a straight line of ionization events along that direction. Target ions with large

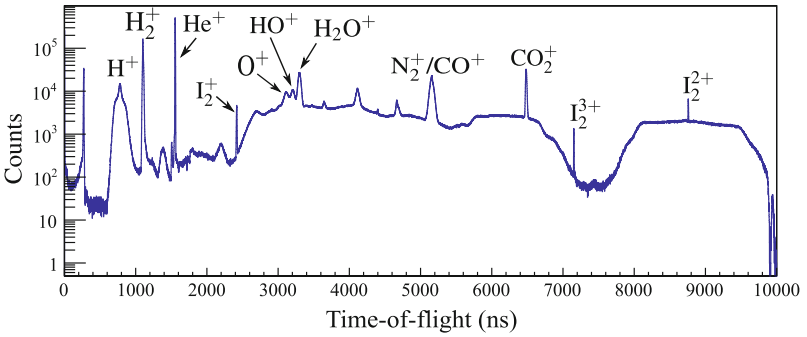

Fig. 5.2 Folded time-of-flight spectrum composed of the individual spectra from Fig. 4.6. The *peaks* that were used for the calibration of the time-of-flight offset are indicated and assigned to the element they originate from

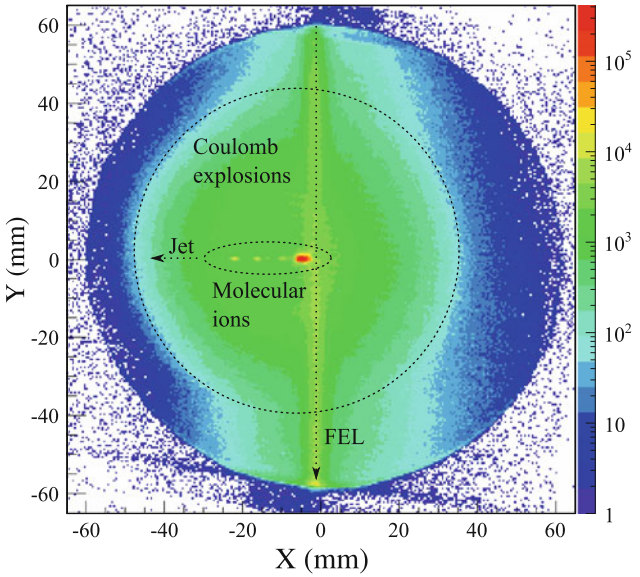

Fig. 5.3 Detector image recorded during the I_2 experiment. The *vertical line* along the y-direction through the *center* of the detector shows the path of the FEL beam passing the interaction chamber and thereby ionizing the residual gas. The increased rate in the center stems from interaction with the gas jet. Molecular ions with a high mass-to-charge ratio exhibit a large offset from the *center* due to the jet velocity in that direction (here: x). Molecules that fragment into two charged ions in a so-called Coulomb explosion gain high momenta and consequently are spread over a large area of the detector, which is indicated by a *dashed circle*

TOFs, such as I_2^+, have an offset in negative x-direction due to the velocity of the jet in that direction. It is often difficult to distinguish events emerging from target ionization from background events in a TOF spectrum. However, due to the velocity of the jet all target molecules will have an offset in x-direction as compared to the residual gas

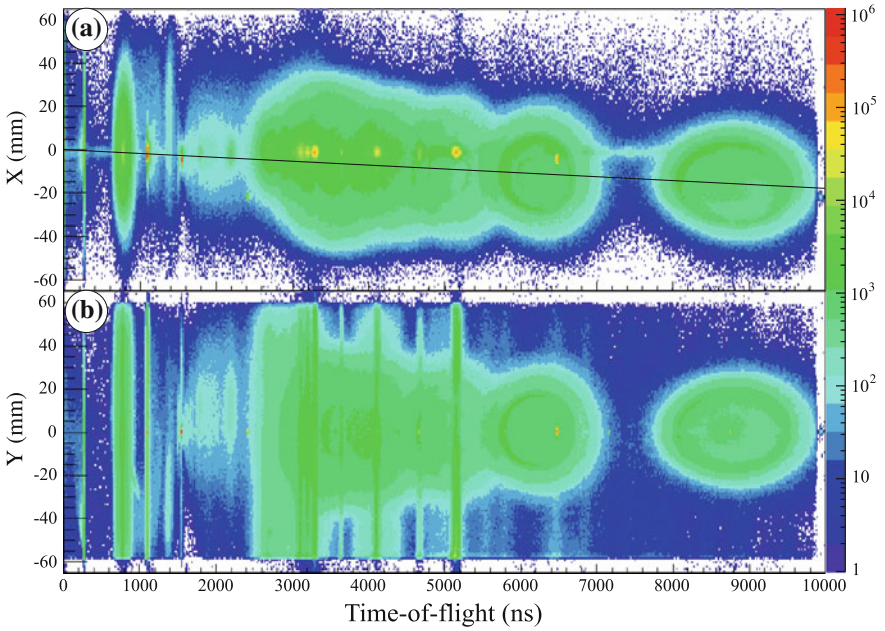

Fig. 5.4 **a** x-position on the detector plotted versus the TOF. Ions emerging from within the jet have an offset in x-direction due to the velocity of the jet. They are thus centered around the *black line*, which indicates the jet velocity, and not around the x-axis. Ions from the residual gas, e.g., the bright spots in the region from 2,500 to 5,500 ns, have a random velocity distribution and are therefore centered around the x-axis. **b** y-position on the detector plotted versus the TOF. The y-direction coincides with the propagation direction of the FEL. While passing the vacuum chamber the FEL ionizes rest gas along the whole pathway resulting in events occurring along the y-direction. Instead, ionization of the target takes only place in the intersection of the jet and the FEL in the middle of the vacuum chamber and is therefore centered around the y-axis

that has a random velocity distribution due to thermal motion. Therefore by plotting the TOF versus the impact position in x-direction, particles emerging from the jet are identified, as shown in Fig. 5.4. In addition, bound molecular ions have a much narrower momentum distributions than ionized rest gas atoms and molecules due to the low temperature within the jet. The spherical shapes in the spectrum emerge from fragments with high, distinct momenta, emerging from Coulomb-exploding molecules.

5.3 Calculate Step

In the Calculate step the momenta of all detected ions are calculated by means of the TOFs and detector positions determined in the previous Unpack step. Using momentum conservation two ions emerging from the same molecule are identified,

which are denoted as a coincident ion pair. Coincidences are a very powerful tool to identify associated fragments even if the TOF spectra of both fragments overlap. Other methods used to study the correlation of dissociating ions, like covariance mapping [4, 13], fail under these conditions [7]. One important observable of coincident ions is their kinetic energy release (KER), which allows to study the dynamics of the molecular break-up.

5.3.1 Calculation of Momenta

The momentum of a particle with mass m and charge Q is calculated using the respective TOF t, position coordinates on the detector (x, y) and the length of the acceleration distance d_a with the voltage U applied to it. The particle's motion in TOF direction (i.e., along the z-axis) is composed of the initial momentum $p_z = m\, v_z$ transferred during the interaction and acceleration in the spectrometer field. The acceleration a in the field is expressed via

$$F = m\, a = Q\, \frac{U}{d_a} \quad \rightarrow \quad a = \frac{U\, Q}{m\, d_a}. \tag{5.6}$$

Thus the distance to the detector is written as the sum of the two superimposed motions:

$$d_a = \frac{1}{2} a t^2 + v_z\, t = \frac{1}{2}\, \frac{U\, Q}{m\, d_a} t^2 + v_z\, t. \tag{5.7}$$

Which leads to the momentum in z-direction

$$p_z = m\, v_z = \frac{2m\, d_a^2 - U\, Q\, t^2}{2t\, d_a}. \tag{5.8}$$

The motion in x- and y-direction is independent of the applied electric field, which only acts in z-direction. Thus the momenta p_x and p_y are expressed as a function of the impact positions (x, y) on the detector and the TOF:

$$p_x = m v_x = m \left(\frac{x}{t} - v_{\text{jet}} \right), \tag{5.9}$$

$$p_y = m v_y = m \frac{y}{t}. \tag{5.10}$$

As the x-component lies in the propagation direction of the jet, a constant offset from the jet velocity v_{jet} must be subtracted from the measured momentum in that direction to obtain the initial momentum p_x. Exemplarily, the reconstructed momenta of I^{2+} ions emerging from the photoionization of I_2 are shown in Fig. 5.5.

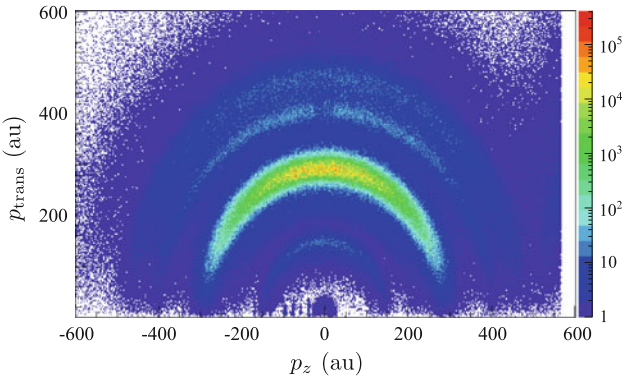

Fig. 5.5 Longitudinal momentum p_z in TOF-direction plotted versus the transversal momentum p_{trans} in the detector plane for all I^{2+} ions. The *rings* indicate fragmentation of the molecule into $I^{2+}+I^{Q+}$: The *innermost ring*—with the lowest momentum—stems from fragmentation into $I^{2+}+I$, the *second ring* from $I^{2+}+I^{+}$ and so forth

5.3.2 Assignment of Coincidences

The assignment of coincident particles is based on momentum conservation: As long as their temperature is not considered, the constituents of a molecule have no relative momentum before the fragmentation, thus the fragments have to have zero total momentum afterwards. For a diatomic molecule this directly implies that the summed momentum components of the two constituents must sum up to zero for each spatial direction:

$$\boldsymbol{p}_{\mathrm{sum}} = \boldsymbol{p}_{\mathrm{ion\,1}} + \boldsymbol{p}_{\mathrm{ion\,2}} = \mathbf{0}. \tag{5.11}$$

The momenta of potentially coincident ion pairs, i.e., ions occurring within a certain time-window, are tested for the momentum sum condition and assigned to each other in the case that all momentum components meet Eq. (5.11). As the molecules already have momentum before their fragmentation due to their finite temperature and the recoil momentum from the electrons, condition Eq. (5.11) is not fulfilled exactly. This is taken into account by assigning a certain window in which the condition is assumed to be fulfilled. Due to the large momenta occurring in the Coulomb explosions of I_2 and Ne_2 the recoil momenta of the electrons are negligible. The momentum sums in x-, y- and z-direction for the exemplary coincidence channel $I^{+}+I^{2+}$ are shown in Fig. 5.6. Note that, the condition can also be fulfilled randomly by a target and a background ion, which would result in a false coincidence.

Even without the calculation of momenta, coincident ions are identified by plotting the TOF of the ion that arrives first at the detector (TOF1) versus that of the ion impinging second (TOF2), as shown in Fig. 5.7. As the momentum in z-direction is approximately proportional to the TOF, the sum TOF1 + TOF2 must be constant for all particles originating from the same molecule. In a spectrum where TOF1 is plotted

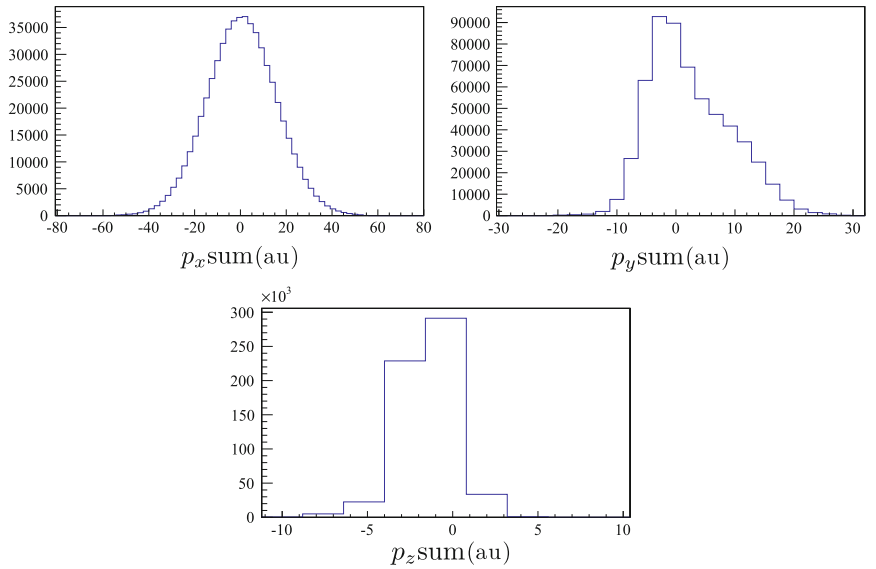

Fig. 5.6 Momentum sums of the exemplary coincidence channel $I^+ + I^{2+}$ in x-, y-, and z-direction

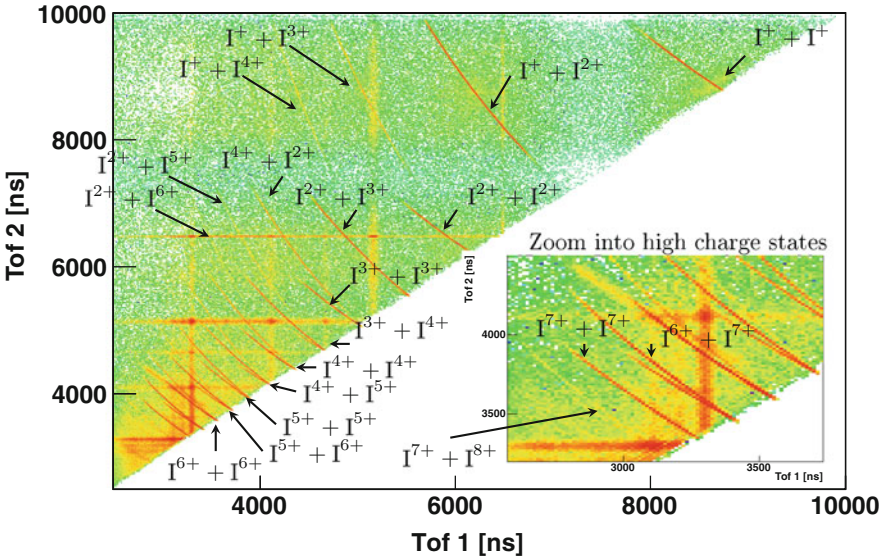

Fig. 5.7 Photo-Ion-Photo-Ion Coincidence (PiPiCo) spectrum: TOF1 of the first particle impinging on the detector plotted versus the TOF2 of the second particle for photoionization of I_2 at 87 eV

versus TOF2 this condition manifests itself as diagonal lines. Figure 5.7 shows an overview of the charge state distribution for the photoionization experiment on I_2 at a photon energy of 87 eV.

5.3.3 Kinetic Energy Release

The kinetic energy release (KER) is the most important observable in our Coulomb-explosion experiments on molecules as it allows to draw conclusions on the geometry of the molecule at the time it was fragmented. The KER equals the summed kinetic energy of all atomic or ionic fragments emerging from photoionization of the molecule. The KER of coincident fragments equals the difference in potential energy of the initial molecular geometry E_0 minus the asymptotic energy E_∞ for infinitely separated particles:

$$\mathrm{KER} = E_0 - E_\infty. \tag{5.12}$$

For a diatomic molecule this reduces to $\mathrm{KER} = E(R_0) - E(R = \infty)$, as illustrated in Fig. 5.8. Due to momentum conservation the fragments of diatomic homonuclear molecules will always have the same kinetic energy. Therefore the KER is the doubled kinetic energy of one of the fragments. However this assumption is only true, if the recoil momentum of the ejected electrons is negligible. For charged fragments emerging from I_2^{n+} and Ne_2^{n+}, this assumption is well justified as an electron recoil of ≤ 1 au barely affects the fragments' total momenta of hundreds to a thousand atomic units.

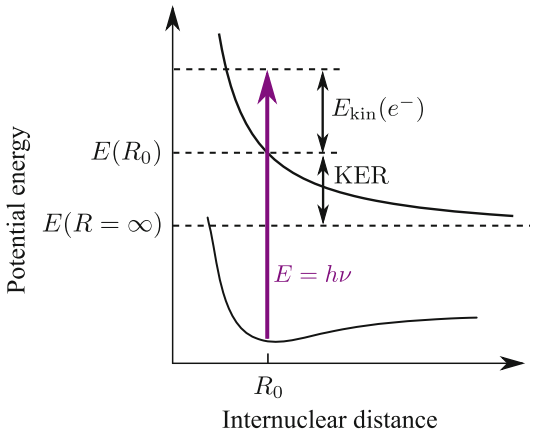

Fig. 5.8 Illustration of the kinetic energy release (KER) for a diatomic molecule. According to the Franck–Condon principle, a photon with energy $h\nu$ ionizes a diatomic molecule at the internuclear distance R_0. The ejected electron gains a kinetic energy of $E_{\mathrm{kin}}(e^-) = h\nu - E(R_0)$ that is equal to the photon energy minus the ionization $E(R_0)$ potential of the molecule. The energy of two asymptotically far away fragments is denoted as $E(R = \infty)$, thus $\mathrm{KER} = E(R_0) - E(R = \infty)$

5.4 Momentum Resolution

The momentum resolution is influenced by many effects. Some of them stem from imperfections of the apparatus, which could in principle be corrected, while other effects are fundamental and thus unavoidable. Due to the geometry of the experiment some effects impact only certain momentum components.

In z-direction the resolution is mainly limited by imperfections of the spectrometer electric field and tilts of the detector with respect to the field lines. The intrinsic detector resolution, which lies in the order of several hundred picoseconds for an MCP [15], is negligible. In x- and y-direction the detector resolution is limited by the width of the signals traveling on the delayline. These signals are broadened due to the dimension of the electron cloud leaving the MCP. However for the large momenta emerging from Coulomb explosions the quality of the electric field is the limiting factor and not the detector resolution.

Furthermore the uncertainty of the starting point of the ions within the jet must be taken into account. For the x- and z-direction, which are perpendicular to the FEL beam, the starting point is confined by the focus size of the laser. This amounts to only 20 and 35 µm per direction, for the neon and iodine measurement, respectively. In contrast, in FEL propagation direction ions are produced along the whole width of the jet, that is adjustable between 1 mm and 200 µm. Thus the spatial uncertainty will be largest in y-direction.

The jet temperature is a further factor broadening the momentum distribution. However, this effect is only relevant for the x-direction as the target temperature is highest in propagation direction of the jet. It is negligible for the y- and z-direction because skimmers reduce the temperature perpendicular to the jet, as discussed in Sect. 4.1.1. The jet temperature could not be determined exactly in the experiment due to the recoil momentum of the electrons transferred to the ions, as shown in Sects. 4.2.1 and 4.3.1.

Due to the high FEL intensity, tens of ions are produced within less than 100 fs in the focus region ($<10^{-4}$ mm^3). This leads to a strong repulsion between the ions that results in space charge broadening of the ion cloud. The expansion of the starting region leads to a non-negligible broadening of the momentum distribution [9]. Only if the number of ions in the focus could be reduced to one, this effect could be avoided. However reduction of the target density requires longer measurement times, which is at this time not feasible due to the limited amount of FEL beamtime.

The high count rates lead to further degrading of the resolution due to saturation effects: For the most abundant target species the number of ions created per FEL pulse usually exceeds by far the possible rate that can be processed by the detectors and the data acquisition system. Therefore the number of created ions is not counted correctly, which is obvious for He^+ in the I_2 experiment (cf. Sect. 4.2.1) and Ne^+ in the Ne_2 experiment (cf. Sect. 4.3.1). However, as we are not interested in the ionized monomer species, but the molecular fragments emerging from Coulomb explosions, these saturation effects do not directly affect the results of the experiments.

Table 5.1 Momentum uncertainty Δp for the I_2 and the Ne_2 experiments for vanishing initial momentum

	x	I_2 y	z	x	Ne y	z
Detector (ns)	0.5	0.5	0.5	0.5	0.5	0.5
Start (μm)	35	200	35	20	1,000	20
Temperature (K)	17	–	–	1	–	–
Δp (FWHM) (au)	12	2.0	0.1	0.35	7.5	0.08

Δp is calculated by applying the law of propagation of uncertainties to Eqs. (5.9), (5.10) and (5.8). The uncertainty in the detector position is estimated to be 0.5 ns and the uncertainty of the start position depends strongly on the direction. Only the longitudinal jet temperature is considered, which was determined in Sect. 4.2.1 for I_2 and for Ne_2 an estimate from similar experiments [8] was taken

The momentum uncertainty of ions with low initial momenta are dominated by the initial temperature of the gas jet for the I_2 measurement and by the width of the jet for the Ne_2 measurement, which is illustrated in Table 5.1. As already mentioned, for large initial momenta the inhomogeneity of the spectrometer field becomes more relevant, as shown in Fig. 5.9. In x- and y-direction the momentum sums should be straight, but they are significantly bend. This introduces an additional uncertainty increasing with the charge of the fragments.

After all, the uncertainty for large momenta in the I_2 measurement amounts to tens of atomic units, but it does not limit the experiment as the different reaction fragments are resolved and separated, as shown in Chap. 6. The most important criterion for

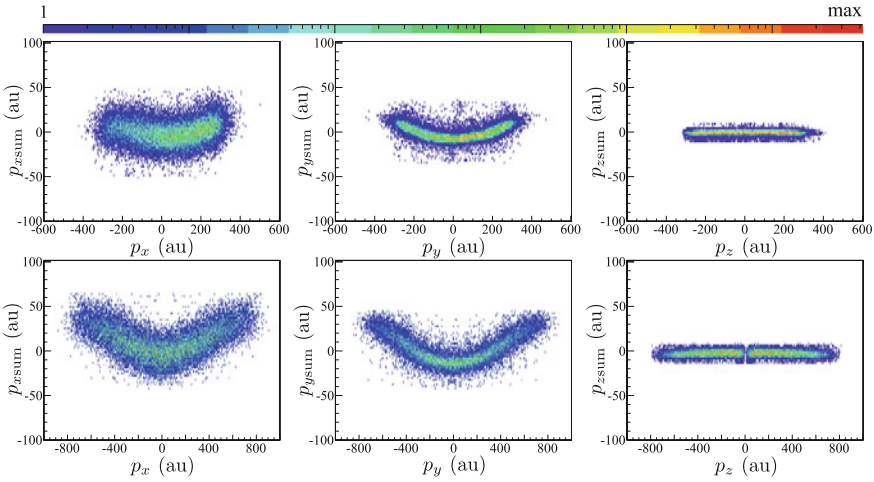

Fig. 5.9 Momentum in x-, y- and z-direction plotted versus the respective momentum sum for the coincidence channel (1, 2) in the *top row* and for (4, 4) in the *bottom row*. The widths of the distributions is broadest in x-direction due to the jet temperature. The bending of the momentum distributions in x- and y-direction is due to inhomogeneities of the spectrometer field. This is the dominant contribution in y-direction and also contributes significantly in x-direction

the Ne_2 measurement was a dense target in order to obtain a high ionization rate for the small rate of dimers present in the jet at the cost of degrading the resolution. For the lifetime determination the momentum resolution is only a minor issue which does not influence the result.

5.5 Acceptance

For the large recoil ion energies that arise from Coulomb explosions, high electric fields must be applied to the spectrometer in order to guarantee full angular acceptance. If the ions' displacement in the (x, y)-plane is larger than the detector radius they are not imaged on the detector area anymore and are lost. As the detection of all particles is crucial for a coincidence measurement, acceptance for all charge states and particle species is needed. Here, only diatomic homonuclear molecules are considered, which are always emitted back to back in a Coulomb explosion. In the studied examples the angular distribution is almost isotropic resulting in momentum spheres with a characteristic radius for each fragmentation charge state.

Full angular acceptance for a certain applied voltage is reached if all ionic fragments from a molecule, in particular those emitted perpendicular to the spectrometer axis, reach the detector. As the jet propagates in x-direction all ions do already have a constant momentum offset in that direction before they interact with the FEL. Therefore the acceptance is worst for particles that are emitted in the x-direction, perpendicular to the spectrometer field. The maximal velocity in that direction v_x is composed of the jet velocity v_{jet} and the velocity emerging from the Coulomb explosion v_{Coul}:

$$v_x = v_{\text{jet}} + v_{\text{Coul}}. \tag{5.13}$$

The KER for a diatomic homonuclear molecule is split equally among the two fragments: $E_1 = E_2 = \text{KER}/2$. This results in a velocity of

$$v_{\text{Coul}} = \sqrt{\frac{\text{KER}}{m}}, \tag{5.14}$$

with m being the mass of each fragment. The KER is approximated by considering the molecular fragments as two point-charges P and Q that repel each other with the Coulomb force at the equilibrium internuclear distance of the molecule R_{eq}:

$$\text{KER} = \frac{P\,Q}{R_{\text{eq}}}. \tag{5.15}$$

The maximal distance x_{max} in x-direction covered by an ion with charge P depends on the particle's velocity and its TOF

Table 5.2 Parameters used to evaluate the acceptance

	U (V)	d_{rad} (cm)	d_a (cm)	v_{Jet} (m/s)	v_{Jet} (au)	R_{eq} (au)
I_2	350	6	10.3	1595	0.00073	5.01
Ne_2	350	6	10.3	919	0.00042	6

$$t = d_a \sqrt{\frac{2m}{PU}}, \tag{5.16}$$

which depends on the spectrometer length d_a, the applied voltage U and the mass-to-charge ratio m/P:

$$x_{\max} = v\,t = \left(v_{\text{Jet}} + \sqrt{\frac{\text{KER}}{m}} \right) t = \left(v_{\text{Jet}} + \sqrt{\frac{\text{KER}}{m}} \right) d_a \sqrt{\frac{2m}{PU}}. \tag{5.17}$$

Full angular acceptance is reached as long as the distance $d_{\max}$ is smaller than the detector radius $d_{\text{rad}} = 6\,\text{cm}$.

First, the acceptance for the iodine experiment will be discussed. One pair of coincident ion pairs $I^{P+} + I^{Q+}$ will be denoted as (P, Q). The experimental parameters are summarized in Table 5.2. The highest charge state observed in the experiment I^{9+} is not covered with full angular acceptance according to Fig. 5.10. However the

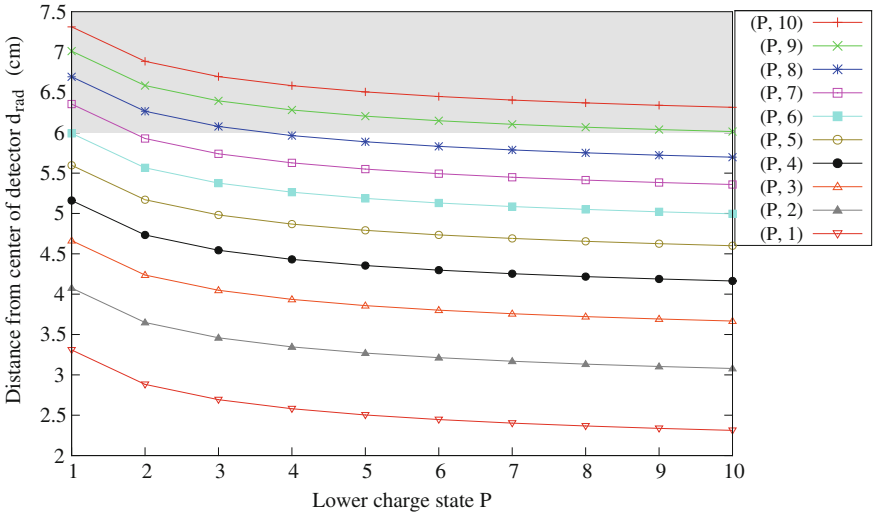

Fig. 5.10 Spectrometer acceptance for the Coulomb explosion of I_2 into $I^{P+} + I^{Q+}$. The acceptance of two coincident ions with different charge states is not the same as the higher charged one has a shorter TOF and thus a better acceptance. The fragment for which the acceptance is considered is denoted as P with its coincident partner Q represented by a *line* for each Q. The *gray shaded area* indicates the limit of acceptance

number of I^{9+} ions is expected to be negligible anyway. The lower charged fragment of the coincidence channels (1, 8), (2, 8), (3, 8) and (1, 7) also cannot be detected at all angles. For all other channels full acceptance is reached.

For the neon experiment the crucial coincidence channel is $Ne^{+} + Ne^{2+}$ as it is used to determine the ICD lifetime. For the applied settings (cf. Table 5.2) full angular acceptance is achieved.

References

1. CERN, ROOT (2013), http://root.cern.ch/
2. CERN, searchHighRes (2013), http://root.cern.ch/root/html/TSpectrum2.html
3. L. Foucar, Auslese von Delaylinedetektoren mit Hilfe von Transientenrekordern. Ph.D. thesis, Frankfurt, 2008, p. 190
4. L.J. Frasinski et al., Dynamics of hollow atom formation in intense X-ray pulses probed by partial covariance mapping. Phys. Rev. Lett. **111**, 073002 (2013)
5. D. Gedcke, W. McDonald, A constant fraction of pulse height trigger for optimum time resolution. Nucl. Instrum. Methods **55**, 377–380 (1967)
6. GSI, Go4 (2013), http://go4.gsi.de/
7. O. Kornilov et al., Coulomb explosion of diatomic molecules in intense XUV fields mapped by partial covariance. J. Phys. B: At. Mol. Opt. Phys. **46**(16), 164028 (2013)
8. K. Kreidi, Untersuchung der Zerfallsmechanismen und der Lokalisierung von Vakanzen in Ne2. Ph.D. thesis, Frankfurt, 2005, p. 201
9. M. Kurka et al., Differential cross sections for non-sequential double ionization of He. New J. Phys. **12**(7), 073035 (2010)
10. M. Kurka, Zwei- und Drei-Photonen Doppelionisation von Helium und Neon am Freie-Elektronen-Laser in Hamburg. Diploma thesis, Heidelberg, 2007, p. 76
11. W.R. Leo, *Techniques for Nuclear and Particle Physics Experiments. A How-to Approach* (Springer, Berlin, 1987)
12. M. Mariscotti, A method for automatic identification of peaks in the presence of background and its application to spectrum analysis. Nucl. Instrum. Methods **50**(2), 309–320 (1967)
13. D. Rolles et al., A velocity map imaging spectrometer for electron-ion and ion-ion coincidence experiments with synchrotron radiation. Nuclear Instruments and Methods in Physics Research Section B: Beam Interactions with Materials and Atoms **261**(1–2) (2007). *Proceedings of the Nineteenth International Conference on The Application of Accelerators in Research and Industry*, pp. 170–174
14. A. Senftleben, Kinematically complete study on electron impact ionisation of aligned hydrogen molecules. Ph.D. thesis. Heidelberg, 2009
15. Q. Zhang, K. Zhao, Z. Chang, Determining time resolution of microchannel plate detectors for electron time-of-flight spectrometers. Rev. Sci. Instrum. **81**(7), 073112 (2010)

Chapter 6
Ionization Dynamics of I_2 in XUV and IR Laser Pulses

The study of shape resonances (cf. Sect. 2.3.1) in atomic shells with high angular momentum has been an active area of research since synchrotron sources are routinely available [8, 15, 58]. Two prominent examples that feature shape resonances in their $4d$ shells are Xe [4] and I_2 [14] for photon energies around 90 eV. The resonance leads to high $4d$ photoionization cross sections and the removal of inner-valence electrons, that triggers Auger cascades [3, 43]. Consequently the absorption of a single photon may result in triply ionized atoms and molecules.

With the advent of FELs, which deliver orders of magnitude higher brilliances than synchrotrons, the large cross sections have been exploited to study multi-photon absorption in the regions of the resonances [57, 74, 75]. One prominent experiment, performed at FLASH, has reached Xe^{21+} within a single FEL pulse [68]. The goal of these studies is to identify the pathways of multi-photon absorption in highly intense FEL radiation, which have also been pursued for higher photon energies at LCLS and SACLA: Ne was fully stripped [22, 40, 77] and the ionization dynamics of heavier atoms was studied by means of Xe [35], which was ionized 36 fold [60] and 16 electrons were removed from Kr [61]. The production of these high charge states is possible via sequential single-photon ionization and direct multi-photon absorption, as introduced in Sect. 2.1.1. The observed charge state yield for Xe and Kr was enhanced compared to the model of sequential photon absorption due to the resonant population of intermediate excited states. The effect is called resonance-enabled X-ray multiple ionization (REXMI) [60].

While the previously presented studies gave insight into the interaction of intense XUV and X-ray radiation with single atoms, the interesting question arises, how molecules respond to it. This question was for instance addressed in an experiment on the multiple ionization of N_2 [39]. It showed a suppressed formation of high charge states for few femtosecond pulses, which were present for longer pulses. Further studies on small molecules were carried out with emphasize on the creation of double core holes [17, 31, 49, 63], a process that became only recently accessible with the high intensities of FELs.

Understanding the dynamics of molecules, initiated by the absorption of X-ray photons, is crucial for the realization of single-molecule imaging at FELs. As imaging

K. Schnorr, *XUV Pump-Probe Experiments on Diatomic Molecules*,
Springer Theses, DOI 10.1007/978-3-319-12139-0_6

relies on the "diffract before destroy" concept [51], it must be ensured that the reconstructed structure is still that of the intact molecule. Therefore charge relaxation, transfer and the accompanied nuclear motion must be investigated on the femtosecond time scale, the duration of the FEL pulses. Particularly, the localized photon absorption at heavy constituents efficiently triggers electron transfer throughout the molecule within a few femtoseconds. This has been investigated in two recent studies on methylselenol [27] and ethylselenol [28], which contain selenium atoms as heavy absorption center. Even for 5 fs FEL pulses charge rearrangement and considerable displacement of the constituents was observed.

Charge transfer within a molecule is studied best by the underlying dynamics by means of the the most simple system, a diatomic molecule. The iodine molecule serves as an excellent model system due to the large photoabsorption cross section in the region of the shape resonance and the slow dissociation dynamics. IR/XUV pump-probe studies at FLASH have already exploited I_2 for time-resolved dissociation studies [44].

In this chapter the dynamics of iodine molecules induced by intense XUV and strong IR pulses is studied. While XUV photons efficiently remove electrons from inner shells, the IR laser only acts on the least bound valence electrons. In Sect. 6.1 the interaction of a single FEL pulse with I_2 is discussed. This knowledge enables the interpretation of XUV pump-probe experiments that are presented in Sect. 6.2. The interaction of a strong IR laser (800 nm) on I_2 is discussed in Sect. 6.3. The chapter closes with the interpretation of IR/XUV pump-probe spectra.

6.1 Single XUV Pulse Measurements

The 4*d* shape resonance in I_2 results in large photoionization cross sections around 90 eV, that is presented in Sect. 6.1.1. The interaction of a single photon with I_2 is discussed in Sect. 6.1.2. Multi-photon absorption is introduced in Sect. 6.1.3 by means of Xe atoms, which feature a well studied similar shape resonance. Bearing in mind the gained knowledge from Xe, multi-photon absorption in I and I_2 is discussed in Sect. 6.1.4. The charge-state yield for exemplary coincidence channels for different intensities is compared in Sect. 6.1.5. Part of this section has been published in [66].

6.1.1 Cross Section in the Region of the Shape Resonance

The chosen photon energy of 87 eV is close to the maximum of the 4*d* shape resonance in I_2 (cf. Sect. 2.3.1): Earlier studies found the maximum to be at 92 eV [14] and 96 eV [7]. The total cross sections for atomic and molecular iodine around 90 eV are dominated by the contribution from the 4*d* subshell which accounts to more than 80 % of the total cross section [71]. The contributions from subshells other than 4*d* mainly stem from 5*p* valence ionization. The absolute value for the cross sections in neutral

iodine are controversial: The 4*d* subshell cross section at 90 eV was experimentally determined for methyliodine to be 11 Mb [47, 54]. For atomic iodine, dissociated from I_2, the contribution was determined to be 6.5 Mb [71]. Another experiment, in which the individual subshell contributions were not measured, yielded a total cross section of 19 Mb for I_2 at 90 eV [14].

All mentioned measurements on neutral iodine disagree with calculations predicting cross sections of significantly higher values of approximately 30 Mb for a single iodine atom [2]. However, the same calculations for I^{1+} and I^{2+} ions do agree with measurements, which determine cross sections of 23 and 24 Mb, respectively [43]. The experimental results for neutral iodine have large error bars due to uncertainties in the gas density. In contrast, for charged targets a beam is formed allowing a direct density measurement. Therefore we estimate the 4*d* cross section of I_2 by taking twice that of I^+, i.e., roughly 40 Mb at 87 eV.

The assumption of a high cross section is also supported by measurements on atomic Xe which has a similar 4*d* shape resonance. In Xe, Xe^+ and Xe^{2+} the photoionization cross sections of all subshells except 4*d* are almost negligible (<10 %) and the absolute cross sections lie between 20 and 30 Mb at the maximum of the shape resonance [3]. In contrast to iodine the measured cross sections for neutral and charged Xe species agree well. One reason could be that for Xe well calibrated gas cells are used that allow a more precise determination of the gas density [43].

6.1.2 Single-Photon Absorption in I_2

The absorption of one 87 eV photon in I_2 leads most likely to the creation of a 4*d*-type vacancy. The binding energies of the 4*d* electrons lie between 56 and 61 eV [50]. The maximum of the distribution of $4d_{5/2}$ electrons is located at 57.2 eV and that of the $4d_{3/2}$ electrons at 59.0 eV. The highly excited 4*d* hole-state relaxes via a single Auger decay (A1) leading to I_2^{2+} or via a cascade of two Auger processes (A1 + A2) resulting in I_2^{3+} [7]. A1 occurs within a few femtoseconds (≈5 fs) [18] and is consequently assumed to take place instantaneously. It is reasonable to neglect the influence of the finite lifetime of A1 on the dissociation dynamics since nuclear motion is roughly two orders of magnitude slower: Two singly-charged point-like particles, repelling each other with the Coulomb force, need for instance 150 fs to expand from the I_2 equilibrium internuclear distance of 5 au to the doubled distance. The lifetime of A2 was determined recently to be 23 fs [44], which can still be considered fast compared to the slow dissociation.

In our experiment, only a small fraction of I_2^{2+} and I_2^{3+} molecular ions remains stable until they reach the detector. This was investigated in a low intensity study with an attenuated FEL beam where roughly 10 % of the detected I_2^{2+} ions and less than 1 % of the I_2^{3+} ions did not dissociate. An earlier synchrotron measurement found similar ratios [7]. This observation is not surprising considering the abundance of dissociative I_2^{2+} states compared to bound ones in Fig. 6.5 as well as the small energy difference necessary to overcome the dissociation barrier.

Molecular ions mostly break up into fragments with symmetric charge-state distribution as this is energetically more favorable. However we also find a small fraction of I_2^{2+} ions that dissociate asymmetrically into $I^{2+} + I$, but they account for less than 1 % of all fragmented doubly charged molecular ions. In summary, a single 87 eV photon creates I_2^{2+} and I_2^{3+} molecular ions that mainly fragment according to

$$I_2 \xrightarrow{h\nu} I_2^{+*} \xrightarrow{A1+A2} I_2^{3+} \longrightarrow I^{1+} + I^{2+}, \tag{6.1}$$

$$I_2 \xrightarrow{h\nu} I_2^{+*} \xrightarrow{A1} I_2^{2+} \longrightarrow I^{1+} + I^{1+}, \tag{6.2}$$

$$I_2 \xrightarrow{h\nu} I_2^{+*} \xrightarrow{A1} I_2^{2+} \longrightarrow I + I^{2+}. \tag{6.3}$$

6.1.3 Multi-photon Absorption in Xe

The maximum of the 4*d* shape resonance in Xe is shifted to a slightly higher energy of 100 eV [24] as compared to I because of the additional electron. Many synchrotron studies on the properties of the shape resonance in Xe have been carried out [64]. In recent years this area has experienced a revival when intense XUV sources, such as FLASH, became available and allowed to extend measurements into the multi-photon absorption regime [57, 68, 74, 75]. A pioneering experiment exploited the large photoabsorption cross sections in the region of the shape resonance in Xe resulting in spectacular high charge states up to Xe^{21+} with intensities of $10^{16}\ \frac{W}{cm^2}$ at 93 eV [68]. This required the absorption of 60 photons within the 10 fs pulse duration.

The high charge states are produced by sequences of one or multi-photon processes. The created ion serves as target for further photon absorption in order to perform the next ionization step. Exemplarily, we sketch the first few steps of multi-photon absorption in Xe: One 93 eV photon creates Xe^{2+} or Xe^{3+} via photoionization and subsequent Auger decay. The created ions are targets for the next photon that is absorbed within the same pulse resulting in the creation of Xe^{4+}. If Xe^{4+} is produced via the intermediate Xe^{2+} state, photoionization with subsequent Auger decay is the relevant mechanism [3]. From Xe^{3+} onwards the photon energy is not anymore sufficient to directly remove another 4*d* electron, thus 5*p* photoionization becomes the most probable process [6, 26]. However this is only possible until the 5*p*-shell is depleted, which is reached with the charge state Xe^{6+}. An exception is the ionization of Xe^{4+} which is enhanced by an autoionization resonance [1], which will also become relevant for I_2 as described in Sect. 6.1.5. In order to remove a 5*s* electron from Xe^{6+} an energy of 92 eV is needed which is close but still below the photon energy. The following ionization step from Xe^{7+} to Xe^{8+} requires the direct absorption of two photons and the transition from Xe^{10+} to Xe^{11+} even requires three-photon absorption.

We have performed a calibration measurement with Xe at 87 eV in order to estimate the present FEL intensity. The highest charge state reached is Xe^{8+}, as shown in Fig. 6.1. The first charge state which can only be produced via direct two-photon

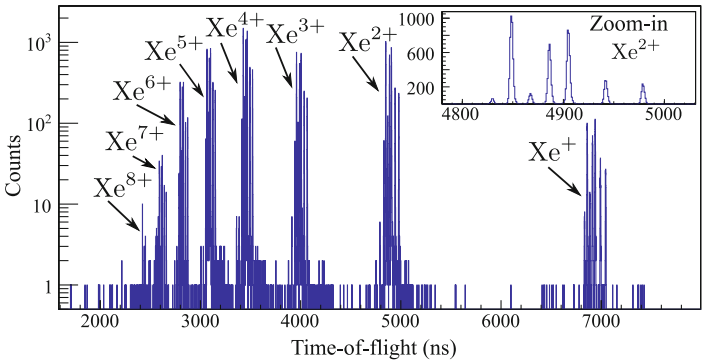

Fig. 6.1 TOF spectrum of Xe, recorded at a photon energy of 87 eV with an intensity of roughly $10^{14}\ \frac{\mathrm{W}}{\mathrm{cm}^2}$. The two highest charge states Xe^{7+} and Xe^{8+} are only producible via direct two-photon absorption. The *inset* shows a zoom into the charge state Xe^{2+} with its isotopes. The isotope ratio for all charge states was found to be the same, which is a good method to check whether saturation effects affect the charge state yield

absorption is Xe^{7+}. As the two highest charge states, requiring direct two-photon absorption, show up in the data weakly, we conclude that the dominant process was sequential single-photon absorption. Some of the aforementioned mechanisms of photon absorption in Xe are well reproduced in our spectrum: The expected suppression of Xe^{+} ions due to the dominance of the 4*d* subshell cross section and the enhancement of Xe^{4+} due to its two precursor states. By comparing the recorded charge state yield with that of earlier measurements at FLASH [57, 68] the present FEL intensity is estimated to be $10^{14}\ \frac{\mathrm{W}}{\mathrm{cm}^2}$.

6.1.4 Single-Photon Absorption in Iodine

We studied the multi-photon absorption in I_2 at two different FEL settings, which are summarized in Table 6.1. For Setting 1 the intensity was similar to that of the Xe experiment yielding charge states as high as I_2^{14+}. The measurement with Setting 2 at higher intensities reached charge states up to I_2^{17+}. In order to explain the creation of the lower charge states (up to I_2^{7+}) photoionization as well as Auger decay must be taken into account, while the higher charge states are dominantly produced via sequences of single-photon and direct two- and three-photon absorption.

Table 6.1 Summary of the pulse parameters for Setting 1 with lower intensity and shorter pulses, and Setting 2 with higher intensity and longer pulses

Setting	Photon energy (eV)	Pulse length (fs)	Intensity ($\frac{\mathrm{W}}{\mathrm{cm}^2}$)	No. of minibunches
1	87	<57	1×10^{14}	30
2	87	<103	3×10^{16}	30

The pulse length is estimated in Sect. 6.2.4 and the intensity is obtained by comparison to Xe spectra

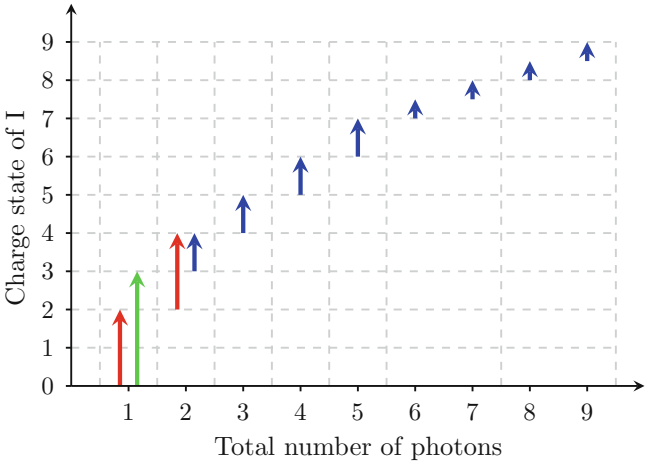

Fig. 6.2 Stepwise ionization of atomic iodine as a function of the total number of required photons: *Red arrows* indicate photoionization followed by one Auger decay, the *green arrow* indicates photoionization followed by a cascade of two Auger decays, *blue arrows* represent photoionization only. When the energy of one photon is not sufficient to overcome the next ionization threshold, two photons must be absorbed, which is illustrated by *arrows* of half length. The required ionization potentials are taken from Table 6.2

6.1.4.1 Multi-photon Absorption in I

To understand the pathways leading to the observed charge states in I_2 we will briefly discuss the ionization of atomic iodine, which is very similar to xenon. The production of the relevant iodine charge states is summarized in Fig. 6.2 and the ionization potentials are listed in Table 6.2. One photon creates a $4d$ inner-shell vacancy that relaxes by one or two Auger processes [71] resulting in I^{2+} or I^{3+}, respectively, as indicated by the red arrows in Fig. 6.2. The cross section of I^{2+} is also dominated by the ionization of the $4d$ subshell, which initiates another Auger process leading to I^{4+} [43]. From I^{3+} on, $5p$ valence shell ionization becomes dominant augmenting the charge state by only one per absorbed photon, as indicated by the blue arrows in Fig. 6.2. The $5p$ shell is completely depleted by the time I^{5+} is reached and thus the $5s$ shell will be emptied. The ionization energy of the transition from I^{6+} to I^{7+} is at the limit of the photon energy of 87 eV, but may still be accessible due to the finite bandwidth of the FEL. For the transition from I^{7+} to I^{8+} two photons are required to overcome the ionization threshold, which is indicated by the two short blue arrows in Fig. 6.2. Finally, for the transition from I^{9+} to I^{10+} even three photons are needed.

6.1.4.2 Multi-photon Absorption in I_2

In order to evaluate each ionization step in I_2 the ionization potentials up to the highest observed charge states I_2^{17+} are required. As the highest experimentally explored

Table 6.2 Lowest ionization potentials E_Q for I^{Q+} and estimated potentials E'_Q for $I_2^{Q'+}$

$Q+ \rightarrow (Q+1)+$	E_Q (eV) $I^{Q+} \rightarrow I^{(Q+1)+}$	Photon number	E'_Q (eV) $I_2^{Q+} \rightarrow I_2^{(Q+1)+}$	Photon number
$0 \rightarrow 1$	10.4 [30]	1	9.35 [34]	1
$1 \rightarrow 2$	19.1 [29]	1	15.7	1
$2 \rightarrow 3$	29.6 [69]	1	24.4	1
$3 \rightarrow 4$	40.4 [70]	1	29.7	1
$4 \rightarrow 5$	51.2 [42]	1	40.2	1
$5 \rightarrow 6$	74.4 [42]	1	45.5	1
$6 \rightarrow 7$	87.6 [41]	1	56.3	1
$7 \rightarrow 8$	150.8 [12]	2	61.6	1
$8 \rightarrow 9$	171.0 [59]	2	72.4	1
$9 \rightarrow 10$	197.0 [59]	3	77.7	1
$10 \rightarrow 11$	–	–	100.9	2
$11 \rightarrow 12$	–	–	106.2	2
$12 \rightarrow 13$	–	–	119.4	2
$13 \rightarrow 14$	–	–	124.7	2
$14 \rightarrow 15$	–	–	187.9	3
$15 \rightarrow 16$	–	–	193.2	3
$16 \rightarrow 17$	–	–	213.4	3
$17 \rightarrow 18$	–	–	213.4	3

The latter is calculated under the assumption that I_2 remains at the equilibrium internuclear distance $R_{eq} = 5.01$ au. The photon number indicates how many photons must be absorbed in order to reach the next charge state

valence ionization potential is that for I_2^{2+} [25], we have to find a way to estimate the missing values. In this estimate only the ionization potential of the least bound electron of each atom is considered as this is most relevant for the production of the high charge states. Molecular properties are neglected in the following. For an iodine ion I^{Q+}, the influence of a neighboring ion I^{P+} is taken into account by assuming that the Coulomb potential of I^{P+} leads to tighter bound electrons of I^{Q+}. Thus, the binding energy of the least bound electron of I^{Q+} ($E_Q < 0$) is increased to

$$E'_Q = E_Q - \frac{P}{R}, \tag{6.4}$$

where R is the internuclear distance between the two ions. The molecule is assumed to fragment into the most symmetric configuration, e.g., I_2^{5+} dissociates into $I^{2+}+I^{3+}$. The estimated ionization potentials of the transition $I_2^n \rightarrow I_2^{n+1}$ at the equilibrium internuclear distance $R_{eq} = 5.01$ au are given in Table 6.2. To test the quality of our estimate we compare the experimentally determined double ionization potential $E(I_2 \rightarrow I_2^{2+}) = 24.95 \pm 0.02$ eV [25] with the calculated value of 25.05 eV from Table 6.2. Both are in very good agreement, supporting our assumption (Fig. 6.3).

We will now return to the discussion of the stepwise ionization of I_2. As described in Sect. 6.1.2, a single photon creates I_2^{2+} or I_2^{3+}. In analogy to iodine monomer ions (I^{1+} and I^{2+}), we assume that a second photon interacting with I_2^{2+} and I_2^{3+} mainly

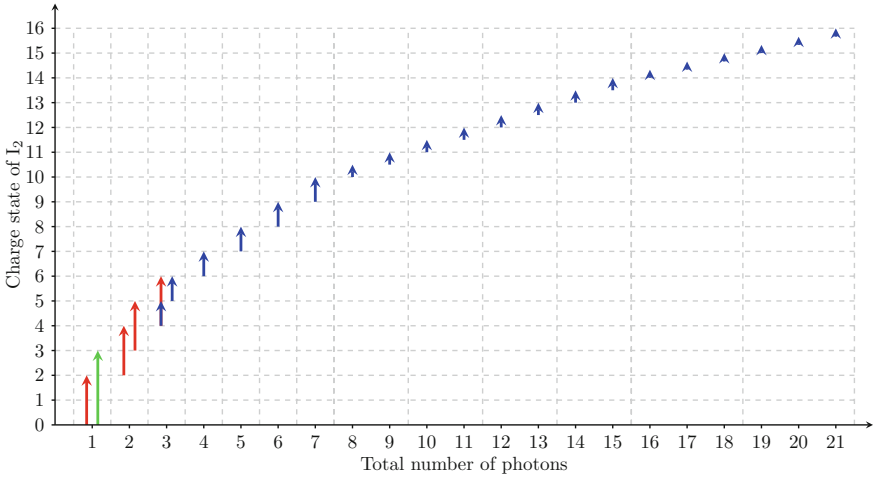

Fig. 6.3 Stepwise ionization of I_2 as a function of the total number of required photons: *Red arrows* indicate photoionization followed by one Auger decay, the *green arrow* indicates photoionization followed by a cascade of two Augers and *blue arrows* represent photoionization only. When the energy of one photon is not sufficient to overcome the next ionization threshold, two or three must be absorbed, which is illustrated by *arrows* of half and one third length. The required ionization potentials are taken from Table 6.2. Note that from I_2^{4+} on valence and inner-shell ionization compete (indicated by *red* and *blue arrow* on *top* of each other)

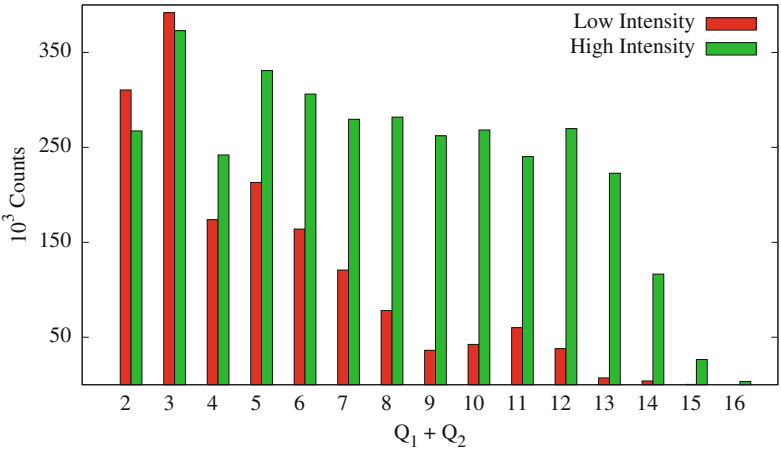

Fig. 6.4 Charge state distribution for the low intensity (*red*) and the high intensity (*green*) measurement. On the x-axis the summed charge of the ion fragments is indicated. The small amount of low charge states in the high intensity measurement may be attributed to saturation effects. In addition the contribution of background in the high intensity data may be slightly larger, as more false coincidences are detected for higher count rates and particularly for high charge state as their TOFs overlap with the dominant background species

creates further $4d$ vacancies. These vacancies relax via Auger decay (A3) [25] leading to I_2^{4+} and I_2^{5+}, respectively:

$$I_2^{2+} \xrightarrow{h\nu} I_2^{*3+} \xrightarrow{A3} I_2^{4+} \longrightarrow I^{2+} + I^{2+}, \tag{6.5}$$

$$I_2^{3+} \xrightarrow{h\nu} I_2^{*4+} \xrightarrow{A3} I_2^{5+} \longrightarrow I^{2+} + I^{3+}. \tag{6.6}$$

These pathways are understood from the comparison with the respective monomer ions. The partial cross sections at 90 eV for the $4d$ subshell ionization of I^+ and I^{2+} are 23 ± 3 Mb and 24 ± 4 Mb respectively, and account for roughly 90 % of the total cross sections [25]. We assume a similar behavior for the molecule, as for instance I_2^{2+} may be considered as combination of two I^{1+} ions.

From I_2^{4+} onwards valence ionization and $4d$ inner-shell ionization compete, which we conclude from the ratio of I_2^{4+} and I_2^{5+} ions in Fig. 6.4. The number of I_2^{5+} ions is enhanced because it features two precursors. However, the exact ratio between inner-shell and valence ionization is not known. Finally, from I_2^{5+} onwards only single valence ionization is energetically allowed and increases the charge state by one per photon.

For the low intensity measurement we observe a sharp drop in the ion yield beyond the coincidence channel $I^{6+} + I^{6+}$, as shown in Fig. 6.4. This drop stems from the increasing height of the ionization potential. From some charge state onwards, here from I_2^{12+}, it cannot be overcome with the energy of one photon. Thus a direct

two-photon absorption is required to reach the next higher charge state. The probability for this process is proportional to the squared intensity and thus much smaller than that of a single-photon absorption, which goes linearly in the intensity. A discussion on the different mechanisms of multi-photon absorption may be found in Sect. 2.1.1.

At first, this may seem in contradiction to our estimated ionization potentials listed in Table 6.2. There, direct two-photon absorption is required from I_2^{10+} onwards. However it should be recalled that these binding energies are only a rough estimate. Particularly they are calculated for a static internuclear distance of 5.01 au. This assumption is invalid once the absorption of several photons within one pulse is required, as being the case for the higher charge states. As the first photon already triggers the dissociation of the molecule and subsequent photons are absorbed at any time during the pulse, the molecular ion is given a whole pulse duration to increase the internuclear distance before it reaches its final charge state. For instance, within 100 fs two singly charged I^{1+} ions increase their internuclear distance to 7 au. As the distance between the ions increases during the pulse, the ionization potential decreases and charge states that cannot be populated at R_{eq} may become accessible. Reaching higher charge states than expected may also be possible due to resonantly excited intermediate states: While a direct transition with one photon is not possible anymore from a certain charge state on, it might well be possible for a previously excited ion. If the excited ion is created by a resonant transition, the ionization may get very efficient, although the required energy is above the single-photon ionization threshold. Resonance enhanced ionization was already observed for Xe and Kr for higher photon energies [60, 61].

For the high intensity measurement we observe a similar sharp drop in the ion yield beyond the coincidence channel $I^{7+} + I^{7+}$ originating from I_2^{14+}, as shown in Fig. 6.4. In analogue to the low intensity case, we conclude that from ionization step $I_2^{14+} \rightarrow I_2^{15+}$ onwards three-photon absorption becomes necessary, which is suppressed due to the higher order in the photon number. The estimated ionization potential with the assumption of fixed nuclei predicts the three-photon absorption from I_2^{14+} onwards, which is in good agreement with the experiment.

It should be noted that the number of photons in Fig. 6.3 is only a rough estimate and the real values may differ from the assumed. Our results hint towards a maximum of direct two-photon ionization for the lower intensity measurement and a maximum of direct three-photon ionization for the higher intensity. For the shorter pulses higher charge states than expected from the frozen nuclei approximation were observed.

All considerations made here assume, that Auger decay has occurred before the next photoionization takes place. The situation would get much more complicated if the first 4*d* photoionization is followed by a second or third one in competition with Auger decays. This way so called hollow atoms with multiple core holes are created, where the inner shells are depleted [31, 33]. In general this occurs in studies with higher intensities, shorter pulses, or higher photon energies where longer, more complicated Auger cascades are initiated. Therefore, we assume that these effects are negligible for our pulse parameters.

6.1.5 Coulomb-Explosion Imaging in I_2^{n+}

To this point the multi-photon absorption which leads to charge states up to I_2^{17+} has been discussed. It is thus convenient to introduce the method used to identify the different charge states. In this approach the kinetic energy release (KER) of coincident ions, as introduced in Sect. 5.3.3, is used to identify their charge states. The detected KER of a coincident ion pair equals in good approximation the energy that a point-like particle with reduced mass gains by moving on the respective potential energy curve (cf. Sect. 2.6). In order to make use of this approximation the potential energy curves must be known. However, the electronic configuration of atomic iodine is complicated due to the large number of electrons and the situation gets even more challenging when the molecule, I_2, is considered. A large number of accessible potential energy curves have to be considered, forming so called molecular bands. The individual populated states are not resolvable in the analysis, particularly without knowledge of the momenta of the ejected electrons. In addition, no theoretical potential energy curves exist beyond I_2^{2+}.

Thus, the situation is simplified by assuming purely Coulombic potential energy curves, which will be referred to as Coulomb-explosion model in the following:

$$\mathrm{KER} \approx E(R) = \frac{P\,Q}{R}, \tag{6.7}$$

with P and Q being the charges of the fragments. In general, the potential curves of dissociating molecular ions are well approximated by purely Coulombic potential energy curves for large internuclear distances. At small distances the curves may have very complicated shapes with potential wells (cf. Fig. 6.5). The assumption is only exact for systems without electrons. Iodine on the other hand features many electrons, which is an adverse prerequisite for the model. However, iodine exhibits a large equilibrium internuclear distance, which justifies the application of the model. In general, any deviation of the data from the KER calculated via Eq. (6.7) allows to draw conclusions on the populated potential energy curves and nuclear dynamics within the molecular ion. From now on, coincident ion pairs will be denoted as (P, Q) instead of $I^{P+} + I^{Q+}$. In the following, a selection of coincidence channels is discussed. In Fig. 6.7 the KERs of exemplary coincidence channels are compared to the result of the Coulomb-explosion model calculated at $R_{\mathrm{eq}} = 5.01$ au using Eq. (6.7). We describe the conclusions that can be drawn from the comparison in the following.

6.1.5.1 Coincidence Channels from Single-Photon Absorption

For the fragmentation into (1, 1) a KER of 5.4 eV is expected according to Eq. (6.7), but a slightly larger one of 5.9 eV is observed in the experiment (cf. Fig. 6.6). Thus, according to our model, the molecule should have decreased its internuclear distance to 4.6 au before its fragmentation, which would then result in a larger KER. Actually,

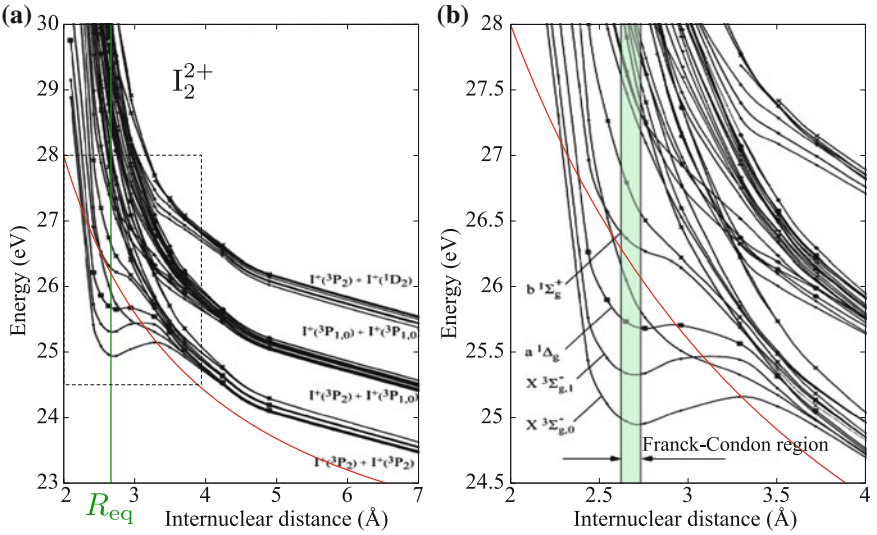

Fig. 6.5 Comparison of a Coulombic potential curve (*red*) with calculated potential energy curves of I_2^{2+}, taken from [25]. The asymptotic value of the Coulomb curve is twice the single ionization potential of I given in Table 6.2. **a** Overview for the region of internuclear distances from 2 to 7 Å. The *dashed rectangle* indicates a zoom-in, which is shown in (**b**)

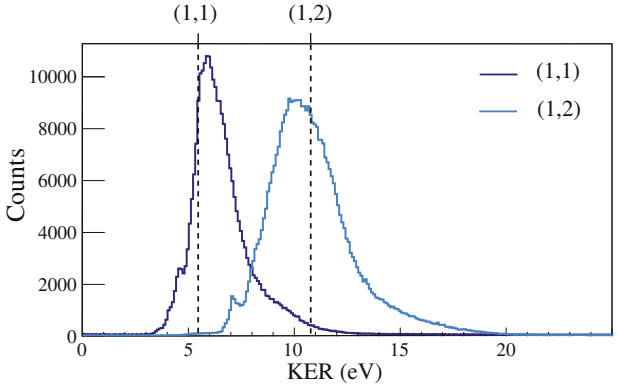

Fig. 6.6 KER of the coincidence channels (1, 1) and (1, 2) in comparison to the expectation values from the Coulomb explosion of charged point-like particles (indicated by *dashed vertical lines*)

we see a limitation of our assumption of purely Coulombic curves here. In Fig. 6.5, a comparison between a Coulomb potential corresponding to two singly-charged point-like particles (in red) and more sophisticated calculated potential energy curves (black) for I_2^{2+} are shown. Within the Franck–Condon region most of the accessible "real" curves have larger values than the Coulombic one. According to Eq. (5.12) this results in larger KERs, which is in agreement with the experimental observation. The coincidence channel (1, 1) shows a slight shoulder at 4.8 eV in Fig. 6.6. It originates

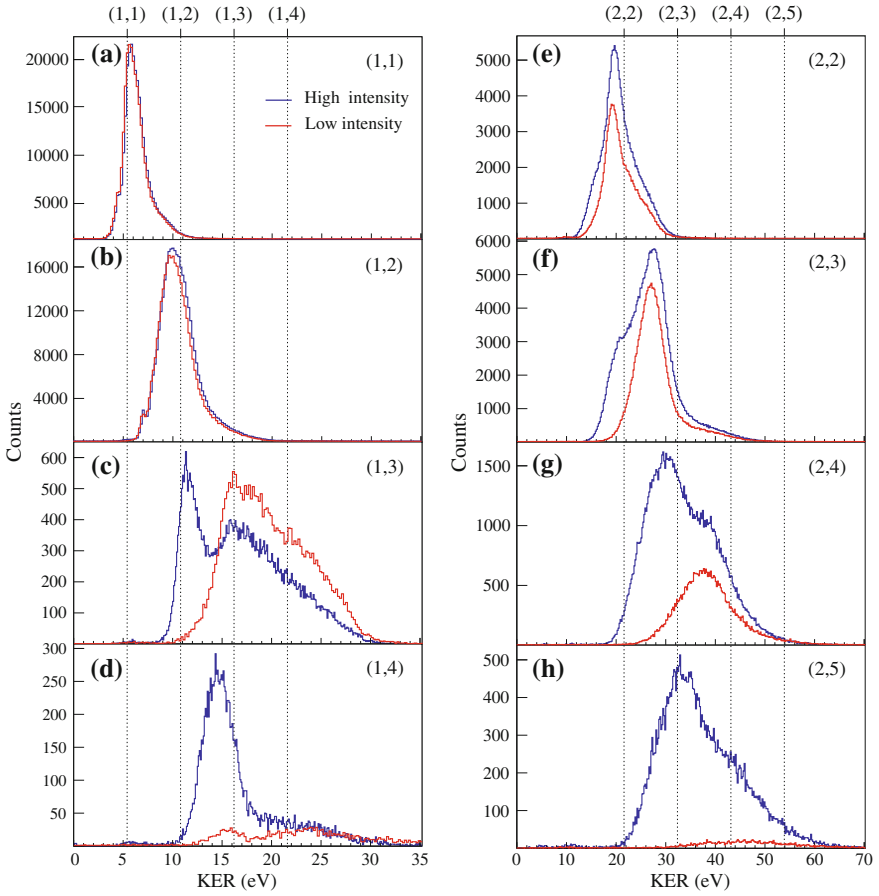

Fig. 6.7 Spectra of coincident iodine ion pairs, denoted by (P, Q) in the *upper right corners*, created within a single XUV pulse. Two different measurements are shown, the *red curves* are recorded with pulses of roughly 57 fs at an intensity of approximately $10^{14}\ \frac{\mathrm{W}}{\mathrm{cm}^2}$ and the *blue curves* with a pulse duration of roughly 103 fs at a higher intensity of approximately $3 \times 10^{14}\ \frac{\mathrm{W}}{\mathrm{cm}^2}$. The *dashed lines* indicate the expected KERs calculated via the Coulomb-explosion model

from metastable I_2^{2+} ions that fragment into two I^+ ions on their way to the detector. Thus the Coulomb explosion is delayed and the spectrometer length is effectively shortened. This results in the reconstruction of smaller KERs as compared to ions that fragment at the interaction point.

The fragment pair (1, 2) has its KER maximum shifted towards lower values than expected from the Coulomb-explosion model. This hints towards expansion of the molecular ion before the final charge state was reached: An excited doubly charged molecular ion starts to dissociate before the second Auger decay, with a lifetime of 23 fs, leads to the final charge state (1, 2):

$$I_2^{2+*} \rightarrow I^{+*} + I^{1+} \rightarrow I^{2+} + I^{1+}. \tag{6.8}$$

In addition, the width of the KER distribution for (1, 2) is broader than for (1, 1) (cf. Fig. 6.6). This is a strong indicator for a smeared-out internuclear distance at which the fragmentation into the final charge states started. This is attributed to the exponential nature of the Auger decay. The small shoulder shifted to smaller energies is explained with the same phenomena of delayed fragmentation of a I_2^{3+} molecular ion, as introduced for the coincidence channel (1, 1) above.

6.1.5.2 Coincidence Channels Produced by Multi-photon Absorption

To this point only coincidence channels that are produced via single-photon absorption were discussed. Therefore pulse shape and length effects could be neglected. For multi-photon absorption they must be taken into account. The effect of a finite pulse length is introduced by means of the coincidence channel (2, 2), which is produced via two-photon absorption within one pulse. The maximum energy is centered around 20 eV (cf. Fig. 6.7e), which is slightly lower than the value expected for instantaneous fragmentation at R_{eq} into (2, 2) amounting to 21.8 eV. As the two photons, required to reach the final charge state, are absorbed at any time during the pulse, the first photon triggers a dissociation which leads to an increased internuclear distance by the time the second photon is absorbed. Therefore, the overall KER decreases with increasing pulse length and with the number of photons needed to reach a specific charge state. The same is true for the high energetic maximum of (2, 3) at 28 eV (cf. Fig. 6.7f), which is shifted towards lower energies as compared to instantaneous fragmentation. A comparison between the KERs predicted for a Coulomb explosion at R_{eq} with the measured KERs of all observed channels is shown in Fig. 6.8. The agreement between the Coulomb-explosion model and the measured KERs gets

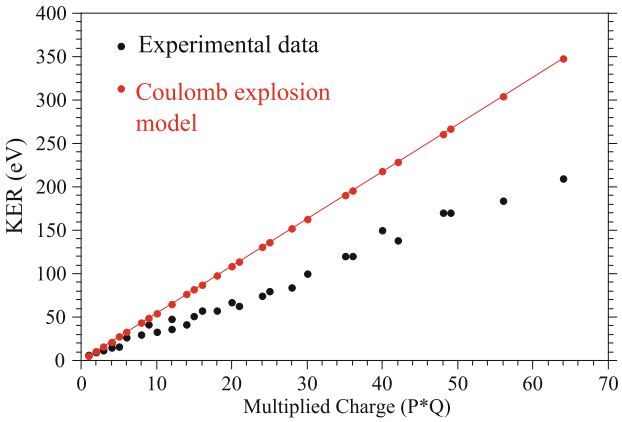

Fig. 6.8 Comparison between predictions made with the Coumlomb-explosion model (*red markers*) at R_{eq} with the measured KERs (*black markers*) for the high intensity setting, for all observed coincidence channels. The *black markers* correspond to the positions of the maxima in the KER distribution

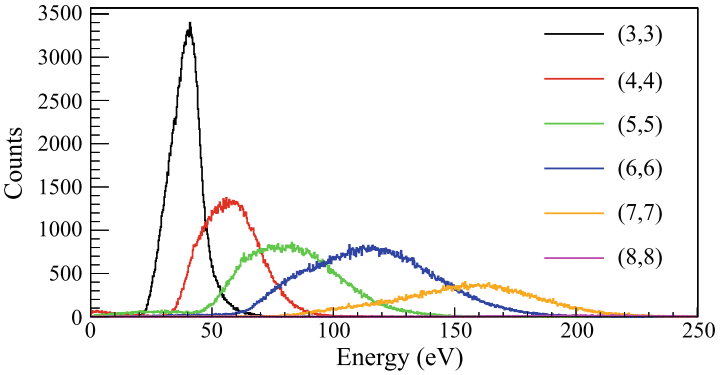

Fig. 6.9 KER distributions for symmetric break-up channels at the high intensity setting. Note that the widths of the distributions increase drastically with the charge state

worse with increasing charge states. As the charge states become higher, more and more photons need to be absorbed, resulting in various intermediate charge states, that are further ionized within the pulse. The higher the charge state the steeper the corresponding Coulomb curve and consequently the created ions move further apart before the next photon is absorbed. This results in smaller KERs compared to channels which require only few photons with low charged intermediate states that dissociate slower.

The width of the KER distribution increases with the charge state, as shown in Fig. 6.9. This is partially attributed to delayed multi-photon absorption within one pulse at random times. Additionally, the momentum uncertainty gets larger for increasing charge states, as shown in Fig. 5.9. Exemplarily, we estimate the influence of the momentum uncertainty by means of the coincidence channel (4, 4). The total uncertainty amounts to roughly 7 eV, while the total width of the KER distribution in Fig. 6.9 is roughly 30 eV. Thus, another effect must severely affect the width of the distribution: The main contribution is due to the spatial width of the ground state wave function and would thus also occur for infinitely short pulses and perfect resolution. So far we have assumed that the population of each potential energy curve starts from the ground state at one well defined distance R_{eq}. This is only an approximation and in contradiction to quantum mechanics. Figure 6.10 illustrates the effect by means of a Gaussian ground state distribution, which is projected onto a rather flat potential energy curve, according to (1, 1), and a steeper one, according to (1, 5). The steeper the potential curve the broader the resulting KER distribution.

The coincidence channel (1, 3) shows an exceptional behavior (cf. Fig. 6.7c): The KER distribution is strongly extended towards higher energies up to 30 eV. In addition, the high energetic tail has an almost linear slope, unlike any other channel. A possible explanation for the high energies is the creation of a highly excited I_2^{4+} molecular ion in which one of the electrons is excited into a Rydberg state and remains only loosely bound. In this situation the excited electron appears "almost ejected" for the rest of the system and the Coulomb-explosion energy of the I_2^{4+*}

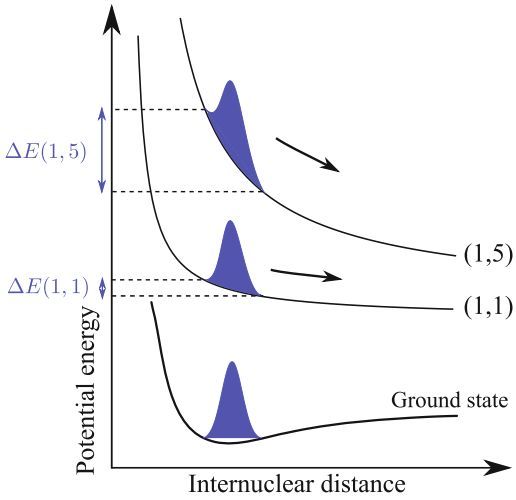

Fig. 6.10 Illustration of the broadening effect of the KER spectra due to the spatial width of the ground state distribution. As this spread translates directly into the observed KER distribution, we conclude that the steeper the potential curve, the broader the resulting KER distribution

molecular ion is shifted towards that of a I_2^{5+} molecular ion. The same feature should therefore show up in the (2, 2) coincidence channel as it also originates from a I_2^{4+} fragmentation. Indeed, the slope of (2, 2) at high energies shows a similar linearly decreasing rate as (1, 3). Our hypothesis is further supported by again bridging the gap to Xe: The photoabsorption cross section of Xe^{4+} is strongly enhanced around 91 eV due to a resonant excitation process $4d \rightarrow nf$ [1]. The excited state autoionizes resulting in Xe^{5+}. It is reasonable to assume the existence of a similar resonance in iodine. Thus, we assume that I_2^{4+} is resonantly excited into a Rydberg state, possibly also autoionizing, by the absorption of one photon. The ions that have not undergone autoionization by the time they reach the detector are assigned to the (1, 3) channel. This results in a broad energy distribution shifted towards larger energies. The molecular ions that have undergone autoionization into I_2^{5+} fragment into (1, 4) or (2, 3). The more symmetric break-up is preferred as it is energetically more favorable. To a smaller amount the high energetic contributions are also present in the channel (1, 4).

Finally, the high and the low intensity measurement, shown in Fig. 6.7, should be compared. The spectra recorded at higher intensities and longer pulse durations have pronounced shoulders and peaks shifted towards lower energies, e.g., fragment pair (2, 3) in Fig. 6.7f. This effect indicates the population of a lower charged precursor state that starts to dissociate until a second photon from the same pulse further ionizes the system. If the pulses have durations on the order of the dissociation time, as it is the case for the measurement with longer pulses, the KERs exhibit additional low-energetic contributions (cf. Fig. 6.7 blue traces). The shift is most pronounced for molecules that break into fragments with asymmetric charge state. In the low

intensity measurement only few of these fragment pairs exist, while a lot show up in the high intensity data. In principle break-up into fragments with symmetrical charge distribution should always be preferable. A symmetric charge state distribution is achieved by electron transfer between unequally charged ions, but only over a certain range of internuclear distances. Therefore creation of the asymmetrically charged coincidence channels indicates that the time difference between the sequentially absorbed photons was relatively long. Thus, by the time the second or third photon impinged, the distance between the dissociating ions was already too large for charge transfer. The relevant time and length scales of this effect were investigated in great detail via an XUV pump-probe measurement and will be presented in Sect. 6.2.5. The question which intermediate states are populated also remained open so far and will be discussed in the following section on time-resolved experiments.

6.2 XUV Pump-Probe Measurements

In order to trace the dynamics of dissociating I_2^{n+} molecules in real time we apply an XUV-pump–XUV-probe scheme. The interaction of a single intense XUV pulse with I_2 has already been discussed in the previous section and serves as a basis for the results obtained by two consecutive XUV pulses. In Sect. 6.2.1 delay-dependent KER spectra are introduced and the applied method for the identification of the underlying ionization mechanism is explained. Some exemplary delay-dependent KER spectra are shown in Sect. 6.2.2. The creation of the lower charged coincidence channels is predicted via the classical simulation presented in Sect. 6.2.3, which will be extended to finite pulse lengths in Sect. 6.2.4. Fragmentation into asymmetrically charged ions, as discussed in Sect. 6.2.5, allows to draw conclusions on charge transfer between the dissociating fragments, which is presented in Sect. 6.2.6. Additionally, model calculations are compared to the delay-dependent KER spectra of asymmetric coincidence channels. These considerations are linked to collision physics, as explained in Sect. 6.2.7. The creation mechanisms of the highest reached charge states are discussed in Sect. 6.2.8. Part of this section has been published in [65].

6.2.1 Interpretation of Pump-Probe Spectra

Applying the knowledge gained in Sect. 6.1 we now address the question of how to interpret spectra originating from two consecutive XUV pulses. Exemplarily, the coincidence channel $I^{2+} + I^{3+}$, again denoted by (2, 3), will be discussed in order to demonstrate how intermediate charge states, produced within the pump pulse, are identified from delay-dependent KER spectra, such as Fig. 6.11a.

Figure 6.11a shows two types of features: a constant band centered around KERs of 27 eV and two time-dependent traces of which the dominant one converges to approximately 11 eV and the weaker one to 3.5 eV. The delay-independent feature has

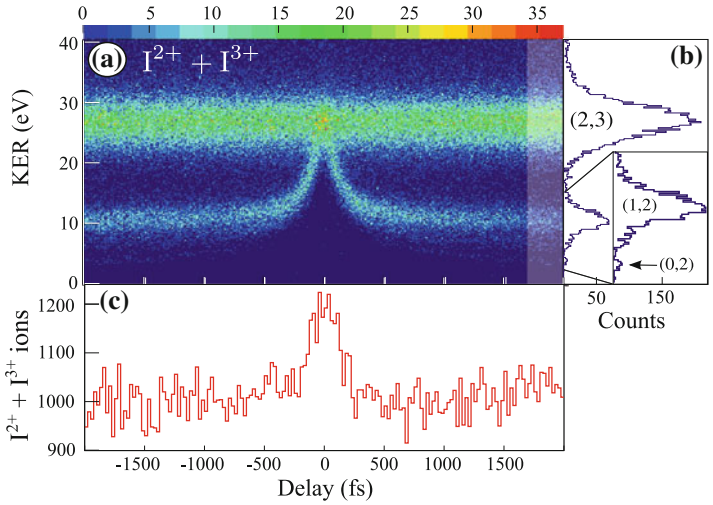

Fig. 6.11 **a** Delay-dependent KER spectrum of the coincidence channel (2, 3). The ion-pair yield is plotted as a function of the KER and the delay time. **b** Projection of KERs for large delays (*shaded area*) onto the KER axis. The *inset* shows a zoom into the low energy region. **c** Projection of all KERs onto the delay axis

already been discussed in the single pulse analysis of Sect. 6.1.5. Thus, we concluded that it originates from sequential two-photon absorption within one of the consecutive pulses. The time-dependent traces in contrast stem from the interplay of photon absorptions during pump and probe pulse. At delays around zero the traces overlap with the constant band because pump and probe pulse act as a single pulse within their temporal overlap. In the overlap region the electric fields of both pulses add up resulting in a quadrupled intensity. This effect manifests in Fig. 6.11a as an increased ion yield around $t_D = 0$ fs and is particularly prominent in the projection onto the KER axis, as shown in Fig. 6.11c.

With increasing delay the KERs of the time-dependent traces get smaller and finally converge to an asymptotic value. This is due to the creation of an intermediate charge state (P_i, Q_i), produced by the pump pulse, and the subsequent ionization to (P_f, Q_f) by the probe pulse impinging at t_D. The pump-induced dissociation leads to an increased internuclear distance by the time the probe pulse arrives. Therefore, the population of the steeper potential energy curve of a higher charge state takes place at a larger distance. This results in smaller KERs compared to the two-photon absorption within a single pulse. Thus, the longer the delay, the smaller the energy gain on the steeper curve. For large delays the energy gain vanishes completely as all potential energy curves are asymptotically flat. Therefore, the KERs for large delays are used to determine the intermediate charge states (P_i, Q_i) for each measured coincidence channel (P_f, Q_f). As an example, the asymptotic value of 11 eV in Fig. 6.11b corresponds to the energy that I^{1+} and I^{2+} gain from the Coulomb force at R_{eq}, as introduced in Sect. 6.1. This suggests a reaction pathway via the precursor

(1, 2) (cf. Eq. (6.11)). The introduced method is applicable if the assumption of Coulombic potential energy curves is justified. This will be discussed in more detail in Sect. 6.2.3 by comparison with a simulation of their temporal evolution.

6.2.1.1 Dissociation into Neutral Fragments

Figure 6.11a also shows a trace at low energies converging to 3.5 eV. It cannot be attributed to a direct fragmentation into charged particles that repel each other with the Coulomb force: According to Eq. (6.7) the lowest KER emerging from a Coulomb explosion into charged fragments is that for (1, 1) amounting to 5.4 eV. One explanation of the low energy trace is the dissociation into a neutral and a charged fragment. This process often leads to smaller KERs as it is represented by shallower potential energy curves compared to fragmentation into two charged fragments. As neutral fragments are not detected in our setup, we have to identify coincidence channels containing them indirectly. This is done by comparing the coincident pump-probe spectra with non-coincident spectra recorded during the single pulse measurement. The most likely break-ups with one partner being a neutral fragment are those into (0, 1) or (0, 2). Therefore, we restrict our consideration to these precursors. However, we expect the latter to be strongly suppressed as the competing symmetric fragmentation channel (1, 1) is energetically favored.

We will explain the identification procedure for the exemplary precursor (0, 2) in the coincidence channel (2, 3). In Fig. 6.12 the spectrum of all detected I^{2+} ions is compared to the spectrum of I^{2+} ions that were detected in coincidence with a I^{3+} ion. The shaded areas indicate coinciding peaks of both spectra. The red region marks I^{2+} ions from a Coulomb explosion $I_2^{5+} \rightarrow (2, 3)$. The green region marks I^{2+} ions with an energy corresponding to the fragmentation $I_2^{3+} \rightarrow (1, 2)$. The latter contribution

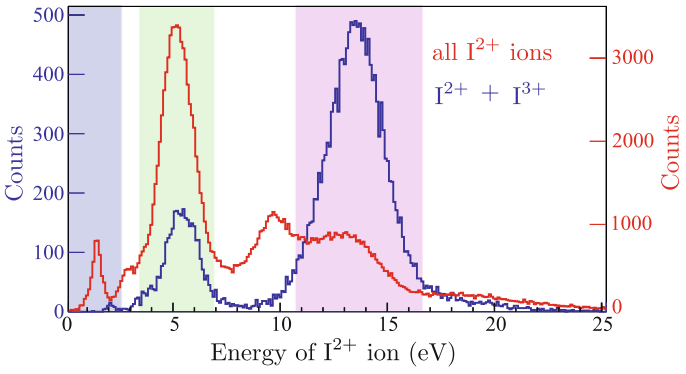

Fig. 6.12 Identification of a fragmentation that contained one charged and one neutral fragment: The *red curve* shows all detected I^{2+} ions, while the *blue curve* contains only those I^{2+} ions that were detected in coincidence with I^{3+} ions for large delays. Please note, that the energy of the fragments is half of the KER, as only the energy of one fragment is considered

shows up in the asymptotic KER spectrum of (2, 3) because it is produced via the precursor (1, 2) and further ionized at large delays. The blue region of interest marks those I^{2+} ions originating from the neutral fragmentation $I_2^{2+} \rightarrow (0, 2)$. The neutral contribution in the coincidence spectrum is only small and shifted towards higher energies. The reason for the higher energy in the pump-probe spectrum is the energy gain when the neutral fragment is further ionized to I^{3+}. Even at large delays the gain is still comparatively large due to the much steeper potential curve corresponding to (2, 3) compared to the neutral precursor curve (0, 2).

In summary, the three different contributions in Fig. 6.11 are assigned to the following reaction pathways:

$$I_2 \xrightarrow{\text{pump}} I_2^{5+} \longrightarrow I^{2+} + I^{3+} \qquad \text{(red)}, \tag{6.9}$$

$$I_2 \xrightarrow{\text{pump}} I_2^{3+} \longrightarrow I^{1+} + I^{2+} \xrightarrow{\text{probe}} I^{3+} + I^{2+} \qquad \text{(green)}, \tag{6.10}$$

$$I_2 \xrightarrow{\text{pump}} I_2^{2+} \longrightarrow I^{0+} + I^{2+} \xrightarrow{\text{probe}} I^{3+} + I^{2+} \qquad \text{(blue)}. \tag{6.11}$$

The color coding for the shaded areas in Fig. 6.12 is given in parentheses.

6.2.2 Relevant Charge States and Dissociation Channels

Complementary to the aforementioned identification in the measured data via the asymptotic KER, our suggested pathways can be predicted using our knowledge from the single pulse discussion in Sect. 6.1.4. At large delays the fragments behave like individual particles and are therefore treated in good approximation as isolated iodine ions. According to Eq. (6.3), a single photon from the pump creates one of the precursors (0, 2), (1, 1) or (1, 2). Additionally, a small contribution from valence ionization to (0, 1) will arise. We assume the absorption of a second photon within the probe, which is localized at one of the two fragments for large delays. Thus we have to evaluate the effect of single-photon impact on the individual precursor fragments I, I^{1+} and I^{2+}, which has been discussed already in Sect. 6.1.4.

An overview of possible reaction pathways via precursors created by single-photon absorption within the probe and further ionized by a delayed photon from the probe is given in Fig. 6.13. The validity of the suggested pathways is tested by comparing them to the observed ones. Here, we will only consider time-dependent contributions of the pump-probe spectra, the time-independent features correspond to those discussed in Sect. 6.1.5. For the coincidence channel (2, 3), Fig. 6.13 predicts two precursors (0, 2) and (1, 2), which are also present in the recorded data. Two further coincidence channels, (1, 2) in Fig. 6.14a and (2, 2) in Fig. 6.14b, are discussed in order to test the agreement with the predicted pathways. According to

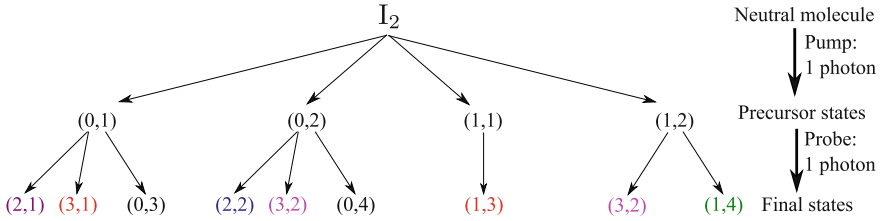

Fig. 6.13 Reaction pathways for single-photon absorption within the pump and delayed single-photon absorption within the probe

Fig. 6.13 (1, 2) is expected to have only one precursor (0, 1), which appears in the data as a weak trace converging to 2 eV in Fig. 6.14a. For (2, 2) the precursor (0, 2) is expected and also confirmed in the measurement in Fig. 6.14b. The channels (1, 3) and (1, 4) are shown in Fig. 6.19 and will be discussed in Sect. 6.2.5, but it should already be mentioned that they exhibit the traces, predicted in Fig. 6.13.

The presented method is extendable to the absorption of more than one photon within the pump or the probe pulse. However, for highly charged break-up channels the number of precursors increases drastically and the method becomes cumbersome.

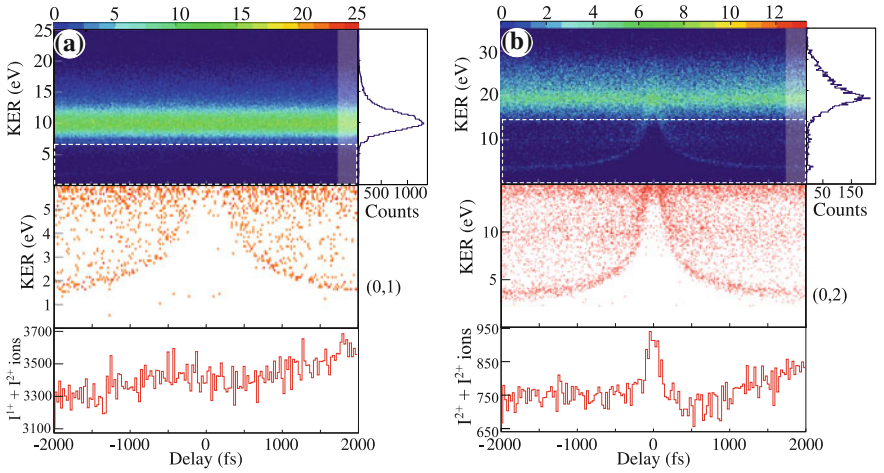

Fig. 6.14 Delay-dependent KER spectra for the coincidence channels **a** (1, 2) and **b** (2, 2). The time-dependent traces are emphasized in a zoom-in, that is given in the *middle panels*. Note that the color scale is set to one. The projection onto the delay axis for all KERs is shown in the respective *lowest panels*. In addition, a projection onto the KER axis for large delays is shown in the *right panels*

6.2.3 Comparison with Simulated Pump-Probe Spectra

Now that we found a method to predict the precursor charge states, a model for their time-dependent behavior will be introduced. In Sect. 6.1.5, the measured KERs were already compared to the predictions for point-like charged particles repelling each other with the Coulomb force. This method turned out to be successful for low charge states. If we assume purely Coulombic potential energy curves for the intermediate states as well, we are able to simulate the time-dependent spectra using the model introduced in Sect. 2.6. For fragmentation channels containing a neutral fragment this method is in principle not applicable as it requires two charged particles. In practice it is nevertheless applied by assuming for instance a charge of $1/2$ for each particle of the break-up channel (0, 1) [56]. This is only a very rough estimate and will not be used here.

Exemplarily, the coincidence channels (3, 3) in Fig. 6.15a and (3, 4) in Fig. 6.15b are compared to their corresponding simulated traces. It is assumed that these charge states were created by the minimum number of photons needed, here three. Thus these channels extend the two-photon scheme shown in Fig. 6.13. Coincident (3, 3) ion pairs are produced via the following pathways:

$$I_2 \xrightarrow{\text{pump: 1 photon}} (1,0) \xrightarrow{\text{probe: 2 photons}} (3,3), \tag{6.12}$$

$$I_2 \xrightarrow{\text{pump: 1 photon}} (1,1) \xrightarrow{\text{probe: 2 photons}} (3,3), \tag{6.13}$$

$$I_2 \xrightarrow{\text{pump: 2 photons}} (1,3) \xrightarrow{\text{probe: 1 photon}} (3,3). \tag{6.14}$$

Precursors with neutral fragments are not simulated as their potential energy curves are usually not well represented by Coulombic ones. A trace corresponding to (1, 3) is not present in the data, as it mostly transforms into the energetically favored charge state (2, 2) by charge transfer. The precursor (2, 2) does also not show up in Fig. 6.15a as the pathway (2, 2) → (3, 3) is heavily suppressed: The absorption of an additional photon at either of the I^{2+} ions leads to the removal of two electrons, resulting in

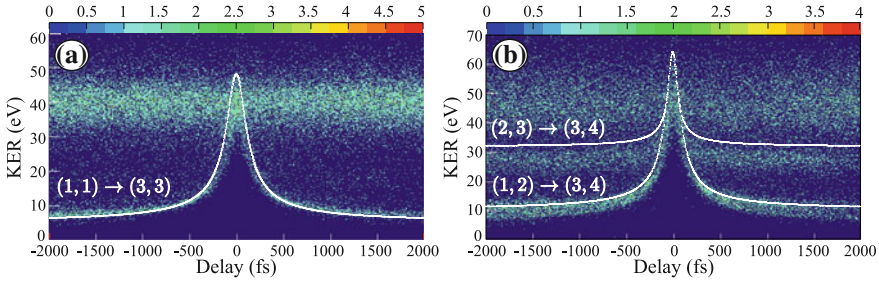

Fig. 6.15 Delay-dependent KER spectra for the coincidence channels (3, 3) and (3, 4). Simulated time-dependent traces are shown as *overlayed white curves*

I^{4+} ions. The overall agreement of $(1, 1) \rightarrow (3, 3)$ with the simulated Coulomb trace is excellent, except for very small delays. This is most likely due to the finite pulse length, which is not taken into account in the simulation, or deviations from the Coulomb potential energy curves.

For the production of (3, 4) (cf. Fig. 6.15b) we propose the possible pathways:

$$I_2 \xrightarrow{\text{pump: 1 photon}} (1, 2) \xrightarrow{\text{probe: 2 photons}} (3, 4), \tag{6.15}$$

$$I_2 \xrightarrow{\text{pump: 2 photons}} (2, 3) \xrightarrow{\text{probe: 1 photon}} (3, 4). \tag{6.16}$$

Both expected traces are present in the data. While the recorded KER via the precursor (2, 3) is lower than expected, the agreement via (1, 2) is very good. This trend has already been observed in the single pulse spectra in Sect. 6.1.5, where lower charge states showed better agreement with the model. The explanation for this effect given there is further underlined by the pump-probe spectra: In order to produce the precursor (2, 3) two photons are needed. As these photons are absorbed sequentially, (2, 3) will not be produced at R_{eq}. This effect is strongest for small internuclear distances, where the potential energy curves are steepest and consequently the ions' energy gain is largest. For the pathway via (1, 2) two-photon absorption within the probe is required. The final charge state is thus created at distances where the potential curves are already flat. There, sequential photon absorption influences the KER only slightly and the result is in good agreement with the simulation.

In conclusion the purely Coulombic potential energy curves are in good agreement with the measured data and the main deviation stems from the assumption of instantaneous ionization to the precursor state.

6.2.4 Simulation with Finite Pulse Length

A more realistic treatment of the delay-dependent KER spectra is obtained by extending the pump-probe simulation from Sect. 6.2.3 to finite pulse lengths. Experimentally, the pulse length is not known precisely. However, an upper limit is gained indirectly from the width of the time-dependent trace in Fig. 6.18a. For small delays, this width is mainly determined by the pulse length and only a small contribution stems from the spatial width of the ground state. The impact of these two contributions is illustrated by means of our classical pump-probe simulation.

We start by determining the total width of the trace at small delays, which is the convolution of the pump and the probe pulse widths. For simplicity we assume two identical Gaussian pulses. A thin slice from 18 to 20 eV of experimental KERs from Fig. 6.11a is projected[1] onto the delay axis, as shown in Fig. 6.16. The distribution is fitted with two Gaussians and the averaged fit result for positive and negative

[1] Please note that the traces are not precisely vertical in the projection region. Therefore the determined width is slightly broadened by the tilt of the curves.

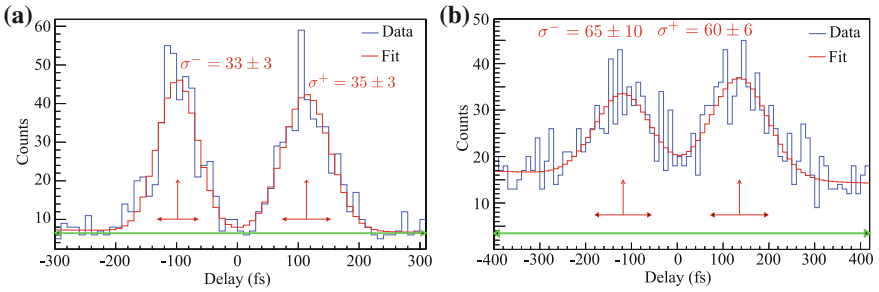

Fig. 6.16 Projection of Fig. 6.11 onto the delay axis for KERs from 18 to 20 eV (in *blue*). Two Gaussian fits are performed and the respective $\sigma^{\pm}$ for negative and positive dealys are given (in *red*). **a** For shorter pulse duration (Setting 2 in Table 6.1), and **b** for longer pulse duration (Setting 1 in Table 6.1)

delays is $\sigma = 34 \pm 3$ fs for the shorter pulses, which corresponds to a FWHM of approximately 80 fs. We also recorded pump-probe spectra for longer pulses (Setting 1 in Table 6.1), which were not yet presented. Performing the same projection and fit as for the short pulses yields $\sigma = 63 \pm 8$ fs, which corresponds to a FWHM of approximately 146 fs. The width of the convoluted curves is calculated from the individual pulse widths $\sigma_{\text{pump}} = \sigma_{\text{probe}} = \sigma_{\text{pulse}}$:

$$\sigma^2 = \sigma^2_{\text{pump}} + \sigma^2_{\text{probe}} = 2\sigma^2_{\text{pulse}}. \tag{6.17}$$

Thus we extract a pulse length of roughly 57 fs (FWHM) for the shorter pulses and 103 fs (FWHM) for the longer pulses.

For all simulations it was so far assumed that the ionization occurs at R_{eq}. This assumption is not consistent with quantum mechanics which predicts the initial state to have a spatial width. An estimate for it is gained by calculating the width of the vibrational ground state wave function in an harmonic oscillator potential, as shown in Sect. 2.2.3. The coupling constant is taken from [38] yielding a Gaussian ground state wave function with a width of 0.6 au (FWHM). In order to calculate the probability density for the ground state, we have to square the ground state wave function and determine a ground state width of 0.5 au (FWHM). A pump-probe simulation with infinitely short pulses and the estimated ground state width is shown in Fig. 6.18b. It yields a total width of (12.1 ± 0.5) fs for the same projection interval as for Fig. 6.16. In general, the broader the spatial ground state distribution the broader the KER traces for asymptotic delays. As illustrated in Fig. 6.17, a broad spread in the ground state translates to the population of a wide energy range on the Coulomb curves, which then results in a broad KER distribution.

Figure 6.18c shows a second simulation with a finite pulse length of 57 fs and no spatial distribution of the ground state. For small delays, the resulting width is identical to the pulse length. The simulated traces converge to the KER expected

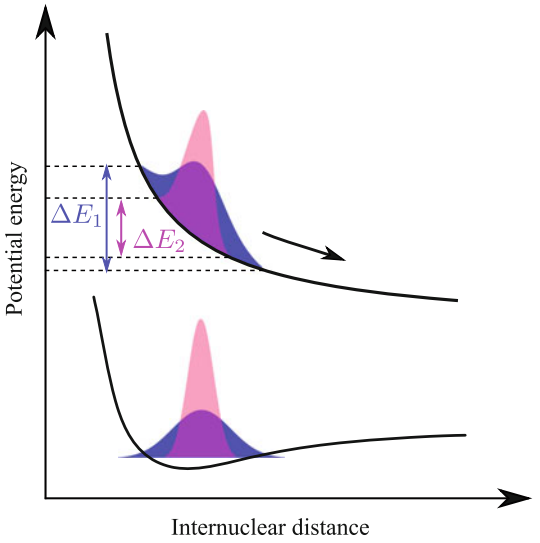

Fig. 6.17 Mapping of the squared ground state wave function onto a Coulomb curve. A narrow distribution (*pink*) leads to a narrow distribution of accessed potential energies that translates directly into the observed KER distribution. In contrast, a broad ground state distribution (*blue*) causes a broad range of accessible energy, which is then also observed in the KER spectrum. Thus we directly map spatial widths into an energy distribution

from a Coulomb explosion at R_{eq} because the pulse length does not influence the position at which the potential curves are populated.

A third simulation taking into account the pulse length and the ground state distribution is shown in Fig. 6.18d. The width of the convoluted traces is again roughly 57 fs. Thus we conclude that the contribution of the ground state width at small delays is negligible and the pulse length can be estimated from the width of the time dependent traces. The obtained value should be understood as an upper limit because the finite experimental resolution and the tilt of the traces is neglected.

6.2.5 Break-Up into Asymmetrically Charged Fragments

Here we will again apply the notation (P_f, Q_f) for the fragment pair $\mathrm{I}^{P_f+} + \mathrm{I}^{Q_f+}$. Coincidence channels with $|P_f - Q_f| \geq 2$ are referred to as asymmetric channels. Figure 6.19 shows pump-probe spectra of asymmetric coincidence channels with one of the fragments being I^{1+}: $(P_f = 1, Q_f > 2)$. All of them share a depleted ion yield for small delays. This is in contrast to the more symmetric break-up channels presented in the previous Sect. 6.2.1, which showed an increased ion yield for small delays. In order to explain the difference, we first have to identify the precursor charge states for the various coincidence channels in Fig. 6.19.

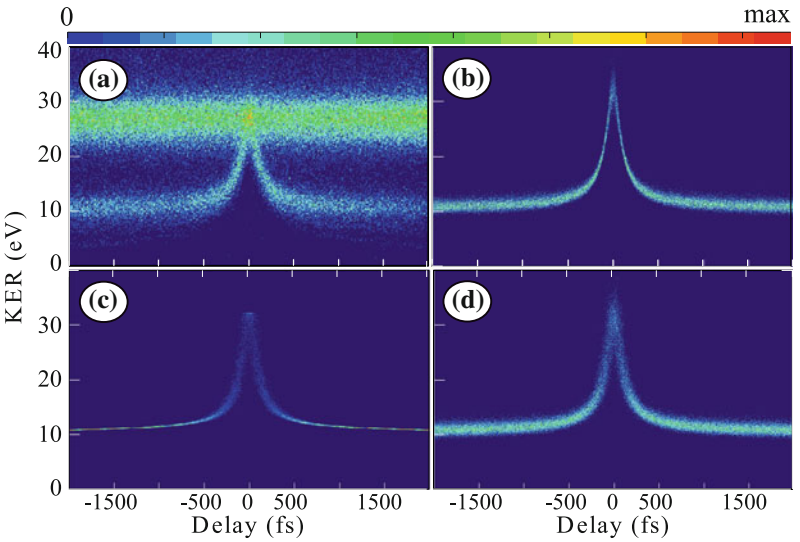

Fig. 6.18 Delay-dependent KER spectra for the coincidence channel (2, 3). **a** Experimental data. **b** Simulation with spatial ground state distribution. **c** Simulation with finite pulse duration of 57 fs. **d** Simulation with spatial ground state distribution and finite pulse length. Note that, for asymptotic delays the measured trace is broader than that of the simulation. This may be attributed to the population of different potential energy curves, that have different energies. In addition the experimental resolution is broadening the trace

As predicted in Fig. 6.13, the coincidence channel (1, 3) in Fig. 6.19a emerges almost exclusively from the precursor (1, 1). The additional time-independent band of KERs centered around 17 eV was already identified as a highly excited I_2^{4+} ion by the analysis of single pulse KER spectra in Sect. 6.1.5.

The channel (1, 4) in Fig. 6.19b shows a broad time dependent trace, that is attributed to two partially overlapping precursor states. The dominant contribution is centered around 11 eV and thus corresponds to the precursor (1, 2) as predicted in Fig. 6.13. The weaker contribution converging to lower energies stems from the precursor (1, 1). This pathway cannot be explained by one photon absorption within the probe as the ionization $I^{1+} \rightarrow I^{4+}$ requires at least two photons. Besides two-photon absorption, this channel could be created via a highly excited I^{+*} precursor ion, which is then triply ionized by the probe. Both contributions may show up but are indistinguishable.

The creation of the coincidence channel (1, 5) in Fig. 6.19c requires the absorption of an additional photon within the probe compared to (1, 4). Thus it features the same two precursors, (1, 2) and (1, 1). In addition (1, 5) is produced via an excited[2] precursor (1, 3*) by the absorption of a second photon.

[2] Considering the high energetic contributions in Fig. 6.7c we assume that channel (1, 3) will mainly be produced in an excited state.

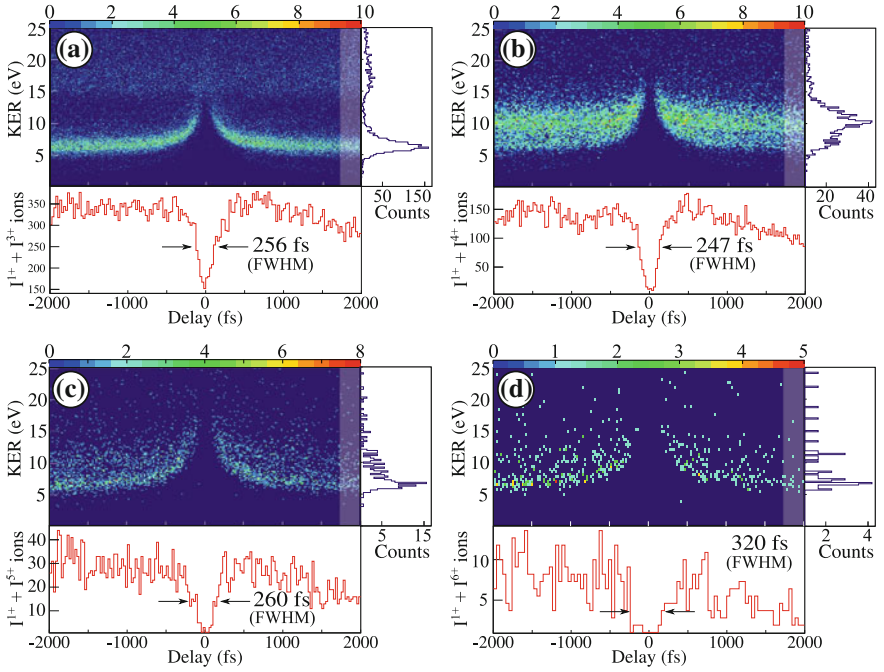

Fig. 6.19 Delay-dependent KER spectra for all observed coincidence channels $(1, Q_f)$, $Q_f \in \{3, 4, 5, 6\}$. Additionally the projections onto the delay axis are shown in the respective *lower panels*. Projections onto the KER axis for large delays are shown are shown in the *right panels*. **a** $(1, 3)$, **b** $(1, 4)$, **c** $(1, 5)$, and **d** $(1, 6)$

In order to create the I^{6+} ion of the $(1, 6)$ channel in Fig. 6.19c the I^{5+} ion from $(1, 5)$ must be further ionized by an additional photon from the probe pulse. Therefore it features the same precursor channels.

The increased ion yield for small delays for the more symmetric channels and the depletion for the asymmetric ones will now be introduced via a pictorial description of the underlying processes, as illustrated in Fig. 6.20. The pump pulse multiply ionizes the molecule and thereby triggers a dissociation. Consequently the probe pulse will experience a target with an internuclear distance that depends on the pump-probe delay. The probe pulse further ionizes one of the ions, which produces a positive net charge at that ion. To balance the charge state distribution and to establish the energetically most favorable state for the molecule an electron from the other ion may transfer. As electron motion is typically a factor of thousand faster than dissociative motion, the transfer process is considered as taking place instantaneously. However, charge transfer is only possible as long as the orbital overlap of the ions is large enough to exchange electrons. Therefore asymmetric coincidence channels are only produced if the orbital overlap has become too small before the probe pulse arrives. Beyond a critical delay time t_{crit}, which is attributed to a critical internuclear distance R_{crit}, the electron transfer is not possible anymore. Thus, the width of the depleted

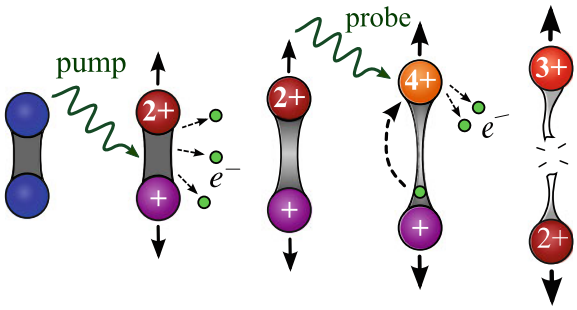

Fig. 6.20 Illustration of the applied pump-probe scheme: the pump pulse triggers the dissociation of the molecule by multiply ionizing it to (1, 2). The molecule is given time to expand to a certain internuclear distance until the probe pulse impinges and further ionizes the upper ion to I^{4+}. As the orbital overlap of the ions is still large enough by the time the probe pulse arrives, charge transfer from I^{1+} to I^{4+} is initiated. This leads to the most symmetric fragmentation channel of the molecule: (2, 3)

ion yield for small delays in Fig. 6.19 marks the transition from a molecular system to two separated ions.

The special role of coincidence channels with asymmetrically charged fragments was already addressed in Sect. 6.1.5. The measurement with longer pulses showed a significant amount of asymmetric channels, while the study with shorter pulses was missing these channels almost completely (cf. Fig. 6.7). With the insight gained from the XUV pump-probe spectra the effect of the pulse length can now be explained directly: If the pulse is long, the molecule has enough time to overcome R_{crit} within it and asymmetric channels are produced. Thus, the pulse length is an important parameter determining the charge state distribution created by multi-photon absorption.

6.2.6 *Determination of the Critical Distance for Charge Transfer*

Charge transfer is at the basis of many fundamental processes in chemistry [19, 20, 23] and plasma reactions [5, 73]. It is also of great importance for applications of intense X-ray radiation, such as the coherent imaging of single non-crystallized biomolecules [51]. Thus, knowing the distances up to which charge transfer occurs is crucial.

All pump-probe spectra were recorded over a symmetric delay range of $\pm 2\,\mathrm{ps}$ with the temporal overlap of the pulses at $t_D = 0$, which means one of the pulses is preceding the other for negative delays and succeeding it for positive delays. Therefore we measure the same spectrum twice, one for positive and the other for negative delays. Thus the critical time t_{crit} of charge transfer is only half of the width of the dip. We determine it from the projection of all KERs onto the delay axis by taking half width at half depth (HWHD) of the dip. It turns out that the width of the

Table 6.3 Critical distances $R_{\text{crit}}^{\text{COB}}$ calculated with the COB model and the corresponding experimentally determined t_{crit} (half width at half depth) for the presented coincidence channels

Channel	$R_{\text{crit}}^{\text{COB}}$ (au)	t_{crit} (fs) (HWHD)
(1, 3)	9.8	128
(1, 4)	10.9	124
(1, 5)	11.9	130
(1, 6)	12.7	160
(2, 4)	9.1	43
(2, 5)	9.9	78

gaps is different for all coincidence channels (Q_f, P_f) (cf. Table 6.3). In order to interpret our findings and gain insight into the charge transfer process we will now compare the results from a model with the measured data.

The charge transfer between two ions can be described by means of the classical over-the-barrier (COB) model that was originally introduced for slow ion-atom collisions [48, 52, 62]. A version of the COB model adapted to our geometry was discussed in Sect. 2.7. There we derived an analytical expression for the maximum distance $R_{\text{crit}}^{\text{COB}}$ of two ions up to which charge transfer takes place. Applying the nomenclature of this chapter, the formula reads

$$R_{\text{crit}}^{\text{COB}} = \frac{(P_f + 1) + 2\sqrt{(P_f + 1)Q_f}}{|E_{P_f}|}, \tag{6.18}$$

with the restriction of $P_f < Q_f + 1$ for each coincidence channel (P_f, Q_f). E_{P_f} is the binding energy of the least bound electron of I^{P_f+} given in Table 6.2. The critical distances calculated via Eq. (6.18) for break-ups with $P_f = 1$ are plotted in Fig. 6.22 as black markers. In accordance with Eq. (6.18), the distance over which charge transfer is possible grows with increasing Q_f. This is due to the higher charge bending the potential of I^{1+} stronger.

The evaluation of the XUV pump-probe spectra in Fig. 6.19 gives only indirectly access to $R_{\text{crit}}^{\text{exp}}$ as the width of the depleted ion yield is given in the time domain. Therefore we need a method to translate the measured t_{crit} into the corresponding distance. In order to do so, we use our classical pump-probe simulation from Sect. 2.6 with Coulombic potential energy curves, that has already proven to be a good approximation.

The simulation, presented in Sect. 6.2.3, requires the knowledge of the precursor state as input parameter because the width of the gap is different for each precursor, as shown in Fig. 6.21. However in the experiment we measure an averaged t_{crit} composed of different precursor states. As all coincidence channels in Fig. 6.19 have the precursor states (1, 1) and (1, 2) two critical distances $R_{\text{crit}}^{\text{exp}}$ will be calculated for each coincidence channel (as shown in green and blue in Fig. 6.22). All predicted distances $R_{\text{crit}}^{\text{COB}}$ lie within the band of data points spanned by $R_{\text{crit}}^{\text{exp}}$ for the both precursor states. Note that all values for $R_{\text{crit}}^{\text{COB}}$ show a tendency to one of the precursors: $R_{\text{crit}}^{\text{COB}}(1, 3)$ is shifted towards (1, 1), which is its only precursor observed in the experiment. $R_{\text{crit}}^{\text{COB}}(1, 4)$ shows a tendency towards (1, 2), which is its dominant

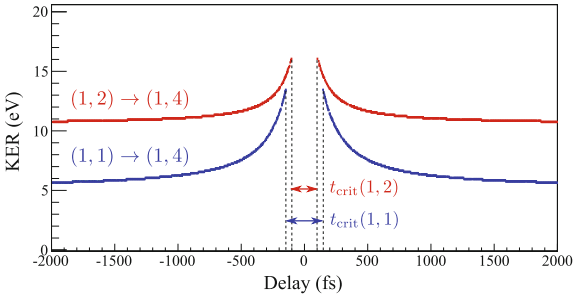

Fig. 6.21 Simulation of time-dependent traces resulting in the coincidence channel (1, 4) including R_{crit}^{COB} of the COB model. As the dissociation via the higher charged precursor proceeds faster, $t_{crit}(1, 2) < t_{crit}(1, 1)$

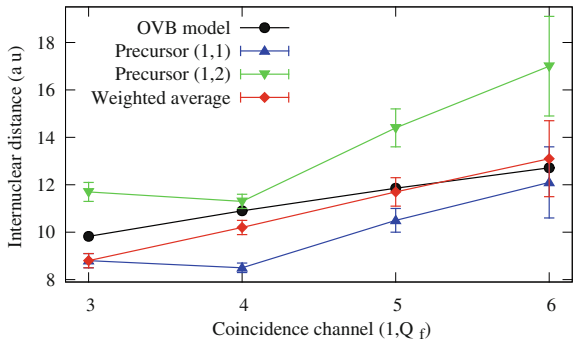

Fig. 6.22 Comparison of experimentally determined R_{crit}^{exp} with those predicted by the COB model for all coincidence channels $(1, Q_f)$ with $Q_f \in \{3, 4, 5, 6\}$: the *blue upwards triangles* indicate R_{crit}^{exp} that were converted by assuming the dissociation took place via the precursor (1, 1), while the *green downwards triangles* stand for the pathway via the precursor (1, 2). The average of both precursors weighted with the relative occurrences of (1, 1) and (1, 2) (taken from the experiment) is plotted as *red diamonds*. *Black dots* show the predictions made by the COB

precursor. The channels (1, 5) and (1, 6) feature both precursors, however predominantly (1, 1). This is in accordance with the prediction of R_{crit}^{COB}, which also tends to (1, 1) for both cases. These trends suggest the use of an averaged critical distance $\bar{R}_{crit}^{exp}$, where the two precursor states are weighted according to their relative occurrence in the experiment. The result is plotted as red diamonds in Fig. 6.22 and coincides perfectly with the trend predicted by the model.

The good agreement with the COB model encouraged us to combine the extended pump-probe simulation introduced in Sect. 6.2.4 with the COB model to simulate the recorded time-dependent spectra. In order to do so creation of the asymmetric channels is only allowed for internuclear distances larger than R_{crit}. The pulse duration was assumed to be 57 fs (FWHM) and the spatial width of the ground state 0.5 au (FWHM). Figure 6.23 shows the comparison of experimental data for the channel (1, 3) in (a) with the result of the simulation via the precursor (1, 1) in (b). The

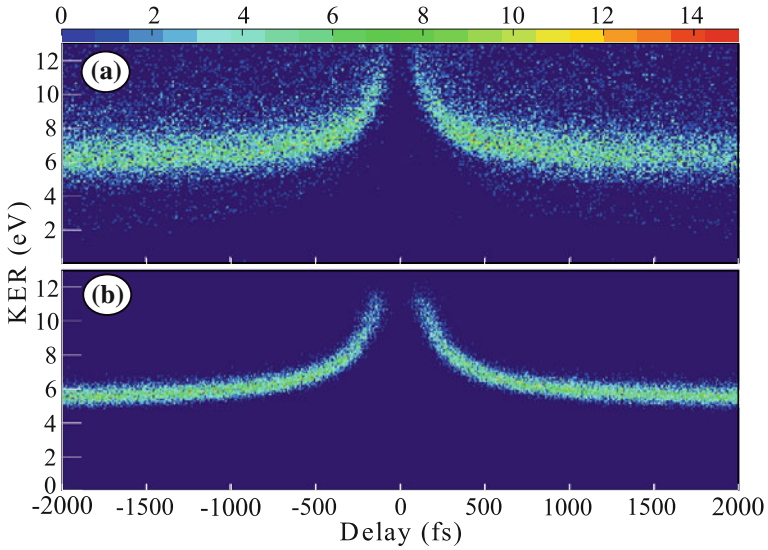

Fig. 6.23 Delay-dependent KER spectrum for the coincidence channel (1, 3) for **a** measured data, and **b** pump-probe simulation in combination with the classical COB model. For the pump-probe simulation the determined pulse length of 57 fs and the estimated spatial ground state distribution of 0.5 au were assumed (cf. Sect. 6.2.4). The critical distance for (1, 3), calculated via Eq. (6.18), was included into the simulation

agreement is very good, which confirms that our models assuming classical motion for the ions deliver a suitable description of the underlying phenomena.

Further asymmetric coincidence channels were recorded in the experiment, particularly those for $(2, Q_f)$ and $(3, Q_f)$. However higher charge states exhibit more than one or two precursor states, mostly three or four (cf. Fig. 6.24). Our method to convert the critical time delay into a distance, as applied for $(1, Q_f)$, relied heavily on knowing the precursor and its relative occurrence. One precursor was always dominating and thus determined the width of the gap. If several precursors contribute equally, each of them with a different gap our method can not be applied anymore. We can give an upper limit for the gap from the slowest dissociating precursor state and a lower limit from the fastest dissociating. But the overall shape of the measured gap is composed of all contributing precursors and their relative occurrences.

Two exemplary coincidence channels (2, 4) and (2, 5) are shown in Fig. 6.24a, b respectively. For (2, 4) the calculated R_{crit} is 9.1 au, similar to that for (1, 4) (cf. Table 6.3). However the measured t_{crit} is 43 fs for (2, 4) and 128 fs for (1, 4). The reason for the difference in t_{crit} are their corresponding precursor states. As (1, 4) features the comparatively slow dissociating precursors (1, 1) and (1, 2) it takes longer to reach $R_{\mathrm{crit}}^{\mathrm{COB}}$ than for (2, 4), which exhibits the much faster dissociating precursors (2, 2) and (2, 3). Therefore $R_{\mathrm{crit}}^{\mathrm{COB}}$ is reached at smaller delays and the gap becomes narrower for (2, 4). As the width is already in the order of the pulse length we have reached the limit of our temporal resolution.

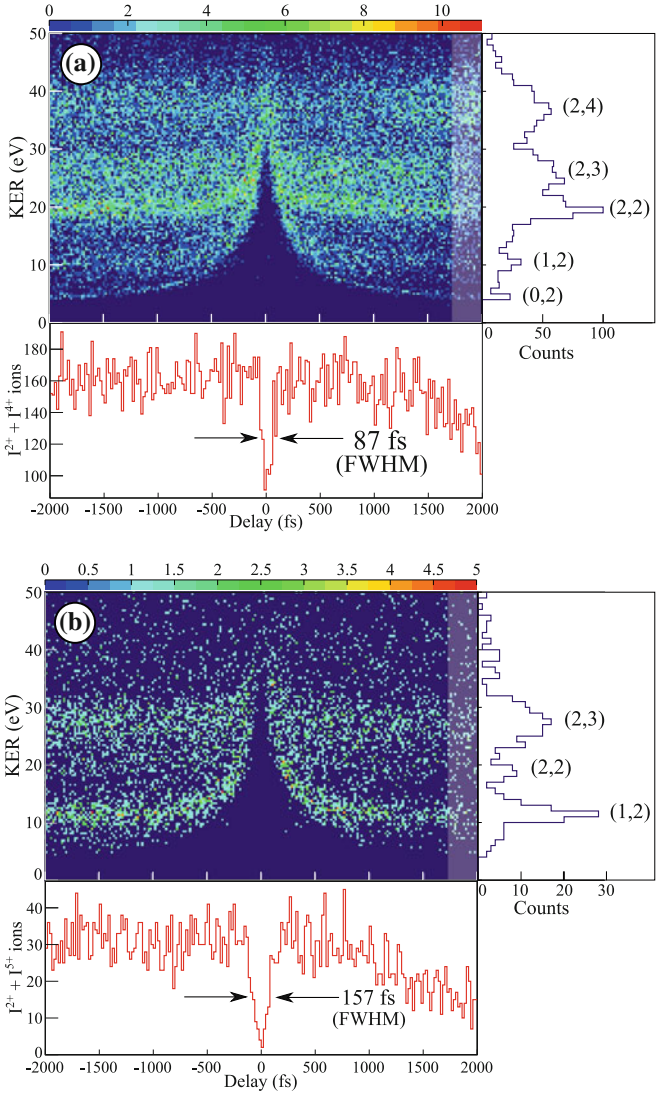

Fig. 6.24 Delay-dependent KER spectra for the coincidence channels **a** (2, 4), and **b** (2, 5) with projections onto the delay axis (*lower panels*) and onto the KER axis for large delays (*right panels*). The precursor states are indicated in *brackets*

Here we should also mention the so-called Coulomb blocking, which is discussed in Sect. 6.3.2, as it also hinders the creation of highly charged molecular ions for small delays. The Coulomb potential of one constituents increases the ionization potential of its neighbor. This leads to similar depletion for small delays in the ion yield spectra as caused by charge transfer. However the origin of this depletion is

fundamentally different. Particularly, also symmetric coincidence channels with high charge states have a depleted ion yield for small delays.

6.2.7 Collision Physics from a Different Perspective

The analogy of our experiment to collision experiments was already drawn by applying the classical COB model, which was originally introduced for electron capture in slow ion-atom collisions ($E_{\text{projectile}} > 10\,\text{eV}$ per nucleon) [9, 21]. While it has proven to be a good description for these slow processes, we would like to point out that some assumptions of the model are usually not fulfilled therein. Thus the question arises how well the requirements are met in our experiment. The first requirement is a *slow* collision, meaning that the electrons of the target and the projectile adjust adiabatically to the changing potential induced when the target passes the projectile. This condition is well fulfilled in our experiment where the ions' kinetic energies emerge from Coulomb explosions only. Thus they are typically below 0.1 eV per nucleon, far smaller than the $E_{\text{projectile}}$ mentioned above. In addition the COB model assumes the motion of atoms and ions to be in one dimension only. Thus it is not able to account for angular momentum that is transferred to a target by a deflected projectile. This requires extensions to the COB model [10]. As the trajectories of the ions in our experiment are determined by Coulomb explosion the two fragments are always emitted back-to-back. This corresponds perfectly to a one-dimensional movement. In summary, our experiment is a more exact realization of the COB model, than the traditional ion-atom collisions for which the model was developed. Thus we open up a new testing ground for charge transfer models in a low-energetic regime that is almost unexplored.

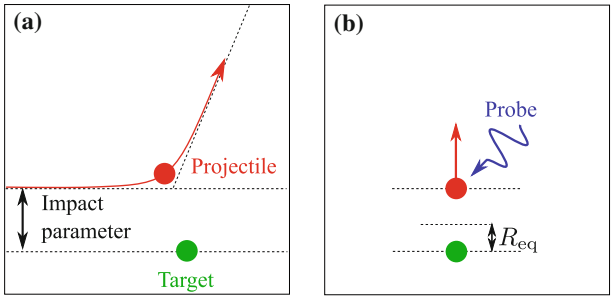

Fig. 6.25 **a** Geometry of a traditional collision, where the projectile approaches the target and gets deflected from its original trajectory. **b** Half-collision in the rest frame of the *green* ion as realized in our experiment. The pump pulse has multiply ionized the molecule at R_{eq} (not shown) and consequently the molecular ion fragments. At an adjustable time delay, which corresponds to a certain internuclear separation of the ions, the probe pulse impinges, which defines the impact parameter of the half-collision

The present experiment can be considered as a "half-collision" [55, 76] without distinction between target and projectile. In a traditional collision experiment the projectile approaches the target up to a certain distance and is deflected from its trajectory by a certain angle. For fixed target and projectile conditions the dynamics of a collision is classically fully determined by the impact parameter, which is the closest distance between target and a non-deflected projectile [46] (cf. Fig. 6.25). Thus, the impact parameter resembles the "control knob" determining the outcome of the collision. However this knob is not directly accessible in a classical collision experiment and can only be read-out afterwards, not actively tuned. This is different in our experiment: Here, the impact parameter is determined by the distance between the dissociating ions at the time when the probe pulse further ionizes one of the fragments and thereby starts the second half of a "collision", as illustrated in Fig. 6.25. It is thus referred to as a half-collision. By choosing a certain delay, which is convertible into an internuclear distance, the impact parameter is predetermined and the outcome of the collision actively controlled. For instance, charge transfer is switched on and off by the variation of the delay, as shown in Sect. 6.2.6.

6.2.8 Reaching the High Charge States

Coincidence channels with high charges show asymmetric delay-dependent KER spectra (cf. Fig. 6.26). In principle, the negative and the positive delay range should

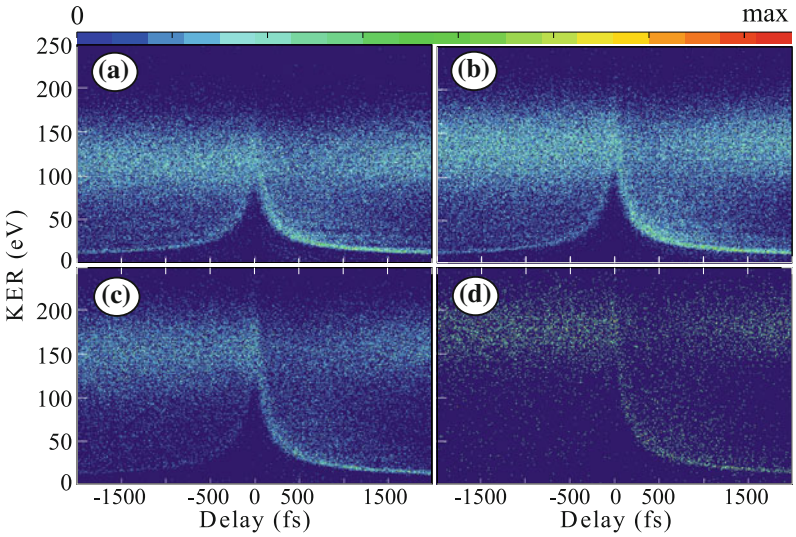

Fig. 6.26 Delay-dependent KER spectra for the coincidence channels **a** (6, 6), **b** (6, 7), **c** (7, 7), and **d** (7, 8). Note that these spectra were recorded with the high intensity setting

be mirror images of each other. However this is only true if the intensity in both pulses is equal and the spatial overlap of pump and probe pulse remains the same for all delays. Since the delay is introduced by mechanically moving mirrors the focal position may well change by several micrometers over a delay range of 4 ps.

The decreasing overlap was already visible in earlier spectra: Fig. 6.19 shows a decreased ion yield for large positive delays as these channels require the interplay of pump and probe pulse. In contrast, the channels in Fig. 6.14 show an increased rate for the same delay values because they are mainly produced within a single pulse, making the spatial overlap irrelevant. Similarly, the spectra in Fig. 6.26 show an increased ion yield for large KERs and large positive delays, where the spatial pulse overlap is fading and thus the single pulse contribution at high KERs dominating. For small positive delays instead the rate in the direct channel is decreased because of good spatial overlap.

The vanishing of the time-dependent traces for negative delays in Fig. 6.26 is caused by the intensity being distributed unequally among both pulses. If the pulse of higher intensity is preceding, it will highly ionize the molecule and the intensity of the probe is not sufficient to further ionize the fragments. Instead, if the pulse of lower intensity is preceding a slowly dissociating molecular ion is produced and both fragments are further ionized by the intenser probe pulse. We note that the dominant precursor for reaching the highest charge states is $(1, 2)$. Other intermediate charge states, particularly those created by more than just one photon, are not visible.

6.3 IR/XUV Pump-Probe Measurements

While the XUV photons mainly interact with inner-shell electrons, the IR laser couples most efficiently to the least bound electrons in the outer shells. In addition the IR field imposes a strong perturbation on the molecule that may lead to tunnel ionization of the molecule, as explained in Sect. 2.1.2. Therefore we deal with two fundamentally different ionization mechanisms combined in an IR/XUV pump-probe experiment. In Sect. 6.3.1 the action of the IR laser alone on the I_2 molecule is discussed and compared to ionization within a single XUV pulse. Combining the knowledge from single-pulse XUV measurements, presented in Sect. 6.1, with that from single-pulse IR studies allows the interpretation of the IR/XUV pump-probe spectra, presented in Sect. 6.3.2. In Sect. 6.3.3 the ion yield of bound I_2 molecules and separated ions or atoms is compared. Part of this section has been published in [66].

6.3.1 Ionization of I_2 in Strong IR Laser Fields

The multiple ionization of diatomic homonuclear molecules with short intense laser pulses in the optical and IR regime has been investigated in many studies, for instance [56, 72, 78]. The internuclear distance between the atoms imposes an additional degree of freedom as compared to atoms and thus offers the interesting possibility

to study the ionization dynamics as a function of that distance. Although I_2 has a complicated electronic configuration it was used as a target in many multi-ionization studies due to its slow dissociation dynamics, e.g., [16, 37, 56].

Once a molecule is multiply ionized it will most likely dissociate and the fragments will repel each other due to the Coulomb force. During the dissociation the molecule may absorb more photons that further ionize it. This accelerates the fragments because the Coulomb repulsion increases with the charge. In literature this process is referred to as multi-electron dissociative ionization (MEDI) [32]. Analyzing the fragments' kinetic energies gives insight into the ionization process on the time scales of the dissociative motion. In principle we have introduced multiple ionization via intense XUV radiation in the same way. However, the ionization with an IR laser involves a much larger number of photons. The MEDI scheme occurs only for some molecules at certain wavelengths but fails for others [13, 53].

An alternative scheme, where the ionization probability was found to be drastically enhanced at certain internuclear distances [67], is the so-called charge-resonance-enhanced ionization (CREI) [11, 78]. The distance of enhanced ionization for I_2 is approximately the double equilibrium internuclear distance. This is explained by using a Coulomb-explosion model based on field ionization [56]. These models are similar to the classical COB model, which we have applied in Sect. 6.2.6 for the interpretation of the critical distances of charge transfer.

Understanding the interaction of a single IR laser pulse with I_2 is important for the interpretation of the IR/XUV pump-probe spectra that will be presented in the following Sect. 6.3.2. All data are recorded at a repetition rate of 10 Hz, a limitation imposed by the IR laser system. The IR laser parameters were already introduced in Sect. 4.2.3, most importantly the pulse length of 120 fs (FWHM) [45] and the intensity of $3.4 \times 10^{14} \frac{\mathrm{W}}{\mathrm{cm}^2}$.

In Fig. 6.27 an overview of the created fragments produced with the IR laser alone is given. In the presence of the strong field the electrons are predominantly emitted in polarization direction as the field bends the potential barrier in that direction. It manifests in our data as a dipole distribution of the ions along the polarization direction. The molecules are oriented randomly in the gas target, but those with their internuclear axis parallel to the laser polarization are ionized most efficiently. We extract the original orientation of the molecule by analyzing the angular distribution of the fragments as they are always emitted back-to-back in a Coulomb explosion. Therefore, target ions are detected predominantly in the direction of the laser polarization axis. As the IR laser couples most efficiently to the least bound electrons from the valence shell, the electrons are most likely removed from the $5p$-like shells. A strong indicator for this hypothesis is the charge state distribution showing a sharp cut-off beyond I^{5+}, which for the iodine atom corresponds to a completely depleted $5p$-shell.

The distribution of each charge state in Fig. 6.27a shows several discrete ring-like structures, with larger radii for higher charge states. The larger the radius, the higher the energy gained from a Coulomb explosion. For instance, the distribution of I^{2+} ions features four rings, each from a Coulomb explosion with one fragment being I^{2+}. As the IR laser mostly creates dissociating molecules with at least one neutral

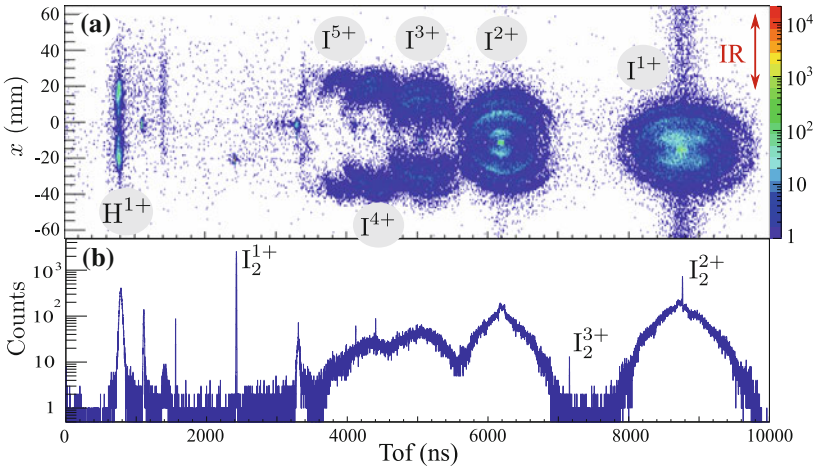

Fig. 6.27 Ionization of I_2 by the IR laser: **a** TOF versus x-position on the detector, which coincides with the laser polarization direction. Dominant fragments originating from Coulomb explosions are indicated. As the jet is propagating in negative x-direction, the fragments emerging from it have constant offset in that direction (cf. Sect. 5.2). **b** Projection of (**a**) onto the TOF axis. The TOFs of molecular iodine ions are highlighted

fragment [44], the lowest energy and thus the innermost ring corresponds to the fragmentation channel $I^{2+} + I$, the next outer one to $I^{2+} + I^{1+}$, and so forth.

As we detect only charged particles, the dissociation channel (0, 0) is not accessible in our experiment. However, channels with one charged and one neutral fragment can be reconstructed indirectly, as already illustrated in Sect. 6.2.1. The spectra of all I^{1+} and I^{2+} ions are shown in Fig. 6.28 and the energy region of break-ups with potentially one neutral fragment is indicated. I^{1+} ions emerge most likely from a

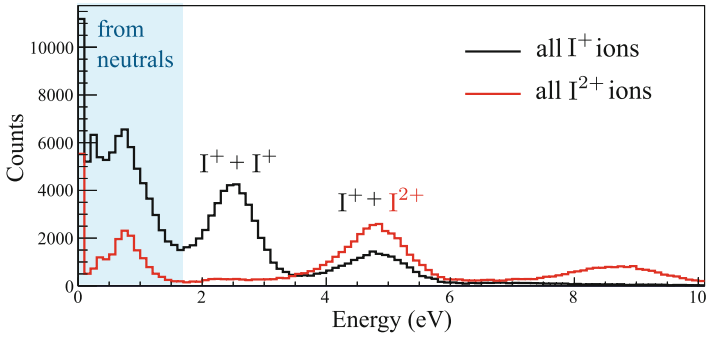

Fig. 6.28 Superimposed energy spectra of all I^{1+} and I^{2+} ions. All fragments with an energy below the lowest Coulomb-explosion energy, i.e., that of (1, 1), may belong to dissociation with one neutral fragment

neutral dissociation into (0, 1), while for I^{2+} fragments the break-up into (0, 2) is also present. The creation of the asymmetric channel (0, 2) might be surprising in the first place as the decay into the symmetric (1, 1) channel is energetically more favorable. However, this is only true if field effects from the IR laser are neglected. For short pulses and at high intensities the IR field bends the molecules' potential strong enough that the (0, 2) channel becomes energetically favorable, which has been investigated in detail experimentally [37, 56] (Figs. 6.29 and 6.30).

Another feature arises in the center of each Coulomb-explosion ring which is thus attributed to a fragment with low kinetic energy. When analyzing the KERs of the coincident ions we find fragments with almost no energy for all charge states. Thus we conclude that these ions were created from already dissociated iodine molecules and therefore have only small KERs. The low-energetic feature is only present in spectra where the IR laser has been used. It thus stems most likely from a prepulse or pedestal of the IR pulse that dissociates the molecule before the main IR and the XUV pulse impinge. This is well possible—even for a weak prepulse—as two 1.55 eV photons are sufficient to neutrally dissociate the I_2 molecule (cf. Fig. 6.31). The highest charge state emerging from an isolated atom is I^{4+} arising around 4,200 ns in Fig. 6.27. It is clearly visible as the background events from rest gas ionization are drastically suppressed compared to analogous spectra for an XUV pulse. While the

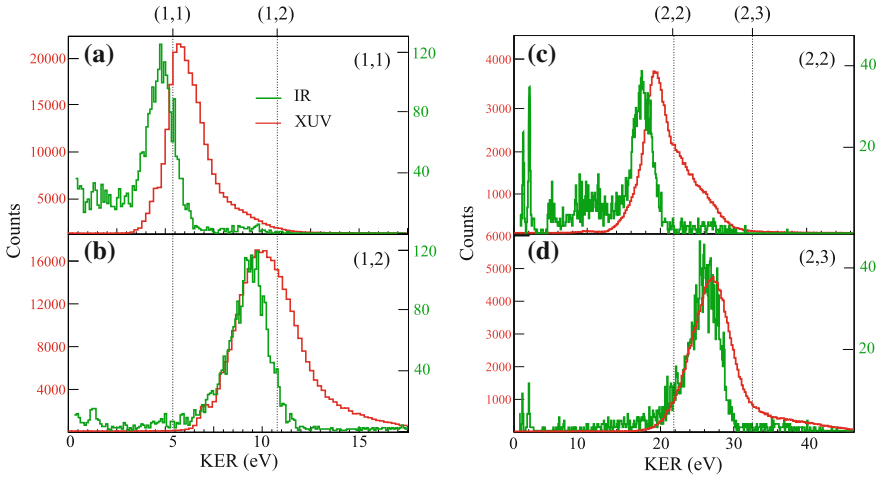

Fig. 6.29 Comparison of single pulse XUV (*red*) and single pulse IR (*green*) KER spectra for exemplary coincidence channels. The intensity of the IR data is scaled to the height of the XUV data, however the different count rates are indicated by the two *y-axes*. The XUV pulses were roughly 57 fs long and the intensity was approximately $10^{14}\ \frac{\mathrm{W}}{\mathrm{cm}^2}$. For the (2, 2) in (**c**) and the (1, 1) channel in (**a**) the IR KER-distribution peaks at smaller values than for the XUV case. This indicates that the final charge states were populated within a longer time resulting in an overall smaller KER. In fact several IR photons are needed to reach (1, 1), while a single XUV photon is sufficient. As (1, 1) is a precursor of (2, 2) the channels are expected to exhibit similar features. The same is true for (1, 2) in (**b**) and (2, 3) in (**d**), where the IR and XUV spectra share their low-energetic cut-off, indicating a slightly delayed population of the final charge states for the XUV pulses as well

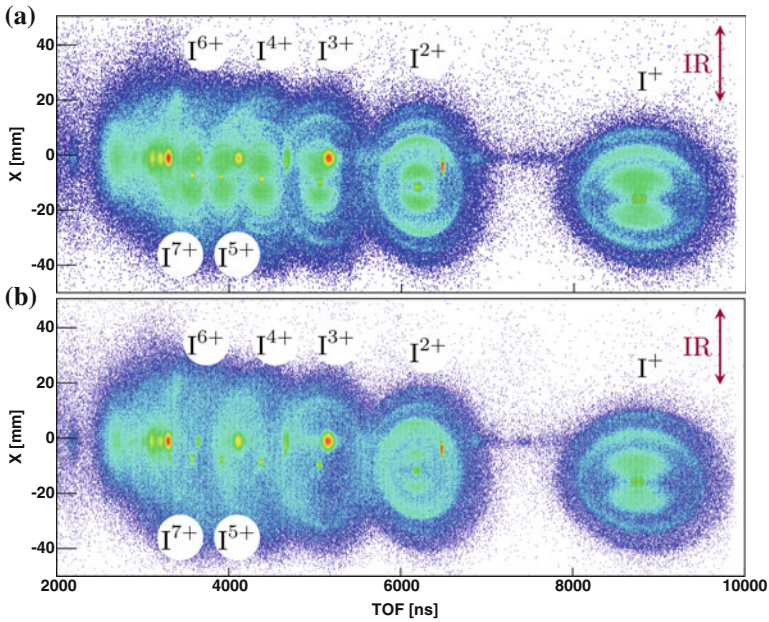

Fig. 6.30 TOF versus the x-position on the detector for **a** the IR pulse arriving before the XUV pulse, and **b** vice versa

XUV radiation ionizes along its whole path through the vacuum chamber, ionization through the IR laser is limited to the focal volume, as the photon density is not sufficient elsewhere.

Figure 6.29 shows a comparison between single pulse IR and single pulse XUV spectra for various coincidence channels. For the IR data, the KER distributions for the channels (1, 1) and (2, 2) are clearly shifted towards lower values compared to the XUV spectra. This behavior is attributed to the different ionization mechanisms governing both wavelength regimes. The removal of two valence electrons in I_2 requires at least 17 photons of 1.55 eV to be absorbed within one pulse. IR/XUV pump-probe studies have shown that the production of I_2^{2+} proceeds within 75 ± 15 fs (FWHM) of the IR pulse [45], while the same degree of ionization is reached almost instantaneously via the absorption of a single XUV photon. In addition the inner-valence-ionized I_2^{2+} molecule may remain in a highly excited state. Thus it dissociates via an entirely different state compared to the IR-induced dissociation. For two-photon XUV ionization, the coincidence channel (1, 1) is a precursor of (2, 2). Thus both channels are expected to show the same behavior when they are compared to the IR spectra: Their peak positions are located at higher KERs than their IR counterparts. With the same reasoning we may find that the XUV channel (2, 3) and its precursor (1, 2) share the low-energetic edge with the corresponding IR spectra. The peak positions of the XUV spectra are in general shifted towards higher KERs as compared to the IR spectra. This is explained by considering their intrinsic difference:

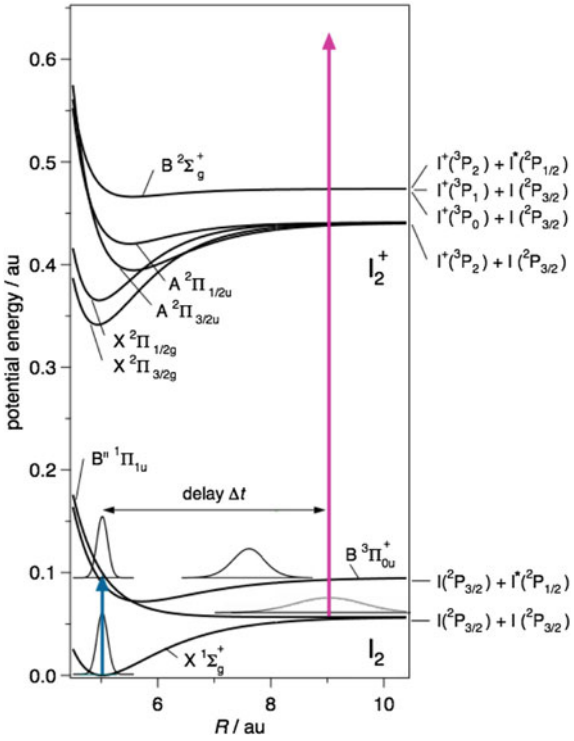

Fig. 6.31 Potential energy curves of I_2 relevant for the interaction with the IR laser. The pump pulse in *blue* induces the dissociation of the molecule, which is probed after a time delay by the probe pulse in *magenta*. Figure adapted from [36]

While (1, 1) is produced via one fast Auger decay, (1, 2) has undergone a second slower Auger decay (cf. Sect. 6.1). The exponential nature of this slower Auger decay has a second effect: The distribution is broadened, as an individual molecule may further decay immediately after the first Auger decay leading to high KERs, or it may live longer leading to smaller KERs.

In conclusion we recall that the peak intensity of the IR laser was sufficient to create fragments up to I^{5+} at an intensity in the transition regime between multi-photon absorption and tunnel ionization.

6.3.2 Combining IR and XUV Radiation

With the effects of a single XUV and a single IR pulse on the iodine molecule introduced, we now study the combination of the both. The TOF and the detector position along the laser polarization axis of all detected particles are shown in Fig. 6.30a for a

preceding IR pulse and in (b) for a preceding XUV pulse. The intensity of the IR pulse is identical to that used for the measurement discussed in the previous Sect. 6.3.1 and the intensity of the XUV pulses is the higher of the two, roughly $3 \times 10^{14} \frac{\mathrm{W}}{\mathrm{cm}^2}$.

If the IR pulse arrives first it initiates the dissociation of the molecule. This determines the emission angle of the coincident fragments with respect to the IR polarization axis. Therefore, a dipole-shaped emission in polarization direction is also preferred for the high charge states that are out of reach with an IR pulse only, as shown in Fig. 6.30. In contrast to the IR-only spectrum from Fig. 6.27, the count rate perpendicular to the polarization direction does not vanish completely, because all charge states can also be produced with a single XUV pulse leading to a homogeneous emission pattern. If the XUV pulse arrives first, the emission characteristic is spherical and the succeeding IR pulse further ionizes the dissociating fragments. For small charge states the emission characteristic remains partially dipole-like. Thus they are created within the IR pulse alone.

In Fig. 6.32 a set of exemplary coincidence channels is shown. As discussed in Sect. 6.2 for XUV pump-probe spectra, all time-independent features are created within a single pulse, either XUV or IR, and the time-dependent traces stem from the joint illumination with XUV and IR radiation. We start by discussing negative delays where the IR pulse is preceding: The coincidence channels (1, 2) and (2, 2) (cf. Fig. 6.32a, b, respectively) show only low-energetic precursors emerging from a dissociation with one neutral fragment. As a delayed XUV pulse will always increase the charge state of one of the fragments by two, the only possibility for the production of channel (1, 2) is via (1, 0) and for (2, 2) via (2, 0):

$$\mathrm{I}_2 \xrightarrow{\mathrm{IR}} (1, 0) \xrightarrow{\mathrm{XUV}} (1, 2), \tag{6.19}$$

$$\mathrm{I}_2 \xrightarrow{\mathrm{IR}} (2, 0) \xrightarrow{\mathrm{XUV}} (2, 2). \tag{6.20}$$

The other presented channels, (2, 3) and (3, 3), feature neutral and charged precursor states as indicated in Fig. 6.32c, d, respectively. The precursors with a neutral fragment are assigned as above. The charged precursors are identified using the Coulomb-explosion model to be (1, 2) and (1, 1), respectively. Thus the spectra with preceding IR laser are summarized in the following way:

$$\mathrm{I}_2 \xrightarrow{\mathrm{IR}} (2, 1) \xrightarrow{\mathrm{XUV}} (2, 3), \tag{6.21}$$

$$\mathrm{I}_2 \xrightarrow{\mathrm{IR}} (2, 0) \xrightarrow{\mathrm{XUV}} (2, 3), \tag{6.22}$$

$$\mathrm{I}_2 \xrightarrow{\mathrm{IR}} (1, 1) \xrightarrow{\mathrm{XUV}} (3, 3), \tag{6.23}$$

$$\mathrm{I}_2 \xrightarrow{\mathrm{IR}} (1, 0) \xrightarrow{\mathrm{XUV}} (3, 3). \tag{6.24}$$

For a preceding XUV pulse the spectra are analyzed in the exact same way, but neutral precursors can be neglected. The coincidence channel (1, 2) for instance is reached by producing the precursor (1, 1) and subsequent removal of a further electron by the

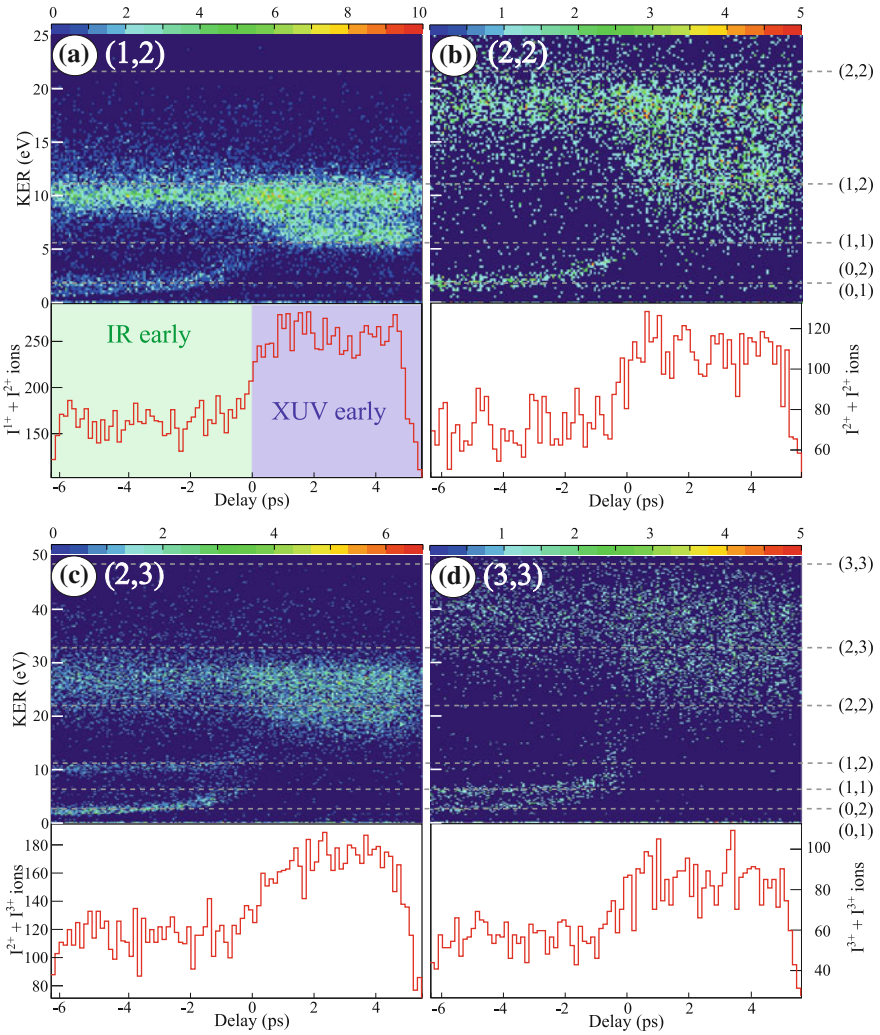

Fig. 6.32 Delay-dependent KER spectra for exemplary (more) symmetric coincidence channels and their projection onto the delay axis: **a** for (1, 2), **b** for (2, 2), **c** for (2, 3), and **d** for (3, 3). Negative delays denote those events with preceding IR pulse and positive values stand for a delayed IR pulse. Predictions from the Coulomb-explosion model are superimposed (*gray dashed lines*) in order to identify the corresponding precursor states of each coincidence channel

IR probe. Similarly, (2, 2) shows the main precursor (1, 2) with a weak contribution from the precursor (1, 1). Interestingly the channel (2, 3) does only show a single precursor, (2, 2), while the next higher coincidence channel (3, 3) again features two precursors. The question arises why (1, 2), the second possible precursor of (2, 3), is missing. As already discussed, the inner-valence-ionized I_2^{2+} molecular ion remains in a highly excited state due to the large excess energy. Thus it is easily further ionized

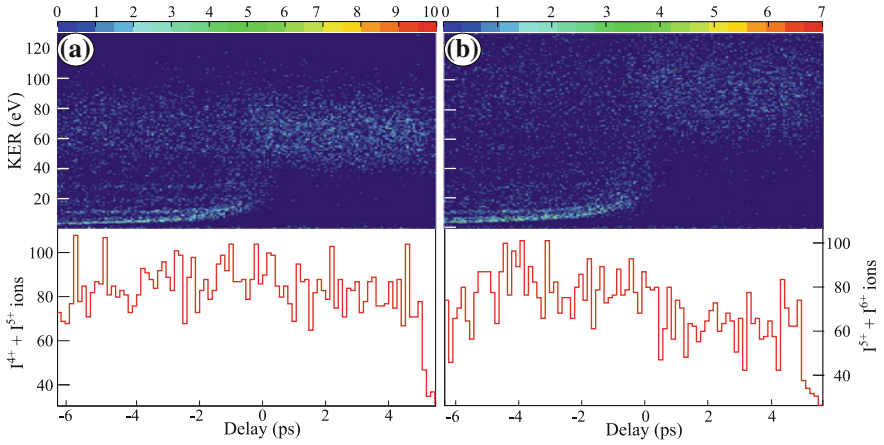

Fig. 6.33 Delay-dependent KER spectra for the coincidence channels (4, 5) in (**a**), and (5, 6) in (**b**) and the projections of all KERs onto the delay axis

by the IR pulse resulting in two precursors of (2, 2). The triply ionized molecular ion I_2^{3+} instead has only little remaining excess energy and thus will be produced in its ground state or at least close to that. Therefore the required energy to remove two further electrons from I_2^{3+} is relatively high and thus the precursor (1, 2) does not show up in (2, 3). The two precursor states of (3, 3) are explained in a similar fashion: We have already identified I_2^{4+}—created within one XUV pulse—to be a highly excited molecular ion that is easily ionized. Therefore the intensity of the IR laser is sufficient to remove the highly excited electron and a second valence electron. We conclude that delayed ionization with the IR pulse gives valuable information on which states were created in an excited state by the XUV pulse.

The delayed ionization by the IR laser is a very efficient process, because it clearly dominates the ion yield of the delay-dependent KER spectra in Fig. 6.32. However this trend of an increased ion yield at positive delays is only present for the more symmetric break-up channels and only up to a certain degree of ionization. For already highly charged molecular ions the IR laser intensity is not sufficient anymore to strip off further electrons, in particular if all electrons are removed from the $5p$ shell (beyond I^{5+}). Thus the asymmetry in the charge state yield should vanish at some point. Two exemplary delay-dependent KER spectra of the channels (4, 5) and (5, 6) are shown in Fig. 6.33a, b respectively. Indeed the positive delay range shows the characteristic spectrum of one XUV pulse alone and the asymmetry is not present anymore for (4, 5). For (5, 6) the situation is even reversed, it shows more coincident ion pairs at negative delays where the IR laser pulse proceeds. This trend continues up to the highest symmetric charge states.

The more efficient creation of highly charged fragments for a preceding IR laser is explained via an effect that we refer to as *Coulomb blocking*. For small delays the charged fragments of a molecular ion are still close to each other. The neighboring ion

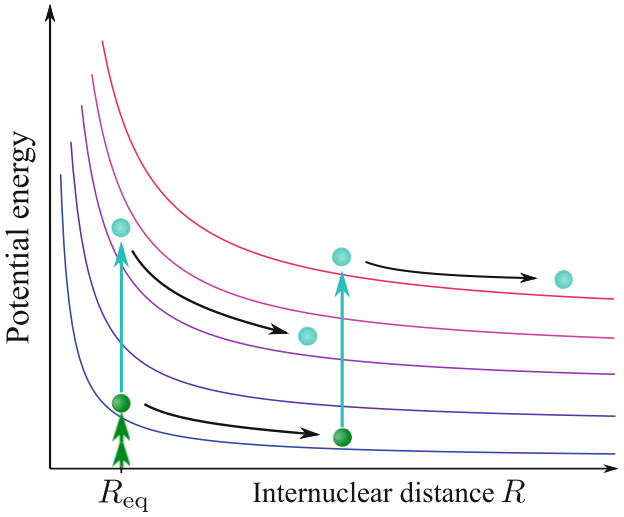

Fig. 6.34 Illustration of Coulomb blocking. At equilibrium internuclear distance the joint illumination with XUV (*light blue arrows*) and IR (*green arrows*) is not sufficient to reach the highest potential energy curve due to the close-by Coulomb potential of the other ion. If, instead the IR laser triggers a dissociation, the energy of one XUV photon is at some point sufficient to reach the next higher charge state

may hinder the creation of the next higher charge state by increasing the ionization potential due to its Coulomb potential. But the further the ions move apart the weaker the influence of the neighboring ion. Eventually the ionization potential may again become accessible with the present pulse settings, as illustrated in Fig. 6.34. The effect is directly visible in the calculated ionization potentials of I_2^{n+} listed in Table 6.2: The energy required to produce two separated ions was found to be lower than that needed to create a molecular ion with the sum charge of both. As the IR laser mostly creates low charged ions or neutrals, the molecule will slowly dissociate and by the time the XUV pulse impinges, the internuclear distance may be large enough so that the Coulomb force of the neighboring ion has become negligible.

Now we will discuss asymmetric channels, which exhibit a strongly increased ion yield for negative delays. Figure 6.35 shows the delay-dependent KER spectra of two exemplary asymmetric coincidence channels (1, 3) and (1, 4). For a preceding XUV pulse the KER distributions show the same behavior as the single-pulse XUV spectra in Fig. 6.7. From this we draw the conclusion that in the creation of these spectra the IR pulse does not play a significant role. Therefore, delayed ionization by the IR laser does not lead to the production of asymmetric charge state distributions. This is attributed to the different ionization mechanisms of the IR and the XUV pulses. While XUV photons act most efficiently on inner-valence electrons, which are well localized at one of the constituents, the IR laser couples best to outer-valence electrons that are not localized at one of the atoms. An IR pulse will thus not create asymmetric charge state distributions, except for very strong fields, when the molecular potential

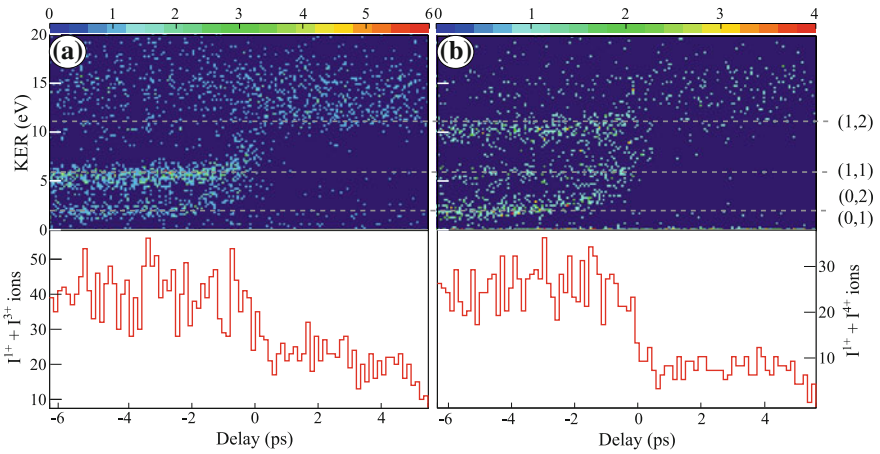

Fig. 6.35 Delay-dependent KER spectra for the asymmetric coincidence channels (1, 3) and (1, 4) and their projections onto the delay axis

is bend so much, that asymmetric break-up gets energetically more favorable than symmetric one [56]. Furthermore, even for large positive delays, where the iodine ions are considered as separated, the IR laser does not create asymmetric charge states. This is due to the suppression of higher multi-photon orders: For instance, the XUV radiation ionizes I_2 into (1, 2) and the ionic fragments are placed into the IR field as separated ions for large delays. The number of photons needed to remove another electron from I^+ is much smaller than that for I^{2+}. Therefore the creation of (1, 3) compared to (2, 2) is suppressed. This explanation is valid for the creation of all asymmetric charge states. In contrast, if the XUV pulse arrives late, a single photon is sufficient to ionize either of the ions and thus asymmetric charge states are created (cf. Fig. 6.35).

We would like to point out that, in principle, the ion yields for small negative delays in Fig. 6.35 should also exhibit the characteristic gaps, discussed in Sect. 6.2.5. Actually the gaps should be even more pronounced, as the dissociation via neutral fragment occurs slower. However, the region of interest is not sufficiently resolvable due to the jitter between FEL and IR pulses, that could not be compensated with the TEO tool, discussed in Sect. 4.2.3.

6.3.3 What Can Be Charged Up Higher, Two Atoms or a Molecule?

The interesting question arises, whether we reach higher charge states in a diatomic molecule or two separated atoms. The role of the preceding IR pulse is to prepare isolated neutrals or ions with low charge states by dissociating the molecule. For the

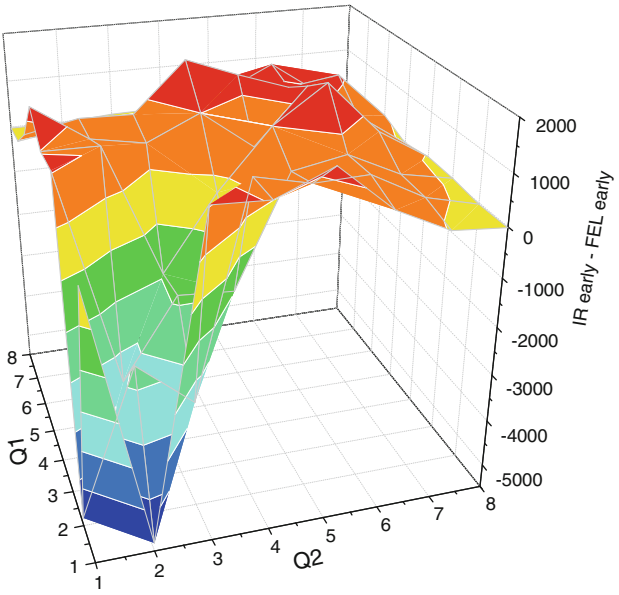

Fig. 6.36 Ion yield of all observed coincidence channels (Q_1, Q_2). The difference between the yield for a preceding IR and a delayed IR pulse as a function of Q_1 and Q_2 is shown. Symmetric break-up channels dominate if the XUV pulse arrives first, mostly because these charge states are dominantly created by the single XUV pulse only. Asymmetric and very high break-up channels are produced more often if the IR laser arrives first and dissociates the molecule prior to the removal of additional electrons by the XUV

highest charge states a delayed IR pulse does not affect the charge state at all. Thus, we have created a situation, in which we can directly compare the response of an isolated atom or ion with that of a molecule irradiated with the same intense XUV radiation.

Our findings are summarized in Fig. 6.36, which shows an overview of the ion yield of all observed coincidence channels (Q_1, Q_2). Shown is the difference between the yield for a preceding IR and a delayed IR pulse as a function of Q_1 and Q_2. The region of low charge states and symmetric break-ups is clearly dominated by a preceding XUV pulse, because the IR efficiently removes remaining valence electrons until the $5p$ shell is emptied. For higher ionized fragments the ion-yield difference becomes positive. Therefore, these charge states are produced more efficiently with a preceding IR pulse, which has already dissociated the molecular ion before the XUV pulse arrives. This effect has been explained via the Coulomb blocking, where the highest charge states are suppressed for small internuclear distances. Furthermore, asymmetric coincidence channels are mostly produced via a delayed XUV pulse from dissociated molecules.

We conclude that the highest charge states were reached for separated atoms or ions. This is in contrast to studies on large Xe clusters, which were found to absorb XUV radiation much more efficiently than monomers due to collective electron

phenomena building up in a cluster [74]. A system of only two constituents, the I_2 molecule, is too small for similar effects and the difference in the reached charge states for monomers and molecules is attributed to the Coulomb blocking.

References

1. A. Aguilar et al., Absolute photoionization cross sections for Xe^{4+}, Xe^{5+}, and Xe^{6+} near 13.5 nm: experiment and theory. Phys. Rev. A **73**, 032717 (2006)
2. M.Y. Amusia et al., Photoionization of atomic iodine and its ions. Phys. Rev. A **61**, 020701 (2000)
3. P. Andersen et al., Absolute cross sections for the photoionization of 4d electrons in Xe^+ and Xe^{2+} ions. J. Phys. B: At. Mol. Opt. Phys. **34**(10), 2009 (2001)
4. U. Becker et al., Subshell photoionization of Xe between 40 and 1000 eV. Phys. Rev. A **39**, 3902–3911 (1989)
5. P. Beiersdorfer et al., Laboratory simulation of charge exchange-produced X-ray emission from comets. Science **300**(5625), 1558–1559 (2003)
6. J.M. Bizau et al., Absolute photoionization cross sections along the Xe isonuclear sequence: Xe^{3+} to Xe^{6+}. Phys. Rev. A **73**, 022718 (2006)
7. B.H. Boo, N. Saito, Dissociative multiple photoionization of Br_2, IBr, and I_2 in the VUV and X-ray regions: a comparative study of the inner-shell processes involving Br(3d,3p,3s) and I(4d,4p,4s,3d,3p). J. Electron Spectrosc. Relat. Phenom. **127**(3), 139–152 (2002)
8. C. Brechignac, J.P. Connerade, Giant resonances in free atoms and in clusters. J. Phys. B: At. Mol. Opt. Phys. **27**(17), 3795 (1994)
9. J. Burgdörfer, P. Lerner, F.W. Meyer, Above-surface neutralization of highly charged ions: the classical over-the-barrier model. Phys. Rev. A **44**, 5674–5685 (1991)
10. J. Burgdörfer, R. Morgenstern, A. Niehaus, Angular momentum distribution in the classical over-barrier model for electron capture into highly charged slow projectiles. J. Phys. B: At. Mol. Phys. **19**(14), L507 (1986)
11. S. Chelkowski, A.D. Bandrauk, Two-step Coulomb explosions of diatoms in intense laser fields. J. Phys. B: At. Mol. Opt. Phys. **28**(23), L723 (1995)
12. S.S. Churilov, Y.N. Joshi, A.N. Ryabtsev, The $4d^{10}\ {}^1S_0 - 4d^9\ (np + n'f)$ transitions in the Pd I isoelectronic sequence from Cd III to Cs X. J. Phys. B: At. Mol. Opt. Phys. **27**(22), 5485 (1994)
13. K. Codling, L.J. Frasinski, P.A. Hatherly, On the field ionisation of diatomic molecules by intense laser fields. J. Phys. B: At. Mol. Opt. Phys. **22**(12), L321 (1989)
14. F.J. Comes, U. Nielsen, W.H.E. Schwarz, Inner electron excitation of iodine in the gaseous and solid phase. J. Chem. Phys. **58**(6), 2230–2237 (1973)
15. J.P. Connerade, The non-Rydberg spectroscopy of atoms. Contemp. Phys. **19**(5), 415–447 (1978)
16. E. Constant, H. Stapelfeldt, P. Corkum, Enhanced ionization of molecular ions in intense laser fields: experiments on the iodine molecule, in *Ultrafast Phenomena X*, ed. by P. Barbara et al. Springer Series in Chemical Physics, vol. 62 (Springer, Berlin, 1996), pp. 105–106
17. J.P. Cryan et al., Auger electron angular distribution of double core-hole states in the molecular reference frame. Phys. Rev. Lett. **105**, 083004 (2010)
18. J.N. Cutler, G.M. Bancroft, K.H. Tan, Ligand-field splittings and core-level linewidths in I 4d photoelectron spectra of iodine molecules. J. Chem. Phys. **97**(11), 7932–7943 (1992)
19. Z. Deng et al., Beyond the Bragg peak: hyperthermal heavy ion damage to DNA components. Phys. Rev. Lett. **95**, 153201 (2005)
20. Z. Deng et al., Reactive scattering damage to DNA components by hyperthermal secondary ions. Phys. Rev. Lett. **96**, 243203 (2006)

21. D. Dijkkamp et al., Subshell-selective electron capture in collisions of C^{4+}, N^{5+}, O^{6+} with H, H_2 and He. J. Phys. B: At. Mol. Phys. **18**(24), 4763 (1985)
22. G. Doumy et al., Nonlinear atomic response to intense ultrashort X rays. Phys. Rev. Lett. **106**, 083002 (2011)
23. J. de Vries et al., Charge driven fragmentation of nucleobases. Phys. Rev. Lett. **91**, 053401 (2003)
24. D.L. Ederer, Photoionization of the 4*d* electrons in xenon. Phys. Rev. Lett. **13**, 760–762 (1964)
25. D. Edvardsson et al., An experimental and theoretical investigation of the valence double photoionisation of the iodine molecule. Chem. Phys. **324**(2–3), 674–678 (2006)
26. E.D. Emmons et al., Photoionization and electron-impact ionization of Xe^{3+}. Phys. Rev. A **71**, 042704 (2005)
27. B. Erk et al., Inner-shell multiple ionization of polyatomic molecules with an intense x-ray free-electron laser studied by coincident ion momentum imaging. J. Phys. B: At. Mol. Opt. Phys. **46**(16), 164031 (2013)
28. B. Erk et al., Ultrafast charge rearrangement and nuclear dynamics upon inner-shell multiple ionization of small polyatomic molecules. Phys. Rev. Lett. **110**, 053003 (2013)
29. M. Eypper et al., Photoionization of iodine atoms: angular distributions and relative partial photoionization cross-sections in the energy region 11.0–23.0 eV. J. Chem. Phys. **133**(8), 084302 (2010)
30. M. Eypper et al., Photoionization of iodine atoms: Rydberg series which converge to the $I^+(^1S_0) \rightarrow I(^2P_{3/2})$ threshold. J. Chem. Phys. **132**(24), 244304 (2010)
31. L. Fang et al., Double core-hole production in N_2: beating the Auger clock. Phys. Rev. Lett. **105**, 083005 (2010)
32. L.J. Frasinski et al., Femtosecond dynamics of multielectron dissociative ionization by use of a picosecond laser. Phys. Rev. Lett. **58**, 2424–2427 (1987)
33. L.J. Frasinski et al., Dynamics of hollow atom formation in intense X-ray pulses probed by partial covariance mapping. Phys. Rev. Lett. **111**, 073002 (2013)
34. D.C. Frost, C.A. McDowell, The ionization and dissociation of some halogen molecules by electron impact. Can. J. Chem. **38**(3), 407–420 (1960)
35. H. Fukuzawa et al., Deep inner-shell multiphoton ionization by intense X-ray free-electron laser pulses. Phys. Rev. Lett. **110**, 173005 (2013)
36. M. Fushitani, A. Matsuda, A. Hishikawa, Time-resolved EUV photoelectron spectroscopy of dissociating I2 by laser harmonics at 80 nm. Opt. Express **19**(10), 9600–9606 (2011)
37. G.N. Gibson et al., Direct evidence of the generality of charge-asymmetric dissociation of molecular iodine ionized by strong laser fields. Phys. Rev. A **58**, 4723–4727 (1998)
38. H. Haken, H.C. Wolf, *Molecular Physics and Elements of Quantum Chemistry. Introduction to Experiments and Theory*. vol. 2 (Springer, Berlin, 2004), p. 592 (English ed.)
39. M. Hoener et al., Ultraintense X-ray induced ionization, dissociation, and frustrated absorption in molecular nitrogen. Phys. Rev. Lett. **104**, 253002 (2010)
40. E.P. Kanter et al., Unveiling and driving hidden resonances with high-fluence, high-intensity X-ray pulses. Phys. Rev. Lett. **107**, 233001 (2011)
41. V. Kaufman, J. Sugar, Ag I isoelectronic sequence: wavelengths and energy levels for I VII through La XI. Physica Scripta **24**(4), 738 (1981)
42. V. Kaufman, J. Sugar, Y.N. Joshi, Wavelengths and energy levels of I V and I VI. J. Opt. Soc. Am. B **5**(3), 619–622 (1988)
43. H. Kjeldsen et al., Absolute photoionization cross sections of I^+ and I^{2+} in the 4d ionization region. Phys. Rev. A **62**, 020702 (2000)
44. M. Krikunova et al., Ultrafast photofragmentation dynamics of molecular iodine driven with timed XUV and near-infrared light pulses. J. Chem. Phys. **134**(2), 024313 (2011)
45. M. Krikunova et al., Strong-field ionization of molecular iodine traced with XUV pulses from a free-electron laser. Phys. Rev. A **86**, 043430 (2012)
46. L.D. Landau, E.M. Lifsic, *Mechanics*, 3rd edn. Course of Theoretical Physics, vol. 1 (Elsevier, Butterworth-Heinemann, Amsterdam, 2007), p. 170 (repr.)

47. D.W. Lindle et al., Inner-shell photoemission from the iodine atom in CH_3I. Phys. Rev. A **30**, 239–244 (1984)
48. R. Mann, Total one-electron capture cross sections for Ar^{q+} and I^{q+} ions in slow collisions on H_2 and He. Zeitschrift für Physik D Atoms, Molecules and Clusters **3**(1), 85–90 (1986)
49. B.F. Murphy et al., Multiphoton L-shell ionization of H_2S using intense x-ray pulses from a free-electron laser. Phys. Rev. A **86**, 053423 (2012)
50. L. Nahon, A. Svensson, P. Morin, Experimental study of the 4*d* ionization continuum in atomic iodine by photoelectron and photoion spectroscopy. Phys. Rev. A **43**, 2328–2337 (1991)
51. R. Neutze et al., Potential for biomolecular imaging with femtosecond X-ray pulses. Nature **406**(6797), 752–757 (2000)
52. A. Niehaus, A classical model for multiple-electron capture in slow collisions of highly charged ions with atoms. J. Phys. B: At. Mol. Phys. **19**(18), 2925 (1986)
53. D. Normand, M. Schmidt, Multiple ionization of atomic and molecular iodine in strong laser fields. Phys. Rev. A **53**, R1958–R1961 (1996)
54. G. O'Sullivan, The absorption spectrum of CH_3I in the extreme VUV. J. Phys. B: At. Mol. Phys. **15**(9), L327 (1982)
55. T. Pattard, J. Burgdörfer, Half-collision model for multiple ionization by photon impact. Phys. Rev. A **64**, 042720 (2001)
56. J.H. Posthumus et al., Field-ionization, Coulomb explosion of diatomic molecules in intense laser fields. J. Phys. B: At. Mol. Opt. Phys. **29**(23), 5811 (1996)
57. M. Richter et al., Extreme ultraviolet laser excites atomic giant resonance. Phys. Rev. Lett. **102**, 163002 (2009)
58. M. Robin, 4f wavefunction collapse and giant resonances in molecules. Chem. Phys. Lett. **119**(1), 33–37 (1985)
59. G. Rodrigues et al., Systematic calculation of total atomic energies of ground state configurations. At. Data Nucl. Data Tables **86**(2), 117–233 (2004)
60. B. Rudek et al., Ultra-efficient ionization of heavy atoms by intense X-ray freeelectron laser pulses. Nat. Photon. **6**(12), 858–865 (2012)
61. B. Rudek et al., Resonance-enhanced multiple ionization of krypton at an x-ray free-electron laser. Phys. Rev. A **87**, 023413 (2013)
62. H. Ryufuku, K. Sasaki, T. Watanabe, Oscillatory behavior of charge transfer cross sections as a function of the charge of projectiles in low-energy collisions. Phys. Rev. A **21**, 745–750 (1980)
63. P. Salén et al., Experimental verification of the chemical sensitivity of two-site double core-hole states formed by an X-ray free-electron laser. Phys. Rev. Lett. **108**, 153003 (2012)
64. V. Schmidt, Photoionization of atoms using synchrotron radiation. Rep. Prog. Phys. **55**(9), 1483 (1992)
65. K. Schnorr et al., Electron rearrangement dynamics in dissociating I_2^{n+} molecules accessed by extreme ultraviolet pump-probe experiments. Phys. Rev. Lett. **113**, 073001 (2014)
66. K. Schnorr et al., Multiple ionization and fragmentation dynamics of molecular iodine studied in IR-XUV pump-probe experiments, in *Faraday Discussions* (2014)
67. T. Seideman, M.Y. Ivanov, P.B. Corkum, Role of electron localization in intense-field molecular ionization. Phys. Rev. Lett. **75**, 2819–2822 (1995)
68. A.A. Sorokin et al., Photoelectric effect at ultrahigh intensities. Phys. Rev. Lett. **99**, 213002 (2007)
69. A. Tauheed, Y.N. Joshi, A. Naz, Extended analysis of doubly ionized iodine spectrum: I III. Physica Scripta **69**(4), 289 (2004)
70. A. Tauheed, Y.N. Joshi, A. Naz, Extended analysis of the fourth spectrum of iodine: I IV. Physica Scripta **69**(4), 283 (2004)
71. J. Tremblay et al., Photoelectron spectroscopy of atomic iodine produced by laser photodissociation. Phys. Rev. A **38**, 3804–3807 (1988)
72. D.M. Villeneuve, M.Y. Ivanov, P.B. Corkum, Enhanced ionization of diatomic molecules in strong laser fields: a classical model. Phys. Rev. A **54**, 736–741 (1996)
73. M. von Hellermann et al., Investigation of thermal and slowing-down alpha particles on JET using charge-exchange spectroscopy. Plasma Phys. Control. Fusion **33**(14), 1805 (1991)

74. H. Wabnitz et al., Multiple ionization of atom clusters by intense soft X-rays from a free-electron laser. Nature **420**(6915), 482–485 (2002)
75. H. Wabnitz et al., Multiple ionization of rare gas atoms irradiated with intense VUV radiation. Phys. Rev. Lett. **94**, 023001 (2005)
76. E. Wells et al., Charge transfer and elastic scattering in very slow $H^+ + D(1s)$ half collisions. Phys. Rev. Lett. **86**, 4803–4806 (2001)
77. L. Young et al., Femtosecond electronic response of atoms to ultra-intense X-rays. Nature **466**(7302), 56–61 (2010)
78. T. Zuo, A.D. Bandrauk, Charge-resonance-enhanced ionization of diatomic molecular ions by intense lasers. Phys. Rev. A **52**, R2511–R2514 (1995)

Chapter 7
ICD Lifetime in Ne_2

ICD lifetimes span over several orders of magnitude from a few femtoseconds up to nanoseconds. The fastest decay times are found for excited ions embedded in an environment with a large number of neighbors. While an isolated excited $Ne^+(2s^{-1})$ ion needs 0.2 ns [9] to return to its ground state, the same ion embedded into a large neon cluster relaxes within a few femtoseconds [24, 31]. The theoretical prediction of only 2 fs for the decay of a neon ion caged into a fullerene is even faster [3]. ICD in large water clusters [22] and dimers [13] was experimentally confirmed to take place within a few to ten femtoseconds. Notably, the dimers were found to relax faster via ICD than via proton transfer, which is known to take tens of femtoseconds [8]. For ICD taking place within a few femtoseconds, accompanied nuclear motion is negligible.

The ICD lifetimes of smaller systems, such as rare gas dimers, usually range from tens to hundred of femtoseconds. As discussed in Sect. 2.5.1.3 the $2s$ hole in Ne^+ is expected to decay within 64–92 fs [1, 30, 41]. Here, the lifetime is in the order of nuclear motion, which thus cannot be neglected, as the decay rate depends severely on the internuclear distance. Similar decay times are predicted for the doubly ionized neon dimer [32] and in NeAr [7].

The slowest ICD processes occur within hundreds of femtoseconds to picoseconds. Typical examples are exchange ICD (cf. Sect. 2.5.1.1) and electron transfer mediated decay [44], which were theoretically predicted in core-ionized Ne_2 dimers [38] and also experimentally confirmed [19]. For these processes nuclear motion is essential because the dimer has to gain orbital overlap by decreasing its internuclear distance, as it occurs via electron transfer. Three-electron ICD [4], predicted to be one of the slowest ICD processes, was recently experimentally observed for the first time [26].

So far, the ICD lifetime was experimentally determined for a $2s$ vacancy in large neon clusters ($>1{,}000$ atoms) to be 6 fs for bulk atoms and 30 fs for surface atoms. The lifetime was extracted by measuring the width of the $2s$ photoline [24]. This method relies on the assumption that the internuclear distance stays constant before ICD takes place, as the photoline would be broadened by the inset of nuclear motion. Therefore it is only applicable for the fastest decaying systems.

K. Schnorr, *XUV Pump-Probe Experiments on Diatomic Molecules*,
Springer Theses, DOI 10.1007/978-3-319-12139-0_7

Table 7.1 Summary of pulse parameters for the Ne_2 measurement

Photon energy	Pulse length	Intensity	No. of minibunches
58.2 eV	60 fs	10^{12} $\frac{W}{cm^2}$	30

Inner-valence ionized dimers undergoing ICD usually end up in Coulomb exploding fragments. It can be shown (cf. Sect. 7.1.3), that the width of the ions' energy distribution is dependent on the ICD lifetime. Thus, by comparing the experimentally obtained energy width with theoretical predictions, that include nuclear motion, an estimate for the lifetime is obtained, as demonstrated for NeAr [25]. Note that this estimate relies heavily on the accuracy of theory and has little predictive power.

Recently another method to extract temporal information on ICD in He_2 [40] was presented, relying on post-collision interaction (PCI) [23, 29]. The measured photoelectron energy distribution was translated into timing-information via a classical model. The KER spectra, recorded as a function of the photo-electron energy, showed good agreement with theoretical calculations performed at different times. Therefore the experiment confirmed the expected ICD lifetime in He_2 to be a few hundred femtoseconds up to picoseconds.

In this chapter the first direct time-resolved determination of an ICD lifetime is discussed. It was measured on Ne_2, applying an XUV pump-probe measurement. We start in Sect. 7.1 by describing single- and multi-photon absorption of atomic and diatomic neon within a single XUV pulse. The pump-probe experiments on Ne_2, enabling the lifetime determination, are presented in Sect. 7.2. The chapter concludes with a discussion of the lifetime result and a comparison with theoretical predictions.

7.1 Single-Pulse Measurements on Ne and Ne_2

Understanding the interaction of a single XUV pulse of 58.2 eV with Ne and Ne_2 is the prerequisite for the interpretation of pump-probe experiments. Therefore, in Sect. 7.1.1 we start by discussing single and multiple ionization in atomic Ne. In Sect. 7.1.2 we introduce the relevant potential energy curves for Ne_2 in the energy range of one photon absorption. We emphasize the coincidence channel $Ne^+ - Ne^+$, because it mostly emerges from dimers that have undergone ICD, as will be shown in Sect. 7.1.3. Additionally, we introduce the alternative $2p$ shake-up processes leading to the same charge state in Sect. 7.1.4.

7.1.1 Photoionization of Ne

The total cross section for photoionization of Ne at 58.2 eV amounts to 7.76 Mb and is dominated by the $2p$ subshell ionization cross section, as shown in Table 7.2. The

Table 7.2 Photoionization of Ne at 58.2 eV

Process	Ionization potential (eV)	Cross section (Mb)
$Ne \rightarrow Ne^+(2p^{-1})$	21.56 [16]	7.22 [43]
$Ne \rightarrow Ne^+(2s^{-1})$	48.42 [5]	0.54 [43]
$Ne^+(2p^{-1}) \rightarrow Ne^{2+}(2p^{-2})$	40.96 [27]	≈7 [17]
$Ne^{2+}(2p^{-2}) \rightarrow Ne^{3+}(2p^{-3})$	60.42 [18]	—

second relevant single-photon process is the creation of a $2s$ inner-valence vacancy. However, the cross section for the latter process is about a factor of 14 smaller. The resulting highly excited $Ne^+(2s^{-1})$ ion can only decay radiatively because relaxation via Auger decay is energetically forbidden: The relaxation energy of $E_{\text{relax}} = E_p(2s^{-1}) - E_p(2p^{-1}) = 26.86\,\text{eV}$ is not sufficient to remove a $2p$ electron bound with 40.96 eV [27]. While Auger decay typically takes place within hundreds of attoseconds to a few femtoseconds, radiative decay occurs within 0.2 ns [9]. As the removal of a $1s$ core electron requires at least 860 eV this it is not accessible in our experiment and will not be discussed here.

Figure 7.1 shows an overview of the fragments created in single XUV pulses with an intensity of roughly $10^{12}\,\frac{\text{W}}{\text{cm}^2}$. The most prominent peak in the TOF spectrum stems from singly ionized $^{20}Ne^+$ ions at roughly 3,600 ns. This ion species occurs so often that it saturates the detector as indicated by the sharp dip to the right of the $^{20}Ne^+$ peak in Fig. 7.1. Apart from ^{20}Ne, neon has two further stable isotopes that occur in nature: ^{22}Ne and ^{21}Ne. The relative abundances are given in Table 4.3. All isotopes show up in the TOF spectrum in Fig. 7.1, however $^{21}Ne^+$ is hard to recognize among the singly charged Ne^+ ions as it partially overlaps with the saturated TOF region. With a single photon of 58.2 eV no charge states higher than Ne^+ are reached as the double ionization threshold is about 61 eV [27]. Therefore, the production of doubly charged Ne^{2+} ions, indicated around 2,600 ns, requires the absorption of another photon. The cross section of Ne^+ is comparable to that of the neutral Ne atom [17]. As the energy to overcome the next ionization step $Ne^{2+} \rightarrow Ne^{3+}$ is 60.42 eV, direct two-photon absorption is needed. A small contribution from Ne^{3+} shows up at 2,100 ns. In summary:

$$\text{Ne} \xrightarrow{h\nu} \text{Ne}^+ \xrightarrow{h\nu} \text{Ne}^{2+} \xrightarrow{2h\nu} \text{Ne}^{3+} \tag{7.1}$$

It should be noted that the intensity for this experiment was kept relatively low in order to suppress background events from multi-photon absorption within one pulse for the ICD measurement, as will be shown later. Thus, the beam was attenuated with a suitable filter combination until only a minimal Ne^{3+} signal remained.

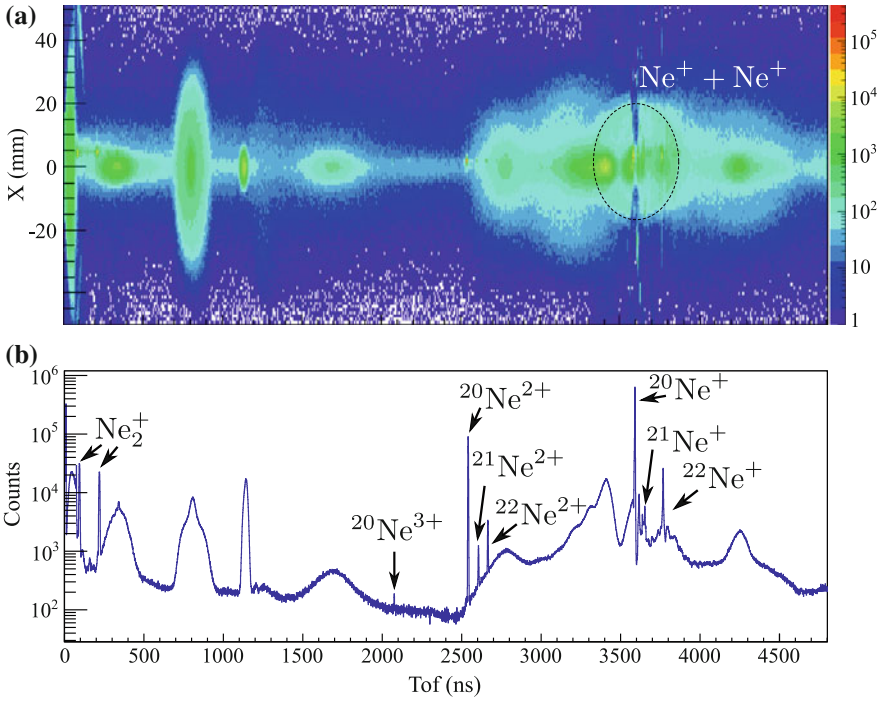

Fig. 7.1 TOF spectrum for a single pulse XUV measurement at a photon energy of 58.2 eV with a neon target containing monomers and dimers. **a** The TOF is plotted versus the x-position on the detector. **b** Projection of (**a**) onto the TOF axis, with the characteristic ion peaks indicated

7.1.2 Photoionization of Ne_2 by a Single Photon

The photoionization cross sections and energies for the removal of a $2p$- or a $2s$-like[1] electron in Ne_2 are very similar to those in an isolated Ne atom because of the weak binding of the dimer. However, the TOF spectrum in Fig. 7.1 is clearly dominated by ionized monomers due to the much smaller amount of dimers (below 2 % of the monomers) in the jet. A small contribution from singly charged dimers Ne_2^+ arises in the region from 100 to 300 ns. Although Ne_2^+ should exhibit a larger TOF than all monomers due to the larger m/Q ratio, it is found at smaller times. This is explained by taking the operation mode of FLASH into account: the next minibunch arrives before the Ne_2^+ fragments have reached the detector (cf. Sect. 5.2). Thus the TOF of these "wrap-around" ions is calculated by adding one minibunch distance of ≈5,000 ns to their observed TOF amounting to values between 5,100 and 5,300 ns. A closer look in the TOF region of the Ne_2^+ ions, as shown in Fig. 4.9, reveals five different peaks corresponding to singly charged dimers that are attributed to the possible

[1] Although the notation $2p$ or $2s$ is only valid for atoms, they are applied here as Ne_2 is only weakly bound and thus the constituents are considered as almost free.

isotope combinations (cf. Table 4.4). The ring-like feature in Fig. 7.1, indicated by a dashed circle, shows fragments emerging from dimers that Coulomb-explode into $Ne^+ - Ne^+$ ions.

7.1.2.1 Relevant Potential Energy Curves

Now we will discuss the relevant states in Ne_2 accessible by irradiation with a single 58.2 eV photon. We start with the initial state of the dimer, the $1^1\Sigma_g^+$ ground state. The minimum of the shallow electronic ground state is located at roughly 3.1 Å and features only two bound vibrational levels [42]: The lowest one has a binding energy of 3 meV and the first excited level is bound with 1.7 meV. Due to the low target temperature (cf. Sect. 4.1.1) we assume that the dimers were prepared in their vibrational ground state. The maximum of the lowest vibrational eigenfunction of the ground state is roughly centered around the aforementioned potential minimum at 3.1 Å. The squared vibrational ground state wave function is shown in Fig. 7.4: Due to the small binding energy of the dimer the width of the distribution is broader than for tightly bound molecules.

The accessible potential energy curves via photoionization by single-photon absorption are shown in Fig. 7.2. Upon removal of a $2p$-like electron the created Ne^+ ion and the neutral Ne atom form four molecular states, with two of them being twofold degenerate (cf. central panel in Fig. 7.2). While the $1^2\Sigma_g^+$ and $1^2\Pi_u$ states lead to the dissociation of the dimer into $Ne{-}Ne^+$, the $1^2\Pi_g$ and $1^2\Sigma_u^+$ states are bound. As the potential minima of the bound states are shifted towards internuclear distances $R < R_{eq}$, the launched nuclear wave packet will propagate towards smaller R.

The removal of a $2s$-like electron from one of the Ne atoms leads to the population of the $2^2\Sigma_u^+$ or $2^2\Sigma_g^+$ state. The potential of the $2^2\Sigma_u^+$ state has its minimum at 2.15 Å and supports eleven vibrational levels with a spacing of roughly 20 meV [34]. The $2^2\Sigma_g^+$ state is virtually flat and exhibits only a shallow potential well at 3.05 Å featuring one vibrational state [34]. Consequently, a wave packet that is created in the $2^2\Sigma_g^+$ state by a Franck–Condon transition from the $1^1\Sigma_g^+$ ground state will remain localized around the ground state equilibrium distance as this distance approximately coincides with the position of the only bound state. In contrast, a wave packet in the $2^2\Sigma_u^+$ state will propagate towards smaller internuclear distances. Because the potential energy curves are almost flat, the nuclear wave packet dynamics takes place relatively slow compared to tightly bound molecules. As the Franck–Condon region for Ne_2 is centered around R_{eq}, mainly high-lying vibrational states of the $2^2\Sigma_u^+$ potential are populated, because those are spatially extended farthest to larger internuclear distances [33].

If $2p$ electrons are removed from each atom in the dimer—resulting in dissociating $Ne^+{-}Ne^+$ ions—18 different molecular states can be formed. The population of these states is strongly suppressed since it requires the removal of a $2p$ electron from each site with a single photon. Thus for high photon intensities two-photon

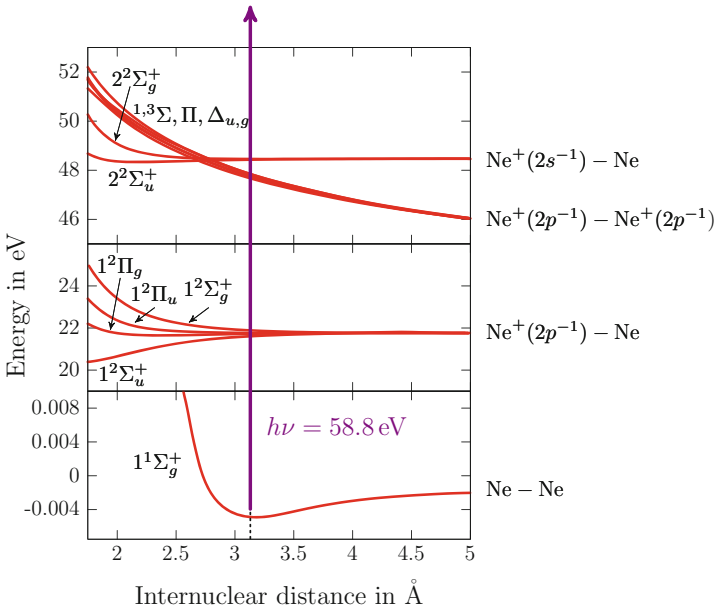

Fig. 7.2 Accessible potential energy curves after photoionization of Ne_2 with one 58.2 eV photon and the corresponding dissociation limits. The *purple arrow* indicates the absorption of an XUV photon from the ground state at equilibrium internuclear distance $R_{eq} = 3.1$ Å. The shown potential energy curves are extracted from [6]

absorption is more probable and will cause some Ne^+–Ne^+ ion pairs. However, the dominant population mechanism is via ICD, as indicated in the KER spectrum of coincident $Ne^+ - Ne^+$ ion pairs, shown in Fig. 7.3. The strongest peak emerges from dimers undergoing ICD after the removal of a $2s$ electron, which is discussed in Sect. 7.1.3. Note that the other peak at larger KERs arises from $2p$ shake-up states, which will be covered in Sect. 7.1.4.

Before we continue with the discussion of these two processes, we have to exclude that the double-hump structure in Fig. 7.3 is an artifact stemming from the structure of the ground state wave function. Fig. 7.4 shows the comparison of KER distributions that would arise from the population of the vibrational ground state or the first excited vibrational level. In this comparison instantaneous access of the $1/R$ curve is assumed, which is usually not true as some intermediate state is populated. Thus the measured KER spectrum carries information about the nuclear dynamics in intermediate and ground states. Here we consider only the influence of the ground state distribution: Population of the first excited vibrational level would lead—even if nuclear motion in an intermediate state was included—to a low-energetic contribution in the KER spectrum. As this is completely absent in the data shown in Fig. 7.3, we conclude that the dimers were created in their vibrational ground state. Note, that this observation is in agreement with the estimate of the jet temperature given in Sect. 4.3.1.

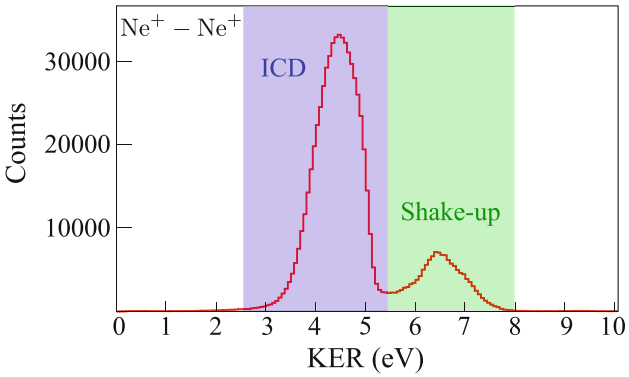

Fig. 7.3 KER of coincident $Ne^+ - Ne^+$ fragments. The two peaks are attributed to ion pairs created via ICD (*purple shaded area*) and those at high energies via shake-up states (*green shaded area*)

7.1.3 Interatomic Coulombic Decay

In order to initiate ICD in Ne_2, a $2s$ vacancy in either of the two Ne atoms has to be created. Here, this is achieved through photoionization by a single photon. Thereby a nuclear wave packet in the molecular $^2\Sigma_u^+$ or $^2\Sigma_g^+$ state is launched. The probability to populate the gerade or the ungerade state is assumed to be equal. This assumption is reasonable since preferences for certain symmetries of states are typically found in experiments with photon energies close to resonances [14], which is not the case at 58.2 eV [12]. If the bound $^2\Sigma_u^+$ state is populated the wave packet travels towards smaller internuclear distances, while it remains around R_{eq} for the $^2\Sigma_g^+$ state. The wave packet propagation continues until ICD occurs, leading to the transition into one of the various molecular states that asymptotically result in $Ne^+(2p^{-1}) + Ne^+(2p^{-1})$ fragments (cf. Fig. 7.2). Thus, the occurrence of coincident $Ne^+ - Ne^+$ ion pairs is a clear fingerprint of ICD.

The unambiguous way to prove that ICD has happened is by detecting the two Ne^+ ions emerging from the Coulomb explosion and the associated electrons. In 2004 Jahnke et al. were able to detect both ions and one of the electrons in coincidence [10]. Figure 7.5 shows their recorded KER distribution of coincident $Ne^+ - Ne^+$ ions as a function of the electron energy. As the experiment was performed with 58.8 eV photons the $2s$ photoelectron is expected to have an energy of roughly 10 eV, which corresponds to the high energetic island in Fig. 7.5. The available kinetic energy for the two Ne^+ ions and the ICD electron consists of the energy difference between the $2s^{-1}$ hole state and that of two asymptotically free $Ne^+(2p^{-1})$ ions. With a $2s$ ionization potential of 48.48 eV for Ne_2 [21] the excess energy, shared by the ions and the ICD electron, is calculated to be:

$$\mathrm{KER} + E_{\mathrm{ICD}e^-} = 48.48\,\mathrm{eV} - 2 \cdot 21.56\,\mathrm{eV} = 5.36\,\mathrm{eV}. \tag{7.2}$$

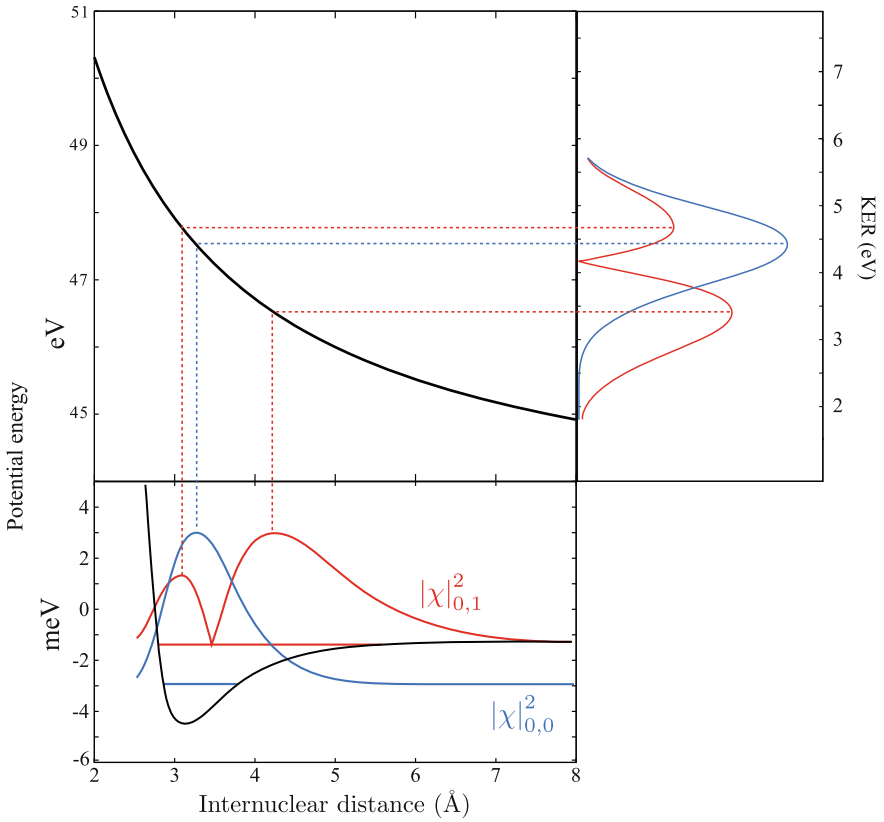

Fig. 7.4 Mapping of the squared nuclear wave function via projection onto the $1/R$ potential energy curve. The squared nuclear wave functions $|\chi|^2_{0,0}$ of the lowest (*in blue*) and $|\chi|^2_{0,1}$ of the first excited (*in red*) vibrational level are mapped onto the $Ne^+ - Ne^+$ Coulomb curve and translated into the corresponding KER distribution. Here, instantaneous population of the Coulomb curve is assumed. However, nuclear motion in the intermediate state will affect the shape of the wave packet. Thus comparing the shape of the measured KER distribution and that expected from the ground state wave function reveals important information on the nuclear dynamics in the intermediate state. Wave functions are taken from [35]

This value is in excellent agreement with the measured energies of the ICD electron and the KER lying on a diagonal line in Fig. 7.5b. The maximum KER, i.e., where no energy is transferred to the ICD electron, lies almost exactly at the predicted energy given in Eq. (7.2). From this the authors have concluded that the ICD electrons have an energy distribution between 0 and 2 eV with their peak intensity lying around 0.2 eV and the KER distribution ranges from 3.2 to 5.3 eV, peaking at 4.6 eV [10].

As we did not detect electrons in our experiment we have to identify ICD from the ion spectra alone. Our data of coincident $Ne^+ - Ne^+$ ion pairs in Fig. 7.3 feature a very similar KER distribution as those in the three particle coincidence study of [10]

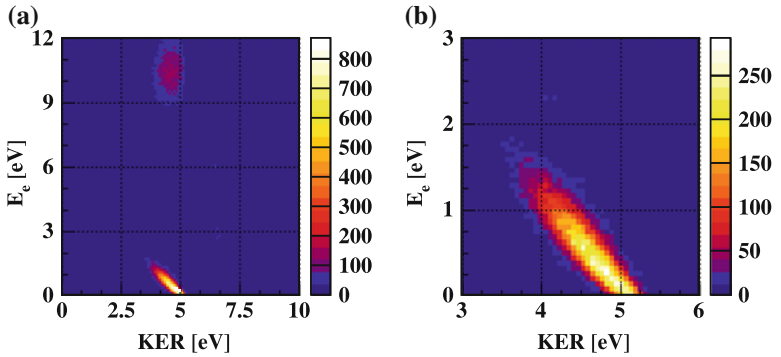

Fig. 7.5 **a** The KER of coincident $Ne^+ - Ne^+$ ions is plotted versus the energy of electrons detected in coincidence with the ions. **b** Zoom into the low energy part of the electrons where the ICD electrons are situated. Figures are taken from [15]

in the energy range around 4.5 eV. Thus we expect that the low-energetic peak in Fig. 7.3 emerges from dimers that have undergone ICD. This assumption is reinforced by comparing the released energy with that expected from instantaneous Coulomb explosion according to the spatial ground state distribution as shown in Fig. 7.4. The distribution has its maximum located at roughly 4.6 eV, which coincides well with the experimental observation. The estimate is made under the assumption that the decay into charged fragments occurs directly after the $2s$ ionization on purely Coulombic potential energy curves and neglects all nuclear wave packet dynamics. It should be noted again that the assumption of purely Coulombic potential energy curves is best at large distances and that the potential curves deviate for small R [34]. From the good agreement with the instantaneous decay, we further conclude that ICD takes place very fast as the wave packet is only given little time to evolve, resulting in a well confined KER distribution. ICD occurs roughly a factor of 10,000 faster than radiative decay, which is the only competing relaxation process in $Ne_2^+(2s^{-1})$. Thus the amount of radiatively decaying inner-valence ionized dimers is negligible.

In principle, the ICD lifetime may be deduced by comparing the shape of the KER spectrum from $Ne^+ - Ne^+$ ion pairs with its theoretical counterpart. In order to do so, very accurate *ab initio* calculations of the potential energy surfaces and transition rates have to be carried out, including nuclear dynamics. This kind of comparison has been performed for an ICD experiment on NeAr with the outcome that the decay width was most likely overestimated in the theoretical calculations [25]. We note that this method requires a theory that describes all underlying phenomena correctly. As we also seek to test the available theories, we apply a different method that allows the lifetime determination from experimental data only (cf. Sect. 7.2.5).

7.1.4 Shake-Up Processes

The second contribution in Fig. 7.3, appearing at larger KERs from 5.8 up to 7.5 eV, will be discussed in the following. In the framework of our Coulomb-explosion model (cf. Sect. 6.1.5), the peak energy of 6.5 eV translates into a mean fragmentation distance of 2.2 Å, according to Eq. (6.7). For ICD we found the most likely break-up distance close to $R_{eq} = 3.1$ Å and concluded that it takes place very fast. In contrast, the present process requires nuclear motion in form of a contraction of the dimer prior to the decay process and is thus expected to occur slower than ICD. The high KER contribution in the spectrum of coincident $Ne^+ - Ne^+$ ions was already observed in an earlier experiment [11] and explained as a dipole-forbidden relaxation of $2p$ shake-up states.

Shake-up states are produced by photoemission of one electron and simultaneous excitation of another electron. Here, shake-up states resulting from $2p$ photoionization and simultaneous excitation of another $2p$ electron are relevant. It is well known that Ne^+ features a rich spectrum of $(2s^2 2p^4 nl)$ satellite states above the $2s$ ionization potential [39]. The present photon energy of 58.2 eV is sufficient to create excited Ne^+ ions, but is below the double ionization threshold. Thus relaxation via autoionization is not possible [37], and the only remaining relaxation pathway in the isolated atom is radiative decay. In a dimer an excited $Ne^+(2s^2 2p^4 nl) - Ne$ state located above the $2s$ ionization potential has the additional possibility to relax via ICD, which is again the dominant process, as illustrated in Fig. 7.6. But if this decay process is again fast, the question arises how the high energetic feature in Fig. 7.3 is produced. As shake-up is not restricted to dipole-transitions it populates a variety of excited states. Relaxation via radiative decay and ICD occurs only if the transition is dipole allowed (at least in the dipole approximation). Thus all excited dipole-forbidden states cannot decay except via an electron transfer process from the neutral Ne neighbor, as indicated in Fig. 7.6. One $2p$ vacancy in $Ne^+(2s^2 2p^4 nl) - Ne$ is filled by a $2p$ electron from the neutral Ne atom and the released energy is transferred to the excited electron, which is then emitted. As electron transfer requires sufficient orbital overlap of the participating atoms in order to take place, the distance between the excited Ne^+ ion and the neutral Ne atom must be reduced by nuclear motion prior to the decay. This translates into higher KERs, as observed in Fig. 7.3.

At first it might seem surprising that a second order process, such as shake-up, which requires the interaction of two electrons and a photon, competes with the first order $2s$ photoionization. Although shake-up is less likely to happen, it shows a clear contribution in Fig. 7.3. This puzzle is solved by considering the differences in photoionization cross sections: It is roughly a factor of 15 more likely to remove a $2p$ electron compared to $2s$ photoionization. Consequently, due to the small cross section of the first order process, the second order process becomes competitive.

Note that the electron transfer process is only relevant for the $2p$ shake-up states and negligible for the inner-valence ionized dimer $Ne_2^+(2s^{-1})$. For the latter configuration the $2s$ hole is filled with any of the $2p$ electrons. It is thus always dipole allowed and ICD will be the dominant process.

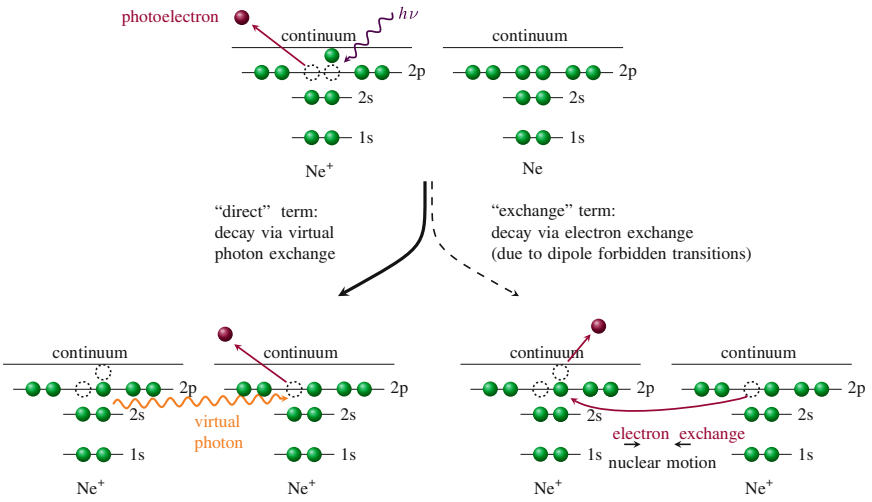

Fig. 7.6 Alternative relaxation pathways of the $2p$ ionized and simultaneously excited Ne_2^+ molecular ion resulting in coincident Ne^+-Ne^+ fragments. For a dipole-allowed transition the excited ion will relax by ICD: The excess energy is transferred to the neutral side of the dimer via a virtual photon and consequently removes a $2p$ electron from there (*lower left panel*). Alternatively, for a dipole-forbidden transition the $2p$ vacancy in Ne^+ is filled by a $2p$ electron from the neutral Ne atom and the released energy is transferred to the excited electron, which is then emitted (*lower right panel*). The latter process occurs much slower than ICD as the electron transfer requires orbital overlap, that must be gained by nuclear motion

7.2 Pump-Probe Measurements on Ne_2

In order to determine the lifetime of the $Ne_2^+(2s^{-1})$ state, which decays via ICD, we apply an XUV-pump–XUV-probe scheme. The delay-dependent KER spectra are introduced by means of the coincidence channel Ne^+-Ne^+ in Sect. 7.2.1. The pump-probe scheme and the relevant potential energy curves for the lifetime determination are explained in Sect 7.2.2. As the lifetime is contained in the ion yield of coincident Ne^+-Ne^{2+} ions, this channel will be discussed in Sect. 7.2.3 and compared to classical simulations in Sect. 7.2.4. The lifetime determination is described in Sect. 7.2.5 and competing processes that may alter the result are presented in Sects. 7.2.6 and 7.2.7. The section closes with a discussion of the result and comparison with calculated values in Sect. 7.2.8. Part of this Section has been published in [36].

7.2.1 Delay-Dependence of Coincident Ne^+-Ne^+ Ions

In Fig. 7.7 the KER of coincident Ne^+-Ne^+ fragments is plotted as a function of the pump-probe time delay. The time independent single-pulse contributions resulting

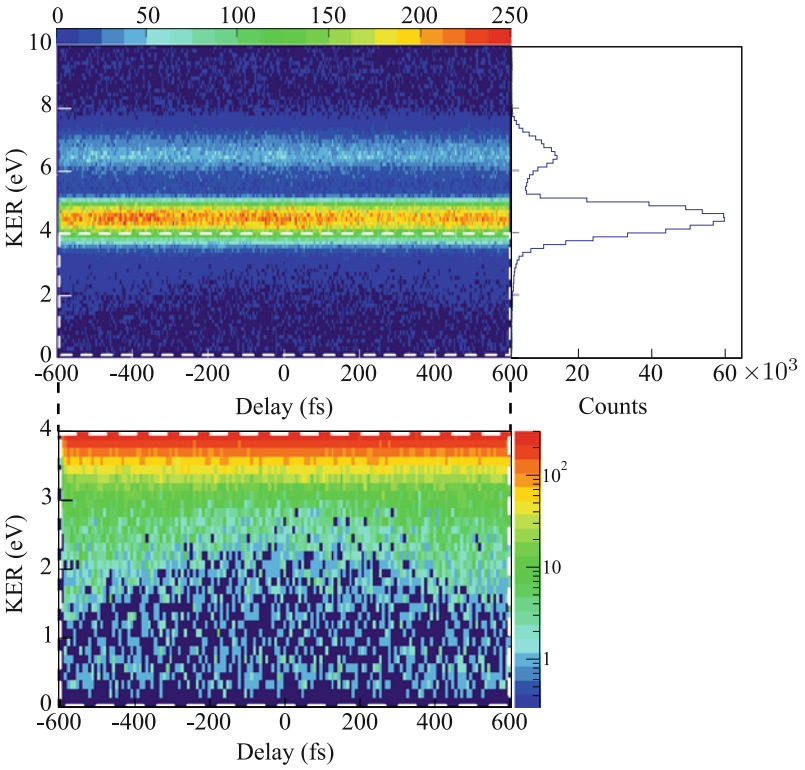

Fig. 7.7 Delay-dependent KER spectrum of the coincidence channel $Ne^+ - Ne^+$. The *upper panel* shows the whole spectrum and a projection onto the KER axis for large delays. In the *lower panel* a zoom into the low-energetic region is shown to make the time-dependent trace visible

in coincident $Ne^+ - Ne^+$ fragments were already discussed in the previous section. Fig. 7.7 shows an additional time-dependent feature rising from KERs as low as 1.5 eV at 600 fs up to higher KERs for smaller delays. This behavior is characteristic for delayed ionization: The molecule is first dissociated by the pump pulse and after an adjustable time delay further ionized by the probe pulse. The time-dependent trace in Fig. 7.7 stems from a dissociating singly ionized dimer Ne_2^+ that is again ionized within the probe pulse resulting in coincident $Ne^+ - Ne^+$ ions. As the removal of $2p$ electrons features the largest cross section the most likely production pathway is

$$\begin{aligned} Ne_2 \xrightarrow{\text{pump}} Ne_2^+ (2p^{-1}) \\ \downarrow \\ Ne + Ne^+(2p^{-1}) \xrightarrow{\text{probe}} Ne^+(2p^{-1}) + Ne^+(2p^{-1}). \end{aligned} \tag{7.3}$$

The method of how to identify precursor charge states in our pump-probe spectra from the asymptotic KER was already introduced in Sect. 6.2.1. From the low asymptotic KER of roughly 1.5 eV, which is smaller than all KERs emerging from two charged fragments, a break-up into one neutral and one charged fragment is inferred. In comparison, the lowest KER expected from a Coulomb explosion of two charged fragments at R_{eq} is that of two singly charged Ne^+ ions which amounts to 4.6 eV. Lower KERs must stem from break-up with one neutral fragment. Unfortunately, particularly at small delays, the time-dependent component overlaps energetically with the dominant single pulse component after ICD. Therefore the shape of the rising curve towards smaller delays, which maps the potential curves of the intermediate $(2p^{-1})$ state, cannot be analyzed.

7.2.2 Pump-Probe Scheme for the ICD Lifetime Determination

In order to explain the XUV pump-probe scheme for the lifetime determination, we introduce the relevant potential energy curves in Ne_2 that are accessible via two-photon absorption from the ground state, as shown in Fig. 7.8. The energy region between 52 and 90 eV supports further potential energy curves, that are not shown.

The role of the pump pulse is to initiate ICD by the creation of a $2s$ inner-valence vacancy at one of the neon atoms. Once the excited $Ne_2^+(2s^{-1})$ state is created the essential question arises how long it takes until the excited dimer decays into coincident Ne^+-Ne^+ ions. In order to answer this question the dimer's charge state has to be tested continuously. Experimentally, this is realized by probing the charge state with a delayed second XUV pulse that further ionizes the dimer into a distinct state, which reveals whether the dimer had already decayed by the time the probe pulse arrived or not. Thus, by scanning the time delay and simultaneously detecting the fragments created after the probe pulse, the lifetime of the excited state, i.e., the ICD lifetime, is determined. Figure 7.8 shows a simplified version of the pump-probe scheme: If ICD has occurred by the time the probe pulse arrives one of the created Ne^+-Ne^+ fragments is further ionized, resulting in a coincident Ne^+-Ne^{2+} ion pair. If instead ICD has not taken place when the probe pulse impinges, a further electron from the dimer ion $Ne_2^+(2s^{-1})$ is removed, resulting in Ne_2^{2+}. This molecular ion will mostly dissociate into $Ne-Ne^{2+}$ or $Ne^{1+}-Ne^{1+}$, as will be discussed in Sect. 7.2.6 in more detail. Thus a potential curve with the dissociation limit Ne^+-Ne^{2+} is only reached for dimers that have already undergone ICD. Therefore we expect a time-dependent Ne^+-Ne^{2+} ion yield that increases with a slope that returns the ICD lifetime. However these considerations do only take into account the situation in which a single photon is absorbed within the pump and a single photon within the probe pulse.

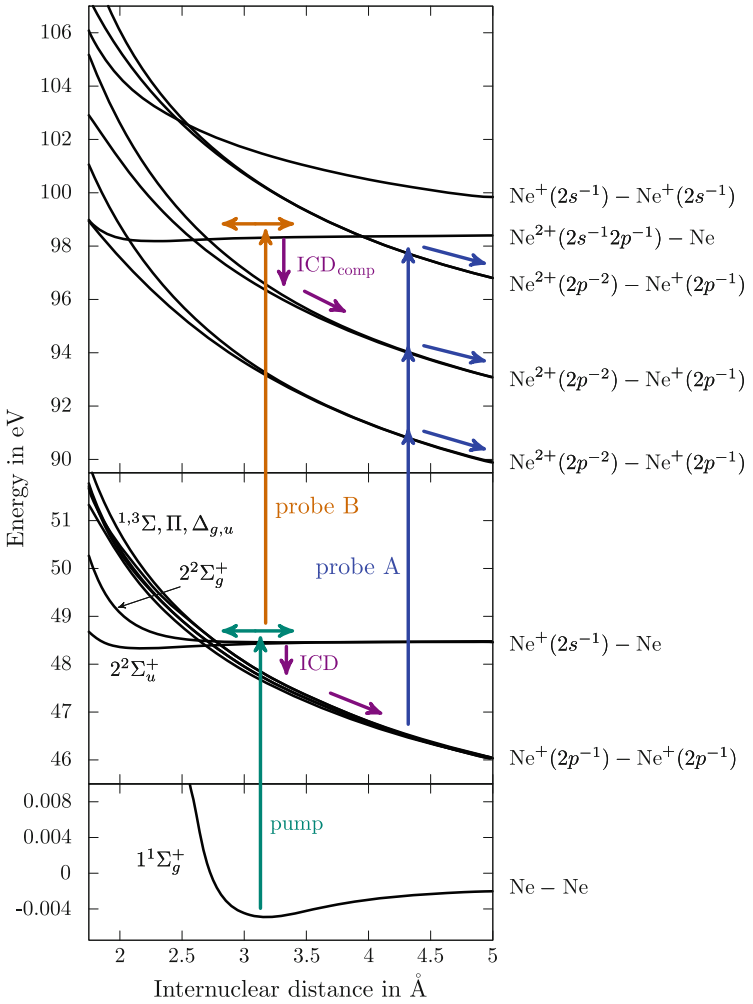

Fig. 7.8 Relevant potential energy curves for two-photon absorption in Ne_2 and illustration of the pump-probe scheme. A first photon initiates ICD by the creation of a $2s$ vacancy in one of the neon atoms. If ICD has occurred before the probe pulse arrives (probe A), one of the $Ne^+ – Ne^{2+}$ curves is accessed. For an early probe pulse (probe B), the unstable $Ne^{2+}(2s^{-1}2p^{-1}) – Ne$ state may be populated, which decays via a competing ICD_{comp} into $Ne^+ – Ne^{2+}$, as will be discussed in Sect. 7.2.6. Potential energy curves extracted from [38]

7.2.3 *Fragmentation Channel $Ne^+ – Ne^{2+}$ as a Function of the Pump-Probe Time Delay*

Since the lifetime of the $2s$ vacancy in Ne_2^+ is determined by analyzing the yield of coincident $Ne^+ – Ne^{2+}$ ion pairs, all possible pathways leading to this

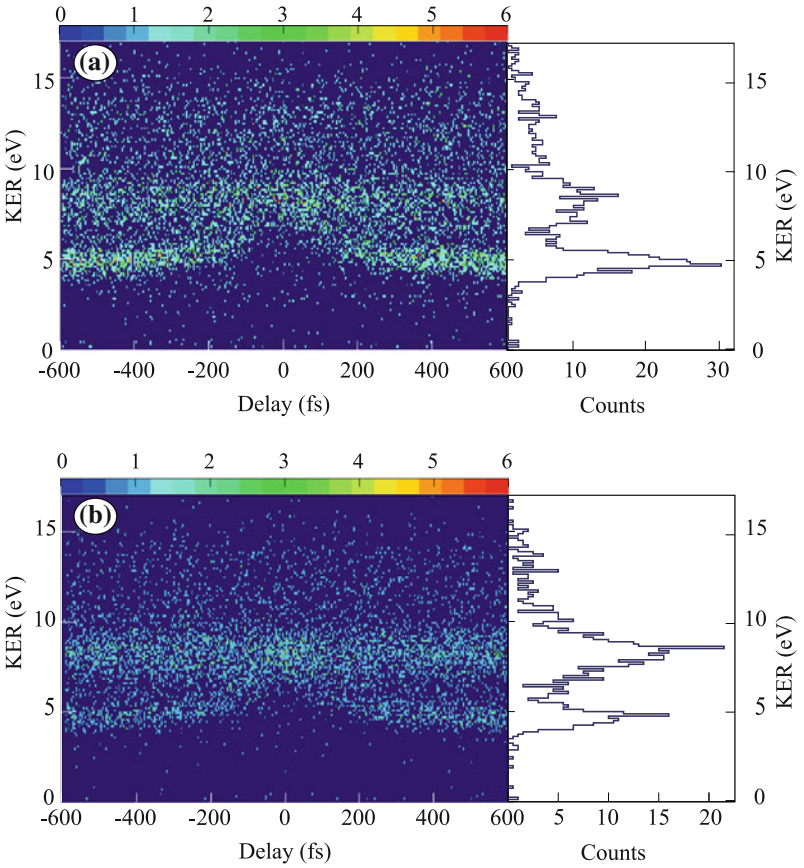

Fig. 7.9 Delay-dependent KER spectra of coincident $Ne^+ - Ne^{2+}$ fragments for lower FEL intensity in **a** and a higher one in (**b**). In addition the projections onto the KER axis for large delays are shown. Note that the multi-photon contribution around 8 eV is pronounced for higher photon intensity in (**b**), while the pump-probe contribution around 5 eV is dominating for the lower intensity in (**a**)

fragmentation channel must be analyzed carefully. The delay-dependent KER of coincident $Ne^+ - Ne^{2+}$ fragments for a data set recorded at low intensity is shown in Fig. 7.9a and another one recorded at high intensity in Fig. 7.9b. The spectra show two dominant features: one with a constant KER around 8.6 eV and a time dependent one converging to 5 eV for large delays. The time-independent band stems from $Ne^+ - Ne^{2+}$ ions that were created by multi-photon absorption within one pulse, which is confirmed by evaluating the KER as follows. For two point-like charged particles, one singly and the other doubly charged, the expected KER within our Coulomb-explosion model amounts to 9.28 eV. Since this value is close to the observed one, a relatively fast ionization process can be assumed. In order to create the triply ionized dimer Ne_2^{3+} directly from the ground state three photons must be

absorbed. Thus an intensity dependence for the multi-photon process is expected. This is clearly visible in the KER distributions when comparing the high and the low intensity spectra in Fig. 7.9: At high intensity the peak at 8.6 eV, which is attributed to multi-photon absorption, is much more pronounced. As our pump-probe scheme relies on single-photon absorption within the pump and the probe, contributions from multi-photon process must be suppressed. This is achieved by keeping a low FEL intensity of roughly $10^{12}\ \frac{\mathrm{W}}{\mathrm{cm}^2}$, which is the setting present in Fig. 7.9a.

The lifetime information is contained in the time dependent trace in Fig. 7.9. As it converges to an energy of roughly 5 eV we conclude that the precursor $Ne^+ - Ne^+$ was populated by the pump pulse. The observed KER is slightly higher than the expected one of 4.64 eV from a Coulomb explosion at R_{eq}. This indicates that the KER has not converged to its asymptotic value after 600 fs. Around time delay zero the ion yield is increased due to the quadrupled intensity in the overlap region of the pulses. At high intensities the multi-photon process becomes more likely, resulting in an increased number of $Ne^+ - Ne^{2+}$ ions. The enhanced ion yield around time delay zero can not be completely suppressed, even for small intensities, and thus causes background events for the lifetime determination. In order to understand how the ICD lifetime is contained in the time-dependent trace of Fig. 7.9 we perform a classical simulation.

7.2.4 Classical Simulation

The classical simulation used to model pump-probe spectra has been introduced already in Sect. 2.6 and applied for I_2 in Sect. 6.2 with various modifications. For Ne_2 the shape of the relevant potential curves is known from calculations and is thus used as input for the simulation. The simulation starts by placing the point-like classical particle, a "ball", either on the $2^2\Sigma_g^+$ or $2^2\Sigma_u^+$ curve at $R_{\mathrm{eq}} = 3.1$ Å, which models single-photon absorption from the dimer ground state. Both states are populated with equal probability. While the ball rolls towards smaller R when placed on the attractive $2^2\Sigma_u^+$ curve, it will more or less stay at rest on the virtually flat $2^2\Sigma_g^+$ potential curve. The ICD of the intermediate state is implemented by assuming an exponential decay probability $e^{-t/\tau}$ with a lifetime τ, leading to a predetermined lifetime for each ball. After the assigned lifetime the ball decays onto the repulsive $1/R$ curve where it pursues its motion until the probe pulse arrives after an adjustable time delay t_d, thereby promoting the ball onto the steeper $2/R$ potential curve.

In Fig. 7.10 the comparison of the classical simulations for $2^2\Sigma_g^+$ and $2^2\Sigma_u^+$ are shown with an ICD lifetime of $\tau = 100$ fs. If the ball is placed on the $2^2\Sigma_g^+$ potential energy curve it will remain close to R_{eq}, thus the shape of the spectrum is determined by the interplay of the exponential decay and the arrival time of the probe pulse. The time when ICD occurs is simulated by an exponential probability distribution, thus it may happen at any time after the creation of the $2s$ vacancy. If ICD takes place immediately after the pump pulse the repulsive $1/R$ curve is populated early giving the

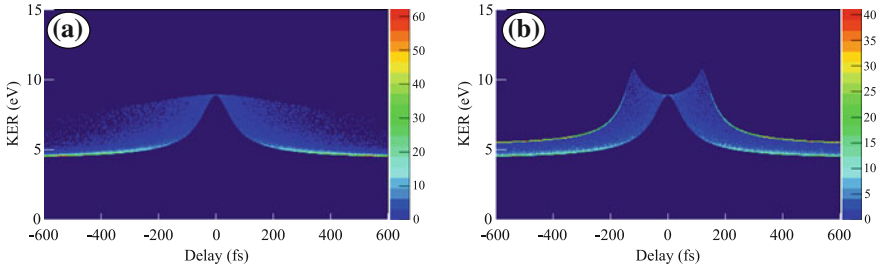

Fig. 7.10 Classical simulation of the delay-dependent KER for $Ne^+ - Ne^{2+}$ ion pairs produced after ICD. **a** Population of the flat intermediate $2^2\Sigma_g^+$ curve. **b** Population of the attractive intermediate $2^2\Sigma_u^+$ curve

nuclei the largest possible time to dissociate before the probe pulse further ionizes the system into $Ne^+ - Ne^{2+}$ fragments. Thus, events with a fast decay time are located close to the low-energy cut-off of Fig. 7.10 because the steep $Ne^+ - Ne^{2+}$ curve is populated at large internuclear distances where the energy gain is already small. In contrast, for dimers decaying just before the probe pulse arrives, the internuclear distance when the fragments are further ionized is still close to R_{eq} resulting in a much larger energy gain on the steep $Ne^+ - Ne^{2+}$ curve. Thus these events occur at larger KERs even for large delays.

In Fig. 7.10b the corresponding spectrum for the population of the intermediate $2^2\Sigma_u^+$ state is shown. It features an additional wing-like structure as compared to the $2^2\Sigma_g^+$ state which is due to nuclear motion before ICD has occurred. The low energy cut-offs in Fig. 7.10a, b are identical because they have the same origin: For a fast ICD, nuclear motion on the intermediate $2^2\Sigma_u^+$ curve is negligible, resulting in the well known behavior of delayed ionization. Instead, if ICD takes place late, the classical particle will start to roll towards smaller R leading to a smaller R by the time the dimer ion decays. Therefore the steeper potential energy curve $Ne^+ - Ne^{2+}$ is accessed at internuclear distances smaller than R_{eq} resulting in KERs higher than those expected at R_{eq}. However the KER in Fig. 7.10b rises only up to a roughly 11 eV, which translates into $R = 2.6$ Å. ICD is only energetically allowed as long as the $2^2\Sigma_u^+$ curve lies above the $Ne^+ - Ne^+$ curve and the crossing region of the two curves lies around $R = 2.6$ Å. This manifests in a sharp cut-off of the decay width, as shown in Fig. 2.9. Thus, no KERs higher than that corresponding to a Coulomb explosion at the crossing point occurs. In our simulation a small number of Ne_2^+ ions reach this point and the question arises how to deal with them. In Fig. 7.10b we have assumed immediate decay at the crossing point onto the $Ne^+ - Ne^+$ curve, which causes the sharp cut-off at high energies beyond 120 fs. Alternatively, we have also performed simulations where the classical particle crosses the intersection. In this region dimers can only decay radiatively, which is not included in our simulation. Therefore those dimers which have crossed the intersection will eventually return to the region of internuclear distances where ICD is allowed. This difficulty demonstrates the limitations of our model of classical point-like particles moving

on potential energy curves. For quantum mechanical calculations employing nuclear wave packet propagation the wave packet exhibits a certain width. The fraction of the wave packet beyond the crossing decays only via radiative decay. However, even if the wave packet propagates to smaller R the decay rate does not vanish completely as some part of the wave function remains before the crossing. This condition is fulfilled for $Ne_2^+(2s^{-1})$ for all times as the highest vibrational levels are predominantly populated by the pump pulse, which exhibit wave functions that are spread to larger R. Therefore the probability density before the crossing never vanishes completely.

Experimentally, we are not able to distinguish between the $2^2\Sigma_u^+$ and the $2^2\Sigma_g^+$ state. Figure 7.11 shows the superposition of the simulation for equal contribution of each intermediate state. The general behavior of the time-dependent experimental trace (cf. Fig. 7.9) is well reproduced by our simulation supporting the proposed pathway. However the characteristic increases of the KER due to nuclear motion on the $2^2\Sigma_u^+$ is not observed. The absence of this feature has various reasons: Counts from direct multi-photon absorption overlap energetically with the expected KER increase and cannot be separated from the pump-probe contribution with statistical significance. In addition, our simulation was performed at a fixed initial internuclear distance R_{eq}, which is in contrast to the spatial distribution of the ground state wave function, as shown in Fig. 7.4. If we perform the simulation with a distribution of initial internuclear distances according to the ground state wave function the wing-like structure gets washed out, as demonstrated in Fig. 7.11b.

Up to now we have not discussed the effect that the simulated rate of Ne^+-Ne^{2+} ion pairs varies with the pump-probe delay, which is especially apparent in Fig. 7.11. In order to closer investigate this time-dependence we have to evaluate the

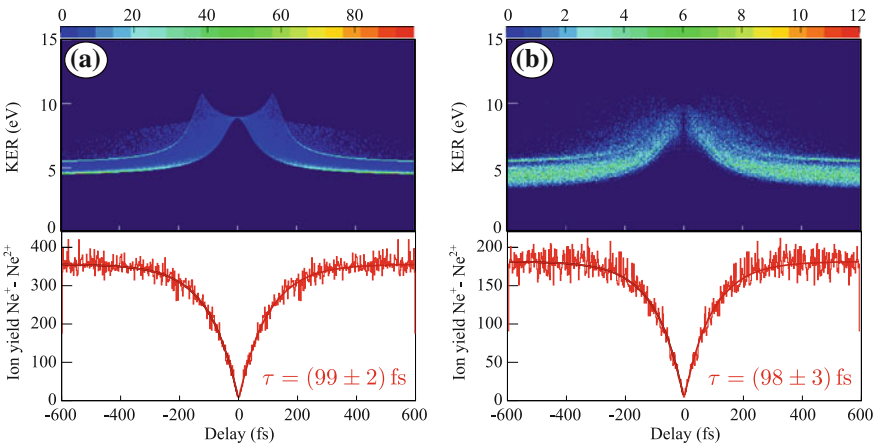

Fig. 7.11 Simulation of the delay-dependent KER spectra of coincident Ne^+-Ne^{2+} ion pairs for both intermediate states for an ICD lifetime of 100 fs. The projection of all KERs onto the delay axis is strongly time dependent and the exponential slope at which the ion yield rises returns the input lifetime. **a** Simulation for an initial fixed internuclear distance of $R_{eq} = 3.1$ Å. **b** Simulation with R distributed according to the squared nuclear ground state wave function, shown in Fig. 7.4

projection of all KERs onto the delay axis, as shown in the lower row of Fig. 7.11. The $Ne^+ - Ne^{2+}$ ion yield vanishes at small delays and saturates at larger delays. This behavior becomes clear when recalling the involved potential energy curves: Coincident $Ne^+ - Ne^{2+}$ ion pairs are only produced when ICD has already occurred by the time the probe pulse impinges. At small delays only few dimers have undergone ICD and consequently only a small number of $Ne^+ - Ne^+$ ion pairs are further ionized to $Ne^+ - Ne^{2+}$. In contrast, at large delays almost all $Ne_2^+(2s^{-1})$ ions have decayed into $Ne^+ - Ne^+$ pairs and thus the number of $Ne^+ - Ne^{2+}$ ions is also large. Performing an exponential fit to the time-dependent slope of the ion yield returns the input lifetime of the simulation. Thus, by analyzing the $Ne^+ - Ne^{2+}$ ion yield we have found a tool to extract the ICD lifetime.

7.2.5 Lifetime Determination

In order to determine the ICD lifetime from our experimental data we proceed the same way as introduced for the simulation: All events in the time-dependent KER spectrum of coincident $Ne^+ - Ne^{2+}$ ions are projected onto the delay axis, as shown in Fig. 7.12. The projection exhibits a clear drop in the ion yield towards small delays as predicted by the simulation. The offset in the time-dependent ion yield is mostly caused by direct multi-photon absorption (cf. Fig. 7.9). To avoid fluctuations in the ion yield due to imperfections of the delay stage the projected spectra are normalized to the total time the delay stage spent at each scanning step.

In order to improve statistics the counts for negative delays are added to those of the respective positive delays as the experiment is mirror-symmetric with respect to time delay zero. Figure 7.13 shows the projection onto the delay axis with an exponential fit yielding an ICD lifetime of 150 ± 50 fs with a purely statistical uncertainty. The limit of our temporal resolution is determined by the uncertainty arising from the finite pulse length: For a 60 fs (FWHM) Gaussian pulse the uncertainty due to the temporal overlap of pump and probe pulse accounts to ± 36 fs, as was introduced in Sect. 6.2.4. Thus, the accuracy of the lifetime determination is not yet limited by the pulse duration. Actually, we expect even a better temporal resolution due to the

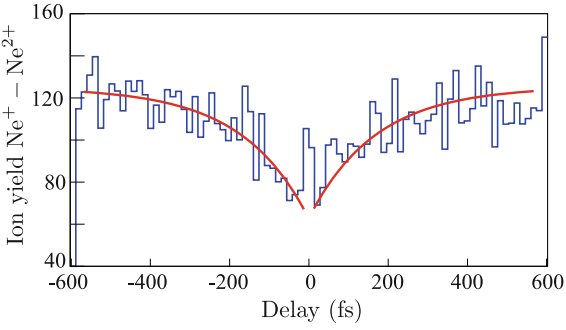

Fig. 7.12 Projection of all KERs in the time-dependent $Ne^+ - Ne^{2+}$ spectrum onto the delay axis. The *red lines* indicate the increasing ion yield from small towards larger delays

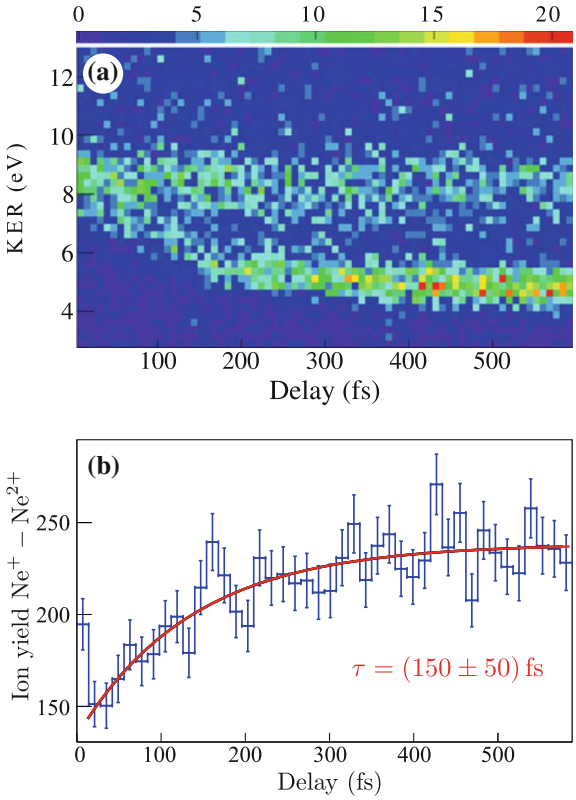

Fig. 7.13 **a** Delay-dependent KER spectrum of coincident $Ne^+ - Ne^{2+}$ ions where negative delays from Fig. 7.9a are flipped onto the positive delay range in order to improve statistics. **b** Projection of KERs between 0 and 11 eV onto the delay axis. The exponential fit (in red) returns an ICD lifetime of 150 ± 50 fs

spiky structure of the FEL pulses [20]. The given pulse length of 60 fs is averaged over a larger number of pulses while each individual pulse exhibits spikes with a width of a few femtoseconds, which is the temporal coherence length [28]. The peak structure manifests in our data as a sharp coherence peak at zero time delay as shown in Sect. 3.3. As it is unrelated to ICD, it has to be ignored for the lifetime fit. Still it influences the fit result to larger lifetimes and consequently our result should be understood as an upper limit for the lifetime. On the other hand the peak allows us to determine the zero of the time-delay axis, when the pulses have perfect temporal overlap, to an accuracy of a few femtoseconds. This is crucial for adding the ion yield of negative delays onto the positive ones.

7.2.6 Alternative Pathways to $Ne^+ - Ne^{2+}$ Ion Pairs

With the help of the classical simulation we test the influence of competing pathways also resulting in coincident $Ne^+ - Ne^{2+}$ ion pairs. As the time-independent

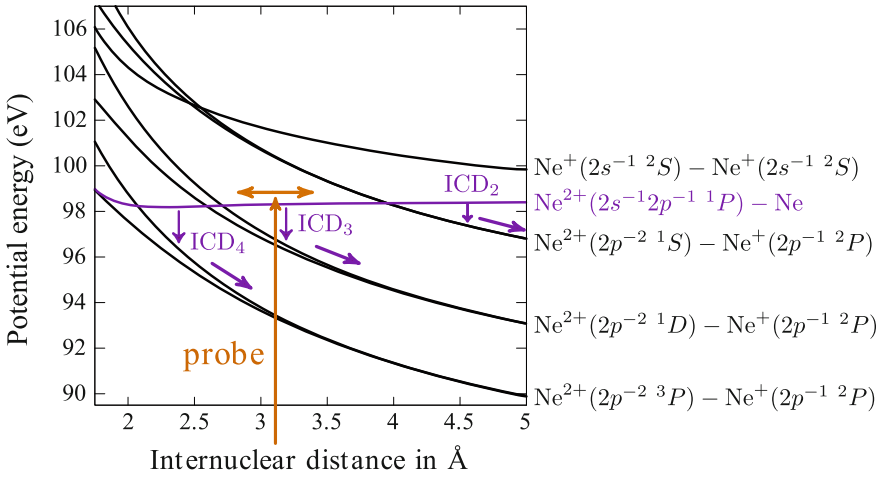

Fig. 7.14 Competing pathways via the population of the $Ne_2^{2+}(2s^{-1}2p^{-1})-Ne$ potential curve (*in purple*). The indicated state can decay into background coincident Ne^+-Ne^{2+} ion pairs via ICD_2, ICD_3 or ICD_4. The *orange arrow* is drawn at R_{eq}. The potential energy curves are taken from [38]

contribution from multi-photon absorption causes only a constant offset in the ion yield spectrum the lifetime determination is not disturbed by this competing pathway. Relevant are only pathways with time-dependent ion yield because those might change the outcome of the lifetime fit. If the inner-valence-ionized dimer $Ne_2^+(2s^{-1})$ absorbs another photon before ICD has occurred it will result in the fragmentation channels Ne^+-Ne^+ or $Ne-Ne^{2+}$. One particular state ($Ne-Ne^{2+}(2s^{-1}2p^{-1})$) also decays via ICD into Ne^+-Ne^{2+} ion pairs and thus causes a time-dependent background. Figure 7.14 shows a zoom into the potential energy diagram into the region from 90 to 106 eV illustrating the decay channels ICD_2, ICD_3 and ICD_4 from the $Ne-Ne^{2+}(2s^{-1}2p^{-1})$ state. These ICD processes were already predicted theoretically [32, 38] and have been confirmed experimentally [19]. However in these studies the population of the decaying state was initiated by the creation of a $1s$ core hole and subsequent Auger decay.

Here, the population of the $Ne-Ne^{2+}(2s^{-1}2p^{-1})$ state is either achieved by sequential photon absorption within one pulse or by a single-photon pump single-photon probe scheme for $Ne_2^+(2s^{-1})$ ions that have not yet undergone ICD (cf. Fig. 7.8). The latter pathway is most prominent for small time delays because shortly after the pump pulse only few dimers have undergone ICD and are consequently probed into the $Ne-Ne^{2+}(2s^{-1}2p^{-1})$ state. For small delays the dimer is given little time for nuclear dynamics in the intermediate $2^2\Sigma_g^+$ and $2^2\Sigma_u^+$ states. Thus the shape of the wave packet accessing the $Ne-Ne^{2+}(2s^{-1}2p^{-1})$ curve should still be close to that of the ground state and peak around R_{eq}. The same argument holds for the population of the curve via two-photon absorption within the pulse length of 60 fs. However, in order to enable decay via ICD_2 internuclear distances beyond the

curve crossing of the initial and final state at 3.8 Å must be populated. Although the wave packet is broad only a very small fraction of the distribution will exceed the crossing allowing the decay

$$\mathrm{Ne{-}Ne^{2+}}(2s^{-1}2p^{-1}\,{}^1P) \xrightarrow{\mathrm{ICD_2}} \mathrm{Ne^{2+}}(2p^{-2}\,{}^1S){-}\mathrm{Ne^{+}}(2p^{-1}\,{}^2P). \tag{7.4}$$

Thus the overall contribution of ICD_2 is negligible.

ICD_3 instead takes place for internuclear distances larger than $\approx$2.6 Å which covers the distance range at which most of the nuclear wave packet is launched. The decay occurs via direct ICD:

$$\mathrm{Ne{-}Ne^{2+}}(2s^{-1}2p^{-1}\,{}^1P) \xrightarrow{\mathrm{ICD_3}} \mathrm{Ne^{2+}}(2p^{-2}\,{}^1D){-}\mathrm{Ne^{+}}(2p^{-1}\,{}^2P). \tag{7.5}$$

The transition time is predicted to be 80 fs [32]. For a fast decay only little nuclear motion takes place resulting in a KER distribution of the $Ne^+{-}Ne^{2+}$ fragments corresponding to distances around R_{eq}. Therefore events from ICD_3 are expected to emerge at similar KERs as those from direct multi-photon absorption and will consequently be indistinguishable from them. The maximal cut-off energy for this decay channel is computed by translating the internuclear distance of the curve crossing (2.6 Å) into the corresponding KER of 11 eV.

The transition ICD_4 in Fig. 7.14 takes place for R as small as 2.13 Å resulting in a maximum KER of 13.5 eV. However it should be noted that our estimate with purely Coulombic potential energy curves is not adequate anymore for these small distances. It is important to note that ICD_4 differs from the ICD transition discussed so far. It is not mediated by exchange of a virtual photon alone. Instead an additional spin-flip would be needed, as a singlet P-state is transformed into a triplet P-state. However, a transition including a spin-flip is dipole-forbidden and thus strongly suppressed [38]. Therefore, different types of ICD occur: exchange ICD or electron transfer mediated decay (ETMD). Both require the exchange of electrons, contrasting the "normal" ICD where energy is transferred via a virtual photon. The decay reads

$$\mathrm{Ne{-}Ne^{2+}}(2s^{-1}2p^{-1}\,{}^1P) \xrightarrow{\text{exch. ICD/ETMD}} \mathrm{Ne^{2+}}(2p^{-2}\,{}^3P){-}\mathrm{Ne^{+}}(2p^{-1}\,{}^2P). \tag{7.6}$$

In exchange ICD the inner-valence vacancy located at the Ne^{2+} ion is filled by a $2p$ electron from the neutral Ne neighbor, thereby ionizing another $2p$ electron from the formerly excited ion resulting in coincident $Ne^+{-}Ne^{2+}$ ions. ETMD is different in the sense, that the excess energy after population of the inner-valence hole is transferred to a $2p$ electron from the formerly neutral neighbor atom, which is then ionized. Both processes are illustrated in Fig. 7.15. As mechanisms involving the migration of electrons require sufficient orbital overlap, exchange ICD and ETMD can only occur at smaller R compared to ICD and thus demand nuclear motion prior to the decay. At smaller distances the decay rates can be strongly enhanced due to the orbital overlap [2]. However, nuclear motion takes time and causes the electron transfer processes to be much slower than ICD via virtual photon exchange [44].

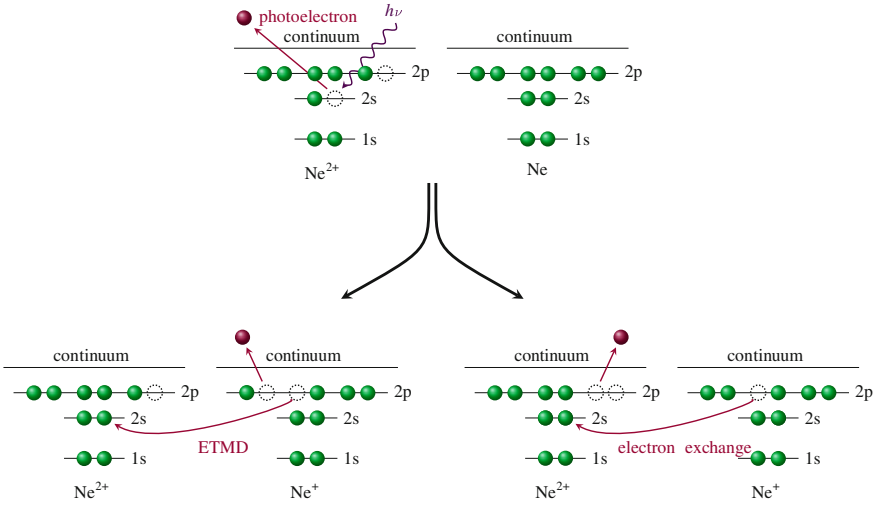

Fig. 7.15 Comparison of exchange ICD (*right*) and ETMD (*left*) for ICD_4. In exchange ICD the relaxation energy is transferred to an electron of the initially inner-valence ionized side, while in ETMD the energy is transferred to the initially neutral side

Figure 7.14 shows an overview of the different processes leading to coincident $Ne^+ - Ne^{2+}$ ions and the corresponding relevant energy ranges are indicated in Fig. 7.16. The high energetic contribution in the range from 11 to 16 eV stems most likely from the previously discussed exchange ICD and ETMD processes (indicated as ICD_4 in Fig. 7.14). The peak around 5 eV stems from the discussed asymptotic limit of our desired pump-probe channel. For small time delays it creates a signal in the intermediate KER range of 6–11 eV where it overlaps with the contributions from sequential multi-photon absorption and from ICD_3.

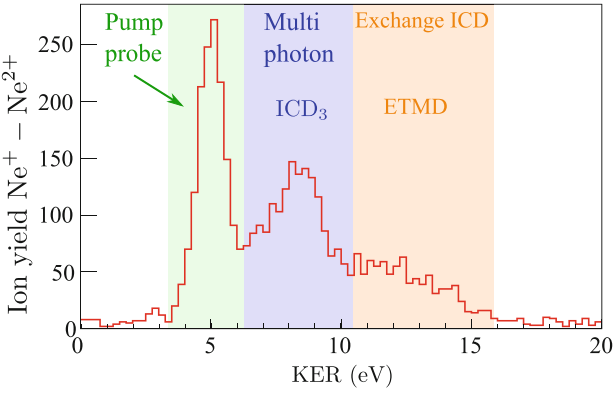

Fig. 7.16 KER spectrum of coincident $Ne^+ - Ne^{2+}$ ions at large delays. Note that the pump-probe region is extended up to 11 eV, when considering all delays

7.2.7 Simulation of Competing Processes

The time-dependent trace returning the ICD lifetime cannot overcome an energy of $\approx$11 eV, which corresponds to a Coulomb explosion at 2.6 Å. At this distance the $2^2\Sigma^+_{g,u}$ curves intersect the repulsive Ne^+-Ne^+ curves and for smaller R, ICD is energetically not possible anymore. Therefore the competing processes occurring via exchange ICD and ETMD, which arise in the KER spectrum at higher values than $\approx$11 eV, are suppressed by projecting only smaller KERs than that onto the delay axis. In fact, this was already done for the lifetime determination in Sect. 7.2.5. All time-independent processes will cause a constant offset for the ion yield but do not disturb the overall shape of the decay curve. The only remaining delay-dependent background stems from $Ne_2^+(2s^{-1})$ ions that are further ionized by the probe pulse to the $Ne-Ne^{2+}(2s^{-1}2p^{-1})$ state and decay via ICD_3. Thus we will further investigate the influence of this pathway on the lifetime fit by utilizing our classical pump-probe simulation.

The simulation starts by placing the classical particle on the intermediate $2^2\Sigma^+_u$ or $2^2\Sigma^+_g$ potential curve, let it evolve in time until ICD occurs or the probe pulse arrives. Only if the latter event takes place first, the particle is placed on the $Ne-Ne^{2+}(2s^{-1}2p^{-1})$ curve from where it decays onto a Coulombic Ne^+-Ne^{2+} curve. The lifetime of ICD_3 does not alter the delay-dependence of the Ne^+-Ne^{2+} ion yield as long as the lifetime is much shorter than radiative decay. This condition is well met and thus all dimers will decay via ICD_3. Therefore the population of the yield of coincident Ne^+-Ne^{2+} ions produced via the competing pathway is expected to be large at small delays and decreasing towards larger delays, which is inverse to the behavior of the primary ICD process.

Figure 7.17 shows the result of a simulation of the competing process with an input lifetime of 100 fs, starting from the equilibrium internuclear distance R_{eq}. The time-independent feature at 9 eV corresponds to the pathway via the intermediate state $2^2\Sigma^+_g$. It is constant because nuclear motion in the intermediate state is negligible and the decay of the doubly ionized dimer is assumed to be instantaneous. The ICD_3 time information is irrelevant for the ion yield as discussed earlier. Introducing the finite lifetime of ICD_3 into the simulation would yield a spread along the KER axis but it would not influence the delay-dependence. The time-dependent trace in the upper panel of Fig. 7.17 corresponds to the population of the intermediate $2^2\Sigma^+_u$ state. The nuclear motion causes the characteristic KER increase within the trace. As we probe the number of ions that still dwell in the intermediate $2s$ hole state the projection of the ion yield produced via the competing process also returns the input lifetime and could in principle also be used for the lifetime determination.

The population of the $Ne-Ne^{2+}(2s^{-1}2p^{-1}\,{}^1P)$ potential energy curve is only one possibility out of many that are reached after single-photon ionization of the intermediate $Ne_2^+(2s^{-1})$ ion. Thus, in order to evaluate the relevance of the competing process we will count the total number of accessible electronic states and compare it with the direct ICD pathway. Figure 7.8 shows only a small selection of accessible curves. A complete overview may be found in [38]. In Table 7.3 the four possible

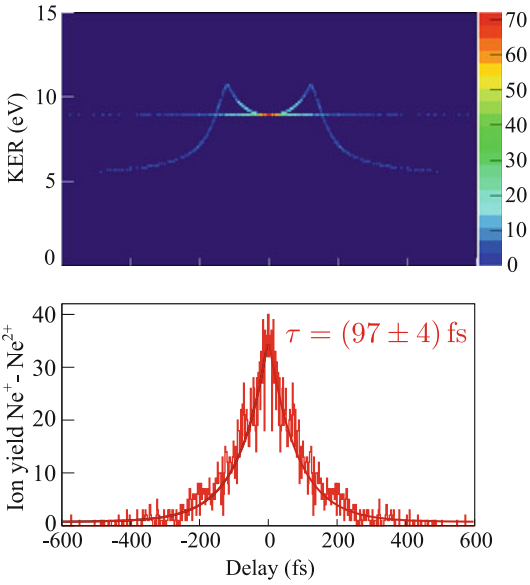

Fig. 7.17 Simulation of the competing process ICD_3 with an input lifetime of 100 fs. The *upper panel* shows the delay-dependent KER of $Ne^+ - Ne^{2+}$ ions and the *lower panel* shows the projection of all events onto the delay axis. An exponential fit (*in red*) also returns the ICD lifetime as the rate of competing ion pairs decreases at the rate the direct ICD rate increases

Table 7.3 Electronic states accessible via single-photon absorption by the $Ne^+(2s^{-1})$ ion, the competing ICD active state is colored red (upper most row)

Configuration	Spin multiplicity	Cross section (Mb)
$Ne-Ne^{2+}(2s^{-1}2p^{-1\,1}P)$	1	7
$Ne-Ne^{2+}(2s^{-1}2p^{-1\,3}P)$	3	7
$Ne^+(2p^{-1\,2}P)-Ne^+(2s^{-1\,2}S)$	2	7
$Ne^+(2s^{-1\,2}S)-Ne^+(2s^{-1\,2}S)$	2	0.5

In addition the spin multiplicity of each state is given. The cross section for each ionization step is that for isolated atoms and ions

electronic states are listed and weighted according to their spin multiplicity. Creating another $2s$ vacancy is unlikely and thus left out of the following considerations. Including the spin multiplicity, the possibility to access the $Ne-Ne^{2+}(2s^{-1}2p^{-1\,1}P)$ state is only 1/6 for a photon that is absorbed by the $Ne_2^+(2s^{-1})$ ion. Note that this is a pessimistic estimate as the third process in Table 7.3 should be more probable because a neutral Ne is ionized and ETMD and exchange ICD, which reduce the rate of ICD_3, are not taken into account.

In Fig. 7.18a comparison between a simulation including the competing pathway and one without is shown with an input lifetime of 100 fs. The direct and the competing process are normalized in the following way: Each dimer that has undergone ICD will end up in a $Ne^+ - Ne^{2+}$ state when further ionized by another photon from the probe. But only 1/6 of dimers that have not yet decayed via ICD will result in $Ne^+ - Ne^{2+}$ ion pairs. Therefore the contribution of the competing process in the

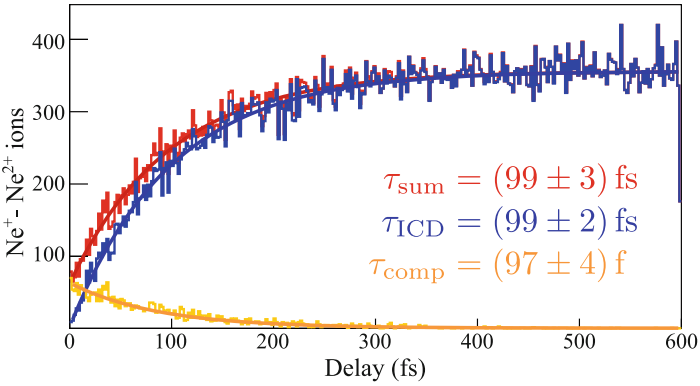

Fig. 7.18 Simulation of the $Ne^+ - Ne^{2+}$ ion yield for the direct ICD (*blue*), the competing pathway (*orange*) and the superposition of both (*red*). The results of an exponential fit for the respective spectra are also given

simulation has been decreased by a factor of 6. The lifetime fit of the total ion yield is almost unaffected. Thus ICD_3 does not disturb the lifetime determination.

7.2.8 Discussion of the Lifetime and Comparison with Theory

In order to determine the ICD lifetime we have assumed that the recorded ion yield can be approximated by an exponential fit. However this is only true for a dimer remaining at a fixed internuclear distance before ICD occurs. As the decay width Γ is R-dependent, the theoretically calculated ICD lifetime is different for all R as shown in Fig. 7.19. In the experiment it is impossible to switch off nuclear motion

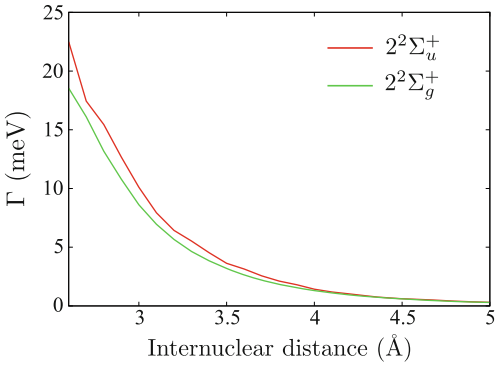

Fig. 7.19 Decay width Γ for ICD in $Ne^+(2s^{-1})$ for both intermediate states as a function of the internuclear distance, calculated with the Fano-ADC method [1]

and thus we measure a decay time averaged over all internuclear distances that are covered from the creation of the inner-valence vacancy to the arrival of the probe pulse. The data include wave packet dynamics in the intermediate state up to 600 fs, the longest delay in the measurement, and an additional broadening due to the spatial width the ground state wave function.

The internuclear distance at which the decay of a dimer occurred is imprinted in the KER. However, in practice the KER does not carry information on how the dimer reached that distance and how long it took for the decay. If all dimers started at R_{eq} on a known potential energy curve we could determine the lifetime of each dimer by the KER only. In the experiment it is not possible to assign the observed events to one of the two different intermediate states because both overlap energetically. For a measurement that detected also the ICD electrons the assignment to an intermediate state would be possible to some extend by considering the angular distribution of the electrons [12]. In addition the KER distribution is smeared out by the width of the squared ground state wave function, as shown in Fig. 7.11. Thus we are neither able to access individual particle information, nor trace back individual dimer lifetimes. In the real experiment the situation is further complicated by the finite pulse width, contributions from multi-photon absorption, limited statistics and limited resolution. Therefore we have to average over both intermediate states and all dynamics taking place within 600 fs, which we do by assuming an exponential slope.

Thus, it is not possible to compare our result to purely electronic calculations performed at a fixed internuclear distance of $R = 3.2$ Å that were presented in Sect. 2.5.1.3. These calculations give values for the decay time ranging from 64 fs to 92 fs [1, 30, 41], which is significantly shorter than our value and therefore hints towards the need for the inclusion of nuclear motion.

Calculations including nuclear dynamics require the knowledge of Γ as a function of the internuclear distance. The determination of Γ for a single R is already time-consuming, thus the decay width is usually calculated for a few internuclear distances only and interpolated in between (cf. Fig. 7.19). In Fig. 7.20a comparison of three different Γ calculations is shown including nuclear motion. The methods and the respective Γ were already introduced and compared in Sect. 2.5.1.3. The calculations accounting for nuclear motion were performed starting from the vibrational ground state with the time-dependent propagation of wave packets, which was discussed in Sect. 2.5.1.4.

We start by discussing the green curves calculated via the CAP-CI method, which shows the least agreement with our measured lifetime, as its prediction is much longer. It was expected that the agreement of this calculation would be rather poor as it showed already a large deviation from the other calculation before nuclear motion was added. The curve of the CAP-MRCI method, shown in purple, was obtained by inferring the R-dependence from the CAP-CI result by scaling it to the single data point calculated with the former. Although this calculation shows better agreement, it clearly underestimates the lifetime. The Fano-ADC result, shown in red, gives the best agreement and lies within the error bars of our data. The strongest deviation of the calculations from the exponential shape occurs for large delays. This is plausible

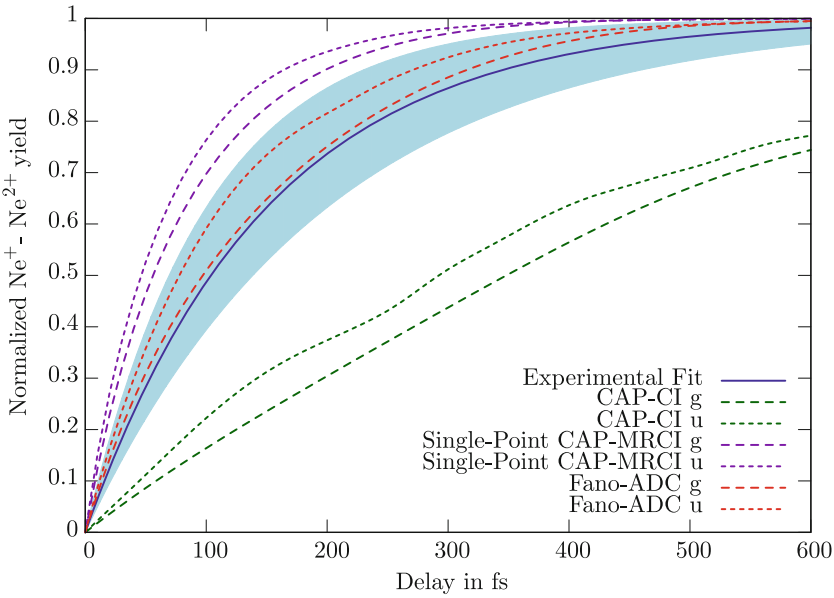

Fig. 7.20 Delay-dependent $Ne^+ - Ne^{2+}$ ion yield for calculations including nuclear motion, starting from the vibrational ground state and comparison to our experimental result (*dark blue*) with uncertainty (*light blue area*). For theory both intermediate states are indicated, *long dashed lines* stand for the $2^2\Sigma_g^+$ state and *short dashed lines* for the $2^2\Sigma_u^+$ state

because the assumption of an exponential decay gets worth the longer the wave packet is given to evolve in time. The distribution of internuclear distances in the intermediate state changes, which strongly influences the lifetime.

Figure 7.21 is similar to the previously discussed Fig. 7.20 with the difference that the wave packet calculations are performed starting from the first excited vibrational state. The agreement is much worse and demonstrates nicely the strong dependence on the ground state. In Fig. 7.4 both vibrational levels in the electronic ground states were shown: The excited state is extended towards larger R where the decay width decreases strongly. Thus a larger lifetime is expected compared to the ground state wave function centered at smaller R.

In conclusion, our measurement agrees only well with theory if nuclear motion prior to the decay is included in the calculations. From this we infer the importance of nuclear motion for small systems, such as Ne_2, undergoing ICD.

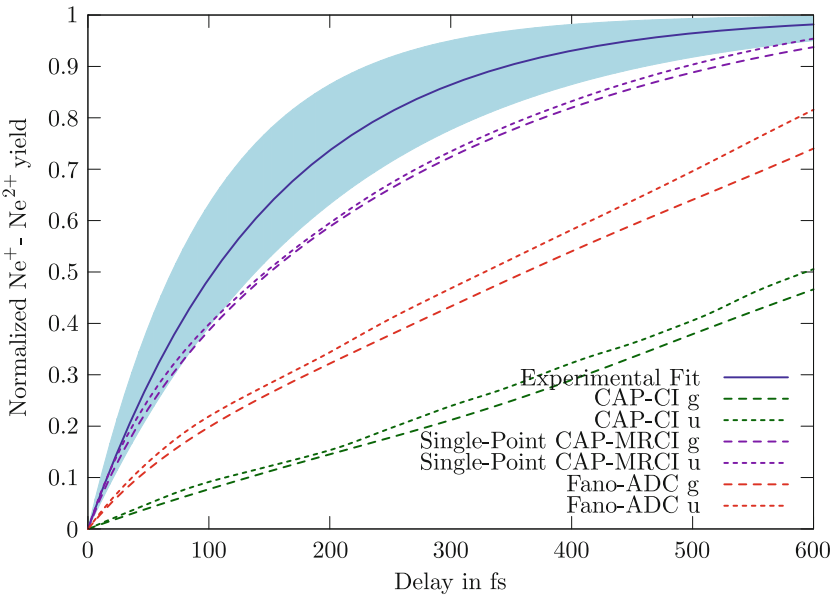

Fig. 7.21 Delay-dependent $Ne^+ - Ne^{2+}$ ion yield for calculations including nuclear motion, starting from the first excited vibrational state and comparison to our experimental result (*dark blue*) with uncertainty (*light blue area*). For theory both intermediate states are indicated, long *dashed lines* stand for the $2^2\Sigma_g^+$ state and *short dashed lines* for the $2^2\Sigma_u^+$ state

References

1. V. Averbukh, L.S. Cederbaum, Calculation of interatomic decay widths of vacancy states delocalized due to inversion symmetry. J. Chem. Phys. **125**, 094107 (2006)
2. V. Averbukh, I.B. Müller, L.S. Cederbaum, Mechanism of interatomic Coulombic decay in clusters. Phys. Rev. Lett. **93**, 263002 (2004)
3. V. Averbukh, L.S. Cederbaum, Interatomic electronic decay in endohedral fullerenes. Phys. Rev. Lett. **96**, 053401 (2006)
4. V. Averbukh, P. Kolorenc, Collective interatomic decay of multiple vacancies in clusters. Phys. Rev. Lett. **103**, 183001 (2009)
5. K. Bartschat, D.V. Fursa, I. Bray, A detailed study of electron impact ionization of Ne(2s) and Ar(3s). J. Phys. B Atm. Mol. Opt. Phys. **43**(12), 125202 (2010)
6. P.V. Demekhin et al., Exploring interatomic coulombic decay by free electron lasers. Phys. Rev. Lett. **107**, 273002 (2011)
7. P.V. Demekhin et al., Interatomic Coulombic decay and its dynamics in NeAr following K-LL Auger transition in the Ne atom. J. Chem. Phys. **131**, 104303 (2009)
8. A. Furuhama, M. Dupuis, K. Hirao, Reactions associated with ionization in water: a direct ab initio dynamics study of ionization in $(H_2O)_{17}$. J. Chem. Phys. **124**(16), 164310 (2006)
9. D.C. Griffin, D.M. Mitnik, N.R. Badnell, Electron-impact excitation of Ne^+. J. Phys. B Atm. Mol. Opt. Phys. **34**(22), 4401 (2001)
10. T. Jahnke et al., Experimental observation of interatomic Coulombic decay in neon dimers. Phys. Rev. Lett. **93**, 163401 (2004)
11. T. Jahnke et al., Experimental separation of virtual photon exchange and electron transfer in interatomic Coulombic decay of neon dimers. Phys. Rev. Lett. **99**, 153401 (2007)

12. T. Jahnke et al., Photoelectron and ICD electron angular distributions from fixed-in-space neon dimers. J. Phys. B Atm. Mol. Opt. Phys. **40**, 2597 (2007)
13. T. Jahnke et al., Ultrafast energy transfer between water molecules. Nat. Phys. **6**, 139 (2010)
14. T. Jahnke et al., Vibrationally resolved K-shell photoionization of CO with circularly polarized light. Phys. Rev. Lett. **93**, 083002 (2004)
15. T. Jahnke, Interatomic Coulombic decay—experimentelle untersuchung eines neuartigen, interatomaren Abregungsmechanismus, p. 201, PhD thesis. Frankfurt (2005)
16. V. Kaufman, L. Minnhagen, Accurate ground-term combinations in Ne I. J. Opt. Soc. Am. **62**(1), 92–95 (1972)
17. L.H.J.H. Kjeldsen, Absolute photoionization cross sections: measurements and applications. PhD thesis, University of Aarhus (2006)
18. A.E. Kramida, G. Nave, New FTS measurements, optimized energy levels and refined VUV standards in the Ne III spectrum. Eur. Phys. J. D Atm. Mol. Opt. Plasma Phys. **37**(1), 1–21 (2006)
19. K. Kreidi et al., Photo- and Auger-electron recoil induced dynamics of interatomic Coulombic decay. Phys. Rev. Lett. **103**, 033001 (2009)
20. K. Meyer et al., Noisy optical pulses enhance the temporal resolution of pump- probe spectroscopy. Phys. Rev. Lett. **108**, 098302 (2012)
21. N. Moiseyev et al., Fingerprints of the nodal structure of autoionizing vibrational wave functions in clusters: interatomic Coulombic decay in Ne dimer. J. Chem. Phys. **114**, 7351 (2001)
22. M. Mucke et al., A hitherto unrecognized source of low-energy electrons in water. Nat. Phys. **6**, 143 (2010)
23. A. Niehaus, Analysis of post-collision interactions in Auger processes following near-threshold inner-shell photoionization. J. Phys. B Atm. Mol. Phys. **10**(10), 1845 (1977)
24. G. Öhrwall et al., Femtosecond interatomic Coulombic decay in free neon clusters: large lifetime differences between surface and bulk. Phys. Rev. Lett. **93**, 173401 (2004)
25. T. Ouchi et al., Interatomic Coulombic decay following Ne 1s Auger decay in NeAr. Phys. Rev. A **83**, 053415 (2011)
26. T. Ouchi et al., Three-electron interatomic Coulombic decay from the inner- valence double-vacancy states in NeAr. Phys. Rev. Lett. **107**, 053401 (2011)
27. W. Persson, The spectrum of singly ionized neon, Ne II. Phys. Scr. **3**(3–4), 133 (1971)
28. T. Pfeifer et al., Partial-coherence method to model experimental free-electron laser pulse statistics. Opt. Lett. **35**(20), 3441–3443 (2010)
29. A. Russek, W. Mehlhorn, Post-collision interaction and the Auger lineshape. J. Phys. B Atm. Mol. Phys. **19**(6), 911 (1986)
30. R. Santra, L.S. Cederbaum, An efficient combination of computational techniques for investigating electronic resonance states in molecules. J. Chem. Phys. **115**, 6853 (2001)
31. R. Santra, J. Zobeley, L.S. Cederbaum, Electronic decay of valence holes in clusters and condensed matter. Phys. Rev. B **64**, 245104 (2001)
32. R. Santra, L.S. Cederbaum, Coulombic energy transfer and triple ionization in clusters. Phys. Rev. Lett. **90**, 153401 (2003)
33. S. Scheit, L.S. Cederbaum, H.-D. Meyer, Time-dependent interplay between electron emission and fragmentation in the interatomic Coulombic decay. J. Chem. Phys. **118**, 2092 (2003)
34. S. Scheit et al., On the interatomic Coulombic decay in the Ne dimer. J. Chem. Phys. **121**, 8393 (2004)
35. S. Scheit, Private Communication
36. K. Schnorr et al., Time-resolved measurement of interatomic Coulombic decay in Ne_2. Phys. Rev. Lett. **111**, 093402 (2013)
37. K. Schulz et al., High-resolution experimental and theoretical study of singly and doubly excited resonances in ground-state photoionization of neon. Phys. Rev. A **54**, 3095–3112 (1996)
38. S.D. Stoychev et al., On the interatomic electronic processes following Auger decay in neon dimer. J. Chem. Phys. **129**, 074307 (2008)
39. S. Svensson et al., Electron shake-up and correlation satellites and continuum shake-off distributions in X-Ray photoelectron spectra of the rare gas atoms. J. Electr. Spectrosc. Relat. Phenom. **47**, 327–384 (1988)

40. F. Trinter et al., Evolution of interatomic Coulombic decay in the time domain. Phys. Rev. Lett. **111**, 093401 (2013)
41. N. Vaval, L.S. Cederbaum, Ab initio lifetimes in the interatomic Coulombic decay of neon clusters computed with propagators. J. Chem. Phys. **126**, 164110 (2007)
42. A. Wüest, F. Merkt, Determination of the interaction potential of the ground electronic state of Ne_2 by high-resolution vacuum ultraviolet laser spectroscopy. J. Chem. Phys. **118**(19), 8807–8812 (2003)
43. J. Yeh, I. Lindau, Atomic subshell photoionization cross sections and asymmetry parameters: $1 \leq Z \leq 103$. Atm. Data Nucl. Data Tables **32**(1), 1–155 (1985)
44. J. Zobeley, R. Santra, L.S. Cederbaum, Electronic decay in weakly bound heteroclusters: energy transfer versus electron transfer. J. Chem. Phys. **115**(11), 5076–5088 (2001)

Chapter 8
Conclusions and Outlook

In the course of this work time-resolved experiments on diatomic molecules have been carried out at the free-electron laser FLASH. Information on the induced processes were retrieved by reconstructing the initial three-dimensional momenta of all ionic fragments by means of a reaction microscope. First, the dissociation of multiply ionized iodine molecules I_2^{n+}, initiated and probed by intense XUV radiation, was traced. This allowed to follow the transition from a molecule to a regime in which the molecular constituents stop acting collectively and start behaving as individual atoms. Multi-photon absorption in both regimes was compared. Second, the most crucial parameter, the lifetime, of interatomic Coulombic decay (ICD), an efficient relaxation mechanism of weakly bound atoms, was determined with an XUV pump-probe experiment on neon dimers Ne_2. Both diatomic systems serve as prototypes for larger molecules allowing to study the reactions occurring therein, charge transfer and ICD, at the most comprehensive level between two atoms. The results of the experiments are summarized in the subsequent sections, followed by an outlook on the perspectives of follow-up experiments. In the latter we emphasize future experimental improvements.

8.1 Results from the I_2 Experiments

FELs have opened up the field of multi-photon absorption studies in the XUV and X-ray regime. Understanding the interaction of highly intense XUV and X-ray radiation with matter is fundamental for all applications of FELs. Here, we have investigated the dynamics of I_2 molecules in intense XUV radiation of up to $3 \times 10^{14}\ \frac{\mathrm{W}}{\mathrm{cm}^2}$ with single-pulse and pump-probe measurements.

The behavior of I_2 molecules in single XUV pulses was compared for two sets of beam parameters, one with shorter pulses (≈57 fs (FWHM)) and lower intensity ($10^{14}\ \frac{\mathrm{W}}{\mathrm{cm}^2}$), the other one with longer pulses (≈103 fs (FWHM))and higher intensity ($3 \times 10^{14}\ \frac{\mathrm{W}}{\mathrm{cm}^2}$). The wavelength of 87 eV was chosen close to the maximum

K. Schnorr, *XUV Pump-Probe Experiments on Diatomic Molecules*,
Springer Theses, DOI 10.1007/978-3-319-12139-0_8

of the $4d$ shape resonance in I_2 [6], which exhibits a large photoabsorption cross section of roughly 40 Mb. We were able to identify the pathways of multi-photon absorption in I_2 by comparison with Xe, which has a similar electronic structure and was investigated in great detail in earlier experiments [31]. Lower charge states are produced by sequences of single-photon absorption, while higher ones require the direct absorption of multiple photons. Up to two photons were absorbed directly for the low intensity study, resulting in the highest charge state I_2^{14+} and up to three photons for the higher intensity, resulting in I_2^{17+}.

The ionic fragments of highly charged molecular ions gain large momenta due to the Coulomb repulsion between the charged constituents. By comparing the measured kinetic energy release (KER) of the fragments with the expectation of a Coulomb explosion at the molecule's equilibrium internuclear distance R_{eq}, we were able to unravel effects caused by the finite FEL pulse length, the spatial width of the ground state and intramolecular dynamics. In general the measured KERs were lower than expected, with increasing deviation for the higher charge states. This was attributed to a delayed absorption of photons throughout the pulse, as well as intramolecular dynamics, e.g., delayed Auger decay. Both effects result in a delayed population of the final potential energy curve at larger internuclear distances, giving rise to a lower KER compared to a direct transition at the equilibrium internuclear distance. Two exceptions from the general trend of KERs lower than predicted were found: The fragments of molecules that dissociated into coincident $I^+ - I^+$ ion pairs showed higher KERs than expected because the potential energy curves deviate from Coulomb curves. Furthermore, the KER distribution of $I^+ - I^{3+}$ ion pairs was by significantly extended to higher values than expected, which was attributed to the resonant population of a highly excited state in I_2^{4+*} ions. The highly excited electron remains only so weakly bound that the detected KER is shifted to that of the next higher charge state, the I_2^{5+} molecular ion.

Some break-up channels, in particular those recorded with longer pulse durations, showed KER distributions with several distinct peaks that were extended to considerably lower KERs than expected. This indicated the population of certain intermediate charge states, which are detectable by XUV pump-probe experiments: The first XUV pulse populates an intermediate charge state by multiply ionizing I_2 and thereby initiating the dissociation into charged fragments that are further ionized after an adjustable delay by a copy of the first pulse. The analysis of the resulting time-dependent KER spectra at large delays enabled us to reconstruct the precursor charge states. Recalling the suggested multi-photon absorption pathways from the XUV single-pulse measurements, allowed to predict the possible precursor states for each fragmentation channel and to compare them to the observed ones. The good agreement of both encouraged us to simulate the pump-probe experiment by modeling the motion of dissociating molecules like that of point-like charged particles repelling each other with the Coulomb force. The time-dependence of the spectra was well reproduced, supporting the assumption of Coulombic potential energy curves. The KER of higher charge states was overestimated due to delayed ionization within one pulse.

The localized absorption of highly energetic photons leads to molecular constituents with high charge states. This induces electron rearrangement throughout the molecule in order to establish the most favorable energetic state. At the same time, the molecule typically starts to dissociate, which raises the question of how far relaxation through electron transfer within the molecule can proceed before it is fragmented into individual ions. This question has already been addressed in earlier experiments by means of ethyl- and methylsolenol, which found charge rearrangement accompanied by considerable displacement of the constituents within 5 fs X-ray pulses [11, 12]. However, the time and length scales of the processes remained open. Applying our pump-probe scheme, we were able to trace the dynamics of dissociating I_2^{n+} ions and thereby determined the critical distances R_{crit} up to which charge transfer took place. To do so, I_2 molecules were first multiply ionized and consequently dissociated, resulting in a target with time-dependent internuclear distance. Then, the delayed probe pulse initiated charge transfer between ions if they were closer to each other than R_{crit}, or the probe pulse further ionized only one of the fragments for distances larger than R_{crit}. Therefore, coincident ion pairs with asymmetric charge state distribution, i.e. I^{P+}–I^{Q+} with $|P-Q| \geq 2$, were only produced for separations larger than R_{crit}. In fact, many asymmetric fragmentation channels were completely absent for small time delays. The time-range where this depletion occurred was converted into an internuclear distance by comparison with the aforementioned pump-probe simulations. It was shown that electrons are transferred over distances larger than 10 au. Furthermore, the distances get larger with increasing charge states. This study mimics the situation of localized X-ray absorption at high-Z constituents, which is most relevant to understand the role of damage for coherent single-molecule imaging at XFELs [18].

The experimentally determined critical distances agree well with predictions from a classical over-the-barrier (COB) model [19, 23] for all asymmetric coincidence channels with one fragment being I^+. The COB model is routinely applied to model charge transfer in slow ion-atom collisions. As the ion energies emerging from Coulomb explosions are much smaller than those in slow collisions, we were able to test the model in a so far unexplored quasimolecular regime. We found excellent agreement with the model, which shows that the motion of the heavy iodine ions is well described by means of classical considerations. Understanding and modeling charge transfer, in particular at small ion energies, is for instance relevant for the interaction of ions with biomolecules [8–10] and for plasma reactions [3, 34].

An IR/XUV pump-probe study allowed to investigate the joint illumination of I_2 with a strong IR laser field, at the transition from multi-photon to tunnel ionization, and the weak XUV field, mostly leading to single- and few-photon absorption. As the IR laser acts on the least bound electrons in the outer-valence shells, it mostly produces neutrals and low charged ions that predominantly dissociate. In contrast, an XUV pulse interacts most efficiently with $4d$ inner-valence electrons and the absorption of a single photon produces a doubly or triply charged molecular ion. The question arises, which charge states are produced more efficiently with a preceding IR and delayed XUV pulse, and vice versa. It turned out that low- and intermediately-charged symmetric break-up channels were produced most efficiently

by first illuminating the molecule with an XUV pulse, followed by a delayed IR pulse. This was attributed to the efficient removal of remaining valence electrons by the IR laser. However, once the $5p$-type valence shell is depleted, a delayed IR pulse does not influence the final charge state anymore and the highest charge states are produced by the XUV alone. In contrast, as a preceding IR laser pulse mostly dissociates the molecule into neutral or low charged fragments, delayed XUV pulses impinge on spatially separated ions or atoms for large delays. Consequently, we have created a situation in which we can directly compare the response of isolated atoms to intense XUV radiation with that of molecules. This raised the question which of both is ionized more efficiently. We found the highest charge states for dissociated molecules, which is due to an effect we refer to as Coulomb blocking: The ionization potential of an ion is increased in the vicinity of another ion, which may hinder the removal of the next electron. For separated ions, the influence of the neighboring ion is fading, which may allow higher charged fragments. These results are in contrast to experiments on large Xe clusters, which were charged significantly higher than the respective monomers [35]. While collective effects determine the behavior of clusters [27, 30], the small I_2 molecule is better described in the picture of interacting ions. It is an interesting question to investigate from which cluster size onwards collective phenomena take over.

8.2 Results from the Ne_2 Experiments

The second experiment presented in this thesis investigated an efficient relaxation mechanism occurring in weakly bound systems, such as rare-gas and van-der-Waals clusters: Interatomic or intermolecular Coulombic decay (ICD). In ICD an excited monomer ion relaxes by transferring its excess energy to a neighboring monomer, which is consequently ionized [5]. The initial ionization typically also triggers nuclear motion, which is a crucial point as the decay probability of ICD is heavily dependent on the internuclear separation between the monomers [26]. The respective decay times were predicted to be only a few femtoseconds for large clusters [2, 25] and around 100 fs for dimers [7, 24, 32]. Thus, nuclear motion, which takes place on typical time scales of hundred to a few hundred femtoseconds, is negligible for the large systems. This assumption was exploited for the first ICD lifetime determination in large Ne clusters, which yielded 6 fs for a $2s$ vacancy in Ne^+ [20]. In order to account for nuclear motion, which is needed for smaller systems, other methods have to be employed. The lifetime can be determined by comparing electron and KER spectra with theoretical counterparts that include the motion of the nuclei prior to the decay. However, this method relies heavily on the accuracy of theory. The drawback of this technique was demonstrated in a study on NeAr, where the theoretically predicted decay width seemed about a factor of two too large when compared to experimental data [21]. Another method to extract information on the temporal evolution of ICD employing post-collision interaction was recently presented [33]. These previous experiments were performed in the frequency domain. In contrast, we have

accessed the dynamics of ICD directly in the time domain by an XUV pump-probe experiment. We have performed a time-resolved measurement on $2s$ ionized neon dimers undergoing ICD and determined an ICD lifetime for the first time directly.

In order to interpret the spectra emerging from two consecutive XUV pulses, we first analyzed the interaction of a single 60 fs (FWHM) XUV pulse of 58.2 eV with Ne_2 by identifying the accessible states. The most important channel is fragmentation into $Ne^+ - Ne^+$: It is predominantly produced by a single photon through population of an intermediate $Ne^+(2s^{-1})$ state, which then decays into coincident $Ne^+ - Ne^+$ ion pairs via ICD. This pathway was identified for a KER region from 3 to 5.5 eV, which agrees well with the expectation of a Coulomb-explosion model. The KER spectrum of $Ne^+ - Ne^+$ ions featured another contribution that was assigned to $2p$ shake-up states that relax by electron transfer [14]. As relaxation via this channel requires a certain degree of orbital overlap it occurs only for smaller internuclear distances, thus yielding larger KERs.

The applied XUV pump-probe scheme for the ICD lifetime determination is based on triggering ICD with one photon from the pump pulse, leaving a $2s$ vacancy in either of the Ne atoms. Thereby, it initiates a nuclear wave packet in the intermediate $2^2\Sigma_g^+$ or $2^2\Sigma_u^+$ state of the Ne_2^+ molecular ion. The delayed probe pulse tests the number of dimers that have already undergone ICD into $Ne^+ - Ne^+$ by further ionizing one of the fragments with a single photon, which results in coincident $Ne^+ - Ne^{2+}$ ion pairs. The presented scheme relies on single-photon absorption within the pump and the probe pulse. Therefore, the experiment was performed at a relatively low intensity of $10^{12}\ \frac{\mathrm{W}}{\mathrm{cm}^2}$ in order to suppress multi-photon processes. Nevertheless, the recorded delay-dependent $Ne^+ - Ne^{2+}$ KER spectra showed events from single pulse multi-photon ionization ontop of the pump-probe contribution that contains the ICD lifetime. From a classical pump-probe simulation we learned that the delay-dependent yield of $Ne^+ - Ne^{2+}$ ions increases with an approximately exponential dependence that reflects the ICD lifetime. As other pathways than the presented one may also lead to a delay-dependent $Ne^+ - Ne^{2+}$ ion yield, it is crucial to analyze the accessible potential energy curves in Ne_2. Particularly, one further state relaxing via ICD was identified that produces a time-dependent background of $Ne^+ - Ne^{2+}$ ions. Nonetheless, our classical simulations showed that the contribution of this state is negligible. By fitting the recorded delay-dependent yield of $Ne^+ - Ne^{2+}$ ions with an exponential, we extracted a lifetime of $150 \pm (50)$ fs.

Our result is significantly larger than expected from quantum mechanical ab initio calculations that neglect nuclear motion. Therein, the decay width was usually calculated for the equilibrium internuclear distance. This assumption is not consistent with our experimental results. There, the ground state already exhibits a spatial width according to the extension of the squared ground state wave function and additional nuclear dynamics taking place in the intermediate states. Thus, in order to compare our result to theoretical calculations, they have to include nuclear motion. This has been done by calculating the decay widths for various internuclear distances and performing time-dependent wave-packet propagation calculations on the involved potential energy curves with the distance-dependent decay rate [28]. If

such dynamical calculations are performed using the decay width obtained via the Fano-ADC method [1], the predicted delay-dependent ion yield agrees well with the experimental data. However, we stress that this is only true for dynamical calculations. Hence, we conclude that nuclear motion significantly affects the dynamics of ICD. The determined lifetime is averaged over both intermediate $2^2\Sigma_g^+$ or $2^2\Sigma_u^+$ states and the dynamics taking place between the pump and the probe pulse. As both states feature different lifetimes it would be desirable to distinguish them, which might be possible by recording electrons in coincidence. Choosing a different system with only one intermediate state, such as NeAr, would also overcome this difficulty and is an option for future experiments. We would also like to extend our time-resolved studies to hydrogen bound clusters, such as ammonia and water dimers. In particular, water is of high significance because ICD is expected to strongly influence radiation tumor therapy through the creation of low-energetic electrons [4, 13].

8.3 Outlook

The presented experiments, as well as earlier ones are constrained by the limited availability of beam time at FLASH. The need for higher statistics is obvious in the Ne_2 experiment. The difficulty of the measurement is easily demonstrated by an instructive estimate: Taking into account the small amount of dimers present in the gas jet, the cross section for 2*s* photoionization and the present FEL intensity yields a rate of 0.15 dimers per shot that decay via ICD. However, the same dimer must be probed, which reduces the event rate to 0.005 per shot. In addition, the probability of detecting two ions in coincidence is only 10 %, which illustrates the need of sufficient count rates. Therefore it would be desirable to have longer measurement periods and higher repetition rates. Within the next year FLASH II, the extension of the current FLASH facility, will become operational. The electron beams for FLASH and FLASH II will be delivered by the currently operating linear accelerator, but both will have their own undulators, which will enable to generate FEL radiation for two experiments at the same time. Our REMI for FLASH will be installed as a permanent endstation at FLASH II. This will increase the amount of available beam time. However, a more drastic gain in statistics is achievable with an increased repetition rate, which is coming in reach at FLASH. New developments are also driven by the demanding requirements for the European XFEL, which is planned to have a repetition rate of 27 kHz [36].

Large statistics are also needed for experiments aiming at detecting more than two particles in coincidence. This is for instance needed to retrieve structural information by Coulomb-explosion imaging on molecules with more than two constituents. The potential of this technique was recently exploited by reconstructing the configuration of the chiral molecule bromochlorofluoromethane (CHBrClF) with the coincident detection of all 5 charged fragments [22]. The feasibility of time-resolved Coulomb-explosion imaging experiments at FELs was also demonstrated by means of the acetylene molecule undergoing isomerization with an XUV pump-probe measurement

[15, 16]. Further studies of structural isomerization, such as the ring formation in allene are planned for the future. Instead of applying XUV pulses as pump and probe pulse, other molecular reactions could also be initiated with visible and UV lasers and probed by intense XUV or X-ray lasers.

In addition, we are currently modifying our setup to improve coincident electron detection. Recently, XUV-pump–THz-probe experiments on electrons emitted from Ne [29] and N_2 [17] were performed with the goal of studying time shifts between the emission of fast and slow electrons. A new split-mirror setup based on gracing-incidence optics instead of back reflection is currently designed in order to avoid stray light from our current mirror hindering electron detection. This will for instance enable time-resolved studies of correlated electron dynamics.

References

1. V. Averbukh, L.S. Cederbaum, Calculation of interatomic decay widths of vacancy states delocalized due to inversion symmetry. J. Chem. Phys. **125**, 094107 (2006)
2. V. Averbukh, L.S. Cederbaum, Interatomic electronic decay in endohedral fullerenes. Phys. Rev. Lett. **96**, 053401 (2006)
3. P. Beiersdorfer et al., Laboratory simulation of charge exchange-produced X-ray emission from comets. Science **300**(5625), 1558–1559 (2003)
4. B. Boudaïffa et al., Resonant formation of DNA strand breaks by low-energy (3 to 20 eV) electrons. Science **287**(5458), 1658–1660 (2000)
5. L.S. Cederbaum, J. Zobeley, F. Tarantelli, Giant intermolecular decay and fragmentation of clusters. Phys. Rev. Lett. **79**, 4778 (1997)
6. F.J. Comes, U. Nielsen, W.H.E. Schwarz, Inner electron excitation of iodine in the gaseous and solid phase. J. Chem. Phys. **58**(6), 2230–2237 (1973)
7. P.V. Demekhin et al., Interatomic Coulombic decay and its dynamics in NeAr following K-LL Auger transition in the Ne atom. J. Chem. Phys. **131**, 104303 (2009)
8. Z. Deng et al., Beyond the Bragg peak: hyperthermal heavy ion damage to DNA components. Phys. Rev. Lett. **95**, 153201 (2005)
9. Z. Deng et al., Reactive scattering damage to DNA components by hyperthermal secondary ions. Phys. Rev. Lett. **96**, 243203 (2006)
10. J. de Vries et al., Charge driven fragmentation of nucleobases. Phys. Rev. Lett. **91**, 053401 (2003)
11. B. Erk et al., Inner-shell multiple ionization of polyatomic molecules with an intense x-ray free-electron laser studied by coincident ion momentum imaging. J. Phys. B: At. Mol. Opt. Phys. **46**(16), 164031 (2013)
12. B. Erk et al., Ultrafast charge rearrangement and nuclear dynamics upon inner-shell multiple ionization of small polyatomic molecules. Phys. Rev. Lett. **110**, 053003 (2013)
13. P. Harbach et al., Intermolecular Coulombic decay in biology: the initial electron detachment from FADH- in DNA photolyases. J. Phys. Chem. Lett. **4**, 943 (2013)
14. T. Jahnke et al., Experimental separation of virtual photon exchange and electron transfer in interatomic Coulombic decay of neon dimers. Phys. Rev. Lett. **99**, 153401 (2007)
15. Y.H. Jiang et al., Ultrafast dynamics in acetylene clocked in a femtosecond XUV stopwatch. J. Phys. B: At. Mol. Opt. Phys. **46**(16), 164027 (2013)
16. Y. Jiang et al., Ultrafast extreme ultraviolet induced isomerization of acetylene cations. Phys. Rev. Lett. **105**, 263002 (2010)
17. J. Kunz, Analysis of time delays in photoionization of N2 in XUV-THz pump- probe experiments at FLASH. Master thesis. University Heidelberg, 2013

18. R. Neutze et al., Potential for biomolecular imaging with femtosecond X-ray pulses. Nature **406**(6797), 752–757 (2000)
19. A. Niehaus, A classical model for multiple-electron capture in slow collisions of highly charged ions with atoms. J. Phys. B: At. Mol. Phys. **19**(18), 2925 (1986)
20. G. Öhrwall et al., Femtosecond interatomic Coulombic decay in free neon clusters: large lifetime differences between surface and bulk. Phys. Rev. Lett. **93**, 173401 (2004)
21. T. Ouchi et al., Interatomic Coulombic decay following Ne 1s Auger decay in NeAr. Phys. Rev. A **83**, 053415 (2011)
22. M. Pitzer et al., Direct determination of absolute molecular stereochemistry in gas phase by Coulomb explosion imaging. Science **341**(6150), 1096–1100 (2013)
23. H. Ryufuku, K. Sasaki, T. Watanabe, Oscillatory behavior of charge transfer cross sections as a function of the charge of projectiles in low-energy collisions. Phys. Rev. A **21**, 745–750 (1980)
24. R. Santra, L.S. Cederbaum, An efficient combination of computational techniques for investigating electronic resonance states in molecules. J. Chem. Phys. **115**, 6853 (2001)
25. R. Santra, J. Zobeley, L.S. Cederbaum, Electronic decay of valence holes in clusters and condensed matter. Phys. Rev. B **64**, 245104 (2001)
26. R. Santra et al., Interatomic Coulombic decay in van der Waals clusters and impact of nuclear motion. Phys. Rev. Lett. **85**, 4490 (2000)
27. R. Santra, C.H. Greene, Xenon clusters in intense VUV laser fields. Phys. Rev. Lett. **91**, 233401 (2003)
28. S. Scheit et al., On the interatomic Coulombic decay in the Ne dimer. J. Chem. Phys. **121**, 8393 (2004)
29. G. Schmid, XUV-pump THz-probe experiments on neon at the free-electron laser in Hamburg. Master thesis. University Heidelberg, 2013
30. C. Siedschlag, J.-M. Rost, Small rare-gas clusters in soft X-ray pulses. Phys. Rev. Lett. **93**, 043402 (2004)
31. A.A. Sorokin et al., Photoelectric effect at ultrahigh intensities. Phys. Rev. Lett. **99**, 213002 (2007)
32. S.D. Stoychev et al., On the interatomic electronic processes following Auger decay in neon dimer. J. Chem. Phys. **129**, 074307 (2008)
33. F. Trinter et al., Evolution of interatomic Coulombic decay in the time domain. Phys. Rev. Lett. **111**, 093401 (2013)
34. M. von Hellermann et al., Investigation of thermal and slowing-down alpha particles on JET using charge-exchange spectroscopy. Plasma Phys. Control. Fusion **33**(14), 1805 (1991)
35. H. Wabnitz et al., Multiple ionization of atom clusters by intense soft X-rays from a free-electron laser. Nature **420**(6915), 482–485 (2002)
36. XFEL (2013). Technical design report. http://xfel.desy.de/technical_information/

Appendix
Units

Throughout this thesis, wherever physical quantities are given, we tried to ensure that they are presented in the most appropriate unit system. Whenever several representations could prove useful, all of them are shown. This should ensure convenient reading on the one hand and straight-forward comparison of the numbers on the other. Nevertheless, a brief overview of the applied unit systems and of the conversions from one to another is presented in the following.

A.1 Atomic Units

The *International System of Units* (abbreviated SI from French: *Le Système international d'unités*) is not always the most convenient choice. Particularly, for quantities on the molecular or the atomic scale the system of *atomic units* (au) allows a much better grasp of the occurring quantities. As they are *natural units*, au are based on universal physical constants as measures. These constants are chosen to represent the dimensions of the electronic motion in an atom. This is underlined by the strong connection between au and the hydrogenic ground state as described by the Bohr model.

There are two variants of au[1], Rydberg and Hartree units, differing in their choice of the unit of mass and charge. We only make use of the latter, which is gained by setting the electron mass, the elementary charge, the reduced Planck constant and the electrostatic constant to unity:

$$m_e = e = \hbar = \frac{1}{4\pi\epsilon_0} \stackrel{!}{=} 1. \tag{A.1}$$

[1] The abbreviation au might also lead to confusion with *astronomical* or *arbitrary units*. Particularly the latter is thus not used in this work.

K. Schnorr, *XUV Pump-Probe Experiments on Diatomic Molecules*,
Springer Theses, DOI 10.1007/978-3-319-12139-0

Table A.1 Overview of the numerical values of fundamental atomic units

Constant	Symbol	Dimension	SI value
Electron rest mass	m_e	Mass	9.109×10^{-31} kg
Elementary charge	e	Charge	1.602×10^{-19} C
Reduced Planck constant	$\hbar = h/2\pi$	Action	1.054×10^{-34} J s
Electrostatic constant	$1/4\pi\epsilon_0$	Inverse ϵ_0	8.987×10^{9} kg m^3/s^{2}C^2

Here, the vacuum permittivity $\epsilon_0 = 8.854 \times 10^{-12} \frac{\mathrm{F}}{\mathrm{m}}$ is used

Table A.2 Overview of the numerical values of some derived atomic units

Constant	Symbol	Dimension	SI value	Alternative units
Bohr radius	$a_0 = \hbar/m_e\alpha c$	Length	5.292×10^{-11}m	0.529Å
Hartree	$H = m_e\alpha^2c^2$	Energy	4.360×10^{-18}J	27.211 eV
	$\hbar/H$	Time	2.419×10^{-17}s	

Two convenient alternative representations are given, as discussed in Sect. A.2. Note that the au of time corresponds to the time an electron needs for one revolution on the ground state orbit of hydrogen according to the Bohr model

An overview of the numerical values of these constants in SI units is given in Table A.1. From the above definition we can directly infer two important physical constants. The proton mass in SI units can be written $m_p = 1836.153 \cdot m_e$, thus the au equivalent reads $m_p \approx 1836$ au. Using the definition of the dimensionless fine-structure constant

$$\alpha = \frac{e^2}{4\pi\epsilon_0\hbar c} = \frac{1}{137.036} \tag{A.2}$$

and the knowledge that dimensionless constants retain their value independent of the unit system, we can give the vacuum speed of light c in atomic units:

$$c = \frac{1}{\alpha} \approx 137. \tag{A.3}$$

From the fundamental atomic units above a full set of units may be derived, a subset of which is given in Table A.2.

A.2 Other Commonly Used Units

For quantities with the dimension energy, several commonly used representations are available. Besides the SI unit Joule (J) and the atomic unit Hartree (H) (cf. Sect. A.1), the electron volt (eV) is used throughout this work. It is defined as the amount of energy gained by moving an elementary charge e across an electric potential difference of 1V:

$$1\text{eV} = 1.602 \times 10^{-19}\,\text{J}. \tag{A.4}$$

It is also common practice to give quantities that are not energies in eV by applying mass-energy equivalence $E = mc^2$, with the relativistic mass $m = \gamma m_0$, the rest mass m_0, the Lorentz-factor $\gamma = 1/\sqrt{1-\beta^2}$ and the velocity in units of the speed of light in vacuum $\beta = v/c$. For example, the electron rest mass m_e is often given as $m_e = 511\,\text{keV}/c^2$.

Additionally, due to the relation between the frequency ν, the wavelength λ, and the energy of a photon,

$$E = h\nu = \frac{hc}{\lambda}, \tag{A.5}$$

with the Planck constant $h = 6.626 \times 10^{-34}$ J s, the convenient conversion formula

$$E[\text{eV}] \approx \frac{1240}{\lambda[\text{nm}]} \tag{A.6}$$

is widely used.

Eventhough, the atomic unit of length, the Bohr radius a_0 (cf. Sect. A.1), provides a measure on the atomic scale, another length unit is also commonly used, the Ångström denoted by Å:

$$1\text{Å} = 10^{-10}\text{m} \approx 2a_0. \tag{A.7}$$

Obviously it describes the diameter of the lowest orbit in hydrogen, as a_0 is the corresponding radius.